Molecular dynamics simulations of the equilibrium dynamics of non-ideal plasmas

James Patrick Mithen

Trinity College

University of Oxford

A thesis submitted for the degree of

Doctor of Philosophy

Hilary term, 2012

This thesis is dedicated to
Jerome Daligault
for his guidance, encouragement and support.

Molecular dynamics simulations of the equilibrium dynamics of non-ideal plasmas

James Mithen

Trinity College, University of Oxford

A thesis submitted for the Degree of Doctor of Philosophy

Hilary term, 2012

Abstract

Molecular dynamics (MD) simulations are used to compute the equilibrium dynamics of a single component fluid with Yukawa interaction potential $v(r) = (Ze)^2 \exp(-r/\lambda_s)/4\pi\epsilon_0 r$. This system, which is known as the Yukawa one-component plasma (YOCP), represents a simplified description of a non-ideal plasma consisting of ions, charge Ze, and electrons.

For finite screening lengths λ_s, the MD results are used to investigate the domain of validity of the hydrodynamic description, i.e., the description given by the Naviér-Stokes equations. The way in which this domain depends on the thermodynamic conditions of the YOCP, as well as the strength and range of the interactions, is determined. Remarkably, it is found that the domain of validity is completely determined by the range of the interactions (i.e., λ_s); this alone determines the maximum wave number k_{max} at which the hydrodynamic description is applicable.

The dynamics of the YOCP at wavevectors beyond k_{max} are then investigated; these are shown to be in striking agreement with a simple and well known generalisation of the Naviér-Stokes equations.

In the extreme case of the Coulomb interaction potential ($\lambda_s = \infty$), the very existence of a hydrodynamic description is a known but unsolved problem [Baus & Hansen, 1980]. For this important special case, known as the one-component plasma (OCP), it is shown that the ordinary hydrodynamic description is never valid.

Since the OCP is the prototypical system representing a non-ideal plasma, a number of different approaches for modelling its dynamics have been formulated previously. By computing the relevant quantities with MD, the applicability of a number of models proposed in the literature is examined for the first time.

Acknowledgements

Thanks must go primarily to Jerome Daligault at Los Alamos National Laboratory (LANL), whose selfless guidance served to inform, inspire, and motivate in equal measure. The vast majority of the work presented in this thesis was done with help from Jerome during a series of visits to LANL, and through ongoing discussions thereafter. For this I also extend thanks to all of the staff at the lab who were kind enough to facilitate my visits, and to the plasma theory group members who were always friendly and accommodating.

I'd like to thank my supervisor at Oxford, Gianluca Gregori, for providing me with much needed resources and opportunities throughout the project. Hopefully this thesis will provide something to build upon for the future.

Finally, thanks are due to my fellow group members of past and present, Tom, Robin, Chris, Megan and Katja, whose insight and company was always appreciated.

Role of the author in this work

This thesis is devoted to the presentation, analysis and discussion of results from computer simulations of non-ideal plasmas. The results were all produced using a 'molecular dynamics' (MD) code, named 'CoulMD', written by Dr. Jerome Daligault of Los Alamos National Laboratory.

The MD simulations were all performed by the author using a variety of computational resources: the machines at the Oxford Supercomputing Center, the plasma theory group computer cluster at Los Alamos National Laboratory, and the 'cplxint1' machine in the physics department at Oxford. The analysis of the MD data was all performed by the author. To accomplish this, minor modifications were made to a few of the FORTRAN subroutines in CoulMD, and methods to produce high quality data from the raw output of the code, as discussed in Section 3.11, were devised and implemented.

Most of the original research presented in this thesis is contained in Chapters 4-8. The various theoretical models that are compared to the MD data throughout these chapters were all implemented (programmed on computer) by the author. The discussion and conclusions of these chapters represent the outcome of ongoing discussions between the author and Dr. Jerome Daligault. Most of this work has already been published in peer reviewed journals: the research in Chapters 4 and 6 is based on [Mithen *et al.*, 2011b]; Chapter 5 is based on [Mithen *et al.*, 2011a]; Chapter 7 is based on [Mithen *et al.*, 2012a]; Chapter 8 is based on [Mithen *et al.*, 2012b]. Finally, some of the results presented in Appendix H were given previously in [Mithen *et al.*, 2012c]. All of these publications are co-authored papers. The other authors, Dr. Jerome Daligault, Dr. Gianluca Gregori and Prof. Basil Crowley, assisted the author with the writing and revision of the relevant manuscripts both before and after submission.

In the course of the research the author has contributed to experimental work that has led to co-authoring a number of journal articles. None of this experimental work is presented in this thesis. A complete list of publications involving the author that includes the experimental work is given in Appendix I.

Contents

Chapter 1

Introduction

1.1 Historical Context

One of the most pressing problems facing civilization today is how to produce energy sustainably and in sufficient quantity to supply a growing global population. Nuclear fusion, the process that powers the stars, holds the promise of delivering virtually unlimited, clean energy, using input materials that are readily accessible today.

Large scale thermonuclear fusion was achieved with the 'Ivy Mike' nuclear test by the United States in 1952 [Rhodes, 2005]. Since this time, inertial confinement fusion (ICF) has progressed from these large-scale explosions initiated by atomic (fission) bombs to laboratory experiments in which fuel pellets are driven to fusion conditions by high power lasers. These experiments, which began at United States government research labs in the early 1960s [Velarde & Carpintero-Santamaría, 2007], involve the creation of matter in extreme conditions not usually encountered on Earth. In the last decade, the recognition of the need to better understand these extreme states of matter has given birth to the field of research known as 'High Energy Density Physics' (HEDP) [Davidson *et al.*, 2003].

Among the various extreme states of matter of interest in HEDP are plasmas whose thermodynamic conditions (i.e., density and temperature) are such that the conventional framework of plasma physics does not apply. These 'non-ideal' plasmas are currently of great experimental and theoretical interest.

Since analytic solution to the equations that govern the dynamics of non-ideal plasmas is at best highly impractical, and because approximations with which to simplify these equations are not obvious, computer simulation has become an important tool. In this thesis, the method of computer simulation known as 'molecular dynamics' (MD) is used to investigate the dynamics of non-ideal plasmas.

1.2 Non-ideal plasmas

A non-ideal plasma is a plasma for which the conventional framework of classical plasma physics is inapplicable. Classical plasma physics [Krall & Trivelpiece, 1973] is concerned with high temperature, rarefied, 'gaseous' plasmas only—these are 'ideal' plasmas. At lower temperatures and/or higher densities, 'liquid-like' behaviour sets in. Just as a normal liquid is distinguished from a gas by the presence of short range structural order between the atoms or molecules of the liquid, a liquid-like non-ideal plasma is distinguished from a gaseous ideal plasma by the presence of short range structural order between the ions in the plasma. This structural order, which has a profound influence on the physics of non-ideal plasmas, is completely neglected by classical plasma physics, which is therefore inapplicable.

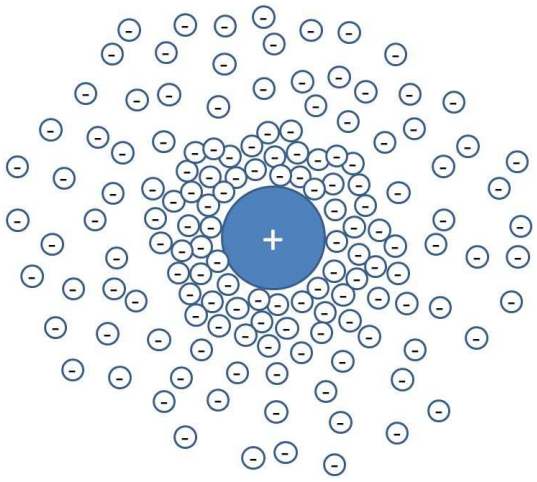

Figure 1.1: Electrons screening ions in a plasma. For an ideal plasma, the Debye length, λ_D, is a measure of the spatial extent of the electron 'cloud' surrounding each ion. For a non-ideal plasma, however, the Debye length ceases to have a clear physical meaning.

A good physical example of the inapplicability of classical plasma physics to non-ideal plasmas is provided by charge screening. Since the pioneering work of Debye and Hückel on electrolyte solutions [Debye & Hückel, 1923], charge screening has been known to be an essential feature of systems with Coulomb interactions. The basic idea is illustrated in Figure 1.1. As shown in Figure 1.1, in a plasma the negatively charged electrons are attracted to the positively charged ions, and thus serve to shield or 'screen' the ionic charge. In classical plasma physics, the spatial extent of the resulting electron 'cloud' surrounding each ion is given by the Debye

length[1],

$$\lambda_D = \sqrt{\frac{\epsilon_o k_B T}{n Z^2 e^2}}\,, \tag{1.1}$$

where n is the ion number density of the plasma, T is the temperature of the plasma, and Z is the ionisation state (meaning that each ion has charge Ze, where e is the charge of an electron). Clearly, this picture of Debye screening is only physically meaningful if the average number of electrons contained in a 'Debye sphere', also known as the plasma parameter,

$$N_D = \frac{4}{3}\pi n \lambda_D^3\,, \tag{1.2}$$

is large (i.e., certainly greater than unity). Indeed, for $N_D \gg 1$ the Debye length offers a good description of charge screening, and this criterion is essentially the very definition of an ideal plasma[2]. The criterion is very well satisfied by many plasmas of interest in research and industry. For example, the ITER tokamak, a device designed to prove the viability of magnetic confinement fusion, will aim to confine a plasma with ion density $n \approx 1 \times 10^{14}\,\mathrm{cm}^{-3}$ and temperature $T \approx 10^8\,\mathrm{K}$ (8 keV) [McCracken & Stott, 2005], which gives $N_D \approx 4 \times 10^8$. At the other extreme is the interior of the planet Jupiter, which consists mainly of a hydrogen plasma ($Z = 1$), with $n \approx 6 \times 10^{24}\,\mathrm{cm}^{-3}$ and $T \approx 10^4\,\mathrm{K}$ (1 eV) [Baus & Hansen, 1980, Ichimaru *et al.*, 1987]. For these conditions, $N_D \approx 0.002$! This is certainly a non-ideal plasma. Of course, the smallness of N_D does not mean that screening of ions by electrons does not occur, but rather that the statistical description offered by classical plasma physics (the Debye length) is inadequate to describe this important phenomenon in non-ideal plasmas. This conclusion also applies to other concepts from classical plasma physics such as the collision frequency (see, e.g., [Dimonte & Daligault, 2008]); in a similar way, the physical picture offered by classical plasma physics breaks down for a non-ideal plasma.

The inapplicability of classical plasma physics to non-ideal plasmas is somewhat analogous to the inapplicability of conventional kinetic theory to describe ordinary gases and liquids. Just as the dynamics of a dilute gas are well accounted for by the Boltzmann kinetic equation, the dynamics of an ideal plasma are well accounted for

[1] The simplest way to derive this result is via the so-called Poisson-Boltzmann equation, see e.g. [Chen, 2006], Chapter 1.

[2] Indeed, N_D is effectively used as the formal definition of a non-ideal plasma given in Section 1.4, since N_D is related to the coupling parameter Γ defined in Section 1.4 by $N_D = 1/(3\Gamma)^{3/2}$.

by the Vlasov kinetic equation[3]. To continue the analogy, the same framework that was created to deal with dense gases and liquids finds application in an essentially unmodified form for describing non-ideal plasmas. Indeed, from the early studies [Brush *et al.*, 1966, Hansen *et al.*, 1975], research on non-ideal plasmas has drawn on techniques that were originally developed to describe ordinary liquids. These techniques include computational methods such as Monte Carlo (MC) and molecular dynamics (MD) [Allen & Tildesley, 1988, Frenkel & Smit, 2001], the latter of which is the primary tool used in this thesis, as well as theoretical formalism including integral equation methods, cluster expansions and projection operator techniques [Balucani & Zoppi, 2002, Hansen & McDonald, 2006].

1.3 Simple models of non-ideal plasmas

A non-ideal plasma is a rather complex state of matter. Therefore, one might expect approaches to modeling the dynamics—even if these are restricted to the *equilibrium* dynamics—to be fraught with difficulty. Indeed, taking into account the detailed atomic physics of these states of matter, including the quantum mechanics of partial electron degeneracy, ionisation and recombination processes, and so forth, is a heady task (see, e.g., [Fortmann *et al.*, 2009, Gregori *et al.*, 2007, Redmer & Röpke, 2010]). The approach taken in this thesis is more akin to that described in the pioneering work of Brush, Sahlin and Teller [Brush *et al.*, 1966], in which the authors state:

> "... it seems appropriate to ... study the properties of some simple models which share at least some of the essential features of real physical systems."

In this thesis, the single most important 'essential feature' shared between the simple models (which shall in fact be referred to as systems) studied and the real physical plasmas of experimental interest is the presence of liquid-like structural order between the ions. The mantra of this thesis is that it is worthwhile having a thorough understanding of the dynamical properties of simple systems that represent non-ideal plasmas before attempting to include additional (complicating) physics.

[3]These Vlasov dynamics are discussed in Section 2.6. Of course, the collision term appearing in the Boltzmann equation can be added to the Vlasov equation (and likewise, the 'mean field' term in the Vlasov equation can be added to the Boltzmann equation), but the two kinetic equations in their unmodified forms are ubiquitous in their application to 'ideal' systems.

1.4 The YOCP and the OCP

This thesis is an investigation of the equilibrium dynamics of two systems[4], collectively known as the one-component plasma: the Yukawa one-component plasma (YOCP) and the Coulomb one-component plasma (OCP)[5]. Both of these are classical systems of a single species of N point particles of charge Ze and mass m that interact via a pair potential. For the YOCP, the interaction potential of two particles separated by distance r is

$$v(r) = \frac{(Ze)^2 \exp(-r/\lambda_s)}{4\pi\epsilon_0 r} \,. \tag{1.3}$$

Here λ_s is called the screening length or, for reasons that will be clarified in Section 1.5, the electronic screening length. For the OCP, the interaction potential is the Coulomb potential, corresponding to $\lambda_s \to \infty$, and therefore

$$v(r) = \frac{(Ze)^2}{4\pi\epsilon_0 r} \,. \tag{1.4}$$

In this thesis, the particles of the system—be it YOCP or OCP—represent ions, and the terms 'particles' and 'ions' are used interchangeably throughout.

A recurring theme in this thesis is that, despite the formal similarity between Equation (1.3) and Equation (1.4), the YOCP can be considered to be akin to an 'ordinary' liquid, e.g., a Lennard-Jones or hard sphere fluid, wheras the OCP cannot[6]. This is because the Hamiltonian of the YOCP,

$$H = (1/2m) \sum_{i=1}^{N} p_i^2 + \sum_{i=1}^{N} \sum_{j>i} v(r_{ij}) \,, \tag{1.5}$$

where p_i is the momentum of the ith ion, and $r_{ij} = |\boldsymbol{r}_i - \boldsymbol{r}_j|$, with $\boldsymbol{r}_i$ and $\boldsymbol{r}_j$ the positions of the ith and jth ions, is formally identical to that of a simple liquid [Hansen & McDonald, 2006]. The Hamiltonian of the OCP, on the other hand, does not take the form of Equation (1.5). This is because in the case of the OCP, for reasons related to the long range of the Coulomb potential (see Section 2.3), the system must be immersed in a uniform background of opposite charge, which means

[4] As mentioned in Section 1.3, in this thesis the YOCP and OCP will be referred to as 'systems' rather than 'models'. This is so that the YOCP and OCP can be distinguished from theoretical 'models' for their dynamical properties, such as the generalised hydrodynamics models for the dynamical structure factor discussed in Chapter 5.

[5] In the literature, the Coulomb one-component plasma is usually referred to as simply the one-component plasma, or OCP. In keeping with this convention, the acronym OCP (rather than COCP) is used in this thesis.

[6] This theme is particularly evident in the work on the hydrodynamic description of the OCP, presented in Chapter 6.

that terms must be added to the Hamiltonian in Equation (1.5). The presence of this uniform background means that the OCP is not simply the limiting case of the YOCP, and therefore the YOCP and OCP are rightly considered as two different systems throughout the thesis.

In equilibrium at temperature T, the YOCP is known to be fully characterised by only two dimensionless parameters [Donkó *et al.*, 2008]. These are: (i) the coupling parameter

$$\Gamma = \frac{(Ze)^2}{4\pi\epsilon_0}\frac{1}{ak_BT}\,, \tag{1.6}$$

where $a = (3/4\pi n)^{1/3}$ (n is the number density) is the average inter-particle distance, and (ii) the screening parameter

$$\kappa = \frac{a}{\lambda_s}\,. \tag{1.7}$$

Since for the OCP $\kappa = 0$ ($\lambda_s = \infty$), the OCP is completely characterised by Γ only.

The coupling parameter Γ is approximately the ratio of the potential energy between two ions to the average thermal (kinetic) energy of an ion. When Γ is small, the potential energy effects are small and the dynamics are dominated by the thermal energy; this is an ideal plasma, which can in principle be adequately described by classical plasma physics. In fact, as mentioned in Section 1.2, classical plasma physics is essentially built around the very assumption that $\Gamma \ll 1$. This is a rather good approximation for many of the plasmas that are of experimental and industrial interest; as an example, for the tokamak plasma with the thermodynamic conditions given in Section 1.2, $\Gamma \approx 1 \times 10^{-6}$.

As Γ increases, both the YOCP and OCP change from a nearly collisionless, gaseous regime into an increasingly correlated, dense, liquid-like regime. For $\Gamma \geq 1$, the system—be it YOCP or OCP—is said to represent a non-ideal or 'strongly coupled' plasma [Ichimaru, 1982]. The terms 'non-ideal' and 'strongly coupled' are used interchangeably throughout this thesis.

As the coupling parameter is increased still further, the system crystallises. This occurs when the free energy of the fluid phase is equal to the free energy of the solid phase, at $\Gamma \equiv \Gamma_m$. For the OCP, $\Gamma_m \approx 175$ [Dubin, 1990]. For the YOCP, Γ_m is found to be an increasing function of κ [Hamaguchi *et al.*, 1997]. Since this thesis is devoted exclusively to the study of *liquid-like* non-ideal plasmas, this crystalline behaviour is of no concern; the study is restricted to the YOCP and OCP in the fluid phase, i.e., to $\Gamma < \Gamma_m$.

The other dimensionless parameter, the screening parameter κ, is the ratio between the inter-particle distance and the electronic screening length. In the OCP,

the ions are unscreened ($\lambda_s = \infty$, $\kappa = 0$), and therefore interact through the bare Coulomb potential. For the YOCP (λ_s finite, $\kappa > 0$), as κ increases, the interaction potential, Equation (1.3), becomes increasingly short ranged. Further discussion of the screening parameter is reserved until the following section.

The work in this thesis is all done in terms of the dimensionless parameters Γ and κ, rather than in terms of the physical parameters, the ion number density n, the ion temperature T and the ionisation state Z. This is sensible since it is the combination of parameters given by Γ and κ in Equations (1.6) and (1.7)—rather than n, T and Z independently—that determine the physical regime (i.e., the degree of non-ideality) of the YOCP and OCP. For the same reason, static and dynamical properties of the YOCP and OCP are examined on spatial scales relative to the average inter-particle distance a (also sometimes called the ion-sphere radius or the Wigner-Seitz radius [Ichimaru, 2004]). As the name suggests, a is of the order of the inter-particle distance: if the particles of the system are arranged in a simple cubic lattice, then it can be easily shown that the separation between adjacent particles is $1.6120a$ [Brush *et al.*, 1966]. The average inter-particle distance a thus provides a convenient lengthscale for the system that for strongly coupled plasmas is certainly more physically meaningful than the Debye length introduced in Section 1.2. A useful relation between a and the Debye length λ_D is

$$\frac{a^2}{\lambda_D^2} = 3\Gamma\,, \tag{1.8}$$

which also serves to illustrate the point made in Section 1.2, since, as Γ increases, the Debye length decreases (relative to a) until it becomes unphysically small. Finally, dynamical properties are examined on timescales relative to the inverse of the ion plasma frequency,

$$\omega_p = \sqrt{\frac{n(Ze)^2}{\epsilon_0 m}}\,. \tag{1.9}$$

To reiterate, ω_p is the *ion* plasma frequency—rather than the electron plasma frequency that the symbol ω_p typically represents—since m in Equation (1.9) is the ion mass and Ze is the ion charge. However, since the OCP and YOCP are single component systems, this distinction is unnecessary, and thus ω_p is referred to as simply the plasma frequency henceforth.

1.5 The YOCP and the OCP as descriptions of real plasmas

A question that is raised immediately is this: exactly how well can the YOCP and the OCP be expected to describe 'real' non-ideal plasmas occurring in nature or created in the laboratory? A few examples of these real non-ideal plasmas are given in Table 1.1. The intended application of the work presented in this thesis is to x-ray scattering experiments on laser produced plasmas; these experiments are discussed in more detail in Section 2.7. As indicated in Table 1.1, laser produced plasmas can access conditions comparable to planetary interiors, which are in turn relevant for ICF studies [Glenzer & Redmer, 2009]. Laboratory astrophysics [Remington *et al.*, 2006] and ICF [Lindl *et al.*, 2004] are certainly important motivations for studying non-ideal plasmas. As discussed in Section 1.3, one way of advancing these areas is to seek a better understanding the physics of the simplest systems that might represent a non-ideal plasma, the YOCP and the OCP. With this in mind, in this thesis the equilibrium dynamics of the YOCP and OCP are investigated for a wide range of the dimensionless parameters Γ and κ, rather than for particular values that could correspond to the thermodynamic conditions created in any given experiment. However, it is certainly worthwhile examining at this point—albeit in limited detail—when these systems might offer a reasonable description of a real non-ideal plasma. The following discussion draws freely from the excellent review article of Baus and Hansen [Baus & Hansen, 1980].

The first approximation evident in both the YOCP and OCP systems is that the ions are taken to obey classical and non-relativistic equations of motion. The classical approximation is a good one provided that the ratio of the ion thermal de Broglie wavelength to the average inter-particle distance,

$$\frac{\Lambda}{a} = \frac{h/(2\pi m k_B T)^{1/2}}{(3/4\pi n)^{1/3}}\,, \tag{1.10}$$

is much smaller than unity. Equation (1.10) shows that this is a high temperature/low density requirement. Although it was already stated that the high temperature, low density plasmas are 'ideal' plasmas, there is a large region of the density-temperature plane for which $\Lambda/a \ll 1$ and $\Gamma \geq 1$ (with the latter condition qualifying the plasma as 'non-ideal'), as shown in Figure 1.2. As for relativistic effects on the ion motion, these will be negligible providing the ion thermal velocity,

$$v_T = \sqrt{\frac{k_B T}{m}}\,, \tag{1.11}$$

	Jupiter (interior)	White dwarf	Laser produced plasma (Al)
Z	1	6	3
$n\,(cm^{-3})$	6×10^{24}	5×10^{30}	2×10^{23}
$a\,(\mathring{A})$	0.34	0.36×10^{-2}	1.1
$T\,(eV)$	1	10^4	1
Γ	50	17	120
Λ/a	0.5	0.1	0.03
$k_B T_F\,(eV)$	10^2	3×10^6	26
T/T_F	7×10^{-3}	3×10^{-3}	4×10^{-2}
λ_{TF}/a	0.8	5.6	0.6

Table 1.1: A few examples of real non-ideal plasmas. The parameters for the interior of Jupiter interior and a typical white dwarf are taken from Table 1 of [Baus & Hansen, 1980]. The parameters for a laser produced plasma are based on those given in [García Saiz *et al.*, 2008] for a partially ionised Aluminium plasma, and represent typical plasma conditions created in high power laser experiments.

is much smaller than the speed of light[7]. For $Z = 1$, $v_T/c = 0.1$ gives $k_B T \approx 10\,MeV$, which is far higher than the temperatures of the real non-ideal plasmas listed in Table 1.1 . It should also be noted in this regard that the condition $v_T \ll c$ also allows the transverse electromagnetic interactions between ions to be neglected [Baus & Hansen, 1980].

The second point to make is that a plasma is a many-body system consisting of ions *and* electrons. The YOCP and OCP are, however, single component systems. Since in both cases the particles of the system represent ions, the electrons are not included explicitly. This means that nothing about electron dynamics in non-ideal plasmas can be learned by studying the OCP and the YOCP; only ion dynamics can be studied. It should be noted, however, that although the electrons are not included explicitly in either system, their physical effects are accounted for to some extent—this is done through the electronic screening length λ_s in the interaction potential of Equation (1.3)[8].

[7] Obviously, this criterion does not necessarily mean that relativistic effects are negligible for the (much lighter) electrons. It is also worth mentioning that, although the particle dynamics are not affected by relativistic effects at these sub-relativistic velocities, recent studies suggest that the light scattering experiments discussed in Section 2.7 can still be sensitive to relativistic effects [Ross *et al.*, 2010].

[8] The situation here is not unlike the modeling of a monatomic liquid (or, indeed, a more complicated material), where it is common take the electronic degrees of freedom into account by using

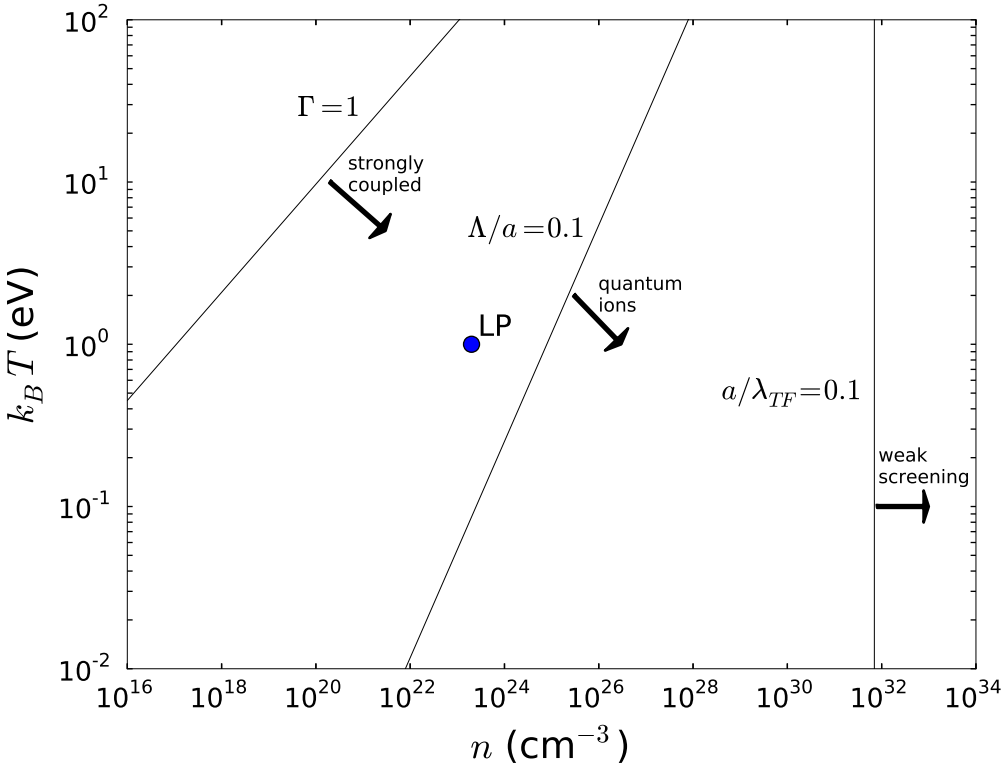

Figure 1.2: Density-temperature plane showing the lines $\Gamma = 1$, $\Lambda/a = 0.1$ and $a/\lambda_{TF} = 0.1$. Since laser produced plasmas are the intended application of the work presented in this thesis, aluminium ions with $Z = 3$ (i.e., a partially ionised plasma) have been chosen; the particular case given in Table 1.1 is shown as 'LP'.

In the OCP, the screening length is infinite. The electrons form a uniform 'smeared out' background of neutralising charge. Although the uniformity of this background would seem to run contrary to the picture of charge screening illustrated in Figure 1.1, in certain extreme conditions it offers a reasonable description of a real plasma. The reason for this is that even when the ion dynamics are well approximated by the classical equations of motion, the electrons—due to their much smaller mass m_e—can be highly quantum mechanical. For example, in many astrophysical phenomena—as well as in laser produced plasmas (cf. Table 1.1)—T can be less than the Fermi temperature of the electrons,

$$T_F = \frac{\hbar^2}{2m_e k_B}(3\pi^2 Z n)^{2/3}\,, \tag{1.12}$$

which are therefore highly degenerate. This highly degenerate electron gas can be

an 'effective' interatomic potential, e.g., the Lennard-Jones potential.

approximated as a rigid uniform background if the Thomas-Fermi screening length,

$$\lambda_{TF} = \sqrt{\frac{2}{3}\frac{\epsilon_0 k_B T_F}{nZe^2}}\,, \tag{1.13}$$

is much larger than the average inter-particle distance a [Baus & Hansen, 1980]. Clearly $T \ll T_F$ and $\lambda_{TF} \gg a$ are both high density requirements. It can be seen in Figure 1.2 that the latter of these criteria for weak screening often requires extremely high densities; indeed, for the conditions in Figure 1.2, the required density is so high that quantum effects become important for the ions, thus calling into question the applicability of the OCP. Remarkably, despite these reservations, the OCP has been shown to reasonably well reproduce certain thermodynamic properties of some liquid metals [Yokoyama & Naito, 1989] (but it should be noted that the main application of the OCP to liquid metals is as a reference system with which to add more realistic features [March, 2005, Mon *et al.*, 1981, Ross *et al.*, 1981]).

In the YOCP, the screening length is finite. Therefore, the high density requirement for the rigid uniform background in the OCP to offer a reasonable description of the electrons in a non-ideal plasma can be relaxed. Of course, the screened Coulomb potential of Equation (1.3) is still an approximation; in reality the electrons in a plasma screen the ion-ion (Coulomb) interactions dynamically. However, because ions are always much more massive than the electrons in a plasma, on the time scale of the ion dynamics it can be assumed that the electrons screen the ion-ion interactions *instantaneously*. In the YOCP, this instantaneous screening is completely specified by a single number, λ_s. The exact value that λ_s should take for a plasma at a given density and temperature is not obvious. As discussed in Section 1.2, the Debye length λ_D can only be expected to give a reasonable account of screening in an ideal plasma. The other limiting case is that of a degenerate electron fluid; in this case λ_s reduces to the Thomas-Fermi screening length λ_{TF} given in Equation (1.13). Between these extremes, no simple expression for the screening length in terms of the density and temperature of the plasma can be given, although a number of models have been proposed [Ichimaru, 2004]. In particular, a general expression for an electron gas at arbitrary degeneracy has been given in terms of Fermi functions [Kremp *et al.*, 2005].

While it may be possible to find an expression for the screening length at a given density and temperature, and hence the κ value that best corresponds to given experimental conditions, the YOCP still neglects the dynamical nature of the electrons. At present it is difficult to quantify precisely the severity of this approximation in general. With increasing availability of data from high power laser experiments in the

future, it is expected that the applicability of the Yukawa model could be examined in more detail. This is reminiscent of the situation in modelling monatomic liquids (and indeed materials in general), in which it is normal to improve/parameterise interatomic potential models by comparison with experimental data [Allen & Tildesley, 1988].

In summary then, besides having to restrict the applicability of the OCP and YOCP systems to a region of the density-temperature plane in which the ions behave classically and non-relativistically, the main shortcoming of both of these systems in describing real non-ideal plasmas found in nature or created in the laboratory is that neither includes dynamical, quantum mechanical electrons. This means one can use these simple systems to study the *ion* dynamics in non-ideal plasmas only. To be clear, the investigation of these ion dynamics is the practical application of the study of the OCP and YOCP. In this practical application, e.g., for laser produced plasmas, one certainly expects the YOCP to offer a more 'realistic' description of a non-ideal plasma than the OCP. Nevertheless, the OCP does serve as a prototypical system on which more sophisticated descriptions of non-ideal plasmas can and have been based.

1.6 Motivation: Why the equilibrium dynamics?

In this thesis, the study of the dynamics of the YOCP and the OCP is restricted to the *equilibrium* dynamics. The main reason for this—in addition to the fact that the non-equilibrium dynamics is a rather vast and difficult topic to study—concerns the application to laser produced plasmas mentioned in Section 1.5: it is the *equilibrium* dynamics of these laser produced plasmas that can in principle be measured in x-ray scattering experiments [Glenzer & Redmer, 2009]. The exact quantity measured experimentally is known as the dynamical structure factor (DSF)[9]. For the experiments, a better understanding of the DSF of non-ideal plasmas is desirable. This is the primary motivation for the studies of the YOCP, which, as discussed in Section 1.5, is a more 'realistic' representation of a non-ideal plasma than the OCP.

The OCP is studied for a rather different reason. The OCP is the prototypical system representing a non-ideal plasma and has been studied for many years. However, due to the peculiarity of the Coulomb potential, there are a number of outstanding questions concerning its dynamical behaviour. The equilibrium dynamics of

[9]Section 2.7 describes exactly how the DSF of the YOCP is related to the DSF measured in the x-ray scattering experiments.

the OCP are studied in order to contribute to the theoretical understanding of this slightly peculiar system.

Thus, the investigation of the equilibrium dynamics is driven more by a 'practical' motivation in the YOCP case, but more by a 'fundamental' motivation in the OCP case. Of course, this is a rather arbitrary division: both systems can always be studied 'for their own sake' and, similarly, one can always find a real plasma somewhere in the universe that either system could be argued to approximate. In any case, the motivations given in this section are the reasons why the research presented in this thesis was undertaken.

1.7 Structure of the thesis

The remainder of this thesis is structured as follows. Firstly, in Chapter 2, the theory of the equilibrium properties of the YOCP and OCP is introduced. Although much of this theory is common to normal fluids and can be found in a number of textbooks (e.g., [Balucani & Zoppi, 2002, Hansen & McDonald, 2006, March & Tosi, 1991]), where appropriate the discussion is tailored to the YOCP and OCP systems, and certain peculiarities that arise for the OCP due to the long range Coulomb potential are pointed out. The most important purpose this chapter serves is to introduce the equilibrium properties—in particular the DSF—that have been computed by the author using MD simulations.

These MD simulations are described in Chapter 3. Again, the techniques described are well known and apply to any interaction potential. However, some difficulties specific to conducting MD simulations of the YOCP and OCP that are not normally encountered in simulations of other fluids are discussed. Also in this chapter, the parameters used in the MD simulations performed by the author are given, along with a detailed account of the analysis that was undertaken to produce high quality data for the DSF. While it would not be accurate to state that new techniques were developed for computing the DSF, a number of details that could prove to be useful to others in the future were worked out.

The original research presented in this thesis naturally splits into 5 distinct sub-projects, each of which are given their own chapter (Chapters 4-8). The sub-projects are united by a common theme: each is an investigation—using MD simulations as the primary tool—of some aspect of the equilibrium dynamics of the YOCP or OCP system in the fluid regime. In the first sub-project (Chapter 4), the question of the applicability of the hydrodynamic description of the equilibrium dynamics (i.e., the

DSF) of the YOCP is examined. This leads naturally to the second sub-project (Chapter 5), a study of theoretical models of the DSF of the YOCP in the regime where the hydrodynamic description does not apply. While the first and second sub-projects are studies of the YOCP, the third and fourth are studies of the OCP. In the third sub-project (Chapter 6), the problem of the very existence of a hydrodynamic description of the OCP—formulated by Baus and Hansen over 30 years ago [Baus & Hansen, 1980]—is addressed. In the fourth sub-project (Chapter 7), two approaches to modelling the dynamical properties of the OCP are examined and compared. Finally, the fifth sub-project (Chapter 8) is a discussion of the methods by which transport coefficients can be computed; although the techniques are applied to the YOCP, the general methodology is also relevant to the OCP. In Chapter 9, the findings of all of these sub-projects are summarised, and some thoughts on interesting studies of the YOCP and OCP that might be carried out in the future are presented.

Chapter 2

Theory of the equilibrium properties of the YOCP and OCP

2.1 Static properties

As mentioned in Chapter 1, the defining feature of a non-ideal plasma is the presence of short range structural order between the ions. This liquid-like property is in contrast to the long range crystalline order present in a solid and the complete disorder in a gas.

The structural order between the ions in a plasma can be quantified by the radial distribution function $g(r)$. This function is introduced by writing the average number of ions contained in a spherical shell of thickness δr at a distance r from any given reference ion as [March & Tosi, 1991]

$$4\pi n \int_{r}^{r\ +\delta r} r^2 g(r) dr \,, \tag{2.1}$$

where n as usual denotes the ion number density. If $g(r) = 1$, then this becomes

$$\frac{4}{3}\pi n[(r+\delta r)^3 - r^3] \,, \tag{2.2}$$

which is simply the ion number density multiplied by the volume of the spherical shell. That is, if $g(r) = 1$, the number of ions one expects in the shell is simply $n \times V_{shell}$. This scenario represents a complete absence of structural order between the ions: regardless of the distance r one looks from a given reference ion, there are always on average the same number of ions per unit volume.

Structural order, as is present in a liquid or non-ideal plasma, is characterised by a non-trivial radial distribution function. An example is given in Figure 2.1, which shows the radial distribution function for the YOCP at $\Gamma = 50$ and $\kappa = 1$. In the

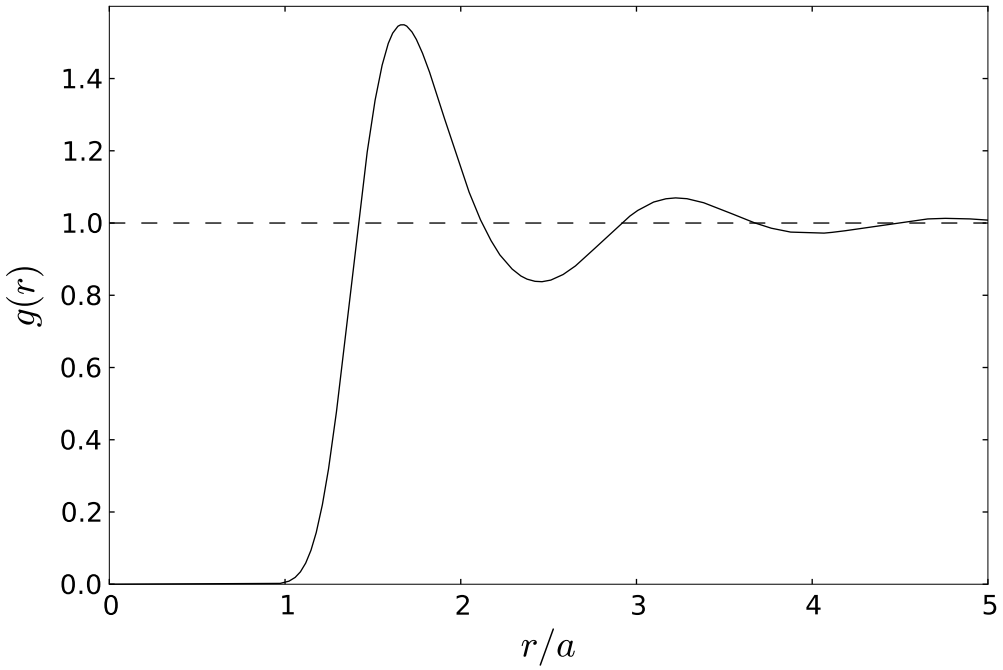

Figure 2.1: Radial distribution function $g(r)$ of the YOCP with $\Gamma = 50$, $\kappa = 1$. The radial distribution function shown here was computed with MD using the method described in Section 3.8. The maximum value of $g(r)$ occurs at $r \approx 1.67a$, which is close to the separation between ions arranged in a simple cubic lattice, $1.61a$.

region where $g(r)$ is greater than unity, one expects to find more than $n \times V_{shell}$ ions. The peaks in Figure 2.1 represent smeared out 'shells' of neighbouring ions. Where $g(r)$ is smaller than unity, there is a decreased likelihood that two ions will be found with this separation. In particular, the smallness of $g(r)$ close to $r = 0$ represents the fact that an ion is very unlikely to be found in the near vicinity of another ion.

If the ions were arranged in a perfect periodic lattice (as in a solid), then the radial distribution function would depend on the vector $\boldsymbol{r}$, and $g(\boldsymbol{r})$ would consist of a sum of delta functions centered on the lattice sites. It is the isotropy of a liquid which means that the radial distribution function depends on the magnitude r of $\boldsymbol{r}$ only. In addition, since a liquid does not possess the long range order of a solid, one expects that as $r \to \infty$, $g(r) \to 1$, as can be seen in Figure 2.1.

The radial distribution function plays an important role in the physics of non-ideal plasmas. This is partly because thermodynamic properties can be written as integrals over $g(r)$ [Hansen & McDonald, 2006]. For example, the average potential energy of the system—or, more formally, the excess internal energy U^{ex}—can be obtained by integrating the total potential energy between a reference particle at $r = 0$ and the

mean number of particles between r and $r + \delta r$, which is $4\pi n r^2 v(r) g(r) \delta r$, between $r = 0$ and $r = \infty$. After dividing by two to avoid double counting and multiplying by the total number of particles, the result is

$$U^{ex} = 2\pi N n \int_0^\infty r^2 v(r) g(r) dr \,. \tag{2.3}$$

By adding to U^{ex} the internal energy of an ideal gas, the total internal energy U of the system is obtained

$$U = \frac{3}{2} N k_B T + 2\pi N n \int_0^\infty r^2 v(r) g(r) dr \,. \tag{2.4}$$

In a similar way, the pressure can be written in terms of $g(r)$ [Hansen & McDonald, 2006]. These relations are valid for any system in which the interactions are pairwise additive.

The expressions relating the microscopic structural order characterised by $g(r)$ to macroscopic thermodynamic properties such as the internal energy U are of particular interest due to the fact that a quantity closely related to the radial distribution function can be measured in light and neutron scattering experiments. This quantity is known as the static structure factor,

$$S(\boldsymbol{k}) = 1 + n \int \exp(-i\boldsymbol{k} \cdot \boldsymbol{r}) g(\boldsymbol{r}) d\boldsymbol{r} \,. \tag{2.5}$$

For an isotropic fluid, Equation (2.5) becomes

$$S(k) = 1 + 4\pi n \int_0^\infty r^2 g(r) \frac{\sin kr}{kr} dr \,. \tag{2.6}$$

Expressions like Equation (2.4) show that measurement of the static structure factor $S(k)$ in x-ray scattering experiments can give information on macroscopic thermodynamic properties of non-ideal plasmas (i.e., the Equation of State (EOS)); this is indeed one of the main motivations for performing the experiments [Glenzer & Redmer, 2009, Pelka *et al.*, 2010].

2.2 Time dependent correlation functions

The radial distribution function $g(r)$ introduced in Section 2.1 describes the structure or 'correlations' in the density at two locations in a fluid: it is a 'correlation function'. While $g(r)$ describes spatial correlations at some fixed instant in time, an obvious generalisation of this is to consider quantities that describe correlations in both space

and time. These are called time dependent correlation functions. Time dependent correlation functions are of central interest to the equilibrium dynamics of fluids.

As a first time dependent correlation function, it is natural to seek a generalisation of the radial distribution function that describes density correlations in both space *and* time. Just as the Fourier space representation of the radial distribution function can be measured in light scattering experiments, it might be expected that this time dependent radial distribution function is linked to a quantity that can be measured experimentally. Indeed, the time dependent 'version' of the radial distribution function, which is known as the van Hove function, is related by Fourier transformation (this time the transformation is done in both space and time) to the dynamical structure factor (DSF), which can be measured experimentally. Compared with the static structure factor in Equation (2.5), the DSF has an additional frequency dependence, which can be measured experimentally by spectrally resolving the scattered light.

The brief overview of time dependent correlation functions presented here draws freely from the excellent books of Hansen and McDonald [Hansen & McDonald, 2006] and Balucani and Zoppi [Balucani & Zoppi, 2002], which should be consulted by the reader for a more comprehensive discussion.

Formally, a time dependent correlation function C_{AB} is defined as

$$C_{AB}(t) = \langle A(t)B^*(0)\rangle \,, \tag{2.7}$$

where A and B are *dynamical variables* — functions that depend on the positions $\{\boldsymbol{r}_i(t)\}$ and momenta $\{\boldsymbol{p}_i(t)\}$ of the N particle system (this dependence has not been written explicitly in the notation of Equation (2.7)). The dynamical variables evolve according to the Hamiltonian of the system, which, for the YOCP, was given in Equation (1.5). The angular brackets $\langle \cdots \rangle$ in Equation (2.7) represent an equilibrium or thermal average. In the canonical ensemble, this is given as

$$\langle \cdots \rangle = \frac{1}{Z} \int \cdots \exp(-\beta H) d\boldsymbol{r}^N d\boldsymbol{p}^N \,, \tag{2.8}$$

where

$$Z = \int \exp(-\beta H) d\boldsymbol{r}^N d\boldsymbol{p}^N \tag{2.9}$$

is the canonical partition function, and $\beta = 1/k_B T$. The time dependent correlation functions of interest to this thesis are all autocorrelation functions, meaning $A = B$.

A particularly important dynamical variable is the microscopic number density,

$$n(\boldsymbol{r}, t) = \sum_{i=1}^{N} \delta(\boldsymbol{r} - \boldsymbol{r}_i(t)) \,, \tag{2.10}$$

whose Fourier components are

$$n(\boldsymbol{k},t) = \int \exp(-i\boldsymbol{k}\cdot\boldsymbol{r})n(\boldsymbol{r})d\boldsymbol{r} = \sum_{i=1}^{N} \exp(-i\boldsymbol{k}\cdot\boldsymbol{r}_i(t))\,, \tag{2.11}$$

where the above convention for the spatial Fourier transform is adopted throughout the thesis. Putting

$$A = B = \frac{1}{\sqrt{N}} n(\boldsymbol{k},t) \tag{2.12}$$

into Equation (2.7) defines the intermediate scattering function,

$$F(\boldsymbol{k},t) = \frac{1}{N}\langle n(\boldsymbol{k},t)n(-\boldsymbol{k},0)\rangle\,, \tag{2.13}$$

where the fact that $n^*(\boldsymbol{k},t) = n(-\boldsymbol{k},t)$ has been used. This thesis is concerned with isotropic systems only (i.e., the YOCP and the OCP in the fluid phase), for which the intermediate scattering function depends on the magnitude k of $\boldsymbol{k}$ only, and is therefore denoted as $F(k,t)$ henceforth.

The intermediate scattering function is the most important time dependent correlation function for the purposes of this thesis. This is because the Fourier transform of the intermediate scattering function with respect to time is the dynamical structure factor (DSF),

$$S(k,\omega) = \frac{1}{2\pi}\int_{-\infty}^{\infty} F(k,t)\exp(i\omega t)dt\,, \tag{2.14}$$

which is the quantity measured in x-ray scattering experiments on non-ideal plasmas. Much of this thesis is an investigation into various aspects of the DSF of the YOCP and the OCP.

To maintain contact with the real space description (which is rather more intuitive than the reciprocal space description), the intermediate scattering function can be related to the van Hove function, which was introduced informally at the beginning of this section as a time dependent version of the radial distribution function $g(r)$. The formal definition of the van Hove function, or density autocorrelation function, is

$$G(\boldsymbol{r},\boldsymbol{r}',t) = \frac{1}{N}\langle n(\boldsymbol{r}'+\boldsymbol{r},t)n(\boldsymbol{r}',0)\rangle\,. \tag{2.15}$$

Clearly, this a time dependent correlation function that describes the density correlations at two distinct points in space and time. After eliminating the dependence on

the choice of origin by integrating over $\boldsymbol{r}'$, the van Hove function can be written as

$$\begin{aligned} G(r,t) &= \frac{1}{N}\left\langle \int n(\boldsymbol{r}'+\boldsymbol{r},t)n(\boldsymbol{r}',0)d\boldsymbol{r}' \right\rangle \\ &= \frac{1}{N}\left\langle \sum_{i=1}^{N}\sum_{j=1}^{N}\delta[\boldsymbol{r}+\boldsymbol{r}_j(0)-\boldsymbol{r}_i(t)] \right\rangle , \end{aligned} \tag{2.16}$$

where again isotropy of the system has been assumed. It is shown in Appendix A that the spatial Fourier transform of the van Hove function is the intermediate scattering function, that is

$$F(k,t) = \int G(r,t)\exp(-i\boldsymbol{k}\cdot\boldsymbol{r})d\boldsymbol{r}\,. \tag{2.17}$$

Comparison with Equation (2.14) then indicates that the DSF is simply the Fourier transform in space and time of the density autocorrelation function $G(r,t)$. The density autocorrelation function of a non-ideal plasma can be interpreted physically as a measure of the probability that, if one ion is located at the origin $r = 0$ of coordinates at a given time, at a time t later an ion is found at some distance r from this original reference ion. By measuring the DSF experimentally (cf. Section 2.7), one indirectly (i.e., in Fourier space) measures these density correlations in space and time.

The radial distribution function and static structure factor, both introduced in the previous section, are simply special cases of Equation (2.7) for which $t = 0$. The static structure factor $S(k)$ is given by the zero time value of the intermediate scattering function,

$$S(k) = F(k,0) = \frac{1}{N}\langle n(\boldsymbol{k},0)n(-\boldsymbol{k},0)\rangle \tag{2.18}$$

Fourier inversion of Equation (2.14) shows that $F(k,0)$, and therefore $S(k)$, can be written as the integral of the DSF over all frequencies,

$$S(k) = \int_{-\infty}^{\infty} S(k,\omega)d\omega\,. \tag{2.19}$$

The radial distribution function is given in terms of the zero time value of the van Hove function

$$G(r,0) = ng(r) + \delta(\boldsymbol{r})\,. \tag{2.20}$$

Getting to Equation (2.20) from Equation (2.16) shows that the formal definition of the radial distribution function is

$$g(r) = \frac{1}{nN}\left\langle \sum_{i=1}^{N}\sum_{j\neq i=1}^{N}\delta(\boldsymbol{r}+\boldsymbol{r}_j-\boldsymbol{r}_i) \right\rangle . \tag{2.21}$$

The $\delta(\boldsymbol{r})$ term in Equation (2.20) represents the contribution from the terms in Equation (2.16) for which $i = j$, as this is not included in Equation (2.21).

Although the study of the DSF is the main focus of this thesis, it is worth mentioning a few other time dependent correlation functions that are also of interest. The velocity autocorrelation function (VACF) is

$$Z(t) = \frac{1}{3}\langle \boldsymbol{v}_i(t) \cdot \boldsymbol{v}_i(0) \rangle \,, \tag{2.22}$$

where $\boldsymbol{v}_i(t)$ is the velocity of any chosen or 'tagged' particle.

The shear stress autocorrelation function is

$$H(t) = \frac{1}{k_B T V} < \sigma^{zx}(0)\sigma^{zx}(t) > \,, \tag{2.23}$$

which is given in terms of the zx component of the microscopic stress tensor,

$$\sigma^{zx}(t) = \sum_{i=1}^{N} \left[m v_{i,z} v_{i,x} - \frac{1}{2} \sum_{j=1 \neq i}^{N} (z_{ij} x_{ij}/r_{ij}) v'(r_{ij}) \right] \,, \tag{2.24}$$

where the notation $v_{i,z}$ means the z component of velocity of particle i at time t, and $x_{ij} = |x_i - x_j|$.

Two further autocorrelation functions can be derived from the microscopic current density,

$$\boldsymbol{j}(\boldsymbol{r}, t) = \sum_{i=1}^{N} \boldsymbol{v}_i(t) \delta(\boldsymbol{r} - \boldsymbol{r}_i(t)) \,, \tag{2.25}$$

which in Fourier space is

$$\boldsymbol{j}(\boldsymbol{k}, t) = \sum_{i=1}^{N} \boldsymbol{v}_i(t) \exp(-i\boldsymbol{k} \cdot \boldsymbol{r}_i(t)) \,. \tag{2.26}$$

$\boldsymbol{j}(\boldsymbol{k}, t)$ can be separated into components parallel and perpendicular to the wavevector $\boldsymbol{k}$, leading to two separate correlation functions, the longitudinal current correlation function

$$C_l(k, t) = \frac{1}{N}\langle \hat{\boldsymbol{k}} \cdot \boldsymbol{j}(\boldsymbol{k}, t) \hat{\boldsymbol{k}} \cdot \boldsymbol{j}(-\boldsymbol{k}, 0) \rangle \,, \tag{2.27}$$

and the transverse current correlation function

$$C_t(k, t) = \frac{1}{2N} Tr \langle (\hat{\boldsymbol{k}} \times \boldsymbol{j}(\boldsymbol{k}, t))(\hat{\boldsymbol{k}} \times \boldsymbol{j}(-\boldsymbol{k}, 0)) \rangle \,, \tag{2.28}$$

where $\hat{\boldsymbol{k}} = \boldsymbol{k}/k$. If the z axis of the Cartesian co-ordinates is chosen to be parallel to $\boldsymbol{k}$, Equations (2.27) and (2.28) reduce to

$$C_l(k, t) = \frac{1}{N} \left\langle \sum_{i=1}^{N} \sum_{j=1}^{N} v_{i,z}(t) v_{j,z}(0) \exp(ik(z_i(t) - z_j(0))) \right\rangle \,. \tag{2.29}$$

and

$$C_t(k,t) = \frac{1}{N}\left\langle \sum_{i=1}^{N}\sum_{j=1}^{N} v_{i,x}(t)v_{j,x}(0)\exp(ik(z_i(t)-z_j(0)))\right\rangle . \tag{2.30}$$

The autocorrelation functions $H(t)$ and $C_t(k,t)$ are briefly investigated in Chapter 8[1], where their physical significance will be made clear. The bulk of this thesis, however, is concerned with the DSF, defined in Equation (2.14), of the YOCP and OCP.

2.3 Effect of background in OCP

Having defined the principal quantities of interest to this thesis in the previous section—in particular the DSF—the subject of the background in the OCP model is returned to briefly in this section.

Loosely speaking, the reason that a neutralising background is required in the OCP is in order to ensure the stability of the system. The proof of this statement in its full generality is of a technical nature that is beyond the scope of this thesis, and for more information the reader should consult Section 2 of the excellent review paper of Baus and Hansen [Baus & Hansen, 1980], and the references therein. In the particular case of periodic boundary conditions—which is the system that is realised in the MD simulations discussed in Chapter 3—a proof that charge neutrality is required in the OCP is given in Section 3.5.

The presence of the background essentially modifies two things. These are (1) the thermodynamic properties and (2) the microscopic dynamics. In a sense, point (1) is obvious. For example, the intuitive derivation of the relation between the excess internal energy and the radial distribution function, Equation (2.4), assumes that the only contribution to the potential energy is from the interactions between all pairs of particles in the system. In the OCP, however, there are additional contributions to the potential energy from the interaction between the particles and the background, as well as the background-background contribution.

That the microscopic dynamics are modified by the presence of the background is not as obvious. It might be assumed that the background only raises the energy of the system, and does not modify the microscopic dynamics of the N particles. The simplest argument of why this is not the case was provided by Brush, Sahlin and Teller (BST) [Brush *et al.*, 1966]. BST considered the potential $\phi(\boldsymbol{r},t)$ at a point $\boldsymbol{r}$

[1] Also, the VACF $Z(t)$ features in Appendix H in connection with computation of the self diffusion coefficient.

in the OCP, which is governed by the Poisson equation,

$$\nabla^2\phi(\boldsymbol{r},t) = \frac{\rho(\boldsymbol{r},t)}{\epsilon_0}\,, \tag{2.31}$$

where $\rho(\boldsymbol{r},t)$ is the charge density. For the OCP, the charge density is $\rho(\boldsymbol{r},t) = Ze\,n(\boldsymbol{r},t) - Ze\,n$, where the second term is the background contribution (to derive this, note that the total charge $N\,Ze$ of the background is uniformly spread over the volume V of the system). Clearly then, the background adds a term to the right hand side of Equation (2.31) that is independent of $\boldsymbol{r}$. Therefore, although $\nabla^2\phi(\boldsymbol{r},t)$ does not change its dependence on $\boldsymbol{r}$, the gradient of the potential, $\nabla\phi(\boldsymbol{r},t)$, does change its dependence on $\boldsymbol{r}$. Since the gradient of the potential is simply related to the force at position $\boldsymbol{r}$ by $\boldsymbol{F}(\boldsymbol{r},t) = -\nabla\phi(\boldsymbol{r},t)$, the forces on the particles of the system, and therefore the microscopic dynamics of the particles, are modified by the presence of the background.

In summary then, the presence of a neutralising background means that some aspects of both the static and dynamic properties of the OCP are peculiar to ordinary fluids. These details of these peculiarities—in particular, the small k behaviour of the static structure factor and the dynamics of plasma oscillations—are discussed as they arise in the latter chapters of this thesis. The main point to be emphasised here is that, despite the similarities in the interaction potential, the OCP and YOCP systems studied in this thesis should be considered as different systems entirely.

2.4 Equilibrium properties for an ideal gas

Calculation of the equilibrium properties such as $g(r)$, $S(k)$ and $S(k,\omega)$ is simply a case of evaluating the relevant expressions given in Section 2.2. This involves evaluating the equilibrium average $\langle\cdots\rangle$, given for the canonical ensemble in Equation (2.8). Of course, this thesis is concerned with calculating the equilibrium properties for the YOCP and the OCP systems, that is, when the Hamiltonian H appearing in Equation (2.8) is given by Equation (1.5) or its OCP counterpart. This cannot be done analytically. In Chapter 3, it will be seen that the molecular dynamics technique can be used to remedy this situation. However, before embarking on this course of action, a system for which the equilibrium properties can be calculated analytically is considered. This is the ideal gas, for which the Hamiltonian is

$$H = (1/2m)\sum_{i=1}^{N} p_i^2\,. \tag{2.32}$$

Since in this case the Hamiltonian is independent of the positions $\{\boldsymbol{r}_i\}$ of the particles, the equilibrium average $\langle \cdots \rangle$ in Equation (2.8)—and hence time dependent correlation functions—can readily be calculated analytically.

The consideration of the equilibrium properties of the ideal gas serves two purposes. Firstly, the analytical results allow for a physical discussion of important features, this being particularly enlightening for the time (or frequency) dependent properties such as the intermediate scattering function and the DSF. The physical insight thus gained provides a starting point for the discussion of these quantities for more complicated systems such as the YOCP and OCP. The second purpose is that in certain regimes, the equilibrium properties of these more complicated systems converge towards those of the ideal gas. An example of this was already given in Section 2.1, where it was noted that, because of the absence of long range order in a liquid, the radial distribution function tends to unity (which is the ideal gas value) at large distances.

To compute the equilibrium properties of the ideal gas, the partition function, defined in Equation (2.9), is required. This is[2]

$$Z^0 = V^N \left(\frac{2\pi m}{\beta}\right)^{3N/2} , \tag{2.33}$$

where the label '0' denotes the ideal gas value of the given quantity. The radial distribution function is

$$\begin{aligned} g^0(r) &= \frac{1}{nN} \left\langle \sum_{i=1}^{N} \sum_{j\neq i=1}^{N} \delta(\boldsymbol{r} + \boldsymbol{r}_j - \boldsymbol{r}_i) \right\rangle . \\ &= \frac{1}{nN} \frac{1}{V^N} \int \left[\sum_{i=1}^{N} \sum_{j\neq i=1}^{N} \delta(\boldsymbol{r} + \boldsymbol{r}_j - \boldsymbol{r}_i) \right] d\boldsymbol{r}^N \\ &= \frac{1}{nN} \frac{1}{V^N} N(N-1) V^{N-1} \\ &= 1 - \frac{1}{N} . \end{aligned} \tag{2.34}$$

The third line above can be obtained by considering the terms in the integrand individually, e.g. $\delta(\boldsymbol{r} + \boldsymbol{r}_1 - \boldsymbol{r}_2)$. The integral of this term over the co-ordinates of the $N-2$ particles whose positions are not in the argument of the delta function gives a factor of V^{N-2}, and the integral over $\boldsymbol{r}_1$ and $\boldsymbol{r}_2$ is independent of $\boldsymbol{r}$ and gives

[2] Often in treatises concerning statistical mechanics, the partition function contains an additional prefactor of $1/h^{3N}N!$ in order to make contact with quantum statistical mechanics (see, e.g., [Hansen & McDonald, 2006], Section 2.3). This additional prefactor, which modifies Equation (2.33) to $Z^0 = \frac{1}{N!}\frac{V^N}{\Lambda^{3N}}$, where Λ the thermal de Broglie wavelength, is not used here.

V. There are $N(N-1)$ terms like this. This means that $g^0(r)$ is not exactly equal to 1, and is dependent on the system size (N). It is possible to make $g^0(r)$ exactly equal to 1 by replacing the prefactor $1/nN$ in its definition with $V/N(N-1)$. However, one is usually interested in very large system sizes, and therefore $g^0(r) \approx 1$.

The static structure factor can be calculated either by using the fact that it is given by the Fourier transform of $g(r)$, Equation (2.5), or by using the definition in Equation (2.18) . From Equation (2.5)

$$\begin{aligned} S^0(k) &= 1 + n \int \exp(-i\boldsymbol{k}\cdot\boldsymbol{r}) g^0(\boldsymbol{r}) d\boldsymbol{r} \\ &= 1 + n \int \exp(-i\boldsymbol{k}\cdot\boldsymbol{r}) \left[1 - \frac{1}{N}\right] d\boldsymbol{r} \\ &= 1 + \frac{N-1}{V}(2\pi)^3 \delta(\boldsymbol{k}) \,, \end{aligned} \tag{2.35}$$

or, using Equation (2.18),

$$\begin{aligned} S^0(k) &= \frac{1}{N}\langle n(\boldsymbol{k},0) n(-\boldsymbol{k},0)\rangle \\ &= \frac{1}{N}\frac{1}{V^N} \int \left[\sum_{i=1}^{N}\sum_{j=1}^{N} \exp(-i\boldsymbol{k}\cdot(\boldsymbol{r}_i - \boldsymbol{r}_j))\right] d\boldsymbol{r}^N \\ &= \frac{1}{N}\frac{1}{V^N} \int \left[N + \sum_{i=1}^{N}\sum_{j\neq i=1}^{N} \exp(-i\boldsymbol{k}\cdot(\boldsymbol{r}_i - \boldsymbol{r}_j))\right] d\boldsymbol{r}^N \\ &= \frac{1}{N}\frac{1}{V^N} \left[NV^N + N(N-1)V^{N-1}(2\pi)^3\delta(\boldsymbol{k})\right] \\ &= 1 + \frac{N-1}{V}(2\pi)^3 \delta(\boldsymbol{k}) \,, \end{aligned} \tag{2.36}$$

where again the fourth line above can be obtained from the third line by considering individual terms in the integrand. Physically, $S^0(k)$ and $g^0(r)$ contain the same information: due to the absence of interactions in the ideal gas, at any given instant of time the distribution of particles is 'structureless', i.e. the likelihood of finding two particles with a given spatial separation is independent of that separation.

The intermediate scattering function, and hence the DSF, is a little more complicated to calculate since it involves correlations in the density at different times,

$$
\begin{aligned}
F^0(k,t) &= \frac{1}{N}\langle n(\boldsymbol{k},t)n(-\boldsymbol{k},0)\rangle \\
&= \frac{1}{N}\frac{1}{V^N(2\pi m/\beta)^{3N/2}}\int \exp\left(-\beta\sum_{i=1}^{N} p_i^2/2m\right) \\
&\times \left[\sum_{i=1}^{N}\sum_{j=1}^{N}\exp(-i\boldsymbol{k}\cdot(\boldsymbol{r}_i(t)-\boldsymbol{r}_j))\right] d\boldsymbol{r}^N d\boldsymbol{p}^N \,. \qquad (2.37)
\end{aligned}
$$

The terms in the above integrand for which $i \neq j$ will give a contribution proportional to $\delta(\boldsymbol{k})$, as can be seen from the derivation of $S^0(k)$ given above. Here, the $\delta(\boldsymbol{k})$ contribution is ignored as it is unimportant[3]. For the $i = j$ terms the integration over $\boldsymbol{r}^N$ gives V^N. Using also the fact that for the ideal gas $\boldsymbol{r}_i(t) = \boldsymbol{r}_i + \boldsymbol{p}_i t/m$ gives

$$
\begin{aligned}
F^0(k,t) &= \frac{1}{N}\frac{1}{(2\pi m/\beta)^{3N/2}}\int \exp\left(-\beta\sum_{i=1}^{N} p_i^2/2m\right)\left[\sum_{i=1}^{N}\exp(-i\boldsymbol{k}\cdot\boldsymbol{p}_i t/m)\right] d\boldsymbol{p}^N \\
&= \frac{1}{N}\frac{1}{(2\pi m/\beta)^{3N/2}} N \int \exp\left(-\beta\sum_{i=1}^{N} p_i^2/2m\right)\exp(-ikp_{i,z}t/m) d\boldsymbol{p}^N \\
&= \frac{1}{(2\pi m/\beta)^{1/2}}\int \exp\left(-\beta p_{1,z}^2/2m\right)\exp(-ikp_{1,z}t/m) dp_{1,z} \,,
\end{aligned}
$$

where the z axis of the Cartesian co-ordinate system has been taken to be parallel to the wave-vector $\boldsymbol{k}$, without loss of generality. Finally, evaluation of the above integral gives

$$
F^0(k,t) = \exp(-k^2t^2/2m\beta) \,. \qquad (2.38)
$$

The DSF of the ideal gas is defined by Equation (2.14) as the Fourier transform in time of the intermediate scattering function, which gives

$$
S^0(k,\omega) = \sqrt{\frac{m\beta}{2\pi k^2}}\exp(-m\beta\omega^2/k^2) \,. \qquad (2.39)
$$

From this, one can verify that Equation (2.18) is satisfied, i.e. that $\int_{-\infty}^{\infty} S^0(k,\omega)d\omega = S^0(k) = 1$.

The fact that the $i \neq j$ terms in Equation (2.37) do not contribute to $F^0(k,t)$, and hence to $S^0(k,\omega)$, represents the fact that for the ideal gas the position of a particle is uncorrelated with the positions of the other particles, this being true for all times[4] .

[3] As discussed in [Hansen & McDonald, 2006], the $\delta(\boldsymbol{k})$ term represents scattering at zero momentum transfer, which can safely be neglected.

[4] The DSF, intermediate scattering function and van Hove function are sometimes split into 'self' and 'distinct' parts [Hansen & McDonald, 2006]. For the ideal gas, the distinct part of each of these quantities is zero.

That is, for the ideal gas, the position of a particle is only correlated with itself. This, of course, will not be the case for a system with interactions, such as the YOCP or OCP. However, even for these more complicated systems, the DSF will tends towards the ideal gas form, $S^0(k,\omega)$, for large wave numbers k. The reason for this is that these large k values correspond physically to small length scales, and at sufficiently small length scales (i.e., sufficiently large k), the particles of any system will behave as if they were 'free'. This is illustrated in Figure 2.2: as shown in Figure 2.2 (bottom two panels), at sufficiently large k values, the DSF of the YOCP and OCP are closely reproduced by the ideal gas DSF $S^0(k,\omega)$.

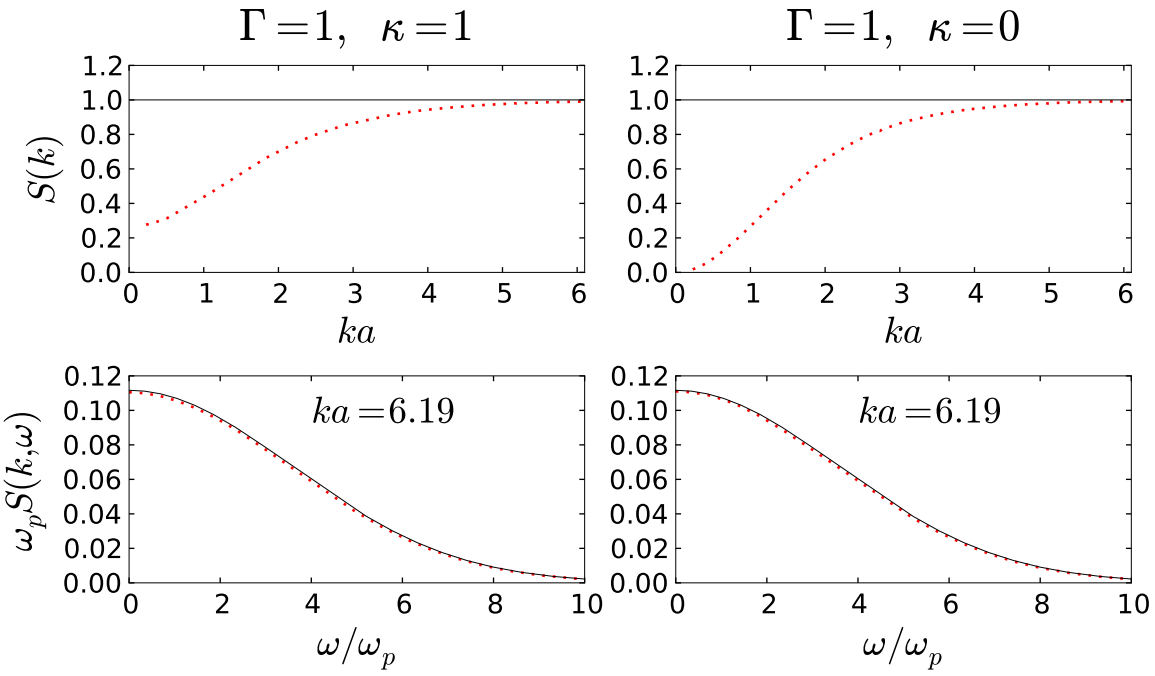

Figure 2.2: Static structure factor $S(k)$ and dynamical structure factor $S(k,\omega)$ at $ka = 6.19$ for the YOCP with $\Gamma = 1$, $\kappa = 1$ (left panels) and for the OCP with $\Gamma = 1$ (right panels). The red dots are the results of MD simulations performed by the author, and the solid lines are the ideal gas values of these quantities, which are given by 1 and Equation (2.39) respectively.

To conclude the discussion of the DSF of the ideal gas the subject of the experimental measurement of the DSF is revisited. For the ideal gas, the Gaussian shape of $S^0(k,\omega)$ at a particular k value corresponds experimentally to observing Doppler shifts of the incident radiation[5] (be it light or neutrons) due to the velocity of each

[5]The incident radiation has frequency $\omega = 0$ from the standpoint of plots such as the bottom two panels of Figure 2.2.

Name	Notation	Ideal Gas Value
radial distribution function	$g(r)$	$g^0(r) = 1$
static structure factor	$S(k)$	$S^0(k) = 1$
intermediate scattering function	$F(k,t)$	$F^0(k,t) = \exp(-k^2t^2/2m\beta)$
dynamical structure factor (DSF)	$S(k,\omega)$	$S^0(k,\omega) = \sqrt{\frac{m\beta}{2\pi k^2}}\exp(-m\beta\omega^2/k^2)$
velocity autocorrelation function	$Z(t)$	$Z^0(t) = 1/m\beta$
shear stress autocorrelation function	$H(t)$	$H^0(t) = n/\beta$
longitudinal current correlation function	$C_l(k,t)$	$C_l^0(k,t) = 1/m\beta$
transverse current correlation function	$C_t(k,t)$	$C_t^0(k,t) = 1/m\beta$

Table 2.1: Time dependent correlation functions and their values for the ideal gas. The quantities $Z^0(t)$, $H^0(t)$, $C_l^0(k,t)$ and $C_t^0(k,t)$ are independent of time since they involve velocity correlations, and for the ideal gas $\boldsymbol{v}_i(t) = \boldsymbol{v}_i$.

individual particle. Because the temperature gives a measure of the average velocity of the particles, $S^0(k,\omega)$ broadens with temperature. For the x-ray scattering experiments on non-ideal plasmas that are of relevance to this thesis, the knowledge that at large k values the plasma exhibits 'ideal' behaviour is certainly of use. By designing the experimental geometry such that the DSF is measured at these large k values, the temperature of the plasma can in principle be determined. Indeed, measurement of the temperature is often one of the main aims of these x-ray scattering experiments (another is measurement of the density) [Glenzer & Redmer, 2009].

Finally, in Table 2.1, the ideal gas expressions for all of the time dependent correlation functions defined in Section 2.2 are collected together. $Z^0(t)$, $H^0(t)$, $C_l^0(k,t)$ and $C_t^0(k,t)$ are straightforward to derive from their definitions given in Section 2.2, but are of little significance (unlike $F^0(k,t)$ and $S^0(k,\omega)$). The reason for this is that these quantities involve velocity correlations, and since for the ideal gas the velocities of the particles are constant in time, these quantities are also constant in time. For more realistic systems such as the YOCP and OCP, 'collisions' between particles (i.e., the presence of interaction terms in the Hamiltonian) mean that the velocities de-correlate over time, and hence these quantities decay to zero (cf. Chapter 8).

2.5 Sum rule approaches to computing the DSF

It was seen in the previous section (cf. Figure 2.2) that at small length scales, the DSF of the YOCP and OCP converges towards the DSF of the ideal gas, with this being a general feature of any system. Another general feature of the DSF can be ascertained by considering—this time instead of small length scales—small *time* scales. As in the case of small length scales, at sufficiently small time scales, a particle behaves as if it were 'free', and therefore the short time behavior of the system (be it YOCP, OCP, or any other system) is identical to that of the ideal gas.

The foregoing discussion can be formalised by considering the Taylor series expansion about $t = 0$ of the intermediate scattering function [Balucani & Zoppi, 2002]:

$$F(k,t) = F(k,0) + \ddot{F}(k,0)(t^2/2!) + \dddot{F}(k,0)(t^4/4!) + \cdots . \tag{2.40}$$

where only even powers of time appear because $F(k,t)$ is itself even (see Appendix B). Since, from the definition of the DSF in Equation (2.14),

$$F(k,t) = \int_{-\infty}^{\infty} S(k,\omega)\exp(-i\omega t)d\omega\,, \tag{2.41}$$

Equation (2.40) can be written as

$$F(k,t) = S(k) - \langle\omega^2\rangle(t^2/2!) + \langle\omega^4\rangle(t^4/4!) - \cdots \tag{2.42}$$

where the fact that $F(k,0) = S(k)$ has been used, and the *frequency moments* of $S(k,\omega)$ have been defined as

$$\langle\omega^n\rangle = \int_{-\infty}^{\infty} \omega^n S(k,\omega)d\omega\,. \tag{2.43}$$

Clearly, $S(k) = \langle\omega^0\rangle$ (cf. Equation (2.19)).

The utility in considering the short time expansion of the intermediate scattering function is both formal and practical. A limited amount of formal knowledge of the DSF is gained since, although the DSF of—for example—the YOCP and OCP, cannot be calculated analytically, expressions *can* be derived analytically for some of the $\langle\omega^n\rangle$. These expressions are known as *sum rules*. The practical utility gained is that these sum rules, and their k dependence, provide some useful insight into the dynamics of the system. For example, the second moment sum rule is

$$\langle\omega^2\rangle = \frac{k^2}{m\beta}\,, \tag{2.44}$$

which holds for any system, regardless of the interaction potential $v(r)$. In particular, this expression is the same for as for the ideal gas, for which $v(r) = 0$ (this can easily be verified by taking the second derivative of $F^0(k,t)$ in Table 2.1), and therefore the dynamics of the system at short timescales is identical to that of a system of free particles. Equation (2.44) can be written in a reduced (dimensionless) form that is useful for the YOCP and OCP

$$\frac{\langle\omega^2\rangle}{\omega_p^2} = \frac{q^2}{3\Gamma}\,, \tag{2.45}$$

where $q = ka$ is the reduced wave number. As well as the second moment, the fourth moment can also be calculated analytically; in this case, unlike for $\langle\omega^2\rangle$, the sum rule is found to depend on the interaction potential. For both the YOCP and OCP, the fourth moment sum rule can be written in reduced units as

$$\frac{\langle\omega^4\rangle}{\omega_p^4} = \frac{1}{3\Gamma}\left[\frac{q^4}{\Gamma} + q^2\frac{\Omega_E^2}{\omega_p^2} - q^2 M(q\bar{r}, \kappa\bar{r})\right]\,. \tag{2.46}$$

Here $\bar{r} = r/a$, and the Einstein frequency Ω_E is given as

$$\frac{\Omega_E^2}{\omega_p^2} = \frac{\kappa^2}{3}\int_0^\infty \bar{r}\exp(-\kappa\bar{r})g(\bar{r})d\bar{r}\,, \tag{2.47}$$

for the YOCP, and

$$\frac{\Omega_E^2}{\omega_p^2} = \frac{1}{3} \tag{2.48}$$

for the OCP. For both the YOCP and OCP,

$$M(x,y) = \int_0^\infty \frac{1}{\bar{r}}g(\bar{r})\exp(-y)\left[2\left(\frac{y^2}{3} + y + 1\right)\times \left(\frac{\sin x}{x} + \frac{3\cos x}{x^2} - \frac{3\sin x}{x^3}\right) + \frac{y^2\sin x}{3x}\right]d\bar{r}\,. \tag{2.49}$$

A derivation of the results for $\langle\omega^2\rangle$ and $\langle\omega^4\rangle$ given in Equations (2.45) and (2.46) can be found in Appendix C. Clearly, these results are specific to the case of the intermediate scattering function (and DSF). Of course, the same short time expansion of Equation (2.40) can equally well be applied to other time dependent correlation functions, e.g. the transverse current correlation function $C_t(k,t)$. This results in different equations for the frequency moments of the corresponding frequency dependent quantity (in this case $C_t(k,\omega)$). As usual, it is the intermediate scattering function that is of primary relevance to this thesis.

It would certainly be good to know exactly how many terms in the short time expansion of Equation (2.42) are required for an accurate representation of the intermediate scattering function (and hence the DSF). For the YOCP, it turns out that

a quantitative investigation of this question is rather impractical, since the shape of the intermediate scattering function varies significantly in the three dimensional (Γ, κ, k) parameter space (the same statement is also true for the two dimensional parameter space of the OCP). However, in general it is possible to say that the number of sum rules needed is far greater than the number that are known analytically, which are the first three frequency moments (i.e., $n = 0, 2$ and 4 in Equation (2.43)) only[6]. A justification of this statement is provided by Figure 2.3. As shown in Figure 2.3, truncating the short time expansion of the intermediate scattering function after only three terms is certainly not sufficient to capture its general behaviour, even in the region of k space where it decays monotonically. And in the region of k space where $F(k,t)$ exhibits sustained oscillations, the sum rule approach (even with a large number of terms) cannot capture this oscillatory structure.

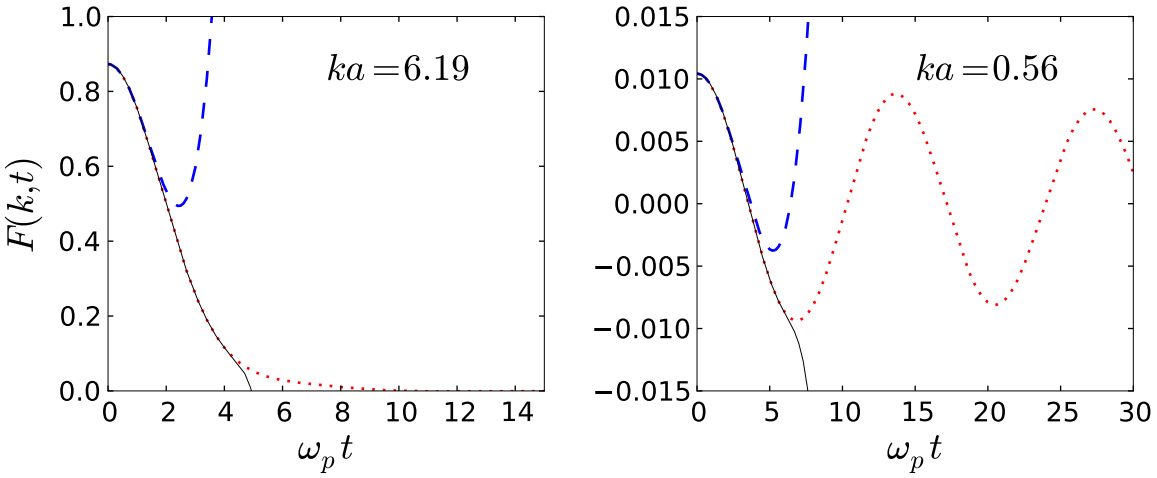

Figure 2.3: Intermediate scattering function $F(k,t)$ for the YOCP with $\Gamma = 50$, $\kappa = 1$ at two different reduced wave numbers. The dots are the results of MD simulations performed by the author. The dashed line is the result of the short time expansion of $F(k,t)$ given by Equation (2.42), including the first three terms (up to t^4) only, where the sum rules have been calculated using Equations (2.45) and (2.46) . Including three additional terms (up to t^{10}) gives the solid line (the three additional coefficients have been calculated by fitting to the MD data).

While the foregoing discussion would seem to rule out the possibility of using the short time expansion of the intermediate scattering function to directly evaluate the DSF, the known sum rules for the OCP and YOCP are still useful as constraints that approximate models of the DSF can be made to satisfy. These models for the DSF

[6]Although analytical expressions for $\langle\omega^6\rangle$ are also available (e.g., for the OCP see [Hansen *et al.*, 1975]), these are rather difficult to evaluate and therefore are of limited utility.

can be compared to the 'exact' DSF obtained from the MD simulations (see Chapter 3). The aim of this comparison is to evince a better understanding of the physics of the system of interest—in this thesis, the YOCP and the OCP. Although approaches to modeling the DSF that are based predominantly on sum rules—many of which exist for the OCP in particular [Arkhipov *et al.*, 2010, Hansen *et al.*, 1975, Hong & Kim, 1991, Ichimaru & Tanaka, 1986]—might not be expected to fare well, a number of other approaches to modeling the DSF are possible. For example, the investigation in Chapter 4 of this thesis is devoted to exploring when exactly the hydrodynamic model of the DSF of the YOCP is applicable. It is the comparison of such models with the results of MD simulations that forms the bulk of this thesis. This thesis makes an original contribution to this long running program (for an overview, see e.g., [Donkó, 2009]) since, despite the existence of a number of models for the DSF of the YOCP and OCP, these models have never be tested (largely due to the difficulty of conducting accurate MD simulations)—at least not as comprehensively as they are in Chapters 4-7 of this thesis.

2.6 Equilibrium properties from Vlasov equation

In the previous section, the idea of modelling the DSF (or equivalently, the intermediate scattering function) of the YOCP and OCP was introduced. This modelling is absolutely essential, since mere knowledge of the equilibrium properties such as the DSF (which, as will be seen in Chapter 3, can be gained from MD simulations) is meaningless without some form of physical interpretation. This physical interpretation is evinced from models, which necessarily involve approximations; these approximations can be either formal or phenomenological in origin.

One particular well known framework for developing models for liquids, gases and plasmas is kinetic theory. Formally, the aim of kinetic theory is to reduce the description of a many ($N > 10^{23}$) particle system from an exact evolution equation for the N-particle distribution function, the Liouville equation [Hansen & McDonald, 2006], to a description in terms of the one-particle distribution function. The one-particle or single particle distribution function is denoted

$$f(\boldsymbol{r}, \boldsymbol{v}, t)\,,$$

and $f(\boldsymbol{r}, \boldsymbol{v}, t)\delta\boldsymbol{r}\delta\boldsymbol{v}$ gives the number of particles in the system at time t with positions between $\boldsymbol{r}$ and $\boldsymbol{r} + \delta\boldsymbol{r}$ and velocities between $\boldsymbol{v}$ and $\boldsymbol{v} + \delta\boldsymbol{v}$. Thus f is normalised

such that

$$\int\int f(\boldsymbol{r},\boldsymbol{v},t)\,d\boldsymbol{r}d\boldsymbol{v} = N\,.$$

Equations for the time evolution of f, which necessarily involve some approximation[7], are known as kinetic equations. The most famous kinetic equation is the Boltzmann equation, named after the eminent Austrian physicist Ludwig Boltzmann. In physical terms, the Boltzmann equation assumes that the particles of the system undergo uncorrelated binary collisions, which turns out to be a good approximation to physical reality for the atoms or molecules of gases in a certain range of densities [Ferziger & Kaper, 1972]. Thus, from the Boltzmann equation, many quantities of physical interest can be calculated [Ferziger & Kaper, 1972].

Kinetic equations are relevant to this thesis since they describe the dynamics of a many body system, and therefore provide models for the dynamical properties (in particular, the *equilibrium* dynamical properties). Kinetic theory is not delved into deeply here since the research presented later on in this thesis (Chapters 4-7) is more concerned with hydrodynamic (i.e., fluid dynamic) models of the DSF of the YOCP and OCP than with models from kinetic equations. Rather, the point of this section is to introduce a particular kinetic equation, the Vlasov equation, and to describe how this equation (after linearisation) yields models for the equilibrium properties of interest: $S(k)$, $g(r)$, $F(k,t)$ and $S(k,\omega)$. These models are of special significance since the Vlasov equation is the standard kinetic equation in plasma physics. While it is well known that the Vlasov equation does not give a good account of the physics of *strongly coupled* plasmas, these models often serve as a prototype on which to build other models that attempt to include the strong coupling or 'collisional' effects neglected by the Vlasov equation (the dynamic local field correction investigated in Chapter 7 is an example of this).

The Vlasov equation can be written as [Balescu, 1997]

$$\left[\frac{\partial}{\partial t} + \boldsymbol{v}\cdot\nabla - m^{-1}\nabla\left\{\int v(|\boldsymbol{r}-\boldsymbol{r}'|)f(\boldsymbol{r}',\boldsymbol{v}',t)d\boldsymbol{r}'d\boldsymbol{v}'\right\}\cdot\frac{\partial}{\partial\boldsymbol{v}}\right]f(\boldsymbol{r},\boldsymbol{v},t) = 0\,, \quad (2.50)$$

[7]The exact evolution equation for $f(\boldsymbol{r},\boldsymbol{p},t)$ can be given in terms of the two-particle distribution function, whose time evolution is in turn given in terms of the three-particle distribution function, and so forth. This system of coupled equations is known as the BBGKY (Bogoliubov-Born-Green-Kirkwood-Yvon) hierarchy. In this formal sense, the problem of deriving kinetic equations is the problem of expressing the two-particle distribution function $f^{(2)}(\boldsymbol{r},\boldsymbol{r}',\boldsymbol{p},\boldsymbol{p}',t)$ in terms of the single particle distribution function, i.e., the closure of the BBGKY hierarchy. The Vlasov equation corresponds to making the closure $f^{(2)}(\boldsymbol{r},\boldsymbol{r}',\boldsymbol{p},\boldsymbol{p}',t) = f(\boldsymbol{r},\boldsymbol{p},t)f(\boldsymbol{r}',\boldsymbol{p}',t)$. A derivation of the Vlasov equation from the BBGKY hierarchy in the mathematical limit $Ze\to 0$, $m\to 0$, $n\to\infty$ with the conditions $e/m = const$, $en = const$ was given in [Rostoker & Rosenbluth, 1960].

where the first two terms represent 'free-streaming', i.e., if the third term is ignored, the above equation gives the exact dynamics of a system without interactions (the ideal gas). Clearly then, this additional term is of the utmost importance: it contains all of the details of the inter-particle interactions. As can be seen by inspecting Equation (2.50), each particle is assumed to interact in the averaged or mean field of all the other particles (as well as itself). That is, the term

$$\bar{v}(\boldsymbol{r},t) = \int v(|\boldsymbol{r}-\boldsymbol{r}'|) f(\boldsymbol{r}',\boldsymbol{v}',t) d\boldsymbol{r}' d\boldsymbol{v}' \tag{2.51}$$

represents the average potential felt by a particle at point $\boldsymbol{r}$, which is given by the interaction with a second particle at $\boldsymbol{r}'$, whose position is averaged over all positions in phase space. Formally, this mean field or Vlasov term in Equation (2.50) is identical to an external force on the particles of the system. Importantly, however, the mean field is 'self-consistent', since it is determined by the instantaneous value of $f(\boldsymbol{r},\boldsymbol{v},t)$; as the particles of the system evolve in time, the mean field experienced by each particle changes—this change is itself governed by Equation (2.50).

As discussed by Balescu ([Balescu, 1997], Section 5.3), the Vlasov or mean field term is only important when the range of the interactions in the system is long in comparison with the characteristic variation of the density gradient. This observation explains why the Boltzmann equation, which is the standard kinetic equation for gases (for which the interaction potential is short ranged), does not include this term. On the other hand, the Vlasov equation does not describe short range 'collisions' à la Boltzmann, and for this reason it is often called a 'collisionless' equation.

In the OCP case, the interaction potential is the Coulomb potential, for which the mean field term is certainly important (more on this theme in Chapter 6). In this case, the Vlasov equation can be written in a form that is more familiar to plasma physics,

$$\left[\frac{\partial}{\partial t} + \boldsymbol{v}\cdot\nabla + \frac{Ze}{m}\bar{\boldsymbol{E}}(\boldsymbol{r},t)\cdot\frac{\partial}{\partial \boldsymbol{v}}\right] f(\boldsymbol{r},\boldsymbol{v},t) = 0\,, \tag{2.52}$$

where

$$\bar{\boldsymbol{E}}(\boldsymbol{r},t) = -\nabla\bar{\phi}(\boldsymbol{r},t) \tag{2.53}$$

now plays the role of an average 'electric field', with

$$\bar{\phi}(\boldsymbol{r},t) = \frac{Ze}{4\pi\epsilon_0}\int \frac{f(\boldsymbol{r}',\boldsymbol{v}',t)}{|\boldsymbol{r}-\boldsymbol{r}'|} d\boldsymbol{r}' d\boldsymbol{v}' \tag{2.54}$$

the average potential, which can be seen to be a solution of the Poisson equation[8]

$$\nabla^2 \bar{\phi}(\boldsymbol{r}, t) = \frac{\bar{\rho}(\boldsymbol{r}, t)}{\epsilon_0}\,, \tag{2.55}$$

where

$$\bar{\rho}(\boldsymbol{r}, t) = Ze \int f(\boldsymbol{r}, \boldsymbol{v}, t) d\boldsymbol{v} \tag{2.56}$$

is the 'macroscopic' charge density (not to be confused with the microscopic charge density, which involves a sum of delta functions).

As a non-linear integro-differential equation, the Vlasov equation is in general difficult to solve. Fortunately, deriving models for the equilibrium properties requires consideration of the *linearised* Vlasov equation only; this is rather simpler to deal with. Linearisation proceeds by writing

$$f(\boldsymbol{r}, \boldsymbol{v}, t) = f^0(\boldsymbol{v}) + \delta f(\boldsymbol{r}, \boldsymbol{v}, t)\,, \tag{2.57}$$

where the equilibrium part of the distribution function, $f^0(\boldsymbol{v})$, is taken to be the Maxwell-Boltzmann distribution, and the fluctuation term $\delta f(\boldsymbol{r}, \boldsymbol{v}, t)$ is assumed to be small. This fluctuation term averages to zero, $\langle \delta f(\boldsymbol{r}, \boldsymbol{v}, t) \rangle = 0$, but it is the average of the product of fluctuations, $\langle \delta f(\boldsymbol{r}, \boldsymbol{v}, 0) \delta f(\boldsymbol{r}', \boldsymbol{v}', t) \rangle$, that determines the density correlations (and hence the DSF). Substituting the ansatz of Equation (2.57) into Equation (2.50) leads to the linearised Vlasov equation,

$$\frac{\partial}{\partial t}\delta f(\boldsymbol{r}, \boldsymbol{v}, t) + \boldsymbol{v} \cdot \nabla \delta f(\boldsymbol{r}, \boldsymbol{v}, t) - m^{-1} \nabla \left\{ \int v(|\boldsymbol{r} - \boldsymbol{r}'|) \delta f(\boldsymbol{r}', \boldsymbol{v}', t) d\boldsymbol{r}' d\boldsymbol{v}' \right\} \cdot \frac{\partial}{\partial \boldsymbol{v}} f^0(\boldsymbol{v}) = 0\,. \tag{2.58}$$

The linearised Vlasov equation can be solved for the DSF; this can be done, e.g., using the density response formalism. In this formalism, the density response function $\chi(k, \omega)$ is introduced in terms of the density fluctuations $\delta n(k, \omega)$ induced in the system as a result of an applied external potential $\phi_{ext}(k, \omega)$:

$$\delta n(k, \omega) = \chi(k, \omega) \phi_{ext}(k, \omega)\,. \tag{2.59}$$

It can be shown the induced fluctuations are related to the equilibrium fluctuations in the system in the absence of an external potential. The formal representation of this statement is a relation between the DSF and the density response function known as the fluctuation dissipation theorem:

$$S(k, \omega) = -\frac{k_B T}{\pi n \omega} \Im m\{\chi(k, \omega)\}\,. \tag{2.60}$$

[8] For the YOCP Equation (2.54) would contain a factor $\exp(-|\boldsymbol{r} - \boldsymbol{r}'|/\lambda_s)$ and the average potential would instead be a solution of the Helmholtz equation.

This important equation means that the DSF is known once the density response function is known. By determining the density response function for the Vlasov equation (see [Ichimaru, 2004] for details), the Vlasov DSF is found to be given by:

$$\omega_p S^V(k,\omega) = \frac{1}{\sqrt{2\pi}} \frac{k_D}{k} \frac{\exp(-x^2)}{\{1+(k_D/k)^2[1-2D(x)]\}^2 + \{(k_D/k)^2\sqrt{\pi}x\exp(-x^2)\}^2}\,, \tag{2.61}$$

where

$$x = \frac{1}{\sqrt{2}} \frac{\omega}{\omega_p} \frac{k_D}{k}\,, \tag{2.62}$$

with

$$k_D = \frac{1}{\lambda_D}\,, \tag{2.63}$$

and

$$D(x) = \exp(-x^2) \int_0^x \exp(-y^2) dy\,, \tag{2.64}$$

which is known as the Dawson function. It is noted that the mean field picture of the dynamics for any interaction potential can be recovered by replacing the two terms (k_D/k^2) in the denominator of Equation (2.61) with $n\beta v(k)$, where $v(k)$ is the spatial Fourier transform of the interaction potential (which, when multiplied by $n\beta$, is equal to (k_D/k^2) in the particular case of the Coulomb potential).

Equation (2.61) is a model of the DSF of the OCP. From previous comparisons with MD simulations [Hansen *et al.*, 1975], it is known that the model is a good description of the DSF for small coupling parameters Γ only; for strongly coupled plasmas ($\Gamma \geq 1$), it is inadequate. Physically, this inadequacy is a result of the neglect of 'collisions' in the Vlasov equation. The models of the DSF investigated throughout this thesis are essentially attempts to include these 'collisional' effects in the DSF. In Chapters 4-6, the models are based on hydrodynamic (or generalised hydrodynamic) equations, while in Chapter 7, the models are based on extending the kinetic description given by the Vlasov equation that has been outlined in this section.

2.7 X-ray scattering experiments

It was stated in Section 1.6 that the primary motivation for studying the DSF of the YOCP is because of its relation to x-ray scattering experiments. A schematic of such an experiment is shown in Figure 2.4. Usually, the plasma to be probed is created by irradiating a solid target with a high power laser. For strongly coupled plasmas, the source in Figure 2.4 must be of around x-ray wavelength so that the probing radiation

can propagate through the plasma. These x-rays can be supplied by irradiating a solid target with a high power laser (e.g., [García Saiz *et al.*, 2008, Gregori *et al.*, 2004, Pelka *et al.*, 2010]), although the recently available x-ray free electron lasers (XFELs) offer the twin advantages of high brilliance and low bandwidth; these sources have already been used to good effect [Fäustlin *et al.*, 2010].

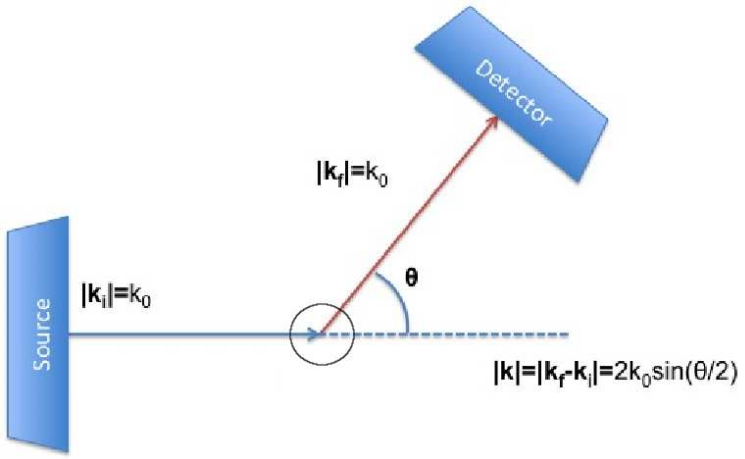

Figure 2.4: Schematic of a typical x-ray scattering experiment. The plasma to be probed with x-rays from the source is contained within the circular region where the two arrows meet.

As shown in Figure 2.4, the scattered radiation from the source is collected by a detector at an angle θ to the incident x-rays. In an elastic scattering experiment, the total intensity of scattered radiation at this particular angle (or, preferably, at a number of different angles) is measured; each angle corresponds to a particular momentum transfer, given by $\hbar k$, where $k = 2k_0 \sin(\theta/2)$ [Glenzer & Redmer, 2009, Hansen & McDonald, 2006]. The momentum transfer can be written in terms of the wavelength of the source, $\lambda_0 = 2\pi/k_0$, as

$$k = \frac{4\pi}{\lambda_0} \sin(\theta/2)\,. \tag{2.65}$$

In an inelastic scattering experiment, the intensity of scattered radiation is frequency (energy) resolved. This corresponds to measuring the intensity of scattered radiation as a function of both momentum and energy transfer.

It can be shown [Evans & Katzenstein, 1969] that the intensity of scattered radiation at the detector with frequency shift ω from the source radiation, $I(k,\omega)$, is proportional to the total electron-electron dynamical structure factor, $S_{ee}(k,\omega)$:

$$I(k,\omega) \propto S_{ee}(k,\omega)\,, \tag{2.66}$$

where the k appearing here is given by Equation (2.65). The electron-electron dynamical structure factor contains the details of the microscopic dynamics of the plasma in thermal equilibrium, which makes x-ray scattering a powerful experimental tool for investigating the basic physics of non-ideal plasmas. Indeed, although the use of an x-ray probe which allows *non-ideal* plasmas to be investigated is relatively novel [Glenzer & Redmer, 2009], this tool has been used for many years to investigate *ideal* plasmas [D. H. Froula & Sheffield, 2010, Evans & Katzenstein, 1969], which can be probed with optical frequency radiation.

Determining $S_{ee}(k,\omega)$ for a strongly coupled plasma theoretically is certainly a challenging task. This is because $S_{ee}(k,\omega)$ describes both bound and free electrons, i.e., the dynamics of both the ions and the electrons in the plasma are important. One approach that has been widely used in the strongly coupled plasma community [García Saiz *et al.*, 2008, Glenzer & Redmer, 2009, Gregori & Gericke, 2009, Gregori *et al.*, 2003a,b] is that of Chihara [Chihara, 1987, 2000], in which $S_{ee}(k,\omega)$ is split into three separate terms:

$$S_{ee}(k,\omega) = |f_I(k) + q(k)|^2 S_{ii}(k,\omega) + Z_f S^0_{ee}(k,\omega) + Z_c \int \tilde{S}_{ce}(k,\omega-\omega')S_s(k,\omega')d\omega' \,. \tag{2.67}$$

The reason for splitting $S_{ee}(k,\omega)$ into these three terms is that it allows each one to be modelled independently, which is expected to be an easier task than modelling the complete $S_{ee}(k,\omega)$. Specifically, the splitting allows $S_{ee}(k,\omega)$ to be represented as the sum of two terms which can be modelled to some extent as isolated systems—these are the first two terms in Equation (2.67), as the third term can often be ignored. Further details are given below.

The first term in Equation (2.67) accounts for electrons that follow the ion motion; this includes bound electrons, weighted by the ion form factor $f_I(k)$, and free electrons, weighted by $q(k)$. The second term, $Z_f S^0_{ee}(k,\omega)$, is the high frequency part of the electron-electron dynamical structure factor, and the final term represents scattering from bound electrons, that is, bound-free transitions, $\tilde{S}_{ce}(k,\omega)$, modulated by the self-motion of the ions, represented by $S_s(k,\omega)$. This final term is often ignored in the analysis of x-ray scattering experiments since it is normally found to be negligible compared to the $S^0_{ee}(k,\omega)$ term [Gregori *et al.*, 2003b, 2004]. If this is done, the spectral features of the scattering spectrum are contained in $S^0_{ee}(k,\omega)$ and the ion-ion dynamical structure factor, $S_{ii}(k,\omega)$, only.

The spectral features of the scattering spectrum due to the high frequency dynamics, encoded in $S^0_{ee}(k,\omega)$ (these are electron plasma waves, or plasmons), have been

observed in several experiments [Fäustlin *et al.*, 2010, Glenzer *et al.*, 2007]. However, the spectral features encoded in $S_{ii}(k,\omega)$—at least for a non-ideal plasma—have never been observed. This is because the features in $S_{ii}(k,\omega)$ occur at far lower frequencies than those in $S^0_{ee}(k,\omega)$ (since the ions move very slowly relative to the much lighter electrons), and these small frequency shifts in the source radiation are usually hidden within its bandwidth. Previous experiments have therefore only been able to access the frequency integrated features of $S_{ii}(k,\omega)$ (that is, $S_{ii}(k)$). Recent developments, however, suggest that it will soon be possible to measure these low frequency ion dynamics. In particular, the development of XFELs has resulted in a source that is of sufficiently low bandwidth (and sufficiently high brightness) to in principle measure the frequency dependence of $S_{ii}(k,\omega)$ [Gregori & Gericke, 2009]. For these future experiments, it is desirable to have a better understanding of the ion dynamics of strongly coupled plasmas. In this thesis, the ion dynamics are studied via the YOCP system. That is to say, the DSF of the YOCP should be thought of as an estimate of the ion-ion structure factor, $S_{ii}(k,\omega)$, appearing in Equation (2.67).

Chapter 3

Molecular dynamics simulations

3.1 Idea of MD

Molecular dynamics (MD) is a technique whereby the classical equations of motion (Newton's equations) are solved for the trajectories of N particles, mass m, interacting via a prescribed potential. Usually, for computational practicality, the potential is taken to be pairwise additive; often any three-body and higher order interactions can be incorporated in an 'effective' pair (two-body) potential [Allen & Tildesley, 1988]. In this thesis, the interaction potentials of interest are the pair potentials corresponding to the YOCP and OCP systems, the Yukawa potential and the Coulomb potential, respectively.

The equations of motion for the N particles can be written as

$$m\ddot{\boldsymbol{r}}_i(t) = \boldsymbol{F}_i(t)\,,\ i = \{1...N\}\,, \tag{3.1}$$

where the force on particle i at time t, $\boldsymbol{F}_i(t)$, depends on the positions of all of the other particles of the system at that time, and is given by

$$\boldsymbol{F}_i(t) = -\nabla_i \sum_{i=1}^{N} \sum_{j>i}^{N} v(r_{ij}(t))\,, \tag{3.2}$$

where $r_{ij}(t) = |\boldsymbol{r}_i(t) - \boldsymbol{r}_j(t)|$. After specifying the initial positions and velocities of each of the N particles, the basic MD procedure, which repeats for the desired number of iterations, is as follows:

1. The force on each particle is calculated according to Equation (3.2)
2. The positions of the particles of the system are evolved in time according to Equation (3.1).

For step 2, an integration algorithm is required. Although many algorithms have been proposed, what is essentially the simplest algorithm, known as the Verlet algorithm, is still thought to be one of the best [Frenkel & Smit, 2001]. There are a number of variations of this algorithm[1]. The original Verlet algorithm [Verlet, 1967] can be derived by considering the Taylor expansion about time t of the coordinate of a particle, which is

$$\boldsymbol{r}_i(t+\Delta t) = \boldsymbol{r}_i(t) + \boldsymbol{v}_i(t)\Delta t + \frac{\boldsymbol{F}_i(t)}{2m}\Delta t^2 + \frac{\dddot{\boldsymbol{r}}_i}{3!}\Delta t^3 + O(\Delta t^4)\,. \tag{3.3}$$

Similarly,

$$\boldsymbol{r}_i(t-\Delta t) = \boldsymbol{r}_i(t) - \boldsymbol{v}_i(t)\Delta t + \frac{\boldsymbol{F}_i(t)}{2m}\Delta t^2 - \frac{\dddot{\boldsymbol{r}}_i}{3!}\Delta t^3 + O(\Delta t^4)\,. \tag{3.4}$$

Adding these equations gives

$$\boldsymbol{r}_i(t+\Delta t) \approx 2\boldsymbol{r}_i(t) - \boldsymbol{r}_i(t-\Delta t) + \frac{\boldsymbol{F}_i(t)}{m}\Delta t^2\,, \tag{3.5}$$

which contains an error of order Δt^4.

Equation (3.5) can be used in an MD simulation to advance the positions of the particles. However, one of the drawbacks of this algorithm is that the velocities of the particles are not defined explicitly. The so-called 'velocity Verlet' algorithm possesses this desirable feature. In this scheme, the same Taylor expansion used in the original Verlet algorithm, Equation (3.3), is coupled to the following update of the velocities:

$$\boldsymbol{v}_i(t+\Delta t) = \boldsymbol{v}_i(t) + \frac{\boldsymbol{F}_i(t+\Delta t) + \boldsymbol{F}_i(t)}{2m}\Delta t\,. \tag{3.6}$$

In the implementation of the velocity Verlet algorithm, the positions are first updated according to Equation (3.3). From these new positions, the new forces can be calculated. Finally, the new velocities are computed according to the Equation (3.6). It can be shown fairly straightforwardly that this algorithm generates identical trajectories to the original Verlet algorithm [Frenkel & Smit, 2001]; it simply has the advantage that both the positions and velocities of the particles are defined at the same instant of time[2]. Because of this latter property, all of the simulations that have been performed for this thesis use the velocity Verlet algorithm.

[1] The algorithms are all variations of each other in the sense that they generate identical trajectories for the particles (see [Frenkel & Smit, 2001]).

[2] This is a useful property since it means that quantities depending on only the velocities and those depending on only the positions are defined at the same instant of time (for example, the kinetic and potential energy of the system).

The choice of timestep Δt is an important consideration in any MD simulation. The most important criterion Δt should satisfy is being small enough that the integration algorithm conserves the total energy of the system. A timestep that is too large in this respect will mean that the particle positions 'jump' too far each iteration, which can result in a particle finding itself unphysically close to another particle; this in turn is reflected in a jump in the potential energy (and thus also the total energy) of the system. For the YOCP and OCP systems investigated in this thesis, this is a particular problem at small Γ, which is equivalent to high temperatures[3], for which the average velocity of the particles is relatively large[4].

Some experimentation was required before choosing a timestep for the main simulations performed for this thesis. For this a number of 'test' simulations were performed using different Δt values. The total energy of the system was monitored during each simulation in order to check that the energy was well conserved, i.e., did not 'jump' from one timestep to the next. The degree of energy conservation was quantified by $\Delta E/E(0) = [E(t) - E(0)]/E(0)$. It was found that a timestep of $\Delta t = 0.01\omega_p^{-1}$ conserves the energy of the system very well ($\Delta E/E(0) \approx 10^{-6}$) for all $\Gamma \geq 1$. This timestep was then used for all of the main simulations, except for the small number of simulations performed for $\Gamma < 1$, for which it was necessary to use a smaller timestep, $\Delta t = 0.002\omega_p^{-1}$, in order to maintain the same degree of energy conservation. While in principle it would be possible to use a different timestep for every Γ value—as done in previous studies (see, e.g., [Hansen *et al.*, 1975], Table 1)—keeping the timestep constant at $\Delta t = 0.01\omega_p^{-1}$ helped to make the ensuing analysis of the MD data more straightforward, as this meant that the time series for, e.g., the intermediate scattering function was the same length in every case.

3.2 A typical MD simulation

Many MD simulations, including all of those performed for this thesis, are concerned with the physics of the system in thermal equilibrium only. This means that before recording any data the system must be 'equilibrated' from its initial state. Usually, this initial state (the positions and velocities of each of the N particles) is chosen so that the system is already 'close' to equilibrium. For the simulations performed for

[3] See the following section.

[4] In this respect, MD simulations of the YOCP and OCP systems are more straightforward when these systems are strongly coupled ($\Gamma \geq 1$) than when they are not. This is in contrast to theoretical approaches to the dynamics of the YOCP and OCP, which are usually more straightforward when $\Gamma \ll 1$.

this thesis, the initial velocities were assigned randomly from a Maxwell-Boltzmann distribution at the desired temperature. The only parameter needed for this was the desired coupling strength Γ, since the thermal velocity v_{th} (which specifies the width of the distribution), defined as

$$\frac{1}{2}mv_{th}^2 \equiv \langle \frac{1}{2}mv_{i,\alpha}^2 \rangle = \frac{1}{2}k_B T\,, \tag{3.7}$$

where $v_{i,\alpha}$ ($\alpha = x, y$ or z) denotes any Cartesian component of the velocity of any given particle, can be written in the reduced units used for the simulations in this thesis (with a the average inter-particle distance and ω_p the plasma frequency of the system as defined in Section 1.4) as

$$v_{th}/a\omega_p = \sqrt{1/3\Gamma}\,. \tag{3.8}$$

Therefore only Γ—and not in fact the temperature, which does not need to be specified—is needed for the velocity initialisation. The initial positions were assigned randomly in the simulation box, with a small region surrounding each particle excluded.

The equilibration is achieved simply by evolving the trajectories in time in the normal way, in other words, using the velocity Verlet algorithm given in the previous section. The only subtlety here is that as the system relaxes from its initial state, it is likely (even if the initial state is chosen very cleverly) that its potential energy will drop, and since the integration algorithm is energy conserving, the kinetic energy will then increase (instantaneously) by the same amount. This means that, although the system will indeed reach a numerical representation of thermal equilibrium, the temperature—i.e., the width of the Maxwell-Boltzmann velocity distribution—will be greater than desired temperature (i.e., the Γ of the system will be lower than specified at the beginning of the simulation). In the simulations performed for this thesis, the well known method of 'velocity scaling' was employed to solve this problem, that is, to ensure that the Γ of the system at the end of the equilibration phase was the same as the value of Γ specified at the beginning of the simulation. In accordance with this scheme, the 'instantaneous temperature' $T_{inst}(t)$, which is defined, in analogy with Equation (3.7), as

$$3k_B T_{inst}(t) = \sum_{i=1}^{N} \frac{mv_i^2(t)}{N}\,, \tag{3.9}$$

where $v_i^2 = v_{i,x}^2 + v_{i,y}^2 + v_{i,z}^2$, was computed at every timestep. Each component (x, y and z) of the velocity of every particle was then scaled (multiplied) by a factor

of $(T/T_{inst}(t))^{1/2}$. For all of the simulations, this velocity scaling was performed at every timestep of the equilibration phase. The length of this equilibration phase was chosen for all values of Γ to be $1000\omega_p^{-1}$, which, for $\Delta t = 0.01$, is 10^5 timesteps.

Once the equilibration phase is complete, the main part of the MD simulation begins. Again, the force on each particle is computed at each timestep and the particle positions are evolved in the usual way. The only difference between this part of the simulation and the equilibration phase is that no velocity scaling is applied. Since the system is now in a numerical representation of thermal equilibrium, the positions and velocities in time represent the microscopic equilibrium dynamics of the system for the values of Γ and κ that were specified at the beginning of the simulation. These positions and velocities are recorded[5] at every timestep until the simulation ends.

The output of any MD simulation is thus simply the positions and velocities of the particles of the system in 'equilibrium', that is, at every timestep of the simulation. Using this information, quantities that are of physical interest can be computed (which is, of course, the reason for doing the simulation in the first place). For example, using only the particle velocities, the average kinetic energy over the entire simulation run (of length τ),

$$\langle E_{kin} \rangle_\tau = \frac{1}{\tau} \int_0^\tau \left[\sum_{i=1}^{N} \frac{1}{2} m v_i^2(t) \right] dt \,, \tag{3.10}$$

can be calculated. In practice, the integral appearing in this equation must be evaluated as a discrete sum over the number of timesteps. Clearly, this type of time averaged quantity is a representation of the overall behaviour of the system in equilibrium. The formal statement of this is known as the 'ergodic hypothesis', which says that, in the limit $\tau \to \infty$, the time average appearing in expressions like Equation (3.10) is equivalent to an ensemble average. This means that time dependent correlation functions such as the intermediate scattering function $F(k,t)$ can be computed with MD.

3.3 The ergodic hypothesis

Using MD simulations, one can measure the microscopic dynamics of a system in thermal equilibrium. From these dynamics, time averages of any given functions of

[5] In practice, only certain functions of the positions and velocities—those that are needed to compute the time dependent correlation functions of interest—are recorded at each timestep. For example, to compute the intermediate scattering function $F(k,t)$, only $n(\boldsymbol{k},t)$, defined in Equation (2.11), needs to be recorded.

the positions and velocities of the particles (cf. Equation (3.10)) can be calculated. However, the quantities of principal interest to this thesis—the DSF $S(k,\omega)$, the intermediate scattering function $F(k,t)$, the radial distribution function $g(r)$ and the static structure factor $S(k)$—have in Section 2.2 all been defined in terms of *ensemble* averages. Thus, to compute these quantities with MD, the task is clear: the time averages computed in MD simulations need to be linked somehow to the ensemble averages. This link is provided by the so-called ergodic hypothesis.

Conceptually, the relation between time averages and ensemble averages is quite clear, and can be best thought of in the context of a 'real' experiment (rather than a computer experiment). When performing a real experiment, one does not measure the positions and velocities of a many particle system, but instead 'coarse-grained' or 'macroscopic' properties. To use the language of ensembles in statistical mechanics (which are motivated by exactly this reason), the microstate of a system is irrelevant. Rather, the system could be in any given microstate consistent with the experimentally imposed external conditions. This leads to the idea of the ensemble average, which is used as a tool to calculate the coarse-grained properties observed experimentally. The calculations of these ensemble averages are simplified by the fact that the question of which ensemble corresponds most closely to the real experimental setup is often irrelevant. This is because in the thermodynamic limit of $N \to \infty$—which is usually a good approximation for the experiments ($N > 10^{23}$)—the results of all ensembles can be shown to be formally equivalent.

Similarly, in an MD simulation, the system makes a 'transition' between microscopic configurations at each timestep. Since the equations of motion (Newton's equations) and their numerical implementation in MD (e.g., the velocity Verlet algorithm) are energy conserving—and since the number of particles N and volume of the simulation box V are held constant—this microscopic configuration is clearly a representation of a microstate in the microcanonical (constant N, V, E) ensemble. Therefore, by computing a certain physical quantity (a function of the positions and velocities of the particles) at every timestep and averaging, an approximation to the ensemble average of that quantity over the microcanonical ensemble is realised.

The intuitive discussion above is formalised by the ergodic hypothesis. A compact statement of this is

$$\langle \cdots \rangle = \langle \cdots \rangle_{\tau\to\infty} \,, \tag{3.11}$$

where $\langle \cdots \rangle$ denotes the ensemble average, and

$$\langle \cdots \rangle_{\tau\to\infty} = \lim_{\tau\to\infty} \frac{1}{\tau} \int_0^\tau \ldots dt \,. \tag{3.12}$$

Equation (3.11) is the essential link that allows the quantities of interest to this thesis to be computed with MD: the time average from MD is taken as the ensemble average. As given, this is an assumption which has not been proven rigorously (see [Frenkel & Smit, 2001] for a more detailed discussion). It should be noted, however, that even if such a proof were possible, the 'exact' ensemble average cannot ever be calculated, since only an approximation to $\langle \cdots \rangle_{\tau \to \infty}$ can be obtained with MD. Specifically, since the simulations are done in discrete time, the integral in Equation (3.12) is approximated by a summation, and since the simulation time is finite, the upper limit of the integral is fixed. The two parameters that characterise these discretisations, the timestep Δt and the number of timesteps $\tau/\Delta t$, are important in determining how accurately the ensemble average can be approximated.

The simulations for this thesis were all performed in the microcanonical ensemble. As mentioned in the foregoing discussion, this is the 'default' ensemble that is sampled from when the equations of motion are integrated directly; more sophisticated techniques are needed in order to use MD to sample from other ensembles (see, e.g., [Allen & Tildesley, 1988, Frenkel & Smit, 2001]).

3.4 Periodic boundary conditions

Usually, and in this thesis, one is interested in computing with MD bulk properties of the system, or, more formally, properties in the thermodynamic limit $N \to \infty$. However, only systems with a finite, and usually relatively small ($N \approx 10^3 - 10^6$) number of particles can be simulated. This introduces the problem of surface effects. For example, in a simulation of a simple cubic crystal consisting of 1000 particles, 512 will be at the surface.

The usual way to overcome (or at least mitigate) the problem of surface effects is to impose periodic boundary conditions. In this scheme, it is imagined that the cubic simulation box containing the particles is replicated throughout space to form an infinite lattice. This is illustrated in the two-dimensional case in Figure 3.1. As shown in Figure 3.1, if a particle moves out of the main simulation box, one of its periodic replicas from a neighbouring box moves in to replace it.

The simulations performed for this thesis were all done using a cubic box with periodic boundary conditions. The box length L was chosen so that $N/L^3 = n$. The density n (like the temperature) does not in fact need to be given explicitly at the

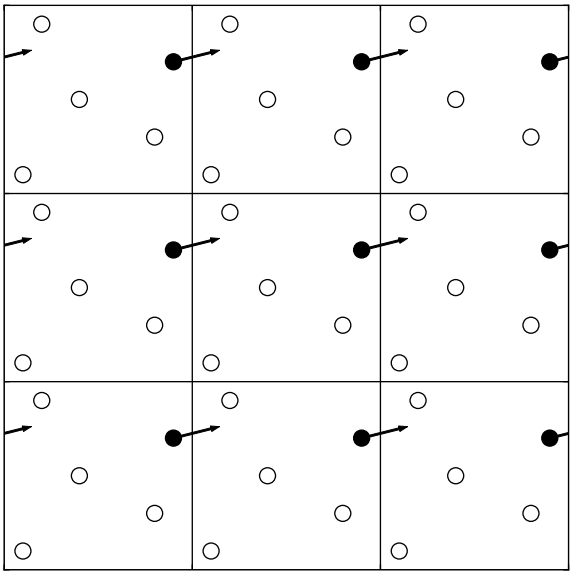

Figure 3.1: Periodic boundary conditions used in MD simulations.

beginning of the simulation since, in dimensionless units, $N/L^3 = n$ gives

$$\frac{L}{a} = \frac{1}{a}\left(\frac{N}{n}\right)^{1/3} = \left(\frac{4\pi}{3}N\right)^{1/3}, \tag{3.13}$$

and therefore the box length is completely specified by the number of particles N. Most of the simulations used for the investigations presented in Chapters 4-8 were done for $N = 5\times10^3$, with a few simulations for $N = 5\times10^4$ and some for $N = 5\times10^5$; where the MD results correspond to either of these larger system sizes, this is stated in the text.

The question of whether $N = 5 \times 10^3$ is sufficiently large to neglect finite size effects certainly merits consideration. A comparison of results at different system sizes suggests that this number of particles is indeed more than sufficient for size effects to be neglected. An example of this is given in Figure 3.2, which shows MD results for the static structure factor $S(k)$ are very similar for $N \geq 100$. A number of previous studies of the OCP and YOCP also indicate that $N = 5 \times 10^3$ is more than large enough to render surface effects negligible: for example, the pioneering Monte Carlo work of Hansen [Hansen, 1973] found that for the OCP $N > 100$ ions yields results close to the thermodynamic limit ($N \to \infty$) in the entire fluid range, and Caillol and Gilles [Caillol & Gilles, 2000a] found that the free energy of the YOCP differs only slightly beyond $N = 600$. In addition to these studies, there have been a number of others devoted to calculation of transport coefficients [Daligault, 2006, Donkó &

Hartmann, 2004, Donkó *et al.*, 2010, Saigo & Hamaguchi, 2002], which, although not designed to be thorough studies of finite size effects, suggest that $\approx 1 \times 10^3$ particles is more than sufficient for size effects to be negligible.

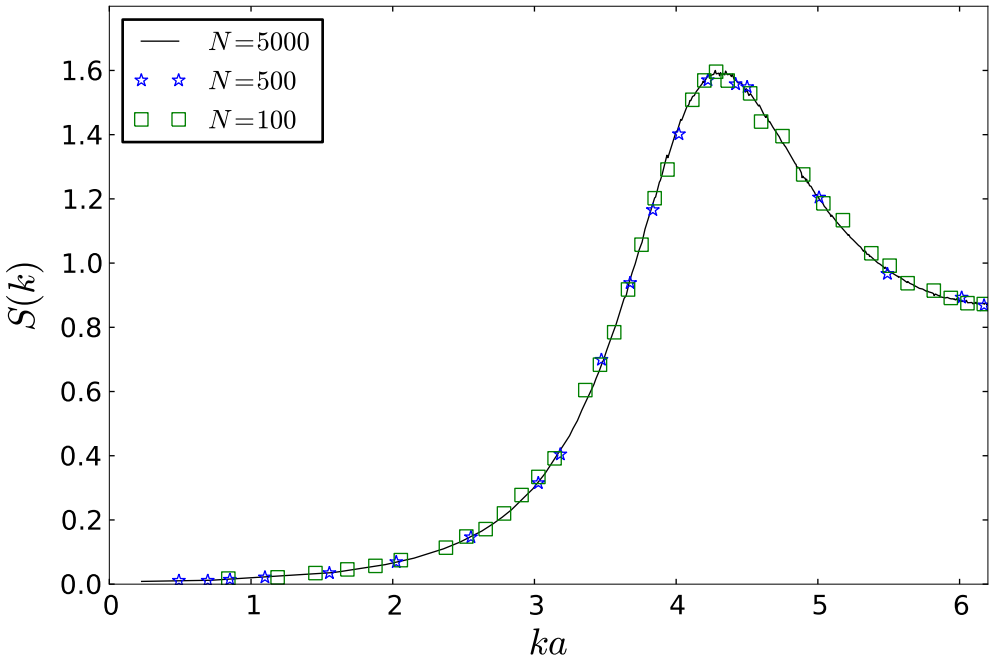

Figure 3.2: Static structure factor computed with MD simulations (see Section 3.9) at $\Gamma = 120$, $\kappa = 1$ for different system sizes (numbers of particles) N.

3.5 Charge neutrality in periodic boundary conditions

As stated in Section 2.3, it is possible to show that when periodic boundary conditions are applied to the OCP system, the total charge in the simulation box must be zero. This then serves as a simple proof that the uniform background of neutralising charge is required for the OCP model to be studied using MD techniques (at least, that is, when periodic boundary conditions are applied).

The proof is based on the following simple consideration: in periodic boundary conditions, since the particles in each box (cf. Figure (3.1)) are assumed to have the same dynamics, the force at the same point in each box must be identical, i.e., the force is periodic, with periodicity L,

$$\boldsymbol{F}(\boldsymbol{r} + L(n_x, n_y, n_z)) = \boldsymbol{F}(\boldsymbol{r})\,, \tag{3.14}$$

where n_x, n_y and n_z are integers. For the OCP, $\boldsymbol{F}(\boldsymbol{r}) = -\nabla\phi(\boldsymbol{r})$, where the potential $\phi(\boldsymbol{r})$ is given by the Poisson equation[6] ,

$$\nabla^2\phi(\boldsymbol{r}) = \frac{\rho(\boldsymbol{r})}{\epsilon_0}\,, \tag{3.15}$$

where $\rho(\boldsymbol{r})$ is the (microscopic) charge density. The Poisson equation can be integrated over a simulation box,

$$\int_0^L\int_0^L\int_0^L \nabla^2\phi(\boldsymbol{r})dxdydz = \int_0^L\int_0^L\int_0^L \frac{\rho(\boldsymbol{r})}{\epsilon_0}dxdydz\,. \tag{3.16}$$

The left hand side of this equation is simply

$$\int_0^L\int_0^L \left[\frac{\partial\phi(\boldsymbol{r})}{\partial x}\right]_0^L dydz + \int_0^L\int_0^L \left[\frac{\partial\phi(\boldsymbol{r})}{\partial y}\right]_0^L dxdz + \int_0^L\int_0^L \left[\frac{\partial\phi(\boldsymbol{r})}{\partial z}\right]_0^L dxdy\,, \tag{3.17}$$

which is equal to zero, since each of the terms in the square brackets is equal to zero (to see this, consider Equation (3.14) for e.g. $n_x = 1, n_y = 0, n_z = 0$, which gives $\frac{\partial\phi(\boldsymbol{r})}{\partial x}|_{x=L} = \frac{\partial\phi(\boldsymbol{r})}{\partial x}|_{x=0}$). Therefore, the right hand side of Equation (3.16) must also be equal to zero. This right hand side is simply the total charge enclosed in the simulation box divided by ϵ_0, and therefore the total charge enclosed in the simulation box must be zero.

3.6 MD for systems with long range potentials

The techniques used in the MD simulations of the YOCP and OCP in the fluid phase undertaken by the author are essentially identical to simulations of normal liquids that have been conducted for many years, save for one important detail: the long range potentials of the YOCP and OCP require special attention in the force calculation part of the MD program.

For normal liquids, the interaction potential is relatively short range (in MD simulations it is often taken to be, e.g., the Lennard-Jones potential). This means that the only significant contributions to the force on any given particle come from particles in its immediate vicinity. Accordingly, often used in MD simulations with periodic boundary conditions is the 'minimum image convention'; as the name suggests, only the nearest periodic image of each particle (whether it is in the main simulation box or one of the adjacent boxes) is taken to contribute to the force calculation. An alternative is to employ a cut-off radius, which is typically taken to be considerably smaller

[6]Note that the periodicity of $\boldsymbol{F}$ does not mean that ϕ must be periodic, only that $\nabla\phi$ must be periodic.

than $L/2$ (the maximum radius of a sphere that can be packed into the cubic box). For long range potentials, these methods are likely to introduce serious errors in the force calculation, and therefore in the resulting trajectories of the particles. Instead, one must include the force contributions from all particles in the main simulation box as well as from all the particles in every periodic replica (i.e., from an infinite number of particles). This seemingly tricky task is accomplished by the so-called Ewald summation, which is the subject of the following section.

3.7 The Ewald summation and the PPPM algorithm

This brief discussion of the Ewald summation is based on the excellent article by Deserno and Holm [Deserno & Holm, 1998], although numerous other accounts in the context of computer simulations are available elsewhere [Allen & Tildesley, 1988, Frenkel & Smit, 2001, Hansen, 1973, Hockney & Eastwood, 1981], and the topic is standard in solid state physics textbooks.

The Ewald summation is a method for evaluating the total potential energy,

$$V = \frac{1}{2} \sum_{i,j=1}^{N} {\sum_{\boldsymbol{m}\in\mathbb{Z}}}' v(\boldsymbol{r}_{ij} + \boldsymbol{m}L) \,, \tag{3.18}$$

of a system of N interacting particles in periodic boundary conditions. It was originally developed for Coulomb systems [Ewald, 1921], and this does indeed remain its main application (in this case, the total potential energy is known as the electrostatic potential energy); however, in principle the Ewald method can be applied for any interaction potential[7]. In Equation (3.18), the sum over $\boldsymbol{m}$ takes into account the periodic images of the particles, the prime indicates that for $\boldsymbol{m} = 0$ the case $i = j$ must be omitted, and $\boldsymbol{r}_{ij} = \boldsymbol{r}_i - \boldsymbol{r}_j$.

In the case of the Coulomb potential, which is relevant to the OCP system studied in this thesis, Equation (3.18) becomes

$$V = \frac{1}{2} \sum_{i,j=1}^{N} {\sum_{\boldsymbol{m}\in\mathbb{Z}}}' \frac{(Ze)^2}{4\pi\epsilon_0 |\boldsymbol{r}_{ij} + \boldsymbol{m}L|} \,. \tag{3.19}$$

Direct evaluation of this sum is problematic, formally because it is ill defined as a result of being only conditionally convergent (see [Deserno & Holm, 1998] and

[7] This is relevant here because the Ewald summation has been applied to the MD simulations in this thesis for both the OCP (Coulomb potential) and the YOCP (Yukawa potential).

references therein), and practically due to the slowly decaying long range part of the Coulomb potential. The essential step in the Ewald method is to split the sum in Equation (3.19) into two parts, using the trivial identity

$$\frac{1}{r} = \frac{f(r)}{r} + \frac{1 - f(r)}{r} \,. \tag{3.20}$$

The idea behind this splitting is as follows: $f(r)$ can be chosen so that the first part of Equation (3.20) is negligible beyond some (small) cutoff radius r_{max}, and so that the second part is a slowly varying function for all r, which means that its Fourier transform is well represented by only a few wave-vectors $\boldsymbol{k}$. This allows the first 'short range' part to be readily evaluated in real space, and the second 'long range' part in reciprocal space. The usual selection for $f(r)$ is the complementary error function,

$$\mathrm{erfc}(r) = \frac{2}{\sqrt{\pi}} \int_r^\infty \exp(-t^2) dt \,, \tag{3.21}$$

which leads to the well-known Ewald formula for the total potential energy of the system [Deserno & Holm, 1998],

$$V = V^{(r)} + V^{(k)} + V^{(s)} + V^{(d)} \,, \tag{3.22}$$

where the contributions from real space ($V^{(r)}$), reciprocal space ($V^{(k)}$), self-energy ($V^{(s)}$) and dipole correction ($V^{(d)}$) are given by

$$V^{(r)} = \frac{1}{2} \sum_{i,j=1}^{N} {\sum_{\boldsymbol{m}\in\mathbb{Z}}}' \frac{(Ze)^2}{4\pi\epsilon_0} \frac{\mathrm{erfc}(\alpha|(\boldsymbol{r}_{ij} + \boldsymbol{m}L)|)}{|(\boldsymbol{r}_{ij} + \boldsymbol{m}L)|} \,, \tag{3.23}$$

$$V^{(k)} = \frac{1}{2L^3} \sum_{\boldsymbol{k}\neq 0} \frac{(Ze)^2}{\epsilon_0 k^2} \exp(-k^2/4\alpha^2) |n(\boldsymbol{k})|^2 \,, \tag{3.24}$$

$$V^{(s)} = -\frac{\alpha}{\sqrt{\pi}} \sum_{i=1}^{N} \frac{(Ze)^2}{4\pi\epsilon_0} \,, \tag{3.25}$$

$$V^{(d)} = \frac{1}{2\pi\epsilon_0(1+2\epsilon')L^3} \left(\sum_{i=1}^{N} Ze\boldsymbol{r}_i \right)^2 \,. \tag{3.26}$$

$$\tag{3.27}$$

The parameter α, which appears in Equations (3.23) and (3.24), can be tuned so that evaluation is as efficient as possible [Deserno & Holm, 1998]. In Equation (3.24), $n(\boldsymbol{k})$ is the Fourier transform of the particle density (as given previously in Equation (2.11)), and the summation is over wave-vectors at the discrete values of $\boldsymbol{k}$ consistent with the periodic boundary conditions.

From Equations (3.22)-(3.26), the force on each particle i in the simulation box can be calculated as (cf. Equation (3.2))

$$\boldsymbol{F}_i = -\nabla_i V = -\frac{\partial}{\partial \boldsymbol{r}_i} V \,. \tag{3.28}$$

This final equation in principle completes the specification of the force calculation part of an MD program dealing with Coulomb interactions[8]. In this force calculation, the real space part of the force resulting from $V^{(r)}$ is directly evaluated, using some cutoff radius, and the reciprocal space sum resulting from $V^{(k)}$ is truncated at some maximum wave-vector.

While the direct evaluation of the Ewald summation as outlined above in principle solves the problem of including long range interactions in an MD simulation, it has one main drawback: poor computational efficiency. This is mainly a result of the fact that direct evaluation (that is, implementing the formulae given above in an MD code) scales with particle number N approximately as N^2 [Deserno & Holm, 1998]. In order to improve this scaling, a number of methods based on evaluating the long range part of the potential on a grid (or 'mesh') have been developed. The idea behind these methods is that they allow the reciprocal space part of the Ewald summation to be evaluated using the fast Fourier transform, which itself scales as $N \log N$ (a significant improvement on N^2). By choosing the real space cutoff to be sufficiently small, this improved scaling then essentially applies to the complete Ewald sum [Deserno & Holm, 1998].

One of the various mesh implementations—which, according to Deserno and Holm, is "the most accurate one and should be the preferred choice" [Deserno & Holm, 1998]—is the so-called particle-particle-mesh (PPPM) algorithm [Hockney & Eastwood, 1981]. For details of this algorithm, the reader is referred to [Deserno & Holm, 1998]. All of the MD simulations performed by the author for this thesis use the PPPM algorithm for the Ewald summation.

As a final comment, it is noted that including the Ewald summation in an MD program makes the force calculation part substantially more complicated and, in addition, more time consuming. Even with sophisticated algorithms such as PPPM, the number of particles used in MD simulations of the YOCP and OCP are commonly an order of magnitude or more smaller than for systems with short range interaction

[8]The full expression for $\boldsymbol{F}_i$ resulting from the differentiation in Equation (3.28) is given in [Deserno & Holm, 1998], Equations (13)-(16). These expressions are readily extended to the case of the Yukawa potential by including the additional exponential decay of the potential in the relevant terms.

potentials; the system sizes of $N \sim 10^3$ and above used for the simulations in this thesis are among the largest performed to date.

3.8 Computing $g(r)$

This section and the two that follow describe the way in which the equilibrium properties of interest to this thesis—$g(r)$, $S(k)$, $F(k,t)$ and $S(k,\omega)$—were computed from the MD data, that is, from the positions and velocities of the particles at each timestep of the simulation. This section covers the radial distribution function, $g(r)$, the following section the static structure factor, $S(k)$, and the final section both the intermediate scattering function, $F(k,t)$, and the DSF, $S(k,\omega)$.

The definition of the radial distribution function, given previously in Equation (2.21), is

$$g(r) = \frac{1}{nN} \left\langle \sum_{i=1}^{N} \sum_{j \neq i=1}^{N} \delta(\boldsymbol{r} + \boldsymbol{r}_j - \boldsymbol{r}_i) \right\rangle . \tag{3.29}$$

This can be written as

$$g(r) = \frac{2}{nN} \left\langle \sum_{i=1}^{N} \sum_{j<i}^{N} \delta(\boldsymbol{r} + \boldsymbol{r}_j - \boldsymbol{r}_i) \right\rangle , \tag{3.30}$$

the only difference being that each pair of particles is now included only once in the summation. Using MD, $g(r)$ cannot be measured at a point r; what can be measured is its average value over a shell of width Δr,

$$\bar{g}(r) = \frac{1}{V(r,\Delta r)} \int_{r}^{r+\Delta r} g(r) 4\pi r^2 dr \, , \tag{3.31}$$

where $V(r,\Delta r) = \frac{4}{3}\pi[(r+\Delta r)^3 - r^3]$ is the volume of the shell. An expression for $\bar{g}(r)$ can be obtained by integrating Equation (3.30) between r and $r + \Delta r$:

$$\int_{r}^{r+\Delta r} g(r) 4\pi r^2 dr = \frac{2}{nN} \left\langle \sum_{i=1}^{N} \sum_{j<i}^{N} \int_{\boldsymbol{r}}^{\boldsymbol{r}+\Delta \boldsymbol{r}} \delta(\boldsymbol{r} + \boldsymbol{r}_j - \boldsymbol{r}_i) d\boldsymbol{r} \right\rangle . \tag{3.32}$$

The left hand side of this is simply $\bar{g}(r)V(r,\Delta r)$, and thus

$$\bar{g}(r) = \frac{2}{nN} \frac{\langle N(r,\Delta r) \rangle}{V(r,\Delta r)} \, , \tag{3.33}$$

where $N(r,\Delta r)$ denotes the number of pairs of particles with separation between r and $r + \Delta r$. In order to cast this into a form suitable for evaluation with MD, the

ensemble average is converted into a time average in the normal way, which gives

$$\bar{g}(r) = \frac{1}{N_{step}} \sum_{i=1}^{N_{step}} \left(\frac{2}{Nn} \right) \frac{N_i(r, \Delta r)}{V(r, \Delta r)} \,. \tag{3.34}$$

Equation (3.34) is in a form that can readily be evaluated from the positions of the particles at each timestep.

Two points concerning this numerical implementation of the radial distribution function are worth mentioning. The first is that, in (cubic) periodic boundary conditions, $\bar{g}(r)$ can only be determined for distances of at most $L/2$, which is the radius of the largest sphere that can be contained in a cube of length L. The second is that, since $\bar{g}(r)$ calculated from Equation (3.34) is essentially the average value of the radial distribution function between r and $r + \Delta r$, the effective r, r_{eff}, at which the value given by Equation (3.34) is taken to correspond to, is not defined. While the most obvious choice is $r_{eff} = (r + \Delta r)/2$, a more refined choice, which produces a 'smoother' result, was given by Poll, Aschcroft and DeWitt [Poll *et al.*, 1988]. In this scheme, r_{eff} is defined by

$$\bar{g}(r) = \frac{1}{V(r, \Delta r)} \int_r^{r+\Delta r} g(r_{eff}) 4\pi r^2 dr \,. \tag{3.35}$$

Thus r_{eff} is simply the value of r which gives $\bar{g}(r)$ defined in Equation (3.31) when $g(r)$ is taken to be constant between r and Δr. To compute r_{eff}, $g(r)$ appearing in Equation (3.31) is Taylor expanded about the point $r = r_{eff}$ to give

$$\bar{g}(r) = \frac{1}{V(r, \Delta r)} \int_r^{r+\Delta r} (g(r_{eff}) + (r - r_{eff}) g'(r_{eff}) + \cdots) 4\pi r^2 dr \,. \tag{3.36}$$

In order to satisfy Equation (3.35), the term proportional to $g'(r_{eff})$ should vanish. Finally then, solving

$$\int_r^{r+\Delta r} (r - r_{eff}) g'(r_{eff}) 4\pi r^2 dr = 0 \tag{3.37}$$

gives

$$r_{eff} = \frac{3}{4} r \left[\frac{(1 + \Delta r/r)^4 - 1}{(1 + \Delta r/r)^3 - 1} \right] \,. \tag{3.38}$$

For the MD simulations performed for this thesis, Equation (3.34) was used to compute the radial distribution function, which was taken to be its value at r_{eff} defined above. For all the simulations, Δr was taken to be $0.005a$. This was found to result in very smooth data for the radial distribution function.

3.9 Computing $S(k)$

Although it is in principle possible to compute the static structure factor $S(k)$ using the radial distribution function $g(r)$ obtained from MD (cf. Equation (2.6)), this requires knowledge of $g(r)$ for all values of r, and will involve errors caused by taking a numerical Fourier transform. A more convenient way to compute $S(k)$ is directly from its definition, which was given previously in Equation (2.18) as

$$S(k) = \frac{1}{N}\langle |n(\boldsymbol{k})|^2 \rangle \,, \tag{3.39}$$

where the property $n(-\boldsymbol{k}) = n^*(\boldsymbol{k})$ has been used. Since, in periodic boundary conditions, the density is periodic (with periodicity L), $S(k)$ can only be computed at the discrete values of k given by[9]

$$k = |\boldsymbol{k}| = \frac{2\pi}{L}|(n_x, n_y, n_z)| \,, \tag{3.40}$$

where n_x, n_y and n_z are integers. Importantly, this means that the minimum k value at which the static structure factor can be computed with MD is $k_{min} = 2\pi/L$, which, using Equation (3.13) for the box length L, can be expressed in reduced units as

$$k_{min}a = 2\pi \left(\frac{3}{4\pi}\frac{1}{N}\right)^{\frac{1}{3}} \,. \tag{3.41}$$

It is noted in passing that this equation—which applies to any property (static or dynamic) that depends on the wave number k—is precisely the reason that the MD simulations for the investigation into the hydrodynamic description of the YOCP presented in Chapter 4 were challenging: since k_{min} scales as the inverse of the cube root of the number of particles, a very large number of particles was needed to measure the long lengthscale (small k) properties of relevance to the hydrodynamic description.

In the MD implementation of the static structure factor, all that is required is to rewrite the ensemble average appearing in Equation (3.39) as a time average:

$$S(k) = \frac{1}{N}\frac{1}{N_{step}}\sum_{i=1}^{N_{step}} |n(\boldsymbol{k})|_i^2 \,, \tag{3.42}$$

The quantity $n(\boldsymbol{k})$ is readily computed at each timestep of the MD simulation using its definition as the Fourier transform of the particle positions, Equation (2.11). A further averaging not denoted above is also afforded due to the isotropy of the systems

[9] This condition is obtained by expanding any space dependent quantity as a Fourier series with a periodicity that is necessarily equal to the box length L.

studied in this thesis: this is over all $\boldsymbol{k}$ values of equal magnitude. For example, to calculate $S(k_{min}a)$, the results of Equation (3.42) when $\boldsymbol{k} = k_{min}(1,0,0)$, $k_{min}(0,1,0)$ and $k_{min}(0,0,1)$—which will all in general be slightly different—are averaged. For larger k values, this multiplicity is often far greater than threefold, and the additional averaging helps to improve the accuracy of the MD data significantly.

Because of the large number of timesteps (as well as the averaging over k) in the simulations performed for this thesis, it was possible to obtain very accurate, smooth data for $S(k)$ that was used in the investigations presented in Chapters 4-7.

3.10 Computing $F(k,t)$ and $S(k,\omega)$

Computation of the DSF, $S(k,\omega)$, is done via the intermediate scattering function, defined previously in Equation (3.43) as

$$F(k,t) = \frac{1}{N}\langle n(\boldsymbol{k},t)n(-\boldsymbol{k},0)\rangle\,. \tag{3.43}$$

Inspection of this equation reveals exactly why the intermediate scattering function, and hence the DSF, is more challenging to compute than static properties like $g(r)$ and $S(k)$: static properties are defined as ensemble averages of a certain dynamical variable at equal times, wheras the intermediate scattering function involves the ensemble average at two different times. Accordingly, for static properties, the conversion of the ensemble average into a time average means that the quantity appearing inside the brackets $\langle\cdots\rangle$ can be computed at every timestep of an MD simulation and averaged over the number of timesteps (cf. Equations (3.34) and (3.42)). On the other hand, to compute $F(k,t)$ at a given value of t, only MD configurations separated by time t can be averaged; thus, as t increases, fewer and fewer MD measurements contribute to the average, with the consequence that the computed value of the intermediate scattering function gets more and more 'noisy' with increasing t. To be clear, the MD implementation of Equation (3.43) is

$$F(k,m\Delta t) = \frac{1}{N}\frac{1}{N_{step}-m}\sum_{j=0}^{N_{step}-m-1} n(\boldsymbol{k},(j+m)\Delta t)n(-\boldsymbol{k},j\Delta t)\,, \tag{3.44}$$

where $m = 0,1,\ldots,N_{step}-1$[10] . In the case of $m = 0$, since $F(k,0) = S(k)$ (Equation (2.18)), this equation is identical to Equation (3.42). It can be seen that a total of N_{step} MD measurements contribute to $F(k,0)$. In the other extreme case of $m = N_{step}-1$,

[10]The allowed values of k and the procedure for averaging over all $\boldsymbol{k}$ values with the same magnitude are the same as given in Section 3.9 for the static structure factor.

only one MD measurement, corresponding to a single pair of particle configurations—the initial and final positions of the particles—contributes to the determination of the intermediate scattering function.

The DSF is computed by taking the discrete Fourier transform (DFT)[11] of Equation (3.44),

$$S(k, m\Delta\omega) = \frac{1}{2\pi} \sum_{j=0}^{N_{step}-1} F(k, j\Delta t) \exp(ij\Delta\omega)\,, \tag{3.45}$$

where $m = 0, 1, \ldots, N-1$, and $\Delta\omega = 2\pi/N_{step}\Delta t$.

For the simulations performed for this thesis, the intermediate scattering function was computed using Equation (3.44). Although $S(k,\omega)$ can then be obtained simply by taking the DFT of $F(k,t)$ according to Equation (3.45), this was found to produce rather 'noisy' data for $S(k,\omega)$. After some experimentation, it was found that a more smoothly varying $S(k,\omega)$—essential for the quantitative analysis of the DSF presented in later chapters—could be obtained by making some simple modifications to the 'raw' $F(k,t)$ before taking the DFT. Since the research presented in Chapters 4-7 is focused on the DSF, a detailed account of these modifications, and their effects, is given in the following section.

3.11 Obtaining high quality data for $S(k,\omega)$

Obtaining MD data for $S(k,\omega)$ that is of sufficiently high quality to facilitate the detailed investigations presented in Chapters 4-7 of this thesis is a significantly more challenging task than obtaining high quality MD data for the static properties such as $g(r)$ and $S(k)$. Indeed, it is expected that the high quality MD data for $S(k,\omega)$ of the YOCP and OCP systems across a wide range of Γ and κ values produced for this thesis will be one of its main contributions to the community of researchers working on non-ideal plasmas.

It is the intermediate scattering function, rather than the DSF itself, that is directly computed in MD simulations. Therefore, when considering how to obtain high quality data for the DSF, it makes sense to first think about how to produce high quality data for the intermediate scattering function. As can be seen by inspecting Equation (3.44), the simplest way to do this is to have a long simulation (i.e., make N_{step} large); this means that at each t value, a large number of measurements are averaged to produce $F(k,t)$. The simulations performed for this thesis all used the

[11] This can be implemented efficiently using the fast Fourier transform algorithm (see, e.g., [Press *et al.*, 1992]).

parameters[12] $N_{step} = 2^{13}$ and $\Delta t = 0.1$, which corresponds to a simulation of length $819.1\omega_p^{-1}$. This is certainly a long simulation: for example, it is approximately 1000 times the length of simulation employed in the study by Hansen et al. of the OCP system [Hansen *et al.*, 1975], which, even after more than 30 years, still remains the primary source of MD data for quantitative studies of the OCP [Arkhipov *et al.*, 2010].

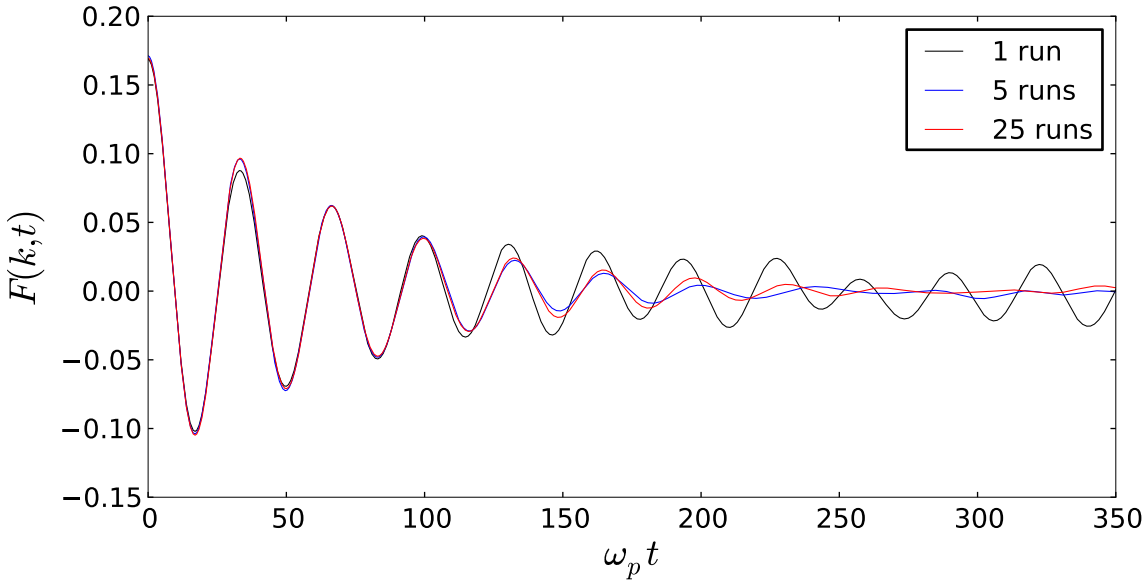

Figure 3.3: Illustration of the effect of block averaging on the intermediate scattering function $F(k,t)$ computed with MD. The data shown is for $\Gamma = 1$, $\kappa = 2$, $ka = 0.39$; at this small k value, corresponding to long lengthscale behaviour, $F(k,t)$ is seen to exhibit oscillations that decay slowly, over hundreds of inverse plasma frequencies. The time discretisation ($\omega_p \Delta t = 0.1$) is too small to be seen on the scale of this plot.

Another, similar, way to improve the MD data for $F(k,t)$ is to perform multiple simulations and average the results. This procedure, known as 'block averaging', is commonplace in MD investigations [Frenkel & Smit, 2001]. To produce the data presented in this thesis a total of 25 separate MD runs were performed for each (Γ,κ) pair, and in each case the intermediate scattering function was computed according to Equation (3.44), with the final estimate being the 'block' average of these 25 runs[13].

[12]Note that for the integration of the equations of motion, $\Delta t = 0.01\omega_p^{-1}$ was used, as stated in Section 3.1; however, since data was only recorded every 10 timesteps, in Equation (3.44) for the intermediate scattering function (and the equivalent formula for other time dependent correlation functions), $\Delta t = 0.1\omega_p^{-1}$.

[13]To achieve this, the initial configuration of the particles for each of these 25 runs was taken to be the final configuration of the particles on the previous run (meaning only a single equilibration was required for each Γ and κ value).

The effect of this block averaging is shown in Figure 3.3; it can be seen that the 'noise' in the intermediate scattering function at long times is reduced as the number of averages increases. In general it was found that $F(k,t)$ does not change appreciably beyond 25 MD runs.

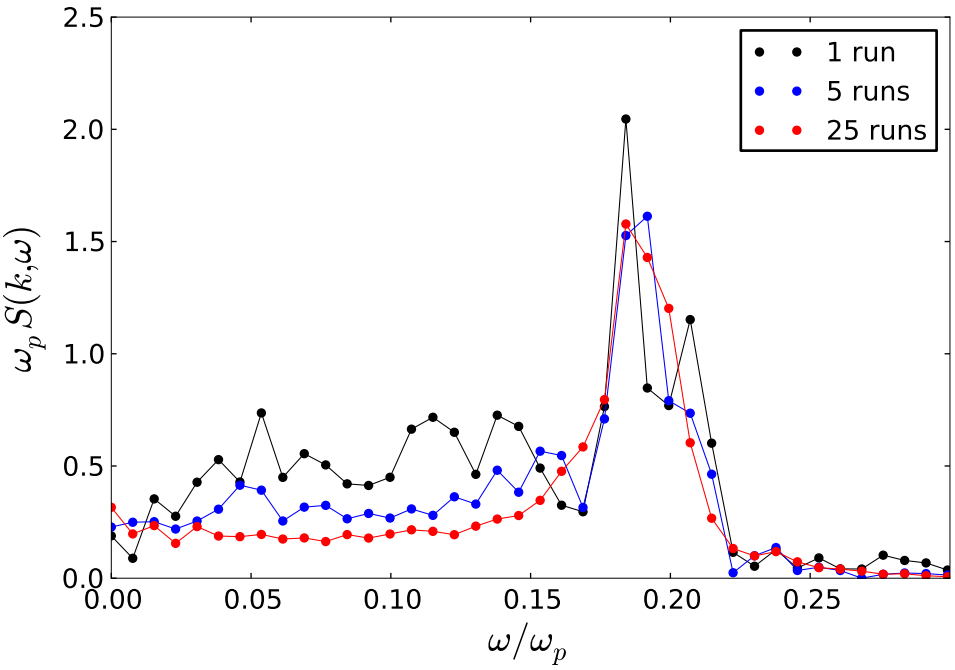

Figure 3.4: Effect of block averaging on the DSF, for the same conditions as in Figure 3.3.

The use of long simulations and block averaging, as discussed above, was found to produce a smoothly varying result for the intermediate scattering function $F(k,t)$. However, despite the satisfactory appearance of $F(k,t)$, the DSF (obtained by taking the DFT of $F(k,t)$ according to Equation (3.45)) was found to be rather 'noisy', and this even after all 25 runs. An example of this is shown in Figure 3.4: although the block averaging does improve the data for the DSF, even after 25 runs a certain amount of numerical 'noise' is evident from the jagged appearance of $S(k,\omega)$. This noise is partly due to the fact that the DSF is obtained at discrete frequencies, separated by $\Delta\omega/\omega_p = 2\pi\omega_p/N_{step}\Delta t \approx 0.0077$ (cf. Equation (3.45)). In any case, to assist with the quantitative investigations of the DSF presented in Chapters 4-7, it was necessary to have a more smoothly varying $S(k,\omega)$ than illustrated in Figure 3.4. After some experimentation, it was found that the simplest way to accomplish this was to smooth the intermediate scattering function 'by hand' before taking its DFT. This 'smoothed' $F(k,t)$ is shown alongside the 'raw' $F(k,t)$ from MD in Figure 3.5

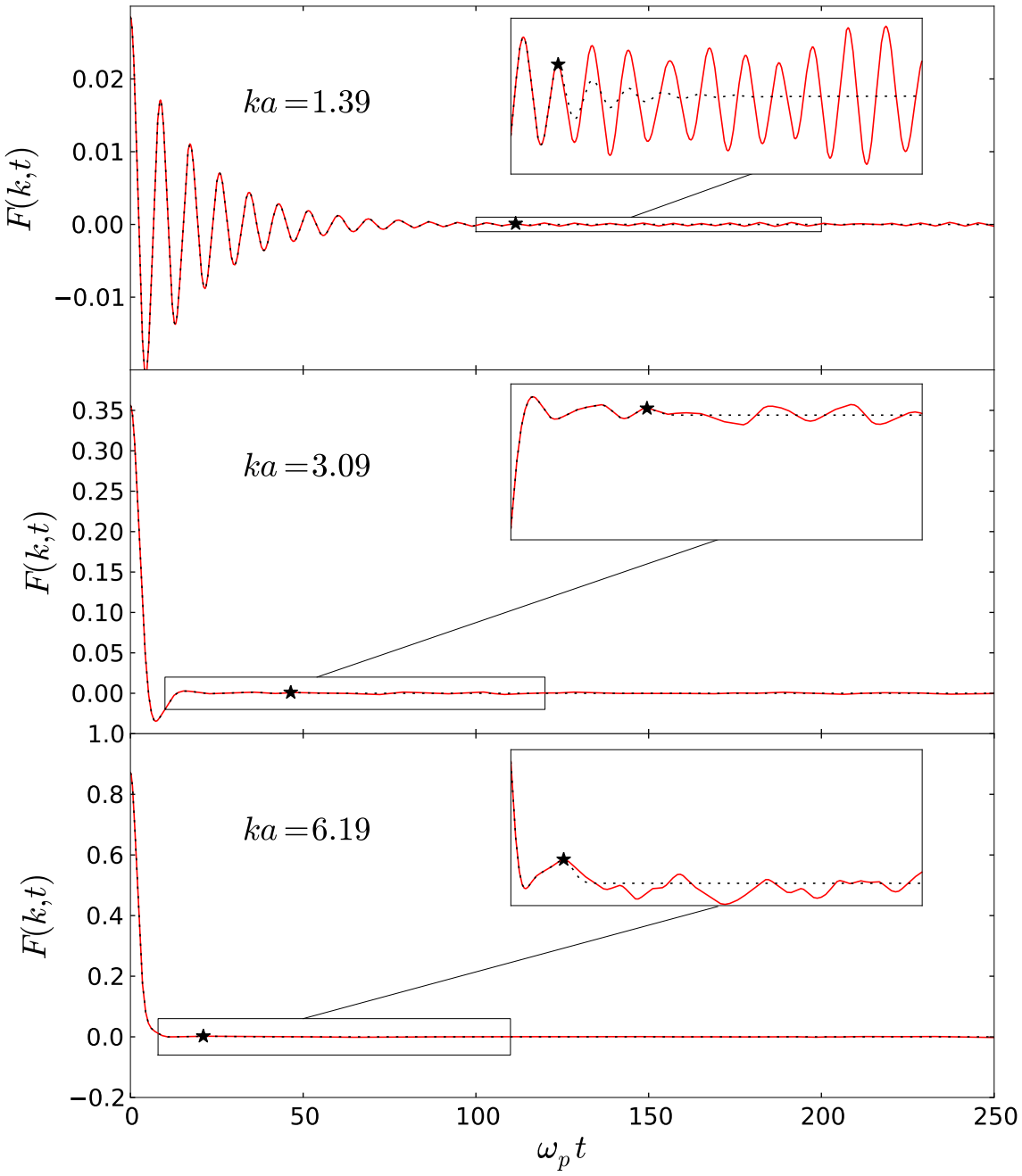

Figure 3.5: Intermediate scattering function $F(k,t)$ for small (top panel), intermediate (middle panel) and large (bottom panel) k values at $\Gamma = 50$, $\kappa = 1$. The solid (red) line is the raw data from the MD simulations, and the dotted (black) line is after smoothing. In each case, the smoothed data is identical to the raw MD data as far as the star symbol at $t = t_{peak}$, after which it is extended to decay to zero in the manner outlined in the text. Note that $F(k,t)$ is shown up to $t = 250\omega_p^{-1}$ only (rather than up to the full $819.1\omega_p^{-1}$ computed in the MD simulations), and that the time discretisation ($\omega_p \Delta t = 0.1$) is too small to resolve on the scale of this plot.

for example small, intermediate and large k values. The main point to make is that, as shown in Figure 3.5, the smoothed version of $F(k,t)$ differs only slightly from the raw $F(k,t)$; however, these differences more or less accomplish the task of smoothing the DSF, as shown in Figure 3.6.

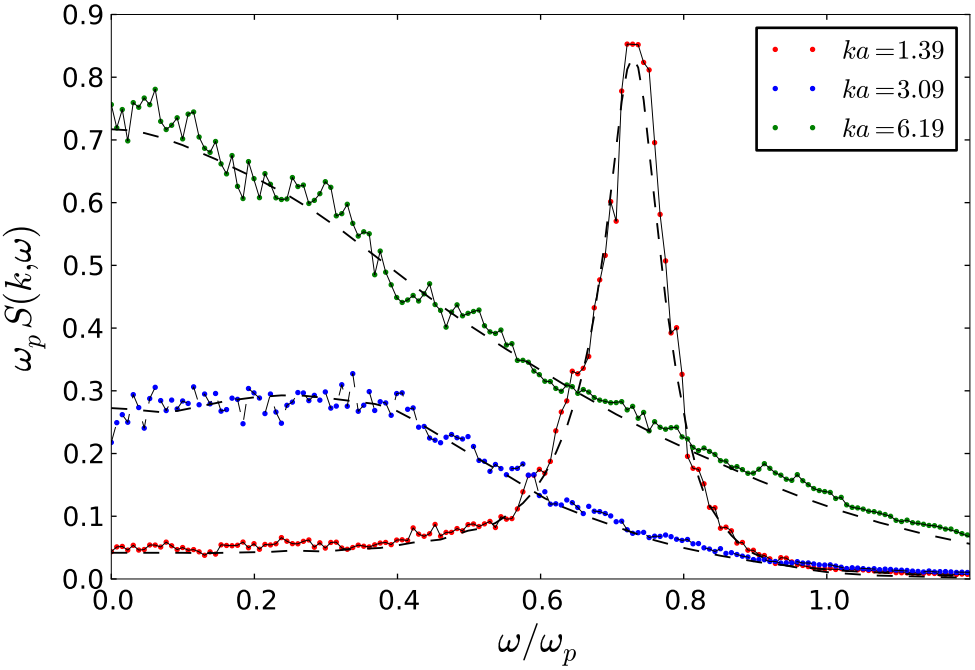

Figure 3.6: Effect of smoothing $F(k,t)$ on the dynamical structure factor (DSF) $S(k,\omega)$ for the same conditions as in Figure 3.5. The points (joined by straight lines) were obtained by taking the DFT of the raw $F(k,t)$ from MD (solid red lines in Figure 3.5) , and the dashed lines from the smoothed $F(k,t)$ (dotted black lines in Figure 3.5).

To conclude this section, the details of how the intermediate scattering function was smoothed are presented. For this purpose, it is convenient to divide spatial lengthscales into regions of 'small', 'intermediate' and 'large' k (the physical interpretation of this splitting will be made clear in later chapters). The shape of intermediate scattering function in each of these regions in k space is shown in Figure 3.5.

At small k values (Figure 3.5, top panel), the raw $F(k,t)$ from MD (red line) is seen to exhibit oscillations which decay on the timescale of hundreds of inverse plasma frequencies. However, as can be seen in Figure 3.5, rather than decaying to exactly zero, $F(k,t)$ exhibits small oscillations about zero. The fact that these small oscillations—which are typically at least two orders of magnitude smaller than $F(k,0)$—do not decay to zero is a result of 'noise' that is unavoidable due to the

finite (although large) number of MD measurements that contribute to $F(k,t)$ at long times. This noise was removed in the following manner: from the oscillation peak immediately before the first peak which is of greater magnitude than its predecessor, the raw MD data for $F(k,t)$ was modified to decay to zero (see inset of Figure 3.5, top panel) as an exponentially decaying cosine. Before this point in time, the smoothed data (dotted line in top panel of Figure 3.5) was taken to be identical to the raw MD data. That is, at small k values,

$$F^{smoothed}(k,t) = \begin{cases} F^{MD}(k,t) & \text{if } t \leq t_{peak} \\ F^{MD}(k,t_{peak}) \times \cos(a(t-t_{peak})) \times \exp(-b(t-t_{peak})) & \text{if } t > t_{peak}\,, \end{cases} \tag{3.46}$$

where t_{peak} is the time point at the peak of the oscillation from which the data is smoothed (this time point is indicated by the star symbol on the top panel of Figure 3.5). The parameters a and b were chosen 'by hand'. The parameter a was chosen such that the oscillation period coincided with the period evident in the MD data, and the parameter b was chosen such that the decay of $F(k,t)$ at long times extended the short time decay.

At intermediate k values (Figure 3.5, middle panel), $F(k,t)$ is seen to pass below the x-axis before decaying to zero (but without exhibiting sustained oscillations as in the case of small k), and, at large k values (Figure 3.5, bottom panel), $F(k,t)$ decays to zero without passing through the x-axis at all. Despite this qualitative difference between the intermediate and large k behaviour, in both cases $F(k,t)$ was smoothed in the same manner:

$$F^{smoothed}(k,t) = \begin{cases} F^{MD}(k,t) & \text{if } t \leq t_{peak} \\ F^{MD}(k,t_{peak}) \times \exp(-b(t-t_{peak})^2) & \text{if } t > t_{peak}\,, \end{cases} \tag{3.47}$$

where t_{peak} was chosen to be at the peak of a 'hump' in the raw MD data. Because of the smallness of these humps (typically at least three orders of magnitude smaller than $F(k,0)$),the exact location of t_{peak} was not found to be an important factor. As can be seen from Equation (3.47), for intermediate and large k values, a Gaussian rather than exponential function was chosen to smooth the MD data: this was in order to avoid a sharp 'cusp' occurring at $t = t_{peak}$. It should be noted that, in all cases (small, intermediate and large k), after the smoothing procedure, the intermediate scattering function is still defined only at discrete points in time separated by $\Delta t \omega_p^{-1} = 0.1$.

Making $F(k,t)$ decay to zero smoothly, as implemented by Equations (3.46) and (3.47), was the most important modification made to the raw MD data. However, two further modifications were also made in order to correct for other known properties of

$F(k,t)$ and $S(k,\omega)$. Both of these modifications were designed to correct the MD data for the fact that $S(k,\omega)$ should decay to zero for $\omega \to \infty$. These modifications only proved to be of any consequence for the investigation of the 'local field correction', presented in Chapter 7, for which the precise nature of the high frequency behaviour of $S(k,\omega)$ was important. Indeed, the difference between the DSF with and without these extra modifications is not nearly large enough to be visible on the scale of Figure 3.6.

Here the additional modifications are discussed with the assistance of Figure 3.7, which shows how each modification affects the high frequency behaviour of $S(k,\omega)$. In Figure 3.7, the solid red line shows the raw MD data, and the dotted black line shows the smoothed data after each additional operation. In each of the cases (a), (b) and (c), the left panel shows the overall effect of the smoothing operation on the DSF, and the right panel is zoomed in to show the high frequency behaviour in more detail. In (a), the smoothed data is after the smoothing described previously (i.e., in Equation (3.46)) was applied. As shown in the right panel, after this smoothing the DSF does not decay to exactly zero (a problem that is also evident in the raw MD data). An effective way to remedy this problem was found to be interpolating $F(k,t)$ between each discrete time point. That is to say, between each point in time at which $F(k,t)$ is defined ($t = 0, 0.1\omega_p^{-1}, 0.2\omega_p^{-1}, \cdots$), n additional time points were inserted, with values of $F(k,t)$ that interpolated between the values at the two adjacent time points. Linear interpolation with $n = 10$ was found to be as satisfactory for this purpose as other more complicated interpolation schemes. In (b), the smoothed data shown is after this linear interpolation has been applied. It can be seen (right panel of (b)) that although the interpolation does improve the high frequency behavior of the DSF, a small offset from $S(k,\omega) = 0$ still remains. Finally, as shown in (c), this small offset from zero was subtracted from the DSF. The two additional operations shown in (b) and (c) were applied in the same way at every k value. As can be seen in the left panels of (a), (b) and (c), none of the smoothing operations changes the overall shape of the DSF from the raw MD data considerably.

In its entirety, the procedure used to smooth the intermediate scattering function that has been detailed in this section is clearly rather ad-hoc, and has the distinct disadvantage that it is difficult to automate (specifically, it is difficult to automate the determination of the parameters a and b in Equations (3.46) and (3.47)). The latter point does indeed make it rather inconvenient; for example, for the 5000 particles used in the MD simulations, 619 distinct magnitudes k of the wave-vector $\boldsymbol{k}$ are possible. Clearly smoothing all of these 619 cases (at each Γ and κ value) by hand

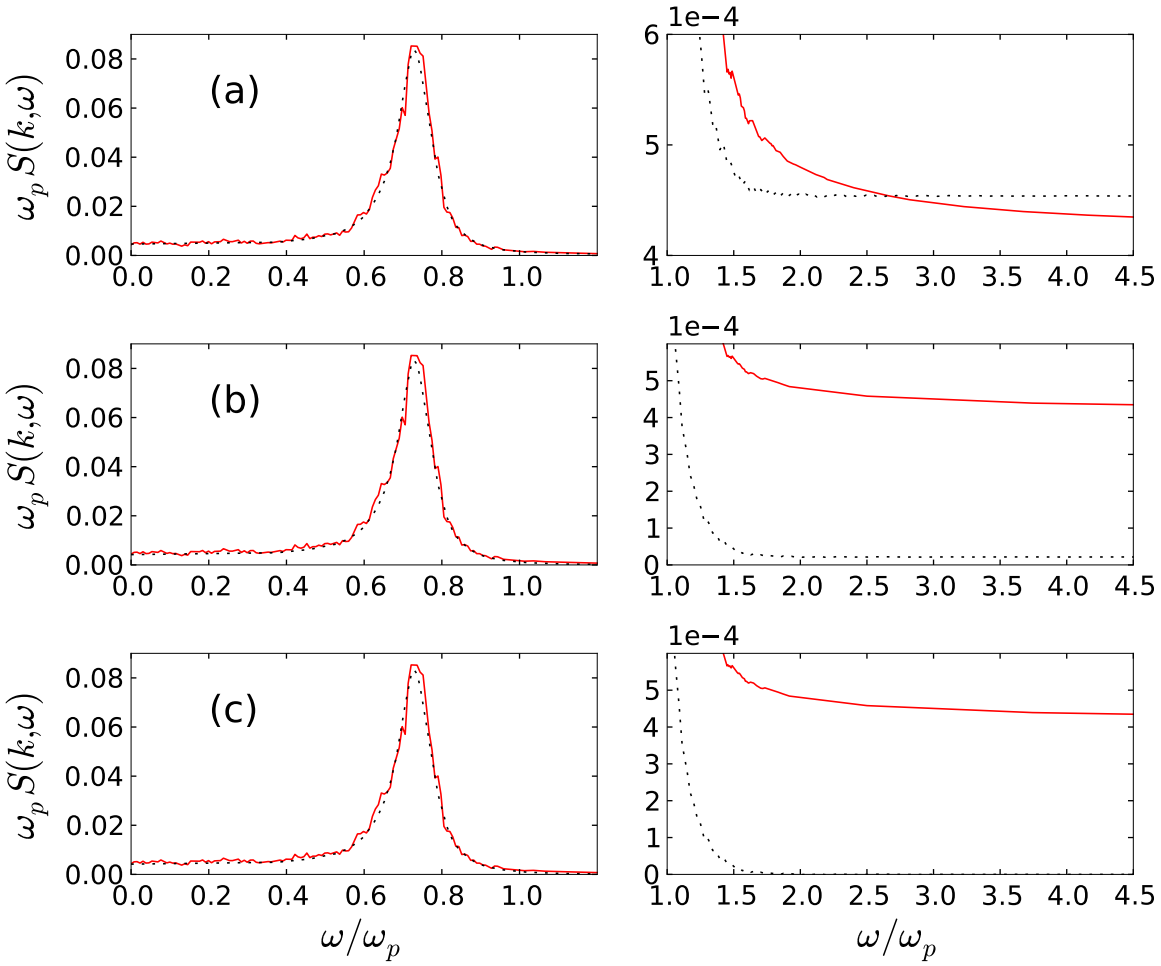

Figure 3.7: Additional smoothing operations applied to correct for the high frequency behaviour of $S(k,\omega)$. The solid (red) line is the raw MD data and the dotted (black) line is after each of the smoothing operations described in the text.

is impractical, and accordingly the results for only a few values of k were smoothed. Despite this drawback, the method was used since it accomplishes the desired result with what was perceived to be the minimum of complexity. It certainly compares favorably with the simplest approach (which is straightforward to automate) of setting $F(k,t)$ equal to zero beyond a certain time, since the oscillations produced by the inevitable discontinuity in $F(k,t)$ make the resulting DSF difficult to analyse. The other alternative of applying filtering techniques in frequency space to the DSF was deemed to be unnecessarily complicated. In the remainder of the thesis, unless stated otherwise, the data presented for the DSF is the smoothed data obtained after the operations detailed in this section were applied.

3.12 Limitations of MD

The main limitation of the MD technique is that it can be used in an 'ab-initio' manner for classical systems only. This certainly appears to be a major drawback since in reality, of course, matter is thought to obey the laws of quantum mechanics. Only in particular cases—e.g., for many monatomic liquids [Allen & Tildesley, 1988]—is the classical approximation a very good one. However, a large amount of the physics of solids, liquids, gases and plasmas can in fact be (and has been) investigated with MD by choosing appropriate inter-atomic, inter-molecular, or—in the case of plasmas—inter-ionic interaction potentials. This is because these potentials can be chosen to incorporate features of the real system that are quantum mechanical in origin.

An example of incorporating quantum mechanical features into 'effective' interaction potentials is provided by the OCP system studied in this thesis: as described in Section 1.5, one thinks of the OCP as representing a plasma in which the electrons are highly degenerate (quantum mechanical), and therefore appear to the ions as a uniform background; the ions as a result interact via the bare Coulomb potential. Of course, the main drawback in this case is the severity of the approximation: as discussed in Section 1.5, the uniform background approximation can only be expected to work well at extremely high densities.

Less drastic approximations can often be used to produce a classical system—which can therefore be studied with MD—that is a better representation of a real system. Of course, such an approximation will in some way reduce the number of degrees of freedom, and thus some information will be lost. This is the story with the YOCP system studied in this thesis: as described in Section 1.5, in the YOCP system the physical effects of the electrons, which are not included as separate entities, is contained in an effective ion-ion interaction potential. In this case the reduction of the degrees of freedom means that all information on the electron dynamics is lost. However, the resulting system, despite being an approximation to reality, still has features that can give qualitative—and sometimes quantitative—information on some physical aspects of the real system (e.g., in the case of the YOCP, the ion dynamics) when studied with MD.

Once it is accepted that only classical systems can be investigated with MD, there are a number of other limitations of MD worth mentioning. These limitations should more properly be considered sources of errors or uncertainty. They can be deduced by examining the statement—frequently taken all too literally—that MD generates 'exact' data for a given system. This is clearly untrue; it is obvious that, in an MD

simulation, the equations of motion must be recast in discrete rather than continuous time, and therefore the original equations cannot ever be solved 'exactly'; the trajectories generated are always only approximate solutions to the classical equations of motion. This is true regardless of the chosen integration algorithm, and the complexity of that algorithm. For the computation of time dependent correlation functions—as discussed in [Allen & Tildesley, 1988]—this is not usually a problem since the algorithm need only approximate the dynamics well over typical correlation times (in this respect, the Verlet algorithm is as good as any other [Allen & Tildesley, 1988]). A second source of error concerns the fact that usually the simulation data is taken to represent an ensemble average. According to the ergodic hypothesis (see Section 3.3), these ensemble averages are equivalent to time averages. But the time averages computed with MD are only ever approximations to the 'true' time averages appearing that appear in Equation (3.11). To compute the true time average, one needs to know the dynamics of the system for an infinite time. In practice, of course, an MD simulation is of finite length. A final source of error concerns ensemble equivalence: only for $N \to \infty$ are the different ensembles (microcanonical, canonical, etc.) equivalent, and therefore one would expect ensemble averages computed with MD (i.e., time dependent correlation functions like the intermediate scattering function) to depend on the choice of ensemble. Thus, in total there exist three main sources of errors in any MD simulation concerned with computing ensemble averages—the discretisation of time, the finite length of simulations, and the finite system size.

3.13 Details of the simulations

The MD simulations in this thesis were all performed by the author using the code 'CoulMD' written by Dr. Jerome Daligault at Los Alamos National Laboratory. Like many MD codes, CoulMD consists of two separate programs. The first program performs the particle initialization and integration of the equations of motion, that is to say, the actual MD simulation. The output of this first program is the (functions of the) positions and velocities of the particles needed to compute the desired physical properties of the system. For example, to compute $S(k,\omega)$ and $S(k)$, $n(\boldsymbol{k},t)$, defined in Equation (2.11), is recorded for every wave-vector $\boldsymbol{k}$ consistent with the periodic boundary conditions and at every timestep . The second program, which is executed after the first, reads this output and uses it to compute the quantities of interest, such as $S(k,\omega)$, $S(k)$ and $g(r)$. The details of the simulations, many of which are repeated from previous sections in this chapter, are gathered together below:

All of the simulations were performed for particles in a cubic box, with periodic boundary conditions. All of the simulations were done in the microcanonical ensemble. Of the simulation data presented in this thesis, the majority of the simulations were done for $N = 5 \times 10^3$ particle systems. A number of simulations were done for $N = 5 \times 10^4$ particles and a small number were done for $N = 5 \times 10^5$; when the MD results corresponding to the larger system sizes are presented, this is indicated in the text. In every simulation (all κ values) the Ewald summation was included in the force calculation using the particle-particle-particle-mesh (PPPM) algorithm. The rms error of the force calculation, defined as $\Delta F = \sqrt{\frac{1}{N}\sum_{i=1}^{N}(\boldsymbol{F}_i - \boldsymbol{F}_i^{exa})^2}$, where $\boldsymbol{F}_i$ is the force on particle i calculated by the code, and $\boldsymbol{F}_i^{exa}$ is the *exact* force on that particle, was 10^{-5}.

The equations of motion were integrated using the velocity Verlet algorithm. The timestep for $\Gamma \geq 1$ was $\Delta t = 0.01\omega_p^{-1}$. This timestep was found to conserve the energy of the system very well ($\Delta E/E(0) \approx 10^{-6}$) in all cases. For $\Gamma < 1$, a smaller timestep of $\Delta t = 0.002\omega_p^{-1}$ was required. In all cases, the system was evolved for a time of $1000\omega_p^{-1}$ before recording data. During this equilibration phase, velocity scaling was used at every timestep to maintain the desired value of Γ. To compute dynamical (and static) properties such as $F(k,t)$, the results of 25 simulations, each with different initial conditions, were averaged. To achieve this, the final configuration (positions and velocities of the particles) of the system was used as the initial condition of the following simulation, and therefore only a single equilibration, at the beginning of the first simulation, was needed for each chosen Γ and κ value. Each of the 25 simulations was of duration $\tau = 819.1\omega_p^{-1}$. Data on the state of the system required to compute time dependent correlation functions was recorded every 10 timesteps, e.g. the time series for $F(k,t)$ consisted of 8192 points. This means that $10 \times 8192 \times 25 \approx 2 \times 10^6$ measurements contributed to the determination of static properties such as $S(k)$ and $g(r)$.

Chapter 4

Domain of validity of the hydrodynamic description of the YOCP

4.1 Motivation

The YOCP is a simple representation of a non-ideal or strongly coupled plasma. In the past decade or so, the advent of high power lasers and fourth generation x-ray sources has made it possible to carry out experiments to produce and diagnose such states of matter in the laboratory [Fäustlin *et al.*, 2010, García Saiz *et al.*, 2008, Glenzer & Redmer, 2009]. The main interest in doing these experiments stems from the promise of gaining a better understanding of ICF plasmas and planetary interiors.

The particular experiments that motivated the investigation presented in this chapter are x-ray scattering experiments. As outlined in Section 2.7, these experiments can measure the microscopic dynamics—that is, the DSF—of non-ideal plasmas. For planning, diagnosing and understanding the experiments, models are needed for the DSF, for a wide range of thermodynamic conditions.

A number of involved approaches to modelling the DSF have proven to be successful in certain regimes [Balucani & Zoppi, 2002, Hansen & McDonald, 2006, Ichimaru, 1982, Kremp *et al.*, 2005]. However, compared to these models, the hydrodynamic description retains a rather simple physical picture in terms of fundamental transport and thermodynamic properties of the plasma. Indeed, this relative simplicity is one of the reasons why the equations of hydrodynamics, such as the Naviér-Stokes equations, are the most widely used framework for investigating the dynamics of fluids in general, including gases [Mansour *et al.*, 1987], liquids [Scopigno *et al.*, 2002], plasmas [Gedalin, 1996] and nuclear matter [Bouras *et al.*, 2009]. Despite this widespread use,

in the particular case of *non-ideal* plasmas, the hydrodynamic description has been rather overlooked[1]. In this chapter, it is shown that the hydrodynamic description is applicable to conditions accessible in contemporary x-ray scattering experiments. It is, therefore, a useful way to think about the dynamics of non-ideal plasmas.

4.2 Applicability of the hydrodynamic picture

One ordinarily thinks of the hydrodynamic picture as applying at long length scales and long time scales, or, equivalently, for small wave numbers k and frequencies ω. Intuitively, the smallness of k and ω is relative to the mean free path, l_f, and the mean collision frequency, ω_c; it can be encoded in the conditions $kl_f \ll 1$ and $\omega/\omega_c \ll 1$. These conditions can in fact be *derived* for a system governed by uncorrelated binary collisions (e.g., a dilute gas). Despite this, they remain qualitative rather than quantitative. What is more, they become even more indeterminate when many-body correlations are present—as in the non-ideal plasma case—because the concepts of mean free path and mean collision time cease to have a clear physical meaning (cf. Section 1.2).

One certainly expects the domain of validity of the hydrodynamic description to depend strongly on the thermodynamic state of the system. For instance, one expects that for the ions in a plasma, the description never applies on length scales smaller than the screening length λ_s of the effective ion-ion potential (i.e., for $k\lambda_s \geq 1$)—in other words, that the domain of validity will shrink as the screening length increases.

4.3 Summary of the investigation

For this investigation, the DSF of the YOCP for a wide range of (Γ,κ) pairs, shown in Table 4.1, was computed using MD, as described in Chapter 3. The DSF from MD was compared to the well known model given by the hydrodynamic description, which can be derived from the Naviér-Stokes equations, as shown in Section 4.4. This comparison allowed the domain of validity (in k and ω space, for each (Γ,κ) pair) of the hydrodynamic description of the YOCP to be assessed.

[1]One notable exception to this is the investigation of 'hydrodynamics inspired' models of the dynamics of the OCP conducted by Tanaka and Ichimaru [Ichimaru & Tanaka, 1986, Tanaka & Ichimaru, 1987] . These models are discussed in Chapter 7; the present chapter is concerned with the YOCP only.

κ	Γ
0.1	1, 5, $10^{\ddagger}$, 50, $120^{\ddagger}$, 175
0.3	$10^{\dagger}$, $120^{\dagger}$
0.5	$10^{\dagger}$, $120^{\dagger}$
0.7	$10^{\dagger}$, $120^{\dagger}$
1	1, 5, 10, 50, 120, 175
2	1, 5, 10, 50, 120, 175

Table 4.1: The (Γ,κ) pairs at which the DSF of the YOCP was computed, using MD simulations, for the investigation presented in this chapter. The † symbol indicates that simulations were performed using $N = 50,000$ particles, and ‡ indicates that $N = 500,000$ particles were used (in all other cases, $N = 5000$).

4.4 Derivation of the hydrodynamic DSF

The hydrodynamic description examined in this chapter is given by the Naviér-Stokes equations. These can be written as three equations, which represent mass (or particle number), momentum and energy conservation respectively [Boon & Yip, 1991, Hansen & McDonald, 2006, Landau & Lifshitz, 1987]:

$$\frac{\partial n(\boldsymbol{r},t)}{\partial t} = -\nabla\cdot(n(\boldsymbol{r},t)\boldsymbol{v}(\boldsymbol{r},t)) \tag{4.1}$$

$$mn(\boldsymbol{r},t)\left[\frac{\partial \boldsymbol{v}(\boldsymbol{r},t)}{\partial t} + (\boldsymbol{v}(\boldsymbol{r},t)\cdot\nabla)\boldsymbol{v}(\boldsymbol{r},t)\right] = -\nabla P(\boldsymbol{r},t)+\eta\nabla^2\boldsymbol{v}(\boldsymbol{r},t)+(\zeta+\frac{\eta}{3})\nabla\nabla\cdot\boldsymbol{v}(\boldsymbol{r},t) \tag{4.2}$$

$$mn(\boldsymbol{r},t)T(\boldsymbol{r},t)\left[\frac{\partial S(\boldsymbol{r},t)}{\partial t} + (\boldsymbol{v}(\boldsymbol{r},t)\cdot\nabla)S(\boldsymbol{r},t)\right] = \phi_\eta + \lambda\nabla^2 T(\boldsymbol{r},t)\,. \tag{4.3}$$

In these equations, $n(\boldsymbol{r},t)$ is the number density at a point $\boldsymbol{r}$ in the fluid and at time t, defined by $n(\boldsymbol{r},t) = \rho(\boldsymbol{r},t)/m$, where $\rho(\boldsymbol{r},t)$ is the mass density. Similarly, $\boldsymbol{v}(\boldsymbol{r},t)$ is the velocity, $T(\boldsymbol{r},t)$ the temperature, $S(\boldsymbol{r},t)$ the entropy and $P(\boldsymbol{r},t)$ the pressure. The parameters that characterise the particular fluid are the shear viscosity, η, the bulk viscosity, ζ, and the thermal conductivity, λ. The term ϕ_η, appearing in Equation (4.3), represents viscous terms that disappear after linearisation [Boon & Yip, 1991]. The momentum balance equation, Equation (4.2), can instead be written in terms of the momentum flux density tensor $\boldsymbol{\Pi}(\boldsymbol{r},t)$ [Landau & Lifshitz, 1987]:

$$m\frac{\partial[n(\boldsymbol{r},t)\boldsymbol{v}(\boldsymbol{r},t)]}{\partial t} = -\nabla\cdot\boldsymbol{\Pi}(\boldsymbol{r},t)\,, \tag{4.4}$$

where the elements of $\boldsymbol{\Pi}(\boldsymbol{r},t)$ are

$$\Pi_{ij}(\boldsymbol{r},t) = mn(\boldsymbol{r},t)v_i(\boldsymbol{r},t)v_j(\boldsymbol{r},t) - \sigma_{ij}(\boldsymbol{r},t)\,, \tag{4.5}$$

and $\boldsymbol{\sigma}(\boldsymbol{r},t)$ is known as the *stress tensor*. The stress tensor can be written as [Baus & Hansen, 1980][2]

$$\boldsymbol{\sigma}(\boldsymbol{r},t) = P(\boldsymbol{r},t)\mathbf{1} - \eta(\nabla\boldsymbol{v}(\boldsymbol{r},t) + \widetilde{\nabla\boldsymbol{v}}(\boldsymbol{r},t)) - (\zeta - \frac{2}{3}\eta)\mathbf{1}\nabla\cdot\boldsymbol{v}(\boldsymbol{r},t)\,. \tag{4.6}$$

In order to derive the hydrodynamic form of the DSF, Equations (4.1)-(4.3) are first linearised by making the following substitutions:

$$\begin{aligned} n(\boldsymbol{r},t) &\to n + \delta n(\boldsymbol{r},t) \\ \boldsymbol{v}(\boldsymbol{r},t) &\to 0 + \boldsymbol{v}(\boldsymbol{r},t) \\ P(\boldsymbol{r},t) &\to P + \delta P(\boldsymbol{r},t) \\ S(\boldsymbol{r},t) &\to S + \delta S(\boldsymbol{r},t) \\ T(\boldsymbol{r},t) &\to T + \delta T(\boldsymbol{r},t)\,, \end{aligned} \tag{4.7}$$

where the homogeneous, time independent terms represent 'equilibrium' values, and the remaining space and time dependent 'fluctuations' are assumed to be small, so that products of these terms can be neglected. Performing the linearisation by substituting the ansatz in Equation (4.7) into Equations (4.1)-(4.3) leads to the *linearised Naviér-Stokes equations*:

$$\frac{\partial}{\partial t}\delta n(\boldsymbol{r},t) = -n\nabla\cdot\boldsymbol{v}(\boldsymbol{r},t) \tag{4.8}$$

$$mn\frac{\partial}{\partial t}\boldsymbol{v}(\boldsymbol{r},t) = -\nabla\delta P(\boldsymbol{r},t) + \eta\nabla^2\boldsymbol{v}(\boldsymbol{r},t) + (\zeta + \frac{\eta}{3})\nabla\nabla\cdot\boldsymbol{v}(\boldsymbol{r},t) \tag{4.9}$$

$$T\frac{\partial}{\partial t}\delta S(\boldsymbol{r},t) = \frac{\kappa}{n}\nabla^2\delta T(\boldsymbol{r},t)\,. \tag{4.10}$$

These equations can be written in terms of $v(\boldsymbol{r},t)$, $\delta n(\boldsymbol{r},t)$ and $\delta T(\boldsymbol{r},t)$ only by writing the pressure and entropy fluctuations in terms of the density and temperature fluctuations:

$$\delta S(\boldsymbol{r},t) = \left(\frac{\partial S}{\partial n}\right)_T \delta n(\boldsymbol{r},t) + \left(\frac{\partial S}{\partial T}\right)_n \delta T(\boldsymbol{r},t)\,, \tag{4.11}$$

$$\delta P(\boldsymbol{r},t) = \left(\frac{\partial P}{\partial n}\right)_T \delta n(\boldsymbol{r},t) + \left(\frac{\partial P}{\partial T}\right)_n \delta T(\boldsymbol{r},t)\,, \tag{4.12}$$

which can be derived from a Taylor series expansion of the functions about their equilibrium values (e.g. $S(\boldsymbol{r},t) = S(n(\boldsymbol{r},T),T(\boldsymbol{r},t))$, in which it is assumed that

[2]Here $\widetilde{\nabla\boldsymbol{v}(\boldsymbol{r},t)}$ is notation for the transpose of the matrix formed from the tensor derivative $\nabla\boldsymbol{v}(\boldsymbol{r},t)$, e.g., the contribution to σ_{ij} from the second term in Equation (4.6) is $-\eta(\nabla_i v_j(\boldsymbol{r},t) + \nabla_j v_i(\boldsymbol{r},t))$ (cf. [Balescu, 1975], Chapter 12, Equation (12.5.9)).

the resulting partial derivatives can be evaluated at their equilibrium values. The linearised Naviér-Stokes equations thus become

$$\frac{\partial}{\partial t}\delta n(\boldsymbol{r},t) = -n\nabla\cdot\boldsymbol{v}(\boldsymbol{r},t) \tag{4.13}$$

$$\begin{aligned} mn\frac{\partial}{\partial t}\boldsymbol{v}(\boldsymbol{r},t) = &-\frac{1}{n\chi_T}\nabla\delta n(\boldsymbol{r},t) - \left(\frac{\partial P}{\partial T}\right)_n \nabla\delta T(\boldsymbol{r},t) \\ &+ \eta\nabla^2\boldsymbol{v}(\boldsymbol{r},t) + (\zeta+\frac{\eta}{3})\nabla\nabla\cdot\boldsymbol{v}(\boldsymbol{r},t) \end{aligned} \tag{4.14}$$

$$\frac{\lambda}{n}\nabla^2\delta T(\boldsymbol{r},t) = T\left(\frac{\partial S}{\partial n}\right)_T \frac{\partial}{\partial t}\delta n(\boldsymbol{r},t) + C_V\frac{\partial}{\partial t}\delta T(\boldsymbol{r},t)\,, \tag{4.15}$$

where the thermodynamic identities

$$\left(\frac{\partial S}{\partial T}\right)_n = \frac{C_V}{T}\,, \tag{4.16}$$

$$\left(\frac{\partial P}{\partial n}\right)_T = \frac{1}{n\chi_T} \tag{4.17}$$

have been used; here C_V is the heat capacity at constant volume and

$$\chi_T = -\frac{1}{V}\left(\frac{\partial V}{\partial P}\right)_T \tag{4.18}$$

is the isothermal compressibility.

To derive the hydrodynamic DSF from Equations (4.13)-(4.15), it is first noted that, since the intermediate scattering function $F(k,t)$ is even in time (see Appendix B), it follows from the definition in Equation (2.14) that the DSF can be given in terms of the Laplace transform of $F(k,t)$ as

$$S(k,\omega) = \frac{1}{\pi}\Re e[F(k,z=\omega)]\,, \tag{4.19}$$

where the Laplace transform of $F(k,t)$ is

$$\begin{aligned} F(k,z) &= \int_0^\infty e^{izt}F(k,t)dt \\ &= \frac{1}{N}\langle\delta n(\boldsymbol{k},z)\delta n(-\boldsymbol{k})\rangle\,, \end{aligned} \tag{4.20}$$

and $\delta n(-\boldsymbol{k}) = \delta n(-\boldsymbol{k},t=0)$. The hydrodynamic DSF can therefore be determined by solving Equations (4.13)-(4.15) for the Fourier-Laplace transform of the density fluctuations,

$$\delta n(\mathbf{k},z) = \int_0^\infty e^{izt}\int \delta n(\mathbf{r},t)e^{-i\mathbf{k}\cdot\mathbf{r}}d\boldsymbol{r}dt\,. \tag{4.21}$$

By taking the Fourier-Laplace transform of each of Equations (4.13)-(4.15) and combining into a single equation for the density fluctuations, one obtains

$$\left[\left(-z^2 - izbk^2 + \frac{c_s^2}{\gamma}\right)(ak^2 - iz) - izk^2\frac{\gamma-1}{\gamma}c_s^2\right]\delta n(\boldsymbol{k},z) = \frac{k^2}{m}\left(\frac{\partial P}{\partial T}\right)_n \delta T(\boldsymbol{k}) + in(ak^2 - iz)\boldsymbol{k}\cdot\boldsymbol{v}(\boldsymbol{k}) + \left(k^2\frac{\gamma-1}{\gamma}c_s^2 + (ak^2 - i\omega)(bk^2 - i\omega)\right)\delta n(\boldsymbol{k})\,, \tag{4.22}$$

where

$$a = \frac{\lambda}{nC_V}\,, \tag{4.23}$$

$$b = \frac{\zeta + 4\eta/3}{nm}\,, \tag{4.24}$$

and the thermodynamic identity [Vieillefosse & Hansen, 1975]

$$\frac{T}{mC_V}\left(\frac{\partial S}{\partial n}\right)_T\left(\frac{\partial P}{\partial T}\right)_n = \frac{\gamma-1}{\gamma}c_s^2 \tag{4.25}$$

has been used. The sound speed c_s can also be written in terms of the isothermal compressibility χ_T as

$$c_s = \sqrt{\frac{\gamma}{nm}\frac{1}{\chi_T}} = \sqrt{\frac{\gamma k_B T}{m}\frac{\chi_T^0}{\chi_T}}\,, \tag{4.26}$$

where

$$\chi_T^0 = \frac{1}{nk_BT} \tag{4.27}$$

is the compressibility of an ideal gas (cf. Equation (4.18)). It can be shown that the initial values of the density, temperature and velocity are statistically independent of one another [Vieillefosse & Hansen, 1975], and therefore that the terms proportional to $\delta T(\boldsymbol{k})$ and $\boldsymbol{v}(\boldsymbol{k})$ in Equation (4.22) do not contribute to the result for the hydrodynamic DSF. Using Equations (4.20) and (4.22), one then obtains

$$F(k,z) = \frac{(1/N)\langle\delta n(\boldsymbol{k})\delta n(-\boldsymbol{k})\rangle\left(k^2\frac{\gamma-1}{\gamma}c_s^2 + (ak^2 - iz)(bk^2 - iz)\right)}{\left[(-z^2 - izbk^2 + c_s^2k^2/\gamma)(ak^2 - iz) - izk^2\frac{\gamma-1}{\gamma}c_s^2\right]}\,, \tag{4.28}$$

where the term $(1/N)\langle\delta n(\boldsymbol{k})\delta n(-\boldsymbol{k})\rangle$ appearing in this equation is simply the static structure factor $S(k)$. According to Equation (4.19), the desired result for the hydrodynamic DSF is then obtained by multiplying the real part of the right hand side of Equation (4.28) by $1/\pi$. Although determining this is straightforward, the rather

complicated result obtained is difficult to gain any physical insight from. Instead, $F(k,z)$ can be written in terms of partial fractions, i.e.,

$$\frac{F(k,z)}{S(k)} = \frac{A}{z-z_1} + \frac{B}{z-z_2} + \frac{C}{z-z_3}\,, \tag{4.29}$$

where z_1, z_2 and z_3 are the three roots of the cubic polynomial on the denominator of Equation (4.28), which can be written as

$$iz^3 - z^2(a+b)k^2 - iz(abk^2 + c_s^2)k^2 + (a/\gamma)c_s^2k^4 = 0\,. \tag{4.30}$$

Although the *exact* roots of this cubic polynomial can be easily determined, again the solutions are rather complicated. More physical insight can be gained by solving instead for approximate roots. To achieve this, Equation (4.30) is first written in reduced units, via the substitution $s = z/c_sk$, which gives

$$s^3 + is^2(\epsilon_1+\epsilon_2) - s(\epsilon_1\epsilon_2+1) - \frac{i}{\gamma}\epsilon_1 = 0\,, \tag{4.31}$$

where the dimensionless coefficients appearing in this equation are $\epsilon_1 = \frac{ak^2}{c_sk}$ and $\epsilon_2 = \frac{bk^2}{c_sk}$. A physical argument suggests that these coefficients are small [Mountain, 1966], particularly at the small values of k at which one would expect the hydrodynamic description to be valid [Hansen & McDonald, 2006]. Therefore, approximate roots of Equation (4.31) can be determined by making a power series expansion of the solutions in terms of ϵ_1 and ϵ_2, and neglecting any terms that are second order or higher in ϵ_1 and ϵ_2, i.e., by making a trial solution of the form

$$\begin{aligned} s &\approx s_0 + \epsilon_1 s_1 + \epsilon_2 s_2 \\ s^2 &\approx s_0^2 + 2\epsilon_1 s_0 s_1 + 2\epsilon_2 s_0 s_2 \\ s^3 &\approx s_0^3 + 3\epsilon_1 s_0^2 s_1 + 3\epsilon_2 s_0^2 s_2\,. \end{aligned} \tag{4.32}$$

Substituting this trial solution into Equation (4.31) gives

$$s_0^3 + 3\epsilon_1 s_0^2 s_1 + 3\epsilon_2 s_0^2 s_2 + is_0^2(\epsilon_1+\epsilon_2) - s_0 - \epsilon_1 s_1 - \epsilon_2 s_2 - \frac{i}{\gamma}\epsilon_1 = 0\,. \tag{4.33}$$

The requirement that the approximate solutions should converge to the exact solutions when ϵ_1 and ϵ_2 vanish is satisfied by setting these parameters to zero in Equation (4.33), which gives

$$s_0(s_0^2 - 1) = 0\,, \tag{4.34}$$

and so the three roots correspond to $s_0 = 0, 1, -1$. For $s_0 = 0$, Equation (4.33) becomes

$$\epsilon_1 s_1 + \epsilon_2 s_2 + \frac{i}{\gamma}\epsilon_1 = 0 \tag{4.35}$$

Setting $\epsilon_1 = 0$ gives $s_2 = 0$, and setting $\epsilon_2 = 0$ gives $s_1 = -\frac{i}{\gamma}$. Therefore the first root of Equation (4.31) is

$$s \approx \frac{-i}{\gamma}\epsilon_1 \tag{4.36}$$

The roots corresponding to $s_0 = 1$ and $s_0 = -1$ can be determined by the same method. The three roots of Equation (4.31) are thus found to be

$$\begin{aligned} s &\approx \frac{-i}{\gamma}\epsilon_1 \\ s &\approx 1 + \frac{i}{2}(\frac{1}{\gamma} - 1)\epsilon_1 - \frac{i}{2}\epsilon_2 \\ s &\approx -1 + \frac{i}{2}(\frac{1}{\gamma} - 1)\epsilon_1 - \frac{i}{2}\epsilon_2 \end{aligned} \tag{4.37}$$

Written in terms of z, these are the three roots, z_1, z_2, and z_3 that are required to express $F(k, z)$ in the partial fraction form of Equation (4.29):

$$\begin{aligned} z_1 &= -iD_T k^2 \\ z_2 &= c_s k - i\sigma k^2 \\ z_3 &= -c_s k - i\sigma k^2 \end{aligned} \tag{4.38}$$

where

$$D_T = \frac{a}{\gamma} = \frac{\lambda}{nC_p} \tag{4.39}$$

is the known as the thermal diffusivity, and

$$\sigma = \frac{a(\gamma - 1)}{2\gamma} + \frac{b}{2} = \frac{1}{2}\left[\frac{(\gamma - 1)}{\gamma}\frac{\lambda}{nC_V} + \frac{4\eta/3 + \zeta}{nm}\right] \tag{4.40}$$

is known as the sound attenuation coefficient. After determining the numerators A, B and C of the partial fractions in Equation (4.29) in the normal way, one finally obtains

$$\frac{F(k, z)}{S(k)} = \frac{\gamma - 1}{\gamma}\frac{1}{z + iD_T k^2} + \frac{1}{2\gamma}\left[\frac{1}{z - c_s k + i\sigma k^2} + \frac{1}{z + c_s k + i\sigma k^2}\right], \tag{4.41}$$

and, using Equation (4.19)

$$\frac{S(k, \omega)}{S(k)/2\pi} = \frac{\gamma - 1}{\gamma}\frac{2D_T k^2}{\omega^2 + (D_T k^2)^2} + \frac{1}{\gamma}\left[\frac{\sigma k^2}{(\omega + c_s k)^2 + (\sigma k^2)^2} + \frac{\sigma k^2}{(\omega - c_s k)^2 + (\sigma k^2)^2}\right]. \tag{4.42}$$

Equation (4.42) is the hydrodynamic DSF that is investigated in this chapter.

4.5 The hydrodynamic form of the dynamical structure factor

As shown in the previous section, solving the linearised Naviér-Stokes equations gives the hydrodynamic DSF:

$$\frac{S^H(k,\omega)}{S(k)/2\pi} = \frac{\gamma-1}{\gamma}\frac{2D_T k^2}{\omega^2+(D_T k^2)^2} + \frac{1}{\gamma}\left[\frac{\sigma k^2}{(\omega+c_s k)^2+(\sigma k^2)^2} + \frac{\sigma k^2}{(\omega-c_s k)^2+(\sigma k^2)^2}\right], \tag{4.43}$$

where the symbol 'H' has been used to distinguish the hydrodynamic DSF from the DSF of the YOCP. The hydrodynamic DSF consists of three Lorentzian peaks. The central peak at $\omega = 0$, known as the Rayleigh peak, corresponds to a diffusive thermal mode. The other two peaks are known as Brillouin peaks: they correspond to propagating sound waves at frequency $\omega = c_s k$. For the YOCP system, in which the particles are taken to represent ions (rather than neutral atoms or molecules, as in the case of an ordinary fluid), these waves are also known as ion-acoustic waves, and, accordingly, the Brillouin peaks can also be referred to as 'ion-acoustic peaks'.

A comparison between Equation (4.43) and the results of MD simulations for the DSF allows the domain of validity of the hydrodynamic description of the YOCP to be assessed. Clearly, for this purpose, values for the four parameters appearing in Equation (4.43)—the ratio of specific heats γ, the thermal diffusivity D_T, the sound speed c_s and the sound attenuation coefficient σ—are required, so that the hydrodynamic DSF is completely specified at any chosen values of k and ω. The determination of these four parameters is the subject of the following section.

4.6 Determining the thermodynamic and transport coefficients

The Naviér-Stokes equations in principle offer a description of the dynamics of any fluid[3], and thus Equation (4.43) for the hydrodynamic DSF can be used for a liquid, gas, or plasma. The only feature that distinguishes between these cases is the values of the four unknown parameters: the ratio of specific heats γ, the thermal diffusivity D_T, the sound speed c_s and the sound attenuation coefficient σ. Many previous investigations have been concerned with estimating these parameters for particular fluids (e.g., [Carraresi *et al.*, 1993, Greytak & Benedek, 1966, Mijakovi *et al.*, 2011]).

[3]The (very relevant) exception to this is a fluid with Coulomb interactions, and the fact that the Naviér-Stokes description is not valid for Coulomb systems is the topic of Chapter 6.

In most cases, this was done by fitting the hydrodynamic DSF to experimental data from inelastic light or neutron scattering experiments. In the spirit of this procedure, it does not seem unreasonable to similarly estimate these parameters using the 'experimental' data from MD simulations. Since Equation (4.43) is expected to be valid only for small wave numbers k, it makes sense to do this at the smallest k value accessible to the MD simulations. Accordingly, for each (Γ,κ) value, Equation (4.43) for the hydrodynamic DSF was fitted to the MD DSF at $ka = 0.23$ (the smallest reduced wave number accessible for the $N = 5000$ particle system) using the least squares method, thereby obtaining values for the parameters γ, D_T, c_s and σ. As shown in Figure 4.1, this produces a very accurate fit.

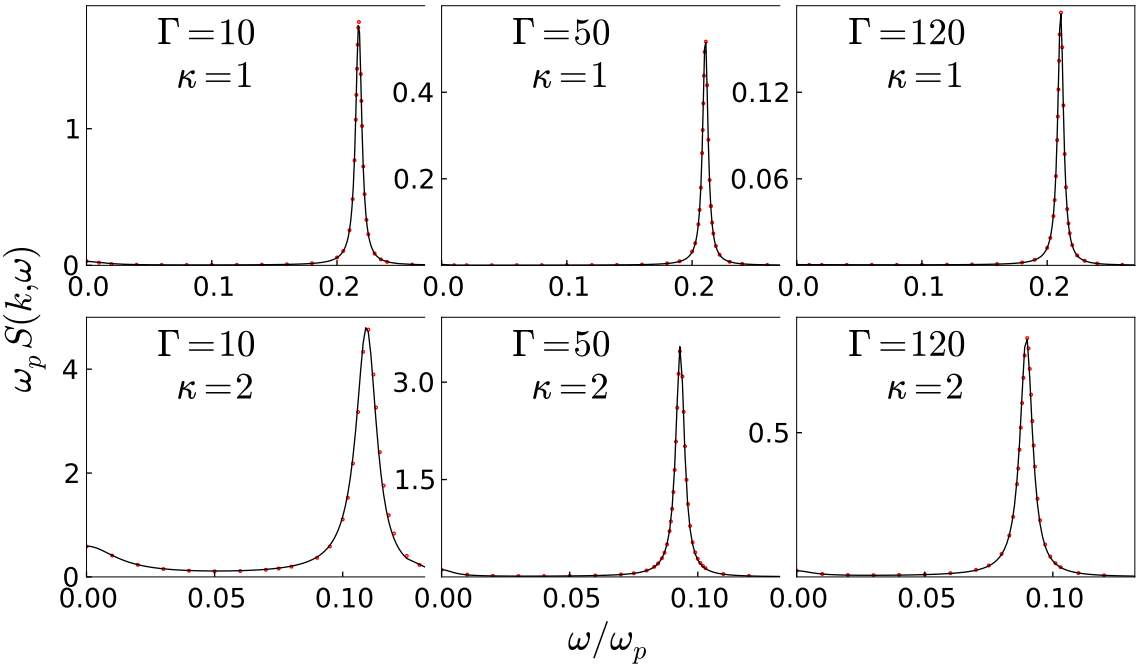

Figure 4.1: Example MD results for $S(k,\omega)$ (dots) at the smallest reduced wave number accessible to the simulations ($ka = 0.23$), plotted alongside the hydrodynamic DSF $S^H(k,\omega)$ given in Equation (4.43) when fitted to the MD data (solid line). This fit was used to determine numerical values for the four parameters, γ, c_s, D_T and σ, at each (Γ,κ) pair.

An important question raised by this procedure is whether the values obtained for the parameters from the fitting *really are* γ, D_T, c_s and σ of the YOCP at the considered (Γ,κ) pair, as opposed to simply arbitrary numbers that fit the MD DSF at $ka = 0.23$. For answering this question, a major advantage is offered by the fact that the YOCP is an idealised model system, and not a 'real' plasma: for the YOCP, the

parameters can, and have been, computed independently of the fit, to a reasonable degree of accuracy, and for a wide range of (Γ,κ) pairs. How this is done is outlined briefly in the remainder of this section. The important point is to note is that—as shown in Table 4.2—when obtained in these independent calculations, the values of the parameters agree well (i.e., within the expected error bounds) with those obtained from the fit to the MD data. This answers the question in the positive: it is reasonable to take the parameters obtained from the fit as the numerical values of γ, D_T, c_s and σ.

Γ	γ (fit)	γ	$\hat{c}_s$ (fit)	$\hat{c}_s$	$\hat{\sigma}$ (fit)	$\hat{\sigma}$	$\hat{D}_T$ (fit)
1	1.281	1.048	1.231	1.131	0.760	0.588	2.152
5	1.058	1.015	0.993	0.974	0.102	0.116	0.402
10	1.043	1.008	0.954	0.950	0.057	0.060	0.308
50	1.002	1.002	0.924	0.929	0.050	0.044	0.059
120	1.026	1.001	0.925	0.926	0.064	0.093	1.574
175	1.022	1.000	0.927	0.925	0.095	0.136	1.039

Table 4.2: Comparison for $\kappa = 1$ between the four parameters appearing in the hydrodynamic DSF when obtained by fitting Equation (4.43) to the MD DSF (first column) and from previous work for the EOS and transport coefficients of the YOCP (second column). The parameters γ and $\hat{c}_s$ (determined using the EOS of Hamaguchi, Farouki and Dubin [Hamaguchi *et al.*, 1996]—see Appendix D for further details) are found to agree to within 10%, and $\hat{\sigma}$ (determined from the shear viscosity calculations of Saigo and Hamaguchi [Saigo & Hamaguchi, 2002]) to within 30% in all cases (expect for the case highlighted).

Firstly, the way in which γ and c_s can be calculated is outlined. These parameters are more straightforward to calculate than D_T and σ, since they depend on *thermodynamic coefficients* only: the isothermal compressibility χ_T and the heat capacities, both at constant volume, C_V, and at constant pressure, C_P. χ_T, C_V and C_P are known as thermodynamic coefficients because they can be determined from knowledge of the equation of state (i.e., the relation between thermodynamic variables) of the YOCP. In Appendix D, it is shown that the following exact expressions for the thermodynamic coefficients can be given in terms of the *reduced excess internal*

energy per particle, $u(\Gamma,\kappa)$:

$$\frac{\chi_T^0}{\chi_T} = 1 + \frac{u(\Gamma,\kappa)}{3} + \frac{\Gamma}{9}\frac{d}{d\Gamma}u(\Gamma,\kappa) \tag{4.44}$$

$$\frac{C_V}{Nk_B} - \frac{3}{2} = -\Gamma^2\frac{d}{d\Gamma}\left[\frac{u(\Gamma,\kappa)}{\Gamma}\right] \tag{4.45}$$

$$\frac{C_P}{Nk_B} = \frac{C_V}{Nk_B} + \frac{1}{9}\left(\frac{C_V}{Nk_B}\right)^2\frac{\chi_T}{\chi_T^0}\,, \tag{4.46}$$

where $\chi_T^0 = \beta/n$ is the isothermal compressibility of the ideal gas. The thermodynamic coefficients, and thus also the parameters γ and c_s, can therefore be computed once the function $u(\Gamma,\kappa)$ is given. Although this function is known analytically in only certain limiting cases (e.g., $\Gamma \to 0$), it can be computed numerically. This has been done to reasonably high accuracy, and for a large number of (Γ,κ) pairs by Hamaguchi, Farouki and Dubin [Hamaguchi *et al.*, 1996], and by Caillol and Gilles [Caillol & Gilles, 2000b]. From Equations (4.44)–(4.46):

$$\gamma = \frac{C_P}{C_V} = 1 + \frac{1}{9}\frac{C_V}{Nk_B}\frac{\chi_T}{\chi_T^0}\,. \tag{4.47}$$

and

$$\hat{c}_s = \frac{c_s}{a\omega_p} = \frac{1}{a\omega_p}\sqrt{\frac{\gamma k_B T}{m}\frac{\chi_T^0}{\chi_T}} = \sqrt{\frac{\gamma}{3\Gamma}\frac{\chi_T^0}{\chi_T}}\,, \tag{4.48}$$

where the sound speed has been expressed in the reduced units used throughout the thesis.

The two remaining coefficients appearing in the hydrodynamic DSF, D_T and σ, are more difficult to calculate since, as well as depending on the thermodynamic coefficients, they also depend on *transport coefficients*: the thermal conductivity λ and the shear and bulk viscosities, η and ζ, respectively. λ, η and ζ are called transport coefficients since they are all measures of how rapidly some macroscopic quantity (e.g., heat in the case of λ) is transferred or 'transported' between different parts of the system. There are several methods by which transport coefficients can be determined[4]. A number of previous studies have used these standard methods to determine the transport coefficients of the YOCP to a reasonable degree of accuracy. As is the case for the thermodynamic coefficients, each of the transport coefficients is in principle a function of Γ and κ. One conclusion of previous studies is that, for all Γ and κ values, the bulk viscosity ζ of the YOCP is small in comparison to the

[4]Two methods are discussed in Chapter 8, which is devoted to a comparing these different methods for computing the shear viscosity.

shear viscosity η [Salin & Caillol, 2003]. Because the two viscosities appear in the hydrodynamic description in the combination $(4\eta/3 + \zeta)$, this means that the bulk viscosity ζ can be neglected. The remaining viscosity, the shear viscosity η, can be conveniently expressed in reduced units as

$$\hat{\eta} = \frac{\eta}{nma^2\omega_p}\,, \tag{4.49}$$

and has been computed by Saigo and Hamaguchi [Saigo & Hamaguchi, 2002]. The other transport coefficient is the thermal conductivity, which can likewise be expressed as

$$\hat{\lambda} = \frac{\lambda}{nk_B\omega_p a^2}\,, \tag{4.50}$$

and has been computed by Donko and Hartmann [Donkó & Hartmann, 2004].

Table 4.2 shows the values of the four parameters—γ, D_T, c_s and σ (each in reduced units)—obtained from fitting the MD DSF to Equation (4.43), alongside the values obtained from the previous studies aforementioned. The results of Donko and Hartmann [Donkó & Hartmann, 2004] for the thermal diffusivity D_T are not shown, for the following reason: as seen in Figure 4.1, the central (Rayleigh) peak in the DSF is in general very small, and accordingly the fitted value of $\gamma \approx 1$ (which, as shown in Table 4.2, agrees well with previous calculations for the EOS of the YOCP). This means that fitted value of D_T—which is the width of this small peak—is subject to considerable uncertainty. Indeed, for the same reason, the precise value of D_T is unimportant, since for $\gamma \approx 1$ the hydrodynamic description of Equation (4.43) reduces from a four to a two parameter description. As can be seen from Table 4.2, for $\kappa = 1$, the only case in which a comparison between the fitted value of D_T and the results of Donko and Hartman would be useful is $\Gamma = 1$ (since in this case the central peak in the DSF is rather larger); unfortunately, however, results for D_T are not available for this (Γ,κ) pair.

As shown in Table 4.2, the fitted values of γ and c_s agree to within 10% with the results of previous investigations (the only exception to this is the highlighted case of $\Gamma = 1$). This margin of error is reasonable, despite the fact that these parameters are derived from the reduced excess internal energy of the YOCP (cf. Equations (4.44)–(4.46)), $u(\Gamma, \kappa)$, which has been computed to rather higher accuracy [Caillol & Gilles, 2000b, Hamaguchi *et al.*, 1996]. The reason for this is that both c_s and γ are given, not in terms of $u(\Gamma, \kappa)$ only, but also in terms of the partial derivative of $u(\Gamma, \kappa)$ with respect to Γ. Although $u(\Gamma, \kappa)$ is known accurately, its partial derivative is based on a formula which interpolates between (a relatively small number of) the computed

values of $u(\Gamma, \kappa)$ (see Appendix D, Equation (D.24) for this formula). This means that the uncertainty in the slope of $u(\Gamma, \kappa)$ is considerably greater than the uncertainty in $u(\Gamma, \kappa)$ itself, which in turn accounts for the discrepancies with the fitted values of c_s and γ. It is presumed that the disagreement at $\Gamma = 1$ can also be partly attributed to this cause: as Γ decreases, the slope of $u(\Gamma, \kappa)$ becomes increasingly difficult to evaluate accurately.

The remaining parameter, σ, is shown in Table 4.2 to agree to within 30% with the values computed by Saigo and Hamaguchi [Saigo & Hamaguchi, 2002]. Again, this is a reasonable margin of error. It is greater than for γ and c_s since σ requires knowledge of the shear viscosity η. As a transport coefficient, η is a 'dynamical' quantity, and is therefore considerably more difficult to compute accurately in MD simulations than the reduced excess internal energy, $u(\Gamma, \kappa)$, which the 'static' thermodynamic coefficients are derived from. Previous studies have indicated that transport coefficients such as η can be computed to within $20 - 30\%$ at best [Donkó & Hartmann, 2004, Saigo & Hamaguchi, 2002], in line with the discrepancies shown in Table 4.2.

In summary then, by fitting the DSF from MD, the values obtained for the four parameters appearing in the hydrodynamic DSF in Equation (4.43)—γ, c_s, D_T and σ—are consistent with the simulation work done by others for the EOS and transport coefficients of the YOCP. For the remainder of this chapter, these fitted values of the parameters are used; this allows the domain of validity of the hydrodynamic description of Equation (4.43) to be assessed.

4.7 Breakdown of the hydrodynamic description

The fact that, for the YOCP, the ratio of specific heats $\gamma \approx 1$ (at least for the (Γ,κ) pairs studied in this chapter) means that the hydrodynamic description reduces to a description of the position, height and width of the ion-acoustic or Brillouin peaks in the DSF. Accordingly, determining when the hydrodynamic description breaks down is a case of looking at when the hydrodynamic 'prediction' for these three features of the ion-acoustic peak[5]—as given by Equation (4.43)—diverges from the result obtained from the MD simulations.

Firstly, the position of the ion-acoustic peak is considered. Figure 4.2 shows the position of the ion-acoustic peak obtained from the MD DSF (at $\Gamma = 10$), along with the linear predictions of the hydrodynamic description. Clearly, for every value of κ, the linear prediction of hydrodynamics is valid within some range of k values. As κ

[5]from hereon in the singular 'peak' refers to the positive ω peak of the symmetric pair.

becomes smaller, corresponding to longer screening lengths λ_s, it is necessary to look at increasingly long length scales (small ka) for the linear prediction to be applicable. For all κ values, at some wave number k, which can be denoted by k_{max}, the position $\omega(k)$ of the ion-acoustic peak in the MD DSF diverges from the linear relation. In order to quantify this divergence, k_{max} can be defined as the minimum k value for which $\omega(k)/(c_s k) > 1.01$. Using this criterion, for all values of the coupling Γ, it is found that

$$k_{max}\lambda_s \simeq 0.43. \tag{4.51}$$

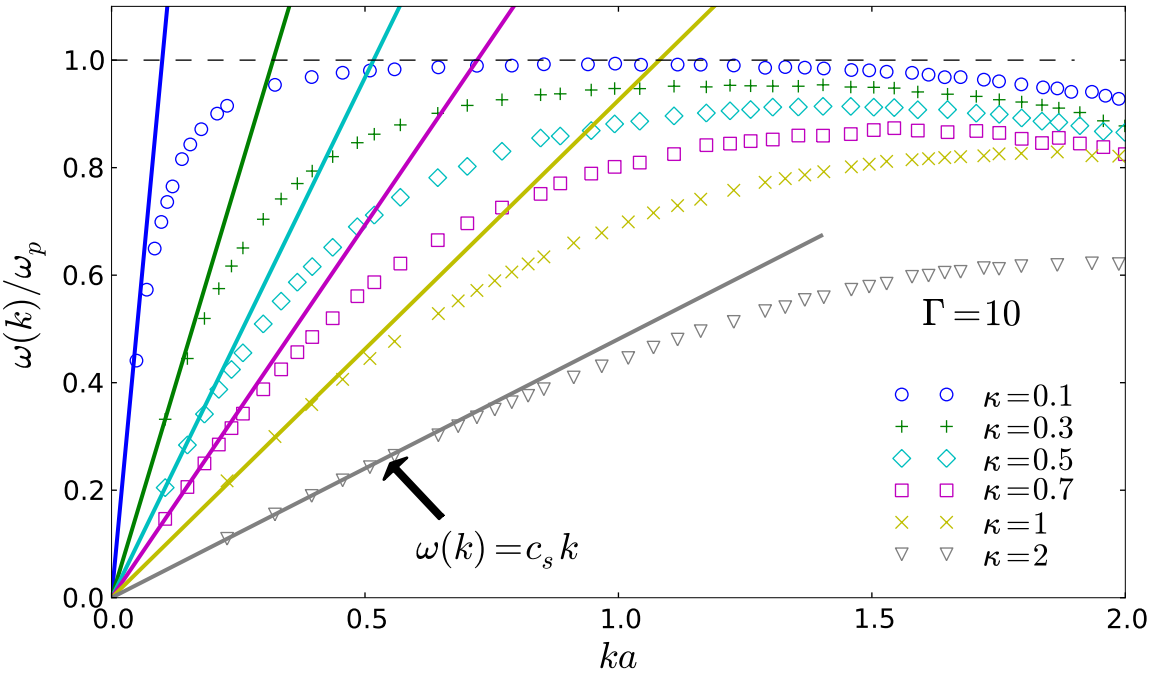

Figure 4.2: Ion-acoustic peak position $\omega(k)/\omega_p$ as obtained from the MD DSF (symbols), along with the corresponding linear relations from the hydrodynamic description $\omega = c_s k$ (solid lines).

Next, the height and width of the ion acoustic peak are considered. Figure 4.3 shows the height and width of the ion-acoustic peak obtained from the MD DSF, for two particular (Γ,κ) pairs, along with the predictions of the hydrodynamic description. The k_{max} obtained from the peak position is found to also characterise well the departure of the height and width of the ion-acoustic peak from the predictions of the hydrodynamic description. This means that k_{max} can be interpreted as the maximum wave number at which the hydrodynamic description of Equation (4.43) is applicable; that is, k_{max} is a quantitative measure of the domain of validity of the hydrodynamic description of the YOCP.

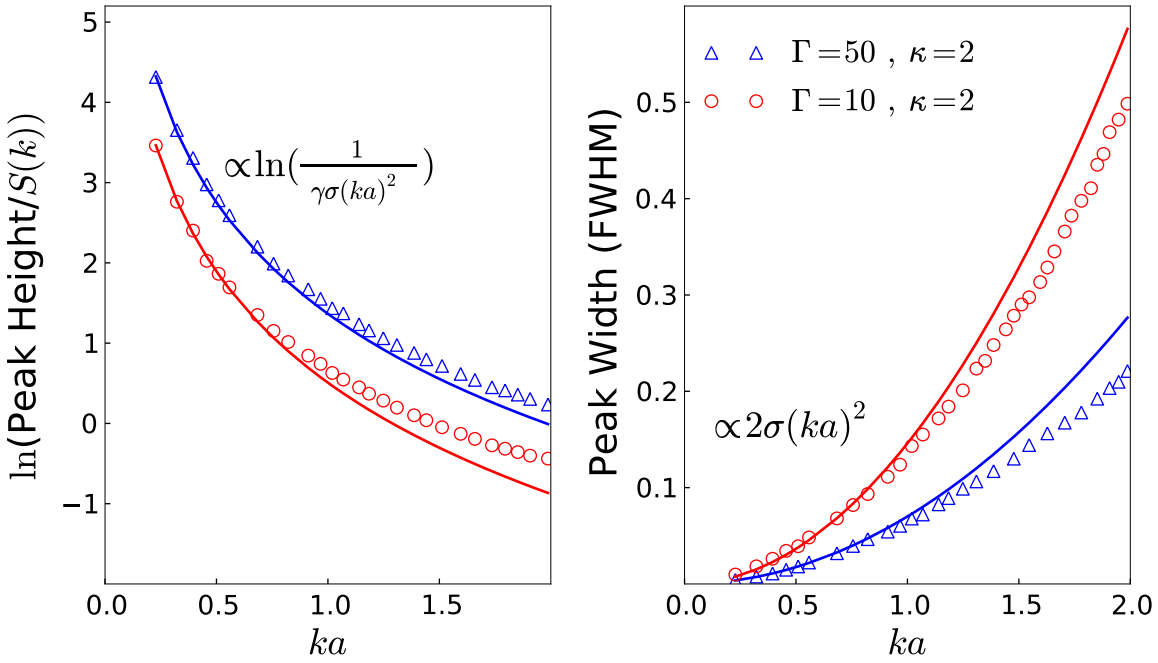

Figure 4.3: Height and width of the ion-acoustic peak as computed from MD for two particular (Γ,κ) pairs (open symbols), and the predictions of Equation (4.43) (solid lines).

The way in which the hydrodynamic description breaks down beyond k_{max} is found to be the same for all (Γ,κ) pairs: as shown in Figures 4.2 and 4.3, the ion-acoustic peak moves out more slowly, its height decreases more slowly, and its width increases more slowly, than predicted by Equation (4.43). This is illustrated for the entire DSF in Figure 4.4.

The criterion for k_{max} given in Equation (4.51) indicates that the hydrodynamic description is valid for a relatively large range of k values, well beyond $k = 0$. The value for k_{max} can be converted into a length scale in real space, $l_{max} = 2\pi/k_{max}$. This length scale is for all (Γ,κ) pairs greater than the short range correlation length over which the radial distribution function $g(r)$ exhibits peaks and troughs.

It is remarkable that the domain of validity of the hydrodynamic description of the YOCP (i.e., the criterion for k_{max}) is not found to depend on Γ; indeed, one would intuitively expect the domain of validity to increase as the system becomes more 'collisional' (i.e., with increasing Γ). It is also noted that, providing $k < k_{max}$, the hydrodynamic approximation of Equation (4.43) for $S(k,\omega)$ is extremely accurate for all ω where $S(k,\omega)$ is not negligibly small; in this range, the ion-acoustic peaks exhaust the frequency sum-rules (see Figure 4.1).

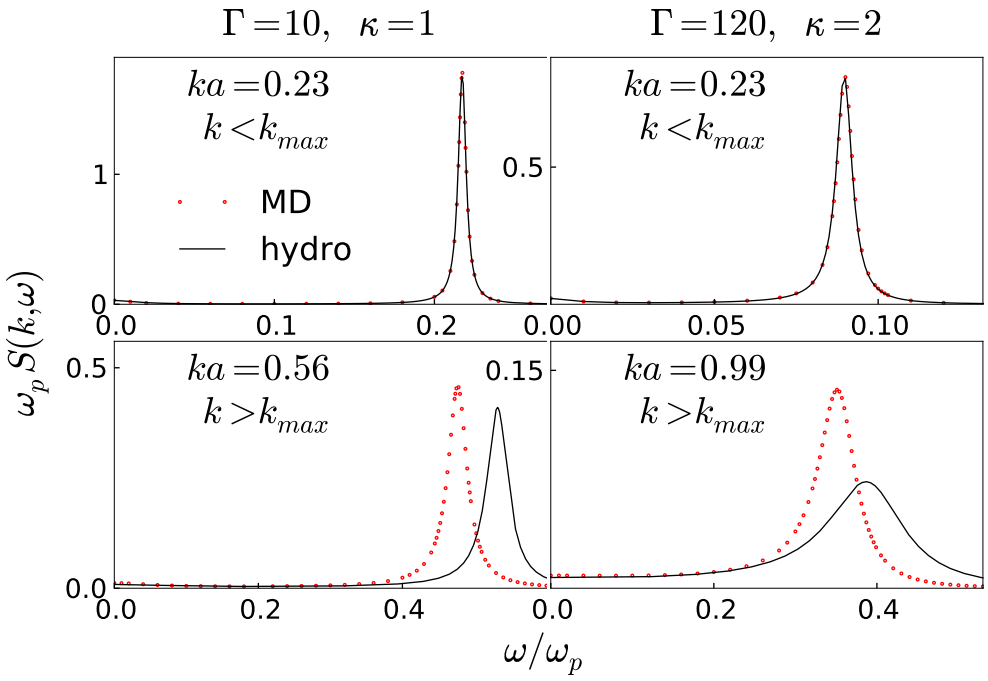

Figure 4.4: Example MD results for $S(k,\omega)$ (dots), plotted alongside the hydrodynamic DSF $S^H(k,\omega)$ given in Equation (4.43) (solid line).

4.8 Applicability to x-ray scattering experiments

The extensive domain of validity given by the criterion for k_{max} in Equation (4.51) certainly has notable experimental applicability. As an illustrative example, one can consider a hydrogen plasma with $n = 1 \times 10^{23}\text{cm}^{-3}$ and $T = 13\,\text{eV}$. These conditions have been chosen as they are similar to those reported in recent experiments that used a high power laser to heat a hydrogen sample [Fäustlin *et al.*, 2010]. The coupling strength Γ for these conditions can be calculated to be $\Gamma \approx 1$, and using the Thomas-Fermi screening length λ_{TF} (defined in Equation (1.13)) as an estimate of λ_s gives $\lambda_s \approx 0.50\mathring{A}$, and thus $k_{max} \simeq 0.86\mathring{A}^{-1}$. This value for the maximum wave number can be translated into a maximum angle in a scattering experiment by using Equation (2.65). For this, it can be assumed that the probe wavelength corresponds to a photon energy of 2 keV, which has recently been used in experiments at the Linac Coherent Light Source x-ray laser [Vinko *et al.*, 2012]. Finally then, the result of this calculation is that the hydrodynamic description can be expected to yield the approximate ionic response in x-ray scattering experiments up to a scattering angle of $\approx 12°$, which is large enough to be attainable in forthcoming experiments [Gregori & Gericke, 2009]. Obviously, this is only an estimate for the particular plasma

conditions considered, which relies on using the Thomas-Fermi screening length for λ_s; the purpose of this calculation is merely to illustrate that the scattering angles required of the experiments can be expected to be large enough to be practically achievable (i.e., tens of degrees and not tenths of a degree).

4.9 Conclusions and future outlook

In summary, the results presented in this chapter show that the hydrodynamic description of the YOCP is applicable for a surprisingly large range of length scales: the criterion $k_{max}\lambda_s \simeq 0.43$ gives a quantitative measure of this. What is more, below k_{max}—which is found to be independent of the level of many-body correlations or non-ideality of the system (i.e., Γ)—the hydrodynamic equations give an accurate description of the entire ion-acoustic peak.

These results indicate that by resolving the ion dynamics in small angle x-ray scattering experiments, transport coefficients of strongly coupled plasmas could in principle be measured. It is expected that these measurements will soon be possible by taking advantage of the low bandwidth and high brightness characteristics offered by fourth generation light sources [Gregori & Gericke, 2009], and a number of experiments are currently being designed to achieve this.

Chapter 5

Beyond the hydrodynamic description of the YOCP

5.1 Motivation

As mentioned in the previous chapter, a recent and exciting development in HEDP is that x-ray Thomson scattering experiments will soon be able to fully resolve the time dependent ion dynamics of non-ideal plasmas [Glenzer & Redmer, 2009, Gregori & Gericke, 2009, Pelka *et al.*, 2010]. These ion dynamics are encoded in the wave number and frequency dependent ion-ion DSF, $S_{ii}(k,\omega)$, which is the Fourier transform in space and time of the ion density autocorrelation function (or van Hove function). Since the particles of the YOCP represent ions in a non-ideal plasma, understanding and modeling the DSF of the YOCP—denoted here as simply $S(k,\omega)$, rather than $S_{ii}(k,\omega)$—is one way in which to gain a qualitative and quantitative understanding of the ion dynamics of non-ideal plasmas.

A first step in achieving this understanding was made by the research presented in the previous chapter: the conventional hydrodynamic description (based on the Naviér-Stokes equations) was shown to approximately reproduce the DSF of the YOCP for $k < k_{max}$, where $k_{max}\lambda_s \simeq 0.43$ and λ_s is the electronic screening length that appears in the interaction potential. In this range of k values, the DSF of the YOCP exhibits a clear ion-acoustic peak, whose position, height and width is accurately given in terms of familiar thermodynamic and transport coefficients, via Equation (4.43).

Despite the success of the conventional hydrodynamic description at long length scales (small k), it would be good to have a model for the DSF of the YOCP that works well at shorter length scales (higher k). This higher k behaviour—which corresponds

experimentally to higher momentum transfer (see Section 2.7)—is often of greater applicability to the experiments. Accordingly, the investigation presented in this chapter is devoted to the search for a model of the DSF of the YOCP that works for values of k beyond k_{max}. It is shown that a relatively simple model exists that offers a very satisfactory description of the DSF for all k values.

5.2 Searching for models

Thus far, two things are known about the DSF of the YOCP: the first is that at small wave numbers k, the DSF is well approximated by the hydrodynamic DSF (cf. Chapter 4), and the second is that, at large k, the DSF is well approximated by that of an ideal gas of non-interacting particles (cf. Section 2.4). Thus it is only in the region of *intermediate* k values that a model for the DSF is needed. At these intermediate k values, the dynamics of the YOCP is not dominated by either the collective behaviour (as in the small k case) or the free particle behaviour characteristic of the ideal gas (as in the large k case). This makes modelling the DSF in this region difficult.

If k_{ideal} denotes the wave number above which the ideal gas DSF gives a good description of the DSF of the YOCP, then the region of intermediate k values is $k_{max} < k < k_{ideal}$. In the previous Chapter, k_{max} was found to depend only on κ (and not Γ); as shown in Section 5.10, this is not the case for k_{ideal}, which depends on both Γ and κ. Therefore, the region of intermediate k values is different for every (Γ,κ) pair[1]. This region is shown in Figure 5.1 for $\Gamma = 50$, $\kappa = 2$, and can be seen to be relatively large for these particular conditions.

The approach taken in this chapter to modelling the intermediate k behaviour is inspired by the success of the conventional hydrodynamic description at small k values. That is, use is made of a well known framework—generalised hydrodynamics—that exists for extending the results of conventional hydrodynamics to higher k values. It is shown that one of the simplest models of generalised hydrodynamics, known as the Gaussian memory function model, offers a very accurate representation of the DSF of the YOCP for all (Γ,κ) pairs. This is true for the problematic intermediate k values, and since the model is an extension of conventional (Naviér-Stokes) hydrodynamics, it is also true for small k values. What is more, the model is found to reproduce the MD DSF at large k, and therefore it is a good model for all k values.

[1]Since, at a particular value of κ, k_{ideal} is an increasing function of Γ (see Section 5.10), the region increases in size with Γ.

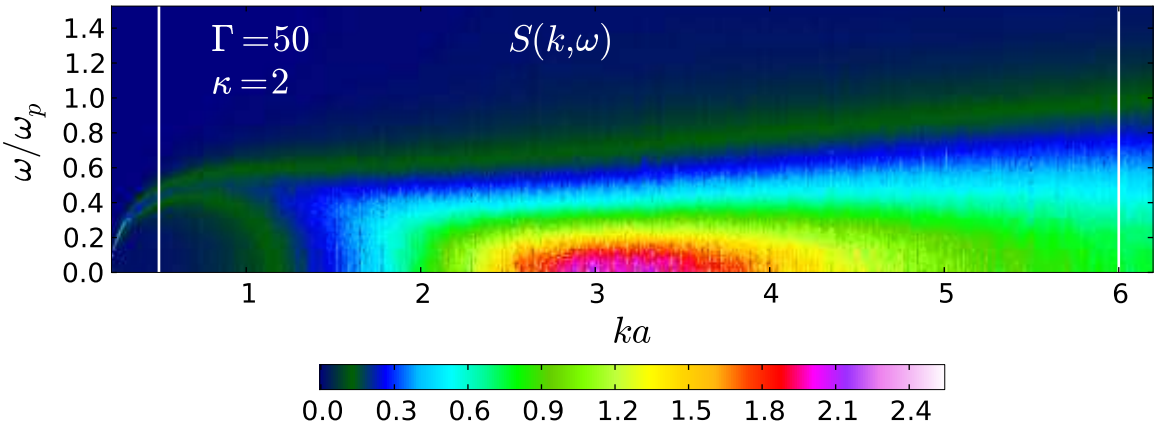

Figure 5.1: DSF of the YOCP for $\Gamma = 50$, $\kappa = 2$, as determined from MD simulations. The vertical lines indicate the approximate values of k_{max} and k_{ideal}.

5.3 Summary of the investigation

For this investigation, the DSF from the MD simulations performed for the previous chapter (see Table 4.1) was compared to the Gaussian memory function model of generalised hydrodynamics. This was done for each (Γ,κ) pair, for a selection of ka values between 0.23 and 6.19, i.e., for small, intermediate and large k values.

5.4 The generalised hydrodynamics approach

If the ratio of specific heats γ is taken to be unity, it is shown in Appendix E that the hydrodynamic DSF of Equation (4.43) can be written

$$\frac{S^H(k,\omega)}{S(k)} = \frac{1}{\pi}\frac{(\tilde{c}_s k)^2 k^2 \eta_l}{[\omega^2 - (\tilde{c}_s k)^2]^2 + [\omega k^2 \eta_l]^2}\,, \tag{5.1}$$

where $\tilde{c}_s$ is the isothermal sound speed and $\eta_l = (\frac{4}{3}\eta + \zeta)/mn$ is the kinematic viscosity. The generalised version of Equation (5.1) is

$$\frac{S^{GH}(k,\omega)}{S(k)} = \frac{1}{\pi}\frac{\langle\omega_k^2\rangle k^2 \phi'(k,\omega)}{[\omega^2 - \langle\omega_k^2\rangle - \omega k^2 \phi''(k,\omega)]^2 + [\omega k^2 \phi'(k,\omega)]^2}\,. \tag{5.2}$$

Equation (5.2) is a well known and exact representation of the DSF[2] . Its derivation from microscopic theory is described in Section 5.6.

[2]i.e., although it is given here in analogy with the DSF obtained from isothermal hydrodynamics, there is no such 'generalised isothermal' assumption in Equation (5.2).

The similarity between Equations (5.1) and (5.2) is no coincidence: Equation (5.2) represents a generalised hydrodynamics in which both the thermodynamic and transport coefficients appearing in conventional hydrodynamics are replaced by suitably defined wave number dependent quantities. In Equation (5.2), $\langle\omega_k^2\rangle = \frac{k_BT}{m}\frac{k^2}{S(k)} = \langle\omega^2\rangle/\langle\omega^0\rangle$ defines a generalised isothermal sound speed $\tilde{c}_s(k) = \sqrt{\langle\omega_k^2\rangle/k^2} = \sqrt{\frac{k_BT}{m}\frac{1}{S(k)}}$ that in the hydrodynamic limit of $k \to 0$ reduces to the conventional isothermal sound speed $\tilde{c}_s(0) = \tilde{c}_s = \sqrt{\frac{k_BT}{m}\frac{\chi_T^0}{\chi_T}}$. The quantities $\phi^{'}(k,\omega)$ and $\phi^{''}(k,\omega)$ are, respectively, the real and imaginary parts of the Laplace transform of the memory function $\phi(k,t)$. Section 5.6 gives a brief overview of memory functions, which are ubiquitous in the description of the dynamics of dense fluids; for now, it is simply noted that, in the analogy between Equations (5.1) and (5.2), the memory function plays the role of a generalised viscosity.

5.5 The Gaussian memory function model

Different models of generalised hydrodynamics correspond to different approximations for the memory function $\phi(k,t)$. The Gaussian memory function model (or simply Gaussian model), which is the focus of this chapter, amounts to using the Gaussian approximation for the memory function:

$$\begin{aligned} k^2\phi(k,t) &= k^2\phi(k,0)\exp(-\pi t^2/4\tau_k) \\ &= [\omega_L^2(k) - \langle\omega_k^2\rangle]\exp(-\pi t^2/4\tau_k)\,, \end{aligned} \tag{5.3}$$

where $\omega_L^2(k) = \langle\omega^4\rangle/\langle\omega^2\rangle$ is given in terms of the frequency moments of the DSF, defined in Equation (2.43). The other parameter appearing in Equation (5.3), τ_k, is a wave number dependent relaxation time. According to Equation (5.3), the real and imaginary parts of the Laplace transform of the memory function are given by, respectively [Ailawadi *et al.*, 1971, Hansen *et al.*, 1975],

$$k^2\phi^{'}(k,\omega) = [\omega_L^2(k) - \langle\omega_k^2\rangle]\tau_k e^{-\tau_k^2\omega^2/\pi} \tag{5.4}$$

and

$$k^2\phi^{''}(k,\omega) = \frac{2\tau_k}{\sqrt{\pi}}[\omega_L^2(k) - \langle\omega_k^2\rangle]D(\tau_k\omega/\sqrt{\pi})\,, \tag{5.5}$$

where the Dawson function $D(x) = \exp(-x^2)\int_0^x \exp(y^2)dy$[3].

The quality of the Gaussian model has been previously identified for the Lennard-Jones fluid [Ailawadi *et al.*, 1971, de Schepper *et al.*, 1988] and by Hansen et al. in a

[3] A method for implementing the Dawson function can be found in [Press *et al.*, 1992].

pioneering study of the OCP [Hansen *et al.*, 1975]; it has also been applied to experimental data for weakly coupled plasma produced by arc jets [Gregori *et al.*, 2002]. However, even for those systems—because of the difficulty of conducting highly accurate MD simulations for the DSF at the time of the previous investigations—a detailed, conclusive comparison of the model in Equation (5.2) with the DSF obtained from MD simulations was not possible[4]. Furthermore, for the YOCP system in particular, just as the applicability of the conventional hydrodynamic description had not been addressed prior to this thesis, generalised hydrodynamics models for the DSF do not appear to have been investigated.

5.6 Memory Functions

As seen in the previous sections, the generalised hydrodynamics description of the DSF introduces a new quantity known as the memory function. This quantity is not specific to case of the DSF: memory functions are the central objects in generalised hydrodynamics, and are ubiquitous in the study of time dependent correlation functions in general. A typical equation relating a time dependent correlation function $C(t)$ to its memory function $K(t)$ is

$$\frac{d}{dt}C(t) = -\int_0^t K(t')C(t-t')dt' \,. \tag{5.6}$$

Clearly, if $K(t)$ is known, then $C(t)$ is known, and vice-versa. The memory function can therefore be seen as an alternative representation of a time dependent correlation function. Its utility stems from the fact that simple approximations for $K(t)$ are expected to be effective in describing $C(t)$, which itself could exhibit complicated behaviour. That this is indeed the case is evident from the results presented later in this chapter (see Section 5.9)—a Gaussian memory function offers an excellent description of the DSF of the YOCP, despite the fact the DSF itself shows a range of complicated behaviour.

From its definition in Equation (5.6), it is clear why $K(t)$ is called the memory function: the decay rate of $C(t)$ depends on its past history, and $K(t)$ controls to what extent $C(t)$ 'remembers its past history' [Boon & Yip, 1991]. The system is 'memoryless' if $K(t)$ is taken to be a delta function in time; this is known as

[4]Indeed, for this reason, the analysis of Hansen et. al [Hansen *et al.*, 1975] for the OCP is revisited in this thesis; the results are discussed and presented in Section 7.4 and Appendix F.

the 'Markovian approximation', and gives an exponential decay for $C(t)$ (and thus Lorentzian peaks in the corresponding frequency spectrum[5]).

By differentiating Equation (5.6) with respect to time, the initial value of the memory function is seen to be

$$K(0) = -\ddot{C}(0)/C(0)\,. \tag{5.7}$$

A more formal way to motivate the introduction of memory functions than simply writing down Equation (5.6) is via the so-called 'projection operator approach' pioneered by Zwanzig and Mori [Mori, 1965, Zwanzig, 1961]. An excellent description of this can be found in Chapter 3 of the book by Balucani and Zoppi [Balucani & Zoppi, 2002]. In this approach, it is first shown that the equation of motion of a set of dynamical variables $\{A_1(t), A_2(t) \cdots, A_n(t)\}$ can be formally written as a *generalised Langevin equation*. In terms of correlation functions, and in the case of a single dynamic variable ($n = 1$), this reduces to Equation (5.6).

The relation between the particular memory function discussed in this chapter and its associated time correlation function—the intermediate scattering function—is in fact slightly more complicated than given by Equation (5.6). The first step in seeing this is to take the Laplace transformation of Equation (5.6), defined as

$$C(z) = \int_0^t C(t)\exp(izt)dt\,. \tag{5.8}$$

This gives

$$C(z) = [-iz + K(z)]^{-1}C(0)\,. \tag{5.9}$$

Next, it is noted that the memory function $K(t)$ itself can be written in terms of a 'second-order' memory function $K_1(t)$ (this can also be shown formally using microscopic theory [Balucani & Zoppi, 2002]), i.e., in the same form as Equation (5.6). When Laplace transformed this gives

$$K(z) = [-iz + K_1(z)]^{-1}K(0)\,. \tag{5.10}$$

Substituting this result into Equation (5.9) and iterating leads to an expression of $C(z)$ as a continued fraction:

$$\frac{C(z)}{C(0)} = \frac{1}{-iz + K(0)/(-iz + \cdots)} \tag{5.11}$$

[5]The attentive reader may notice that Lorentzian peaks feature in the hydrodynamic DSF, Equation (4.43), investigated in Chapter 4. This is related to the fact that the Markovian assumption for the memory function essentially underlies much of conventional hydrodynamics (see Section 5.13, and for a comprehensive discussion [Balucani & Zoppi, 2002]).

Similarly, by iterating Equation (5.7), the initial value of each of the memory functions can be written in terms of the frequency moments $\langle\omega^n\rangle$ of the spectrum of $C(t)$ (cf. Section 2.5):

$$\Delta_1 = K(0) = -\frac{\ddot{C}(0)}{C(0)} = \langle\omega^2\rangle \tag{5.12}$$

$$\Delta_2 = K_1(0) = -\frac{\ddot{K}(0)}{K(0)} = \frac{\langle\omega^4\rangle}{\langle\omega^2\rangle} - \langle\omega^2\rangle \tag{5.13}$$

$$\dots$$

and Equation (5.11) can therefore be written

$$\frac{C(z)}{C(0)} = \left[-iz + \frac{\Delta_1}{-iz + \Delta_2/(-iz + \cdots)}\right]^{-1} . \tag{5.14}$$

In the case of the intermediate scattering function, this equation becomes

$$F(k,z) = S(k)\left[-iz + \frac{\langle\omega_k^2\rangle}{-iz + K_1(k,z)}\right]^{-1} , \tag{5.15}$$

and using the relation between the Laplace transform of the intermediate scattering function and the DSF, Equation (4.19), gives

$$\begin{aligned}\frac{S(k,\omega)}{S(k)} &= \frac{1}{\pi}\Re e\frac{F(k,z=\omega)}{S(k)} \\ &= \frac{1}{\pi}\Re e\left[-i\omega + \frac{\langle\omega_k^2\rangle}{-i\omega + K_1(k,z=\omega)}\right]^{-1} .\end{aligned} \tag{5.16}$$

Since, from the definition of the Laplace transform,

$$\begin{aligned}K_1(k,z=\omega) &= \int_0^\infty K_1(k,t)\cos\omega t\, dt + i\int_0^\infty K_1(k,t)\sin\omega t\, dt \\ &= K_1'(k,\omega) + iK_1''(k,\omega)\,,\end{aligned} \tag{5.17}$$

this can be written as

$$\frac{S(k,\omega)}{S(k)} = \frac{1}{\pi}\frac{\langle\omega_k^2\rangle K_1'(k,\omega)}{[\omega^2 - \langle\omega_k^2\rangle - \omega K_1'(k,\omega)]^2 + [\omega K_1''(k,\omega)]^2}\,, \tag{5.18}$$

which is simply Equation (5.2), with $k^2\phi(k,\omega)$ replaced by $K_1(k,\omega)$. The specific memory function discussed in this chapter is therefore the 'second-order' memory function, $K_1(k,t)$, in the continued fraction representation of the DSF. The reason for writing this memory function as $k^2\phi(k,t)$ is that the related memory function $\phi(k,t)$ has a more intuitive physical interpretation as a 'generalised viscosity'. This can be seen from a phenomenological derivation of the DSF, as outlined in the following section.

5.7 Phenomenological (macroscopic) derivation of formula for DSF

As described in the previous section, the formula for the DSF (Equation (5.1)) given by the generalised hydrodynamics description can be motivated from formal microscopic theory. However, a more intuitive way in which Equation (5.1) can be derived is via a phenomenological 'generalisation' of the conventional hydrodynamic description. Firstly, the longitudinal component of the linearised Naviér-Stokes equation can be written as [Ailawadi *et al.*, 1971]

$$\frac{d}{dt}J(\boldsymbol{r},t) = -\frac{1}{m}\nabla P(\boldsymbol{r},t) + \eta_l \nabla^2 J(\boldsymbol{r},t)\,, \tag{5.19}$$

where $J(\boldsymbol{r},t)$ is the longitudinal current density and $P(\boldsymbol{r},t)$ is the pressure. Similarly, Equation (5.2) can be derived from a generalised version of Equation (5.19) (see [Ailawadi *et al.*, 1971] for more details),

$$\begin{aligned}\frac{d}{dt}J(\boldsymbol{r},t) = &-\frac{1}{m}\nabla \int d\boldsymbol{r}^{'}\frac{\delta P(\boldsymbol{r},t)}{\delta n(\boldsymbol{r}^{'},t)}\delta n(\boldsymbol{r}^{'},t)\,. \\ &+ \nabla^2 \int_0^t \int ds d\boldsymbol{r}^{'}\phi(\boldsymbol{r}-\boldsymbol{r}^{'},t-s)J(\boldsymbol{r}^{'},s)\,,\end{aligned} \tag{5.20}$$

where $n(\boldsymbol{r},t)$ is the number density. This generalisation is motivated in the following way. At small length scales, the validity of the conventional hydrodynamic description can be expected to break down. Specifically, in the Naviér-Stokes description of Equation (5.19), both the pressure term and viscosity term are local in space and time. The generalisation in Equation (5.20) includes the non-local behavior that is essential at small length scales in two ways. Firstly, it is assumed that a change in pressure at a position $\boldsymbol{r}$ should not be determined completely by density fluctuations at the same position $\boldsymbol{r}$ but also by density fluctuations at neighbouring positions. This means that the pressure gradient due to a density gradient is non-local (hence the functional derivative appearing in Equation (5.20)). Secondly, the viscosity is made to be non-local in space and time to model the viscoelastic effects in a real liquid. The memory function $\phi(\boldsymbol{r},t)$ that models these viscoelastic effects describes the delayed response of the longitudinal part of the stress tensor to a change in the rate of shear [Ailawadi *et al.*, 1971]. In Equation (5.3), this response is modeled by a single relaxation time τ_k. The requirement that the model reproduces the result obtained from the Naviér-Stokes equations in the hydrodynamic limit gives a relation between

the long wavelength behavior of this relaxation time and the kinematic viscosity η_l [Ailawadi *et al.*, 1971],

$$\eta_l = mn \lim_{k\to 0}[\omega_L^2(k) - \langle\omega_k^2\rangle]\tau_k/k^2\,, \tag{5.21}$$

where $\eta_l = (\frac{4}{3}\eta + \zeta)/mn$, with η and ζ the shear and bulk viscosities respectively.

The generalisation included in Equation (5.20) leads to the expression in Equation (5.2) for the dynamical structure factor (see e.g. [Ailawadi *et al.*, 1971]). All that remains is to specify the memory function. As discussed in Sec. 5.5, here a Gaussian memory function is chosen, as this is the simplest model that previous studies have suggested gives a good description of the dynamics of classical fluids. It is found that this choice yields a model of the DSF that matches the MD data for the YOCP remarkably well.

5.8 Fitting the Gaussian memory function model to the MD data

In order to compare the Gaussian memory function model given in Equations (5.2), (5.4) and (5.5) to the MD DSF, values for the parameters that appear in the model—$\langle\omega_k^2\rangle$, $\omega_L^2(k)$ and τ_k—are required for each k value. Since all three of these parameters are in general unknown, they were obtained by fitting to the MD DSF using the least squares method. That is to say, for every (Γ,κ) pair, for each k value, the Gaussian model was fitted to the MD DSF. When the parameters were obtained in this way, is was found that the model reproduces the MD data very accurately for all Γ and κ values; in Section 5.9, it is shown that this is the case for small, intermediate and large k values.

Fitting the three parameters is the correct way to compare the Gaussian memory function model to the MD DSF. This is true despite the fact that two of the parameters, $\langle\omega_k^2\rangle$ and $\omega_L^2(k)$, can in principle be obtained by computing $S(k)$ (or equivalently the radial distribution function $g(r)$) with MD and using the formulae for the frequency moments given in Appendix C. The problem with this alternative method for determining $\langle\omega_k^2\rangle$ and $\omega_L^2(k)$ is that $S(k)$ and $g(r)$ are subject to the numerical uncertainty present in the MD simulations. Therefore, one would expect that constraining $\langle\omega_k^2\rangle$ and $\omega_L^2(k)$—and thus fitting the model to the MD spectrum using only a single parameter τ_k, as done in previous investigations [Ailawadi *et al.*, 1971, Gregori *et al.*, 2002, Hansen *et al.*, 1975]—would result in poorer fits and larger errors. In Figure 5.2, it is shown that in general this is indeed the case.

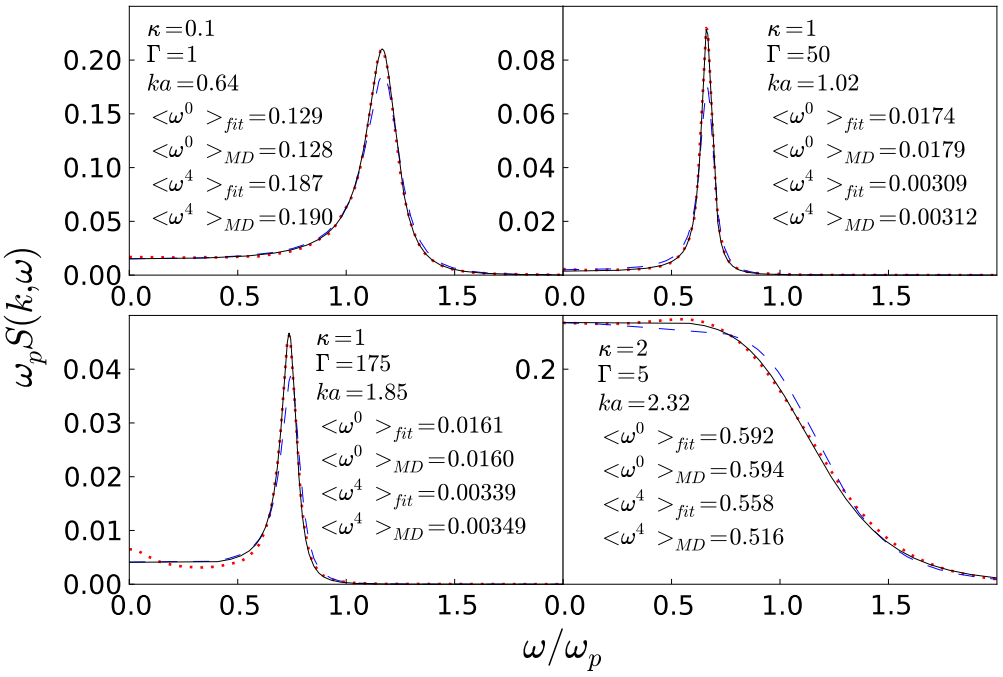

Figure 5.2: Comparison between the Gaussian model when only the parameter τ_k is fitted to the MD spectrum (dashed line), and when all three parameters are fitted (solid line) for four separate (Γ,κ) pairs. The MD results are given by the dots.

The validity of the three parameter fit can be confirmed by comparing the fitted values of the two parameters $\langle\omega_k^2\rangle$ and $\omega_L^2(k)$ to their values when instead computed with MD as described above. As shown in Figure 5.3, the parameters $\langle\omega_k^2\rangle$ and $\omega_L^2(k)$ obtained from the fit to the MD DSF agree very well (within 10%) with those computed from the MD $g(r)$ and $S(k)$. This is only the case because the model works so well. For example, as shown in Figure 5.3, if an exponential rather than Gaussian memory function is used (this is known as the viscoelastic model and is discussed in Section 5.12), the numerical values obtained for $\omega_L^2(k)$ by fitting the model with three parameters do not agree well with those computed from the MD $g(r)$ and $S(k)$. In the following sections, only the results for the Gaussian memory function model with three fitting parameters are shown; the one parameter fits are irrelevant as their comparison with the MD DSF is not indicative of the quality of the model, for the reasons described above.

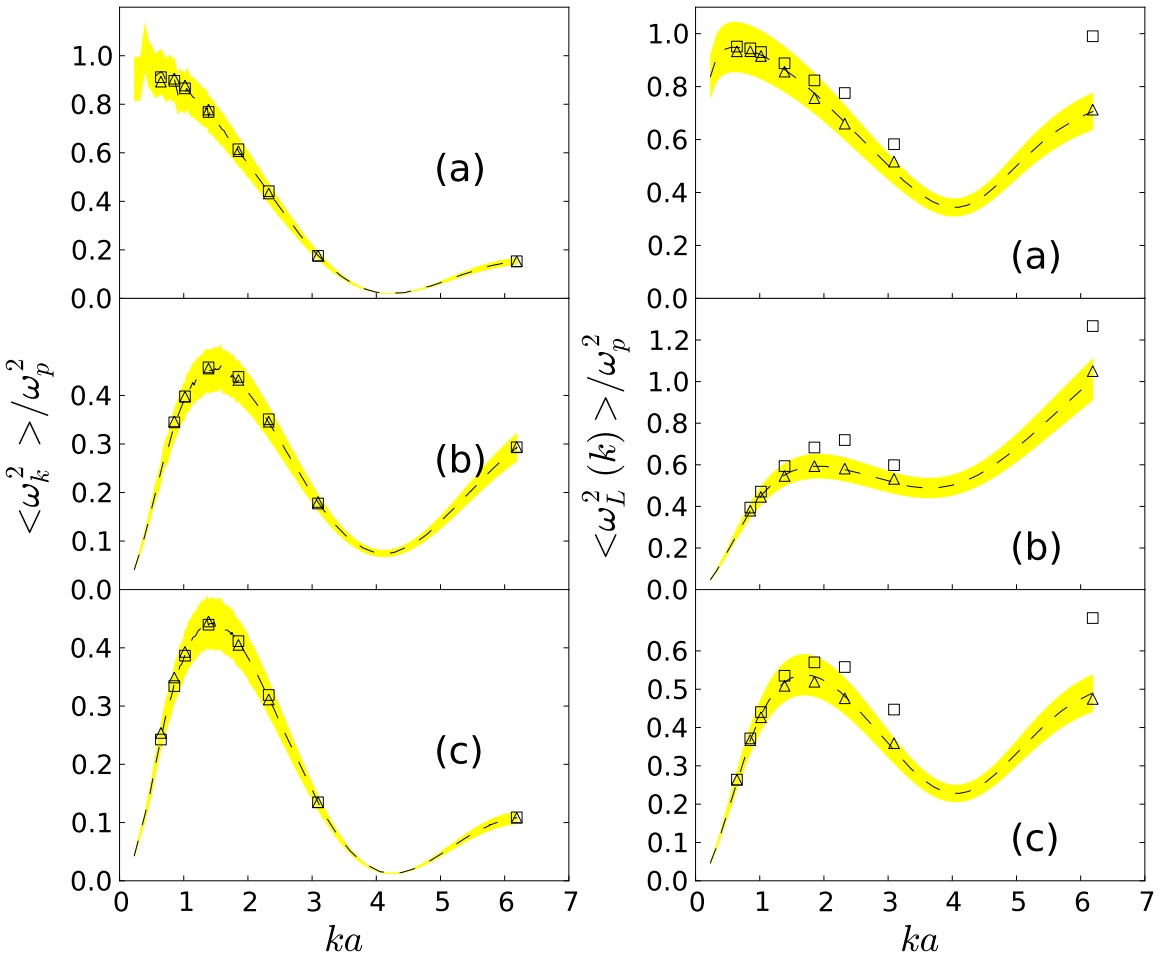

Figure 5.3: Comparison between the parameters $\langle\omega_k^2\rangle$ and $\langle\omega_L^2(k)\rangle$ as computed from MD using the formulas given in Appendix C (dashed line, with 10% error band), and the values obtained from the three-parameter fit of the Gaussian memory function model (triangles) and the viscoelastic model (squares) for three different plasma conditions. (a) $\Gamma = 120$, $\kappa = 0.1$, (b) $\Gamma = 50$, $\kappa = 1$, (c) $\Gamma = 175$, $\kappa = 1$.

5.9 Comparing the Gaussian memory function model to the MD data

In general, the Gaussian memory function model reproduces the MD DSF very well for all of the (Γ,κ) pairs considered (see Table 4.1), at all k values accessible to the simulations ($ka = 0.23 - 6.19$). This is shown in the complete MD results given in Appendix F; in this section, to supplement the discussion, only a selection of these complete results—at small, intermediate, and large k, respectively—are shown (Figures 5.4 - 5.6).

At small k values (Figure 5.4), for all (Γ,κ) pairs, the MD data shows a clear

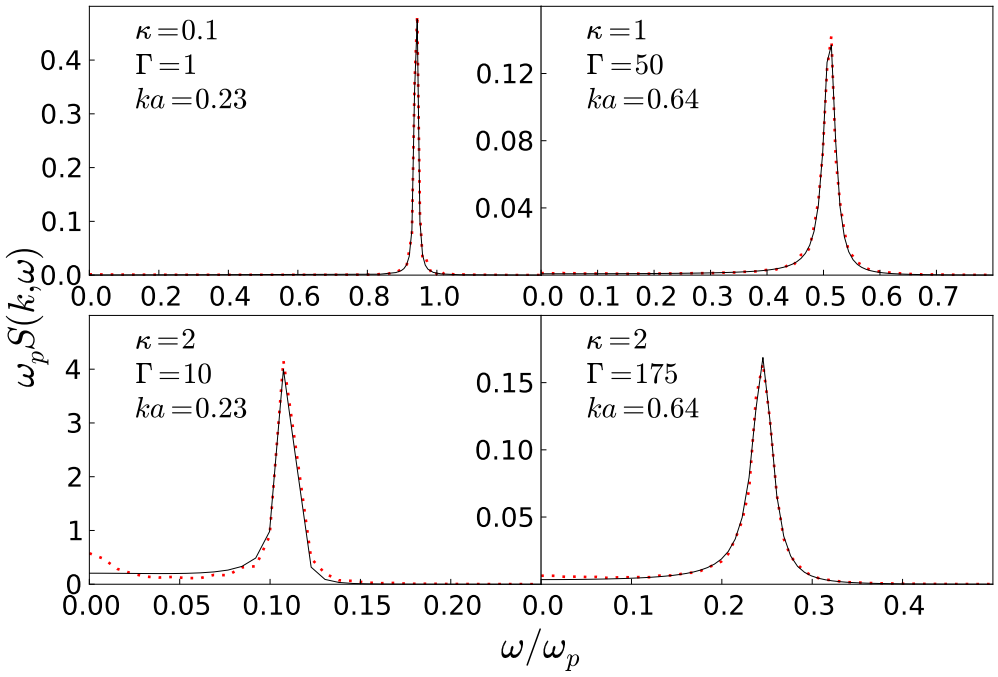

Figure 5.4: Comparison between the MD data for the DSF (dots) and the Gaussian memory function model with three fitting parameters (solid line) for small ka values.

ion-acoustic (or Brillouin) peak that represents a damped sound wave in the plasma (see Section 4.5). In this regime, the model extends the conventional hydrodynamic description to finite k values. Specifically, the generalised sound speed along with the imaginary part of $\phi(k,\omega)$ correct for the fact that the position of the peak does not vary linearly with k as in the hydrodynamic description, and the real part of $\phi(k,\omega)$ corrects for the width of the peak.

At intermediate k values (Figure 5.5), the model is seen to give a surprisingly accurate account of both the width and position of the ion acoustic peak. This is particularly true for $\Gamma \leq 50$. For higher Γ values, the MD DSF does in some cases show additional structure which the model cannot reproduce. In particular, for $\kappa = 0.1$ and 1, a two peak structure is visible for $ka = 2.32$ and a three peak structure for $ka = 3.09$ (e.g. Figure 5.5, top left). The small peak just below ω_p for $ka = 3.09$ is of particular interest—it does not appear to have been seen or commented upon in previous MD calculations.

The additional peak is certainly distinct from the higher harmonic peaks reported in a previous investigation of the DSF of the YOCP [Hartmann *et al.*, 2009]. In fact, at $\kappa = 0.1$ only, a second harmonic peak, at a frequency close to $2\omega_p$, can be seen in the MD DSF. This harmonic peak has been neglected in the analysis presented

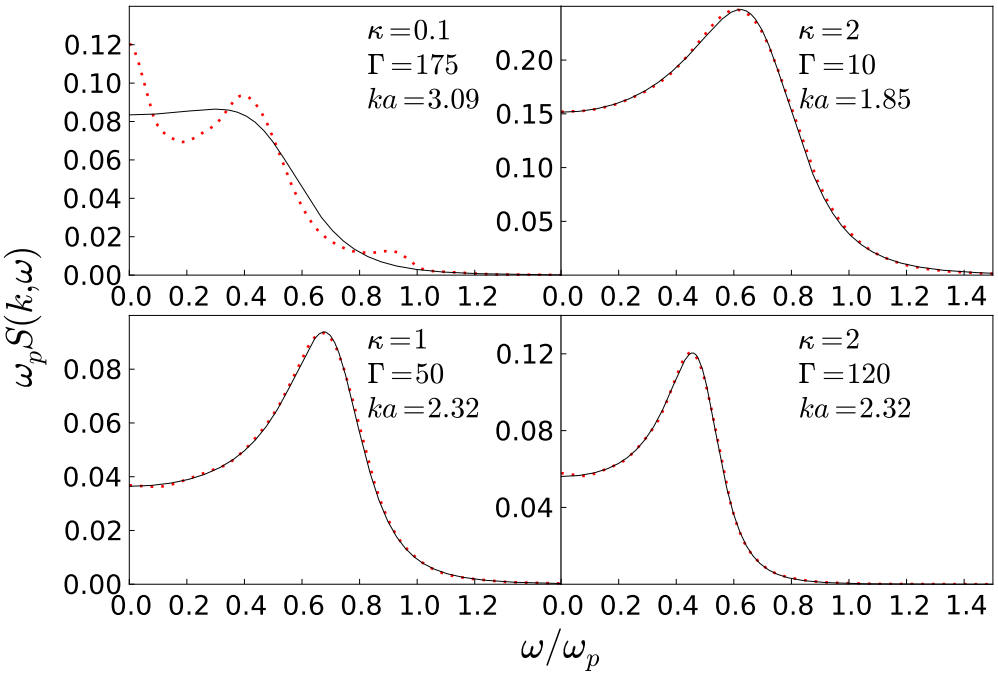

Figure 5.5: Comparison between the MD data for the DSF (dots) and the Gaussian memory function model with three fitting parameters (solid line) for intermediate ka values.

in this chapter, since it is found to be more than three orders of magnitude smaller than the main features in the DSF, in good agreement with [Hartmann *et al.*, 2009]. On the other hand, the peak shown in Figure 5.5 (top left) is of the same order of magnitude as the main features in the DSF. A possible explanation for this peak is that it appears as a result of microscopic 'caging' effects (e.g. [Balucani & Zoppi, 2002, Hansen & McDonald, 2006]). That is, at these length scales, the relatively high frequency oscillations of individual particles in the cages produced by their neighbors are imprinted on the DSF. Although the model does not fully capture the additional structure in the MD DSF for these particular conditions, on average it does still give a good account of the overall shape of the spectrum.

5.10 The ideal gas behaviour

At large k values (Figure 5.6), the DSF is seen to reduce to a single peak at $\omega = 0$. In this regime, the Gaussian model reproduces the MD data very accurately in all cases. As discussed in Section 2.4, as k continues to increase, the DSF should tend

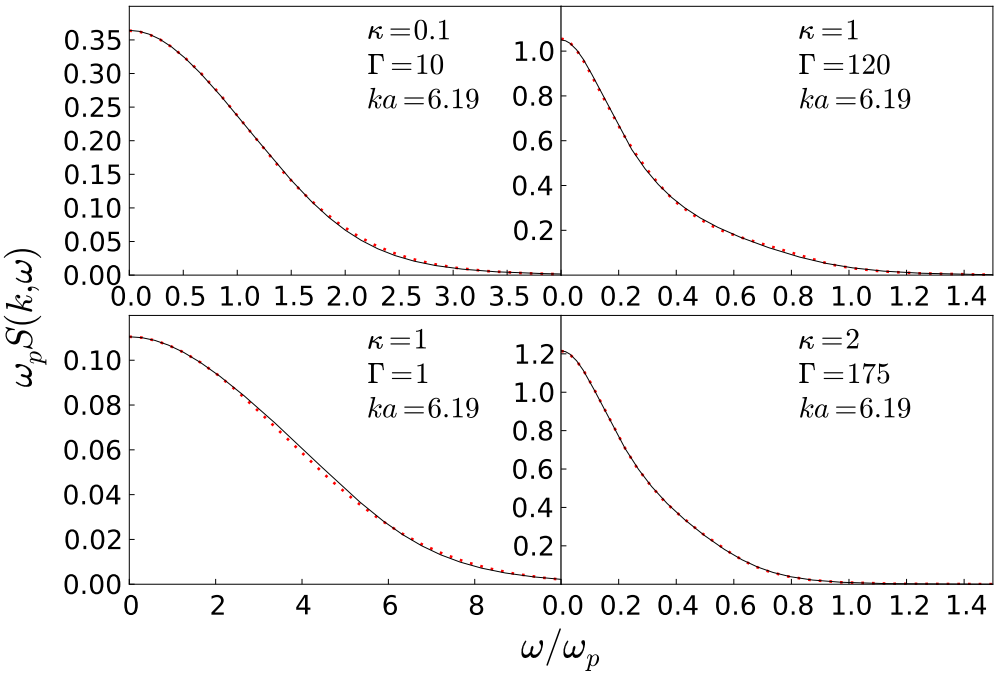

Figure 5.6: Comparison between the MD data for the DSF (dots) and the Gaussian memory function model with three fitting parameters (solid line) for large ka values.

to its ideal gas limit, $S^0(k,\omega)$, which is independent of κ:

$$S^0(k,\omega) = \left(\frac{m}{2\pi k_B T k^2}\right)^{1/2} \exp\left(-\frac{m\omega^2}{2k_B T k^2}\right) . \tag{5.22}$$

As shown in Figure 5.7, at constant κ, as Γ increases, the DSF converges more slowly towards $S^0(k,\omega)$. Indeed, at the highest k value considered in the MD simulations ($ka = 6.19$), the MD result only compares well to its ideal gas limit for $\Gamma \leq 10$ (see Figure 5.7). It is noted that the discrepancy between the MD DSF and its ideal gas limit can more readily be seen by looking at the MD data for the static structure factor $S(k)$; the ideal gas limit will only be approximated at k values for which $S(k) \approx 1$ (since $S^0(k) = 1$).

5.11 Hydrodynamic limit

In the previous investigations of the Gaussian model mentioned earlier (e.g., [Ailawadi *et al.*, 1971]), Equation (5.21) for the long wavelength behaviour of the relaxation time τ_k in the memory function was used to infer the kinematic viscosity. This equation is an expression of the fact that, in the hydrodynamic limit of $k \to 0$, the 'generalised

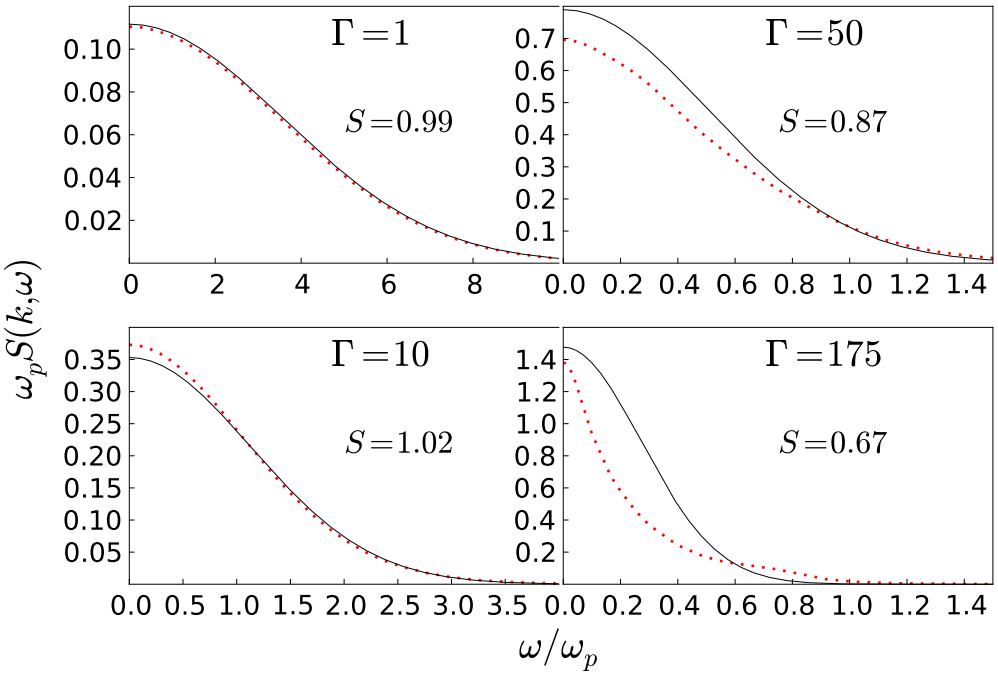

Figure 5.7: Comparison between the MD data for DSF for $\kappa = 1$ and $ka = 6.19$ (dots) and the ideal gas limit given by Equation (5.22) (solid line). Also shown on each panel is the value of the static structure factor $S(k)$ at $ka = 6.19$.

viscosity' reduces to the ordinary kinematic viscosity that appears in the conventional hydrodynamic description.

For the YOCP, since (as mentioned in Section 4.6) the bulk viscosity is in general negligible in comparison with the shear viscosity, the kinematic viscosity reduces to four thirds of the shear viscosity η (divided by mn), and therefore Equation (5.21) could in principle be used to estimate this important transport coefficient. However, due to the inaccuracy inherent in measuring the width of the (very narrow) ion acoustic peak in the DSF obtained from the MD simulations at small k values, the estimate for η obtained from this method is found to be considerably more uncertain than estimates obtained using other methods (i.e., it results in error bars of around an order of magnitude, rather than the $20-30\%$ quoted in [Donkó *et al.*, 2010, Saigo & Hamaguchi, 2002]). Therefore, it is concluded that, compared with these other approaches, this method is of little practical use for computing the viscosity of the YOCP. The alternative approaches—which are described in more detail in Chapter 8—include utilizing the Green-Kubo relation for the shear stress autocorrelation function [Saigo & Hamaguchi, 2002], non-equilibrium molecular dynamics methods [Donkó & Nyíri, 2000], and computation of the transverse current autocorrelation

function [Donkó *et al.*, 2010].

Along with the generalised viscosity, as discussed in Section 5.5, in the hydrodynamic limit $k \to 0$ the generalised sound speed $c_s(k) = \sqrt{\langle\omega_k^2\rangle/k^2}$ reduces to the normal isothermal sound speed $\tilde{c}_s$. Thus, the small k behaviour of the two generalised quantities—the viscosity and sound speed—ensure that using the Gaussian ansatz for the memory function in Equation (5.2) gives a result that is compatible with the result obtained from the linearised Naviér-Stokes equations [Hansen & McDonald, 2006] *when thermal fluctuations are neglected*. This neglect of thermal fluctuations is worth commenting upon. To be clear, Equation (5.2) is an entirely general (i.e., exact) representation of the DSF. Essentially, thermal fluctuations—both in the $k \to 0$ limit as well as 'generalised thermal fluctuations'—are neglected by assuming the Gaussian ansatz in Equation (5.3). This is why, in the case of the Gaussian ansatz, it is instructive to think of the memory function as a sort of generalised viscosity. There is no term in the memory function that represents the effects of thermal fluctuations.

It is straightforward to modify Equation (5.3) so that the result from the Naviér-Stokes equations including temperature fluctuations is recovered in the hydrodynamic limit (see e.g. [Ailawadi *et al.*, 1971, Boon & Yip, 1991]). The simplest extension involves maintaining a generalised sound speed and viscosity, and adding the (non-generalised) thermal conductivity contribution obtained from conventional hydrodynamics (the Naviér-Stokes equations) as an additional term in the memory function. In a more involved scheme, this additional contribution can also be generalised [Boon & Yip, 1991, de Schepper *et al.*, 1988].

For the YOCP with the (Γ,κ) pairs that are considered in this thesis, including the physics of thermal fluctuations in the memory function is unnecessary. This is because the ratio of specific heats, γ, is very close to 1, as indicated by the absence of a Rayleigh peak at $\omega = 0$ for small k in the MD data (see Figure 5.4 and also Section 4.6). The only cases in which this peak—which represents a diffusive thermal mode—is not negligible is for the more weakly coupled ($\Gamma \leq 10$) systems at $\kappa = 2$ (see Figure 5.4, bottom left). As expected, the model does not capture this peak in the MD data.

The fact that $\gamma \approx 1$ for the YOCP with the (Γ,κ) pairs considered here is certainly a reason why the Gaussian memory function works so well. Indeed, the ansatz in Equation (5.3) would not be expected to work as well when the ratio of specific heats γ is noticeably different from unity [Balucani & Zoppi, 2002]; this includes the YOCP for $\Gamma \ll 1$.

5.12 The viscoelastic model

Given the excellent agreement between the MD DSF and the Gaussian memory function model, it hardly seems necessary to undertake an exhaustive comparison with the numerous other forms of memory function proposed in the literature (for a fairly comprehensive review, see [Boon & Yip, 1991]). However, because it is very widely studied and used, one other ansatz for the memory function is worth briefly commenting on:

$$\begin{aligned} k^2\phi(k,t) &= k^2\phi(k,0)\exp(-t/\tau_k^V) \\ &= [\omega_L^2(k) - \langle\omega_k^2\rangle]\exp(-t/\tau_k^V)\,. \end{aligned} \tag{5.23}$$

When combined with Equation (5.2), the exponential decay of Equation (5.23)—which represents the simplest assumption that can be made about the time dependence of the memory function—is known as the viscoelastic model [Balucani & Zoppi, 2002].

As indicated in Figure 5.8 and discussed in detail elsewhere [Ailawadi *et al.*, 1971, Balucani & Zoppi, 2002, de Schepper *et al.*, 1988] (although not for the specific case of the YOCP), the viscoelastic model cannot capture the shape of the DSF across a large range of k values. While the model works well at small k—indeed, for the viscoelastic model the results of isothermal hydrodynamics are again recovered, with a relation between the relaxation time τ_k^V and the kinematic viscosity similar to Equation (5.21)—the model tends to predict rather more structure in the DSF than is evident in the MD data (Figure 5.8). Clearly then, the Gaussian memory function is vastly superior to the exponential one.

5.13 The relaxation time in the memory function

Figure 5.9 shows the relaxation time τ_k as determined from the fit of the Gaussian model to the MD DSF for $\kappa = 2$. As shown in Figure 5.9, as k increases, τ_k is found to decrease. This agrees qualitatively with, e.g., the behavior of the relaxation time determined for the Lennard-Jones fluid in previous investigations [Ailawadi *et al.*, 1971, Levesque *et al.*, 1973]. One certainly expects that at decreasing wave numbers, the relaxation time should increase: as $k \to 0$, the memory function should decay fast enough to guarantee the validity of the Markovian approximation, which itself is related to the fulfillment of the conservation laws [Balucani & Zoppi, 2002].

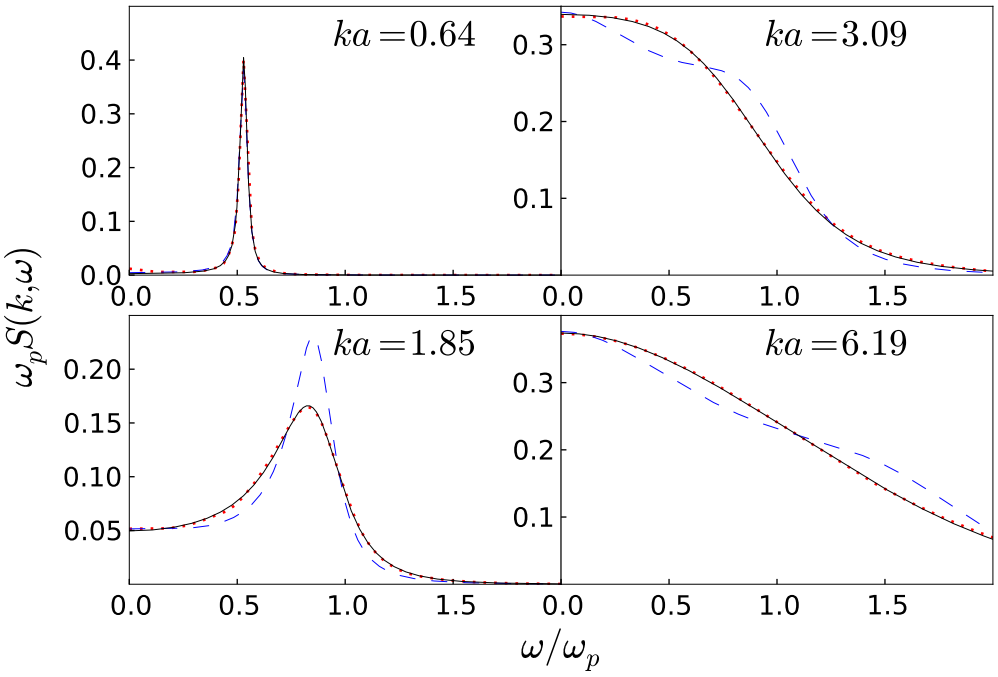

Figure 5.8: DSF for $\Gamma = 10$, $\kappa = 1$. The dots are the MD data, the dashed line is the viscoelastic model, and the solid line is the Gaussian model.

The precise details of the $k \to 0$ behaviour of τ_k are difficult to determine from the MD simulations. This is because, at the very smallest k values accessible to our simulations (specifically, below $ka = 0.64$, which is the minimum k value shown in Figure 5.9), the numerical value of τ_k is difficult to extract from the MD DSF reliably; it is found that the fitted value of τ_k at these small k values does not connect smoothly to the values at higher k values. The reason for this is that the DSF consists of a very sharp peak, for which it is difficult to accurately determine the parameters in the Gaussian model (this is the same reason that the kinematic viscosity is difficult to determine—cf. Section 5.11).

Physically, the relaxation time τ_k controls the nature of the dynamical behaviour of the system: on time scales $t \ll \tau_k$ the system responds 'elastically' (i.e. like a 'frozen' solid-like system), whereas on time scales $t \gg \tau_k$ the viscous mechanisms set in and reveal the inherent dynamic disorder [Balucani & Zoppi, 2002]. Therefore, the decrease in τ_k as k increases corresponds physically to the fact that at increasingly short length scales, viscous behavior is observed at increasingly short time scales.

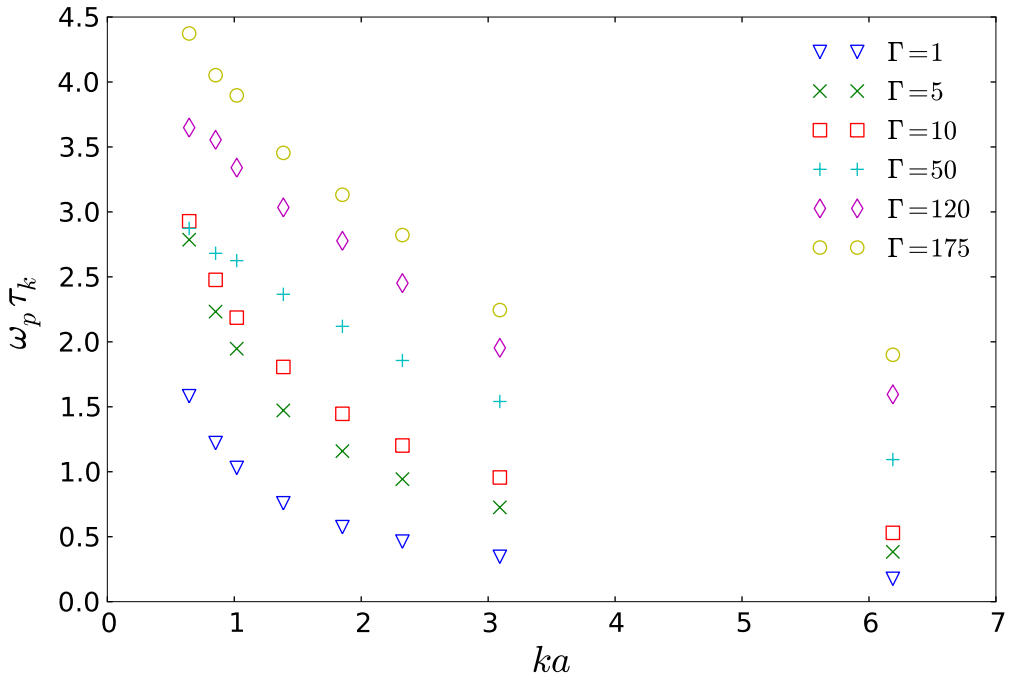

Figure 5.9: The relaxation time τ_k as determined from the fit of the Gaussian model to the MD DSF for $\kappa = 2$ and a range of values.

5.14 Applicability to x-ray scattering experiments

In the previous chapter it was shown that the conventional hydrodynamic description—i.e., Equation (5.1)—is valid providing $k < k_{max}$, where $k_{max}\lambda_s \simeq 0.43$. Thus experiments designed to measure the DSF at these small k values can in principle be used to determine transport coefficients (e.g., shear viscosity) and thermodynamic coefficients (e.g., compressibility) of non-ideal plasmas.

At k values larger than k_{max}, it has been shown in this chapter that the Gaussian memory function model extends the conventional hydrodynamic description very satisfactorily. Thus experiments for $k > k_{max}$ in principle measure the generalised quantities appearing in the memory function model of Equation (5.2).

While these results are certainly of interest to *future* x-ray scattering experiments, present experiments are mostly concerned with diagnosing the density and temperature of non-ideal plasmas [Glenzer & Redmer, 2009]. The usual procedure for this is to fit theoretical models for the DSF—taking density and temperature as the fitting parameters—to experimental measurements. For this task, ideally one would have an accurate equation for the DSF of a non-ideal plasma, with density and temperature as the only unknown parameters.

In the YOCP, the density and temperature are encoded in Γ and κ. Thus, fitting experimental data to the MD results for the DSF of the YOCP could yield a value of a (Γ,κ) pair only. The task is then to map this (Γ,κ) pair to the the density and temperature of a 'real' non-ideal plasma, which, as discussed in Section 1.5, is certainly not straightforward. However, one method for achieving this has been recently suggested [Murillo, 2010], and others are expected in the near future.

With this in mind, it is worth briefly looking qualitatively at how the DSF of the YOCP (as obtained from the MD simulations) changes with Γ and κ: this gives an indication of how the experimental scattering cross section should vary with density and temperature. By restricting this to the region of k values for which the DSF exhibits a clear ion-acoustic peak, its description reduces to the position, width and height of this peak. It can be expected that a given experiment will be able to determine these three properties at a specific wave number, which itself if governed by the scattering angle and x-ray wavelength (Equation (2.65)). The extraction of Γ and κ values could then be done by using these experimental results in conjunction with a set of three plots as shown in Figure 5.10.

Figure 5.10 shows how the position, width and height of the ion-acoustic peak as extracted from the MD simulations vary with reduced wave number ka for a number of (Γ,κ) pairs. As shown in the top left panel of Figure 5.10, the dependence on ka of the ion-acoustic peak position is almost identical for a large range of Γ values (i.e., $\Gamma = 50 - 175$). The peak width and height do show more discernible differences for these Γ values. At smaller Γ values (Γ = 1,5 and 10), the differences in the position, width and height of the peak are greater.

At constant Γ (right panels of Figure 5.10), the peak position is rather different for $\kappa = 0.1$, 1 and 2. In this case, the width and height are more similar, particularly for $\kappa = 0.1$ and $\kappa = 1$.

5.15 Conclusion and future outlook

The Gaussian memory function model of generalised hydrodynamics is an extremely good representation of the DSF of the YOCP for all of the (Γ,κ) pairs investigated in this chapter. This is true for small, intermediate, and large k values. The model very accurately reproduces the DSF obtained from MD simulations in terms of just 3 parameters and, as such, it is a economical way of accurately condensing or representing such data.

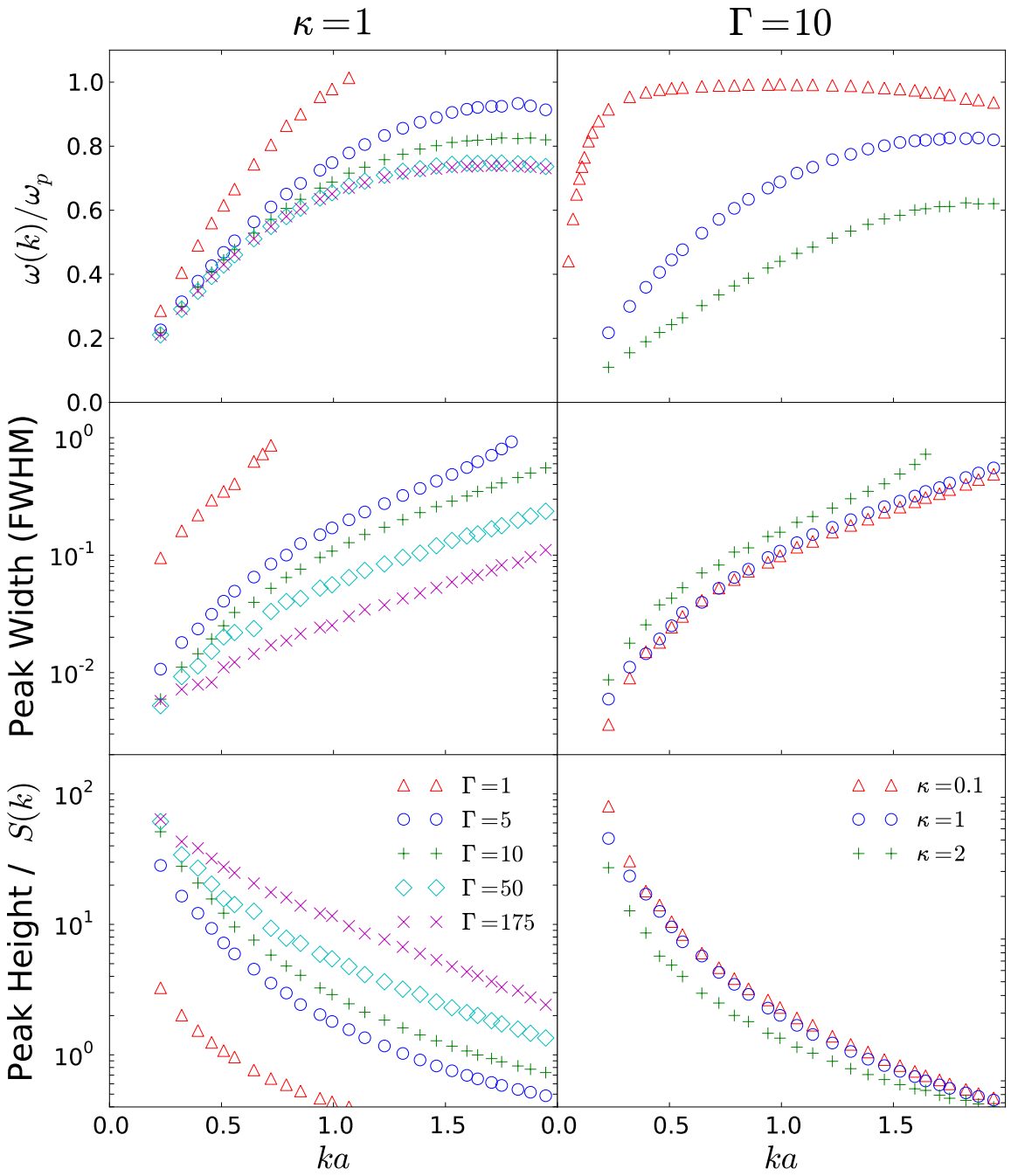

Figure 5.10: Variation of position $\omega(k)$, width (log scale) and height (log scale) of ion-acoustic peak with reduced wave number ka. The left panels are for $\kappa = 1$ and a range of Γ values, and the right panels are for $\Gamma = 10$ and a range of κ values.

Why exactly this approximation for the memory function should work so well is an interesting question that certainly merits further investigation. Other memory function models, such as the viscoelastic model (an exponential memory function) do

not compare well to the MD DSF for a wide range of k values. It is possible that the reason a faster decaying (compared to exponential) Gaussian works well is related to the chaotic nature of classical systems, which is reflected in the relatively short 'memory' of the system.

Since the YOCP is a simple representation of a non-ideal plasma, the results presented in this chapter are of use to future x-ray scattering experiments that will attempt to measure ion dynamics in 'real' non-ideal plasmas [Gregori & Gericke, 2009]. In particular, the MD results for the position, width and height of the ion-acoustic peak in the DSF could—when compared to experimental results—allow the thermodynamic conditions of non-ideal plasmas to be inferred.

Chapter 6

Hydrodynamic description of the OCP

6.1 The special case of the Coulomb potential

The hydrodynamic description given by the Naviér-Stokes equations, outlined in Chapter 4, is ubiquitous; in principle it applies to systems of particles with any interaction potential (that is, to all monatomic fluids). However, there is one important exception to this: the Coulomb potential.

In terms of the ions in a plasma, this exception is in some ways no surprise: it was shown in Chapter 4 that the hydrodynamic description never applies on length scales smaller than the screening length λ_s in the interaction potential, as quantified by the criterion $k_{max}\lambda_s \simeq 0.43$. For the Coulomb potential ($\lambda_s = \infty$, $\kappa = 0$), this criterion gives $k_{max} = 0$!

To be sure, the peculiarity of the Coulomb potential is very well known—in this case the longitudinal waves are not low-frequency sound (ion-acoustic) waves, as for $\kappa > 0$, but instead high-frequency plasma waves ($\omega \approx \omega_p$), even at $k = 0$. The resulting "plasmon" peak in the DSF, the position of which is illustrated in Figure 6.1 (red upward pointing triangles), is certainly not described by the low-frequency hydrodynamic equations that lead to the expression for the hydrodynamic DSF given in Equation (4.43); one can in fact wonder why hydrodynamics should describe plasma oscillations at all. Indeed, for the OCP system, the very existence of a hydrodynamic description is a known but unsolved problem [Baus & Hansen, 1980], and it is this problem that is investigated in the present chapter.

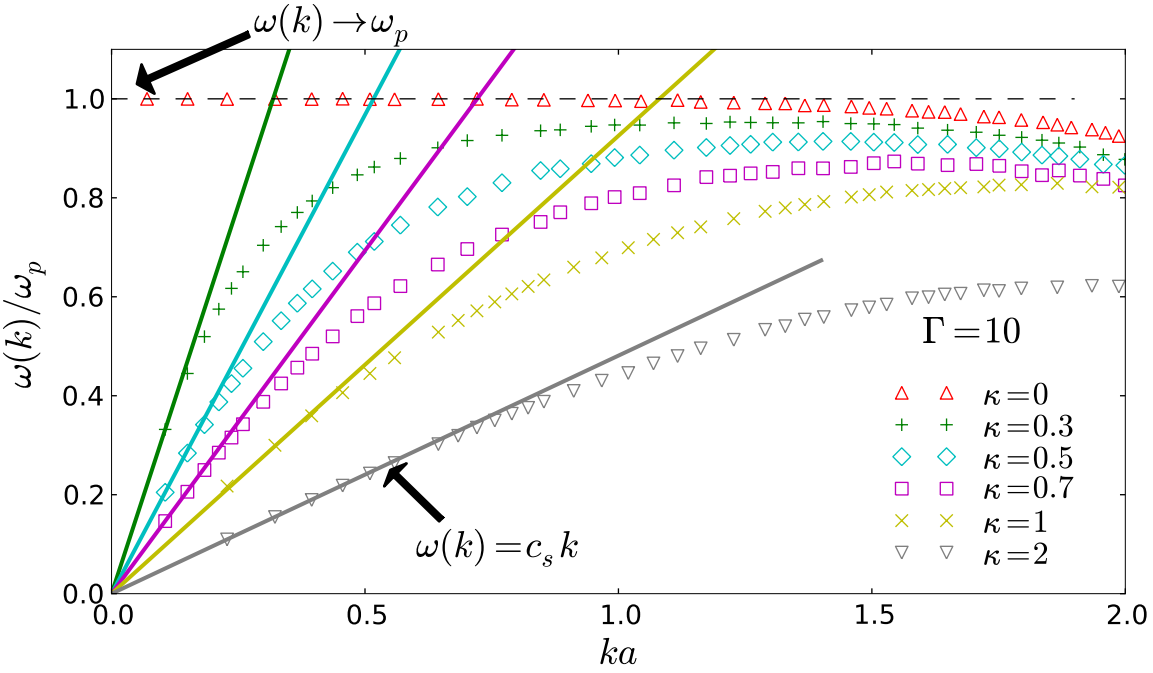

Figure 6.1: Peak position $\omega(k)/\omega_p$ as obtained from the MD DSF (symbols), along with the corresponding linear relations from the hydrodynamic description $\omega = c_s k$ (solid lines).

6.2 The hydrodynamic description of the OCP

A hydrodynamic description of the OCP was proposed in 1975 by Vieillefosse and Hansen [Vieillefosse & Hansen, 1975]. In this scheme, a term representing "electrical stresses" is added to the stress tensor appearing in the Naviér-Stokes equations (Equation (4.6)), which therefore becomes [Baus & Hansen, 1980]

$$\boldsymbol{\sigma}(\boldsymbol{r},t) = P(\boldsymbol{r},t)\mathbf{1} - \eta(\nabla \boldsymbol{v}(\boldsymbol{r},t) + \widetilde{\nabla}\boldsymbol{v}(\boldsymbol{r},t)) - (\zeta - \frac{2}{3}\eta)\mathbf{1}\nabla\cdot\boldsymbol{v}(\boldsymbol{r},t) + Ze n\phi(\boldsymbol{r},t)\mathbf{1}\,, \quad (6.1)$$

where the additional term $Ze n\phi(\boldsymbol{r},t)$ (which is not present in the stress tensor of a normal fluid, as given previously in Equation (4.6)) is related to the density by Poisson's equation. Since, in the Naviér-Stokes description, the stress tensor appears in the momentum balance equation only, the only modification relative to the case of a normal fluid is that this equation becomes

$$mn(\boldsymbol{r},t)\left[\frac{\partial \boldsymbol{v}(\boldsymbol{r},t)}{\partial t} + (\boldsymbol{v}(\boldsymbol{r},t)\cdot\nabla)\boldsymbol{v}(\boldsymbol{r},t)\right] = \\ -\nabla P(\boldsymbol{r},t) + \eta\nabla^2\boldsymbol{v}(\boldsymbol{r},t) + (\zeta + \frac{\eta}{3})\nabla\nabla\cdot\boldsymbol{v}(\boldsymbol{r},t) + nZe\boldsymbol{E}(\boldsymbol{r},t)\,, \quad (6.2)$$

where $\boldsymbol{E}(\boldsymbol{r},t) = -\nabla\phi(\boldsymbol{r},t)$. Linearising the new set of equations (the mass and energy balance equations given previously in Equations (4.1) and (4.3), and the new momentum balance equation in Equation (6.2)) and solving in the same way as outlined in Section 4.4 gives a result for the DSF [Vieillefosse & Hansen, 1975]. Here, the result obtained when the ratio of specific heats $\gamma = 1$ is given, which is

$$\frac{S^{HOCP}(k,\omega)}{S(k)/2\pi} = \frac{\sigma k^2}{(\omega + \omega_p(1+\frac{c_s^2k^2}{2\omega_p^2}))^2 + (\sigma k^2)^2} + \frac{\sigma k^2}{(\omega - \omega_p(1+\frac{c_s^2k^2}{2\omega_p^2}))^2 + (\sigma k^2)^2}\,. \quad (6.3)$$

The only way in which this result differs from the normal fluid case—Equation (4.43) with $\gamma = 1$—is that $c_s k$ is replaced with $\omega_p(1 + \frac{c_s^2k^2}{2\omega_p^2})$. Clearly this difference means that Equation (6.3) describes a plasma wave, rather than a sound wave. However, despite this necessary feature, it is not obvious that this equation is the 'correct' hydrodynamic description for the OCP, even at arbitrarily small k values. In the following sections, the intuitive and formal reasons for questioning the hydrodynamic description of the OCP are examined, and then Equation (6.3) is compared to the results of MD simulations for the DSF of the OCP in order to assess its applicability.

6.3 The insightful analysis of Baus and Hansen

Inclusion of the 'electrical stresses' in the Naviér-Stokes description, in the manner outlined in the previous section, does give a result—Equation (6.3)—for the DSF of the OCP that includes the essential plasmon peak ($\omega = \omega_p$ at $k = 0$). However, this phenomenological procedure was questioned by Baus and Hansen in their seminal review paper ([Baus & Hansen, 1980], Section 4.4):

> "Although this [adding the electrical stresses] is quite reasonable from a macroscopic point of view, the microscopic justification of this procedure is not straightforward."

Baus and Hansen went on to describe exactly why this is the case, with reference to a kinetic theoretical derivation of the hydrodynamic equations, which can be summarised briefly here (see [Baus & Hansen, 1980] and references therein for further details):

The usual method of deriving the hydrodynamic equations from kinetic equations is via the Chapman-Enskog expansion (see, e.g., [Ferziger & Kaper, 1972]). When proceeding with the Chapman-Enskog expansion of the appropriate kinetic equation, the mean field term is usually treated as a small perturbation since in the small-gradient

region of interest to hydrodynamics the kinetic equation is always dominated by the collision term. For the OCP, however, the mean field term cannot be considered to be small since its straightforward small-gradient expansion diverges with the characteristic Coulomb divergence.

Because of these considerations, Baus and Hansen argued that only when the 'collisionality' dominates the mean field, which they predicted would occur at sufficiently high coupling strength Γ, could a hydrodynamic description be expected for the OCP. In this case the hydrodynamic description is that given by Equation (6.3). This equation for the DSF is known to be inapplicable for small values of Γ (see the following section); exactly how large Γ has to be for it to be applicable was left as an open question until now. It is shown in Section 6.5 that in fact the hydrodynamic description of the OCP is not valid for any value of Γ.

6.4 Further analysis

Baus and Hansen [Baus & Hansen, 1980] based the arguments outlined in the previous section on an exact formula for the DSF of the OCP, derived using generalised kinetic theory, which at small k is given by[1]

$$\frac{S^B(k,\omega)}{S(k)/2\pi} = \frac{c_1 k^2/2}{(\omega + \omega_p(1+\frac{k^2}{2}c_2))^2 + (\frac{k^2}{2}c_1)^2} + \frac{c_1 k^2/2}{(\omega - \omega_p(1+\frac{k^2}{2}c_2))^2 + (\frac{k^2}{2}c_1)^2}\,, \quad (6.4)$$

where c_1 and c_2 are generalised coefficients with k and ω dependence (this k and ω dependence has been suppressed in the notation used here). Equation (6.4) is clearly of the same form as the hydrodynamic description of the OCP given in Equation (6.3); by setting c_1 and c_2 to their macroscopic counterparts, 2σ and c_s^2/ω_p^2, respectively, the two equations are identical. However, the point to make is that Equation (6.4) is exact, wheras the validity of Equation (6.3) is under question in this chapter.

If it were possible to calculate the coefficients c_1 and c_2 that appear in Equation (6.4) analytically, and if these were found to be equal to their macroscopic counterparts, then the conclusion would be that the hydrodynamic description of the OCP in Equation (6.3) is applicable. Likewise, if they were found not to be equal to their macroscopic counterparts, then the hydrodynamic description would be seen to be inapplicable. Unfortunately, it turns out that analytic calculation of c_1 and c_2 is only possible in the case of $\Gamma \to 0$; in this case, c_1 and c_2 are found to differ from their macroscopic counterparts [Baus & Hansen, 1980], and, therefore, the hydrodynamic

[1] Again, this is for the ratio of specific heats $\gamma = 1$. Equation (6.4) corresponds to Equation (4.35) in [Baus & Hansen, 1980], where $c_1 = \Gamma_p$ and $c_2 = \gamma_p$.

description of the OCP is formally seen to be inapplicable for small Γ. This conclusion supports the more phenomenological discussion given in the previous section: one would not expect a hydrodynamic description of the OCP to exist for small Γ.

In the general case (of arbitrary Γ), analytic calculation of c_1 and c_2 is not possible. According to the discussion given in the previous section, one might expect that, as Γ increases (and, intuitively, the system becomes more 'collisional'), these coefficients converge to their macroscopic counterparts, and therefore that the hydrodynamic description becomes valid beyond a certain value of Γ.

The approach taken in this chapter is to 'measure' c_1 and c_2 for a number of Γ values ($\Gamma = 1, 5, 10, 50, 120, 175$) using MD simulations, and compare them to their macroscopic counterparts. This was done by computing the DSF of the OCP with MD, as outlined in Chapter 3; the values of c_1 and c_2 at each Γ value can then be estimated from the width and position, respectively, of the plasmon peak in the DSF. A comparison of the width and position of the peak to their macroscopic counterparts, c_s^2/ω_p^2 and 2σ (which are known to a good degree of accuracy from previous investigations of the OCP) then allows the applicability of the hydrodynamic description to be assessed.

6.5 The inapplicability of the hydrodynamic description of the OCP

Figures 6.2 and 6.3 show the width and height of the plasmon peak—i.e., the measured values of the coefficients c_1 and c_2 in Equation (6.4), respectively—as obtained from MD, alongside their macroscopic counterparts appearing in the hydrodynamic description. The MD results were obtained by fitting Equation (6.4) to the MD DSF at the smallest value of k accessible to the simulations ($ka = 0.23$). This was found to produce a very accurate fit. The values for $\hat{\sigma}$ were obtained from the MD computations of Daligault [Daligault, 2006], which are accurate to within 30%[2], and the values for $(\hat{c_s})^2$ were obtained from the EOS given by Dewitt and Slattery [Dewitt & Slattery, 1999] (see also Section 4.6), which is accurate to within 1%.

As shown in Figures (6.2) and (6.3), when computed with MD, c_1 and c_2 do not agree at all with their macroscopic counterparts, even at the highest coupling strength of $\Gamma = 175$, which is close to the freezing point of the system. For example, the width of the plasmon peak, c_1, does not even follow the same trend predicted by

[2]As in the YOCP case, for $\gamma = 1$, determination of $\hat{\sigma}$ reduces to the determination of the shear viscosity η, since the bulk viscosity ζ of the OCP is negligible.

the hydrodynamic scaling 2σ at the higher Γ values: according to the hydrodynamic description, the width of the plasmon peak should increase with Γ at the higher Γ values, but the peak width obtained from MD decreases with Γ (see Figure 6.2). From the disagreement between c_1 and c_2 and their macroscopic counterparts, it can be concluded that the combination of mean field and collisional effects means that the hydrodynamic description à la Naviér-Stokes is not valid for the OCP at any coupling strength Γ.

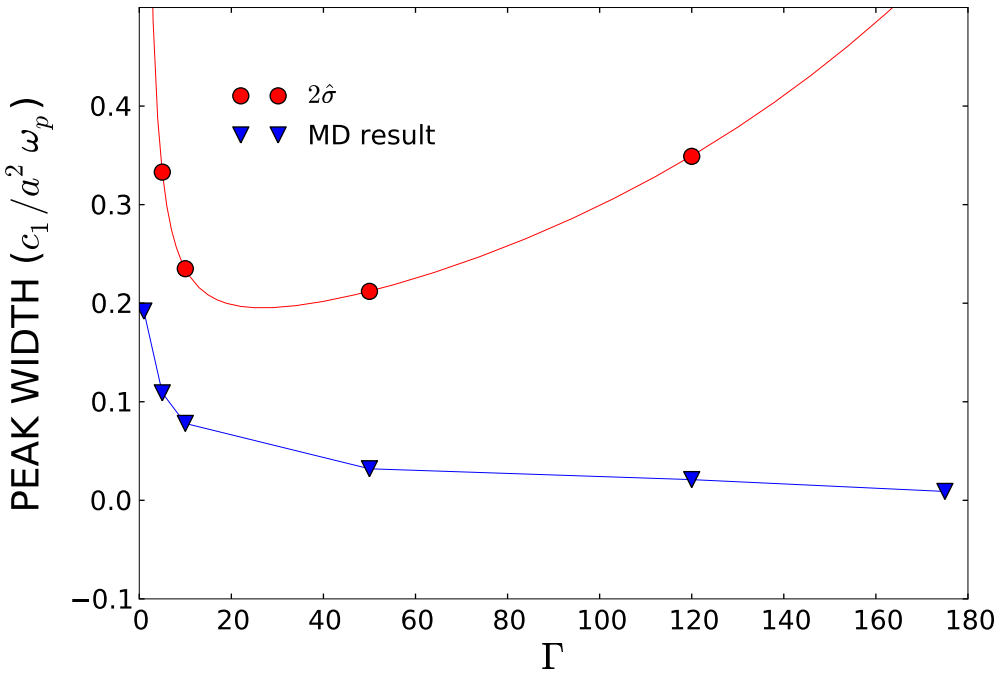

Figure 6.2: Peak width, i.e., the coefficient c_1, in reduced units. The MD result corresponds to the width of the plasmon peak obtained from the MD DSF (the data points are joined for visual clarity), and $2\hat{\sigma} = 2\sigma/a^2\omega_p$ is the prediction of the hydrodynamic description in Equation (4.43).

6.6 Conclusion and future outlook

In this chapter, it was shown that the conventional hydrodynamic description of the OCP is inapplicable. This conclusion was only possible because of the large-scale MD simulations that allowed the DSF of the OCP to be computed to high accuracy; at the time when the question tackled in this chapter was posed (1980), these simulations would not have been possible.

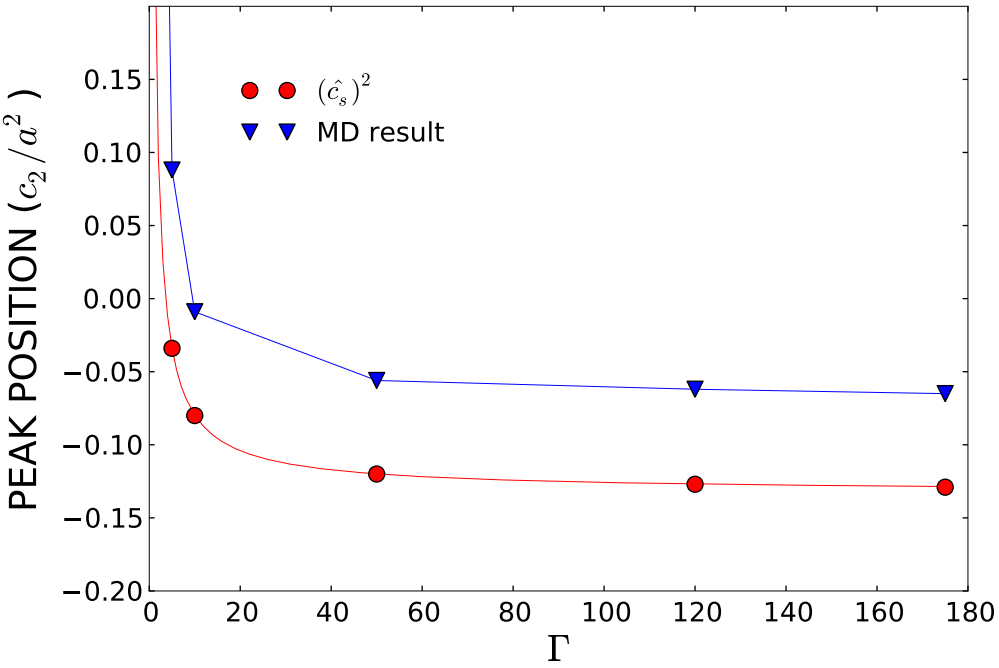

Figure 6.3: Peak position, i.e., the coefficient c_2, in reduced units. The MD result corresponds to the position of the plasmon peak obtained from the MD DSF (the data points are joined for visual clarity), and $(\hat{c_s})^2 = (c_s/a\omega_p)^2$ is the prediction of the hydrodynamic description in Equation (4.43).

Despite this conclusion, given that thermodynamic and transport coefficients such as isothermal compressibility, viscosity, etc. can be defined for the OCP in the fluid phase—and have indeed been calculated in numerous previous investigations [Bernu *et al.*, 1977, Daligault, 2006, Donkó & Nyíri, 2000, Vieillefosse & Hansen, 1975]—one might expect that some expression in terms of these quantities can describe the DSF of the OCP. Finding such a hydrodynamic description of the OCP is work for the future.

Chapter 7

Memory function and dynamic local field correction of the OCP

7.1 Motivation

The previous chapter gave an insight into the peculiarity of the OCP: due to the long range Coulomb interactions, the OCP exhibits certain dynamical features not shared by ordinary liquids. Most notable is the characteristic feature of plasmas: density imbalances lead to high frequency plasma oscillations, rather than low frequency sound waves. These high frequency plasma oscillations led Baus and Hansen to question the hydrodynamic description of the OCP [Baus & Hansen, 1980], which in the previous chapter was indeed shown to be inapplicable, even at large Γ values where the system is highly 'collisional'.

Other features of the OCP *are* shared by ordinary liquids. For example, it has been found that, for $\Gamma > 50$, the transport coefficients (self diffusion, viscosity, etc.) of the OCP obey universal laws satisfied by dense ordinary liquids [Daligault, 2006]. This is because, at these high coupling parameters, the well known physical mechanism of 'caging' [Donkó *et al.*, 2002, Hansen & McDonald, 2006]—which is ubiquitous in dense ordinary liquids—dominates the dynamics of the OCP. It is the fact that the OCP shares some, but not all, properties with ordinary liquids that makes it a challenging yet fascinating system to study.

In this chapter, the complementarity of the liquid and plasma descriptions of the OCP is explored by studying two approaches to modelling its dynamics: the memory function approach, and the dynamic local field correction (LFC) approach. Of the two, the memory function approach—as described in Chapter 5—is the one commonly used for ordinary fluids (i.e., it is the liquid description), and the LFC approach is

more common to Coulomb systems such as the electron gas (i.e., it is the plasma description). Largely due to the lack of 'exact' MD results to compare to theoretical models of the memory function and LFC, it is not clear which of these approaches is more effective. The purpose of the investigation presented in this chapter is to address this problem.

7.2 The two approaches

As discussed in Chapter 5, the memory function approach can be seen as a generalised hydrodynamics in which both the thermodynamic and transport coefficients that appear in the conventional hydrodynamic description are replaced by suitably defined wave number and frequency dependent quantities. In this approach, the DSF is written as in Equation (5.2), which is repeated here:

$$\frac{S(k,\omega)}{S(k)} = \frac{1}{\pi}\frac{\langle\omega_k^2\rangle k^2\phi'(k,\omega)}{[\omega^2 - \langle\omega_k^2\rangle - \omega k^2\phi''(k,\omega)]^2 + [\omega k^2\phi'(k,\omega)]^2}\,. \tag{7.1}$$

The wave number and frequency dependent memory function $\phi(k,\omega)$ appearing in this equation is the principal quantity of interest in the generalised hydrodynamic approach. In Chapter 5, the Gaussian memory function model was studied; this was found to offer an excellent description of the DSF of the YOCP.

The other approach to describing the DSF of the OCP is via another wave number and frequency dependent quantity, the so-called dynamic local field correction (LFC), denoted $G(k,\omega)$. As mentioned previously, this approach is more common to Coulomb systems, e.g., the quantum electron gas [Kugler, 1975]. The LFC is defined by its relation to the density response function of the system, $\chi(k,\omega)$, introduced in Section 2.6 [Ichimaru, 1982, 2004]:

$$\chi(k,\omega) = \frac{\chi^0(k,\omega)}{1 - v(k)[1 - G(k,\omega)]\chi^0(k,\omega)}\,. \tag{7.2}$$

Here $v(k) = (Ze)^2/\epsilon_0 k^2$ is the Fourier transform of the Coulomb potential and $\chi^0(k,\omega)$ is the density response function of the ideal gas, defined in Section 7.5. While the memory function is designed to extend the conventional hydrodynamic (Naviér-Stokes) equations to finite wave numbers, the LFC is designed to correct the deficiencies of the mean field approximation (i.e., the Vlasov equation for the single particle distribution function, which—as discussed in Section 2.6—describes the plasma oscillations but neglects any non-ideal or 'collisional' effects). That is, setting $G(k,\omega) = 0$ gives the mean field approximation for the density response function; this

gives a good description of the OCP dynamics in the weak coupling regime, $\Gamma \ll 1$, only. A non-zero $G(k,\omega)$ represents correlation effects beyond the mean field approximation. Models for the LFC have been proposed by Tanaka and Ichimaru [Ichimaru & Tanaka, 1986, Tanaka & Ichimaru, 1987] and by Hong and Kim [Hong & Kim, 1991], but these models have barely been tested other than for a very few conditions in the original studies.

The two approaches are related since they are both ways of describing of the many body physics of the OCP in equilibrium, i.e., the DSF. That is, since the density response function and DSF are related through the fluctuation-dissipation theorem,

$$S(k,\omega) = -\frac{k_B T}{\pi n \omega} \Im m\{\chi(k,\omega)\}\,, \tag{7.3}$$

the LFC $G(k,\omega)$ is clearly related to the memory function $\phi(k,\omega)$, albeit in a non-trivial way.

In this chapter, it is shown that the memory function is a simpler quantity to model than the LFC. That is, a basic model for the memory function—in fact, the same Gaussian model used for the YOCP in Chapter 5—can describe both mean field and collisional effects that are characteristic of the DSF of the OCP, wheras a LFC that achieves this is much more complicated.

7.3 Summary of the investigation

For this investigation, the intermediate scattering function and the DSF of the OCP was computed with MD for a wide range of coupling parameters in the fluid regime—$\Gamma = 0.3, 1, 5, 10, 50, 120, 160, 175$—as described in Chapter 3. The DSF was compared to the Gaussian memory function model, which was described previously in Chapter 5. From the intermediate scattering function, the LFC was computed. The MD LFC was compared to the existing models mentioned in the previous section. This analysis allowed the memory function and LFC approaches to be compared.

7.4 Memory function approach: model and comparison to MD

The same Gaussian model that was found to offer an excellent description of the DSF of the YOCP can also be used in the case of the OCP. Along with the fact that it was found to be an excellent representation of the DSF of the YOCP, a reason for considering the Gaussian model before any other is that it was previously applied

relatively successfully to the OCP in the pioneering work of Hansen et al. [Hansen *et al.*, 1975]. Because of the difficulty of conducting accurate MD simulations at that time, however, a detailed, conclusive comparison between the model and the MD data was not possible.

This detailed comparison was performed by following exactly the same method described in Section 5.8. The conclusions are found to be essentially the same as for the YOCP: the Gaussian memory function provides an excellent description of the DSF of the OCP across the entire fluid regime (for all $\Gamma \leq 175$), and for all wave numbers k. The complete results justifying this conclusion are shown in Figures F.1 and F.2 in Appendix F.

Before discussing these results, it is worthwhile commenting on the main difference between the OCP and normal fluids, from the perspective of the generalised hydrodynamic formalism. To be clear, Equation (7.1) is exactly the same for all fluids, be it OCP, YOCP, Lennard-Jones etc. However, only in the OCP case is the peak in the DSF a plasmon peak at $\omega \approx \omega_p$. This ubiquitous plasmon peak is ensured by the long wavelength (small k) behaviour of the $\langle \omega_k^2 \rangle$ term in the denominator of Equation (7.1); for the OCP, as $k \to 0$, $S(k) \to k^2/k_D^2$ [Baus & Hansen, 1980], where $k_D^2 = 1/\lambda_D^2 = 3\Gamma/a^2$, and hence $\langle \omega_k^2 \rangle \to \omega_p^2$. This small k behaviour of $S(k)$ is an essential distinction between OCP statics and those of an ordinary fluid: in the latter case, as described in Section 5.4, $S(k)$ approaches the isothermal compressibility of the fluid (i.e., a non-zero constant) in the limit $k \to 0$, which gives rise to a sound wave (rather than a plasma wave) at long wavelengths. To illustrate this point, Figure 7.1 shows the static structure factor of the OCP in the small k region, as obtained from MD; the vanishing of $S(k)$ with $k \to 0$ is seen to be in contrast with the behaviour for the YOCP (an 'ordinary' liquid), as expected.

The brief comparison of the Gaussian memory function model and the MD data that follows is made with reference to Figures F.1 and F.2 in Appendix F. From these figures, it can be seen that at sufficiently small k, the DSF of the OCP exhibits a sharp plasmon peak at $\omega \approx \omega_p$ for all coupling strengths Γ. As k increases, this plasmon peak broadens until, at high k, the DSF reduces to a single central peak at $\omega = 0$. The model accounts remarkably well for this entire evolution, particularly for $\Gamma \leq 50$ (Figure F.1). At higher values of Γ—as was the case for the YOCP (see Section 5.9)—the MD data does show some additional structure at intermediate k values ($ka = 2.32$ and 3.09) that the model cannot reproduce. Again, the small high frequency peak for $ka = 3.09$ does not appear to have been seen or commented upon in previous MD calculations, and can be expected to be caused by microscopic 'caging'

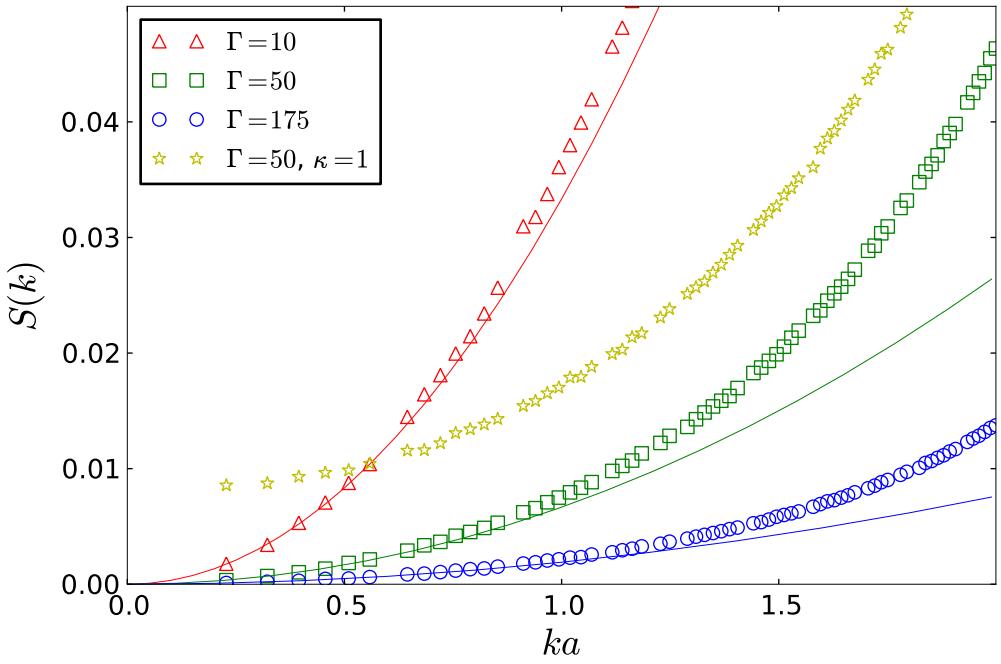

Figure 7.1: Static structure factor $S(k)$ of the OCP at small k values, for $\Gamma = 10$, 50 and 175. The open symbols are the MD results, and the corresponding solid lines show $(ka)^2/3\Gamma$ (the correct form for $S(k)$ of the OCP at vanishingly small k values). Also shown is $S(k)$ for the YOCP with $\Gamma = 50$, $\kappa = 1$. As explained in the text, the difference in the $k \to 0$ behaviour of $S(k)$ between the OCP and 'normal' liquids ensures that the generalised hydrodynamic description of Equation (7.1) describes a plasma wave in the case of the OCP, and a sound wave for normal liquids.

effects. In the OCP case, this deduction is supported by previous work showing that, for $\Gamma \geq 100$, a high frequency peak appears in the velocity autocorrelation function at $\simeq 0.9\omega_p$ [Daligault, 2006]; this is exactly the position of the additional peak in the DSF. As in the YOCP case, although the model does not fully capture the additional structure in the MD data for these conditions, on average it does give a good account of the overall shape of the spectrum. In conclusion then, the Gaussian model is an excellent representation of the DSF of the OCP across the entire fluid regime.

7.5 LFC approach: models

In the LFC approach, as given in Equation (7.2), the dynamics of the OCP are described with reference to the density response function of the ideal gas,

$$\chi^0(k,\omega) = -\frac{n}{k_B T} Z\left(\sqrt{\frac{m}{2k_B T}}\frac{\omega}{k}\right) , \tag{7.4}$$

where $Z(x) = (1 - 2xD(x)) + i\sqrt{\pi}x\exp(-x^2)$, and $D(x)$ is the Dawson function that was introduced in the formulation of the Gaussian memory function model (see Section 5.5).

As mentioned previously, setting $G(k,\omega) = 0$ gives the mean field approximation for the density response function; this only gives a good description of the OCP dynamics in the weak coupling regime $\Gamma \ll 1$. A non-zero $G(k,\omega)$ represents correlation effects beyond the mean field approximation.

One commonly used approximation is to replace the LFC by its $\omega = 0$ value, $G(k,0) \equiv G(k)$. This *static* local field correction $G(k)$ is related to the static structure factor $S(k)$ by

$$G(k) = 1 + \left[1 - \frac{1}{S(k)}\right] \frac{n}{k_B T} \frac{1}{v(k)} \,. \tag{7.5}$$

An alternative scheme is to replace the LFC by its high frequency limit,

$$G(k,\infty) \equiv G(k,\omega \to \infty) = 2I(k) \,. \tag{7.6}$$

Derivations of Equations (7.5) and (7.6), and an expression for $I(k)$ in terms of the radial distribution function $g(r)$ of the OCP, are given in Appendix G. Replacing $G(k,\omega)$ by either $G(k)$ or $G(k,\infty)$ represents a mean field approximation with an 'effective' potential[1]; it has been known for some time that this type of scheme gives only a marginal improvement over the conventional mean field approximation [Hansen *et al.*, 1975]. Thus, in order to describe well the dynamics of the OCP for $\Gamma \geq 1$, it is necessary to take collisions into account by having a frequency dependent LFC.

Two models for the LFC of the OCP feature most prominently in the literature. The model given by Tanaka and Ichimaru [Ichimaru, 2004], based on their viscoelastic formalism[2], interpolates between the known zero frequency and high frequency limits given in Equations (7.5) and (7.6):

$$G(k,\omega) = \frac{G(k) - i\omega\tau_M(k)G(k,\infty)}{1 - i\omega\tau_M(k)} \,. \tag{7.7}$$

In their prescription for computing the relaxation time $\tau_M(k)$, Tanaka and Ichimaru considered either a Gaussian or Lorentzian ansatz [Ichimaru & Tanaka, 1986, Tanaka

[1] The 'effective' potential is the interaction potential whose spatial Fourier transform is $v(k)[1 - G(k)]$, or $v(k)[1 - G(k,\infty)]$, respectively.

[2] Despite being based on the Naviér-Stokes equations with the standard viscoelastic stress-strain relation (see [Tanaka & Ichimaru, 1987]), it should be noted that the model of Tanaka and Ichimaru is not the same as the standard viscoelastic model of generalised hydrodynamics given in Section 5.12. This is due to a number of 'phenomenological' modifications that are required to obtain Equation (7.7) (see [Tanaka & Ichimaru, 1987] for further details).

& Ichimaru, 1987]. In both of these cases, they used a kinetic equation to relate the shear viscosity to the LFC; the unknown parameter appearing in $\tau_M(k)$ was then chosen such that the estimates of the shear viscosity available from MD at the time were matched as closely as possible (see [Tanaka & Ichimaru, 1987] for further details).

The other model, developed by Hong and Kim [Hong & Kim, 1991], generates successive approximations for the LFC. The first order approximation is simply to replace $G(k,\omega)$ by $G(k)$. The second order approximation is

$$G(k,\omega) = G(k) - \frac{1}{2}[G(k) - G(k,\infty)]Q\left(\sqrt{\frac{m}{2k_BT}}\frac{\omega}{k}\right), \tag{7.8}$$

where $Q(x) = 1/Z(x) + 2x^2 - 1$. Because $Q(0) = 0$ and $Q(x \to \infty) = 2$, like the model of Tanaka and Ichimaru the Hong Kim model gives the correct zero and high frequency limits for the LFC. The third order approximation involves the sixth moment of the DSF, $\langle\omega^6\rangle$; since this is difficult to compute theoretically, in the cases where the third order approximation was considered by Hong and Kim, $\langle\omega^6\rangle$ was treated as an adjustable parameter [Hong & Kim, 1991].

7.6 LFC approach: computing the LFC with MD

In the MD simulations, the intermediate scattering function, $F(k,t)$, is calculated at discrete times separated by $0.1\omega_p^{-1}$ (see Chapter 3). From the intermediate scattering function, the response function can be calculated in the time domain:

$$\chi(k,t) = \begin{cases} 0 & \text{if } t < 0 \\ -\frac{n}{2k_BT}\frac{dF(k,t)}{dt} & \text{if } t \geq 0 \end{cases} \tag{7.9}$$

Comparison with Equation (7.3) shows that this is simply the fluctuation dissipation theorem in the temporal domain (see also [Johnson, 1975]). The response function in the frequency domain, $\chi(k,\omega)$, can then be approximated numerically by taking the discrete Fourier transform of $\chi(k,t)$. Finally, using Equation (7.2) gives the MD result for the LFC.

The results obtained for the LFC by this procedure were found to be less accurate and more noisy than those for the DSF. This is despite the fact that both $S(k,\omega)$ and $G(k,\omega)$ are derived from the same MD data for $F(k,t)$. In particular, difficulties were encountered in obtaining accurately the precise way in which the imaginary part of $G(k,\omega)$ decays to zero and the real part decays to its high frequency limit $G(k,\infty)$. The explanation of this is related to the way in which $G(k,\omega)$ is defined in Equation 7.2: as ω increases, both $\chi^0(k,\omega)$ and $\chi(k,\omega)$ decay to zero, and the

accurate measurement of $\chi(k,\omega)$ with MD is difficult when this quantity is negligibly small. Accordingly, in some cases, the MD result for the $\omega \to \infty$ behaviour of the LFC (obtained using the above procedure) could not be reconciled with the known high frequency limit of Equation (7.6); for these cases, only the MD result at smaller ω values is reliable (these are the values of ω for which the value of the DSF, shown in Figures F.1 and F.2, is non-negligible). Despite these difficulties, the data for the LFC was found to be good enough for a qualitative—if not quantitative—comparison with the models of Tanaka and Ichimaru and Hong and Kim outlined above.

7.7 LFC approach: comparing to MD

Figures 7.2, 7.3 and 7.4 show the MD results for the LFC at $\Gamma = 10, 50, 120$ and 160 for small, intermediate and large k respectively ($ka = 1.02, 3.09$ and 6.19). In each of these figures, the model of Hong and Kim, Equation (7.8), is also shown. Since the relaxation time $\tau_M(k)$ appearing in the model of Tanaka and Ichimaru (Equation (7.7)) was only given explicitly for $\Gamma = 160$ (see [Ichimaru & Tanaka, 1986, Tanaka & Ichimaru, 1987]), their model—with both the Gaussian and the Lorentzian approximation for the relaxation time—is shown for this coupling strength only[3].

At the small k value ($ka = 1.02$, Figure 7.2), for all coupling strengths the model of Hong and Kim departs from $G(k)$ and decays to its high frequency limit $G(k,\infty)$ much faster than the MD data. At these long wavelengths (small k), the OCP dynamics occur close to $\omega = \omega_p$; the LFC serves to describe the "collisional broadening" of the plasmon peak neglected in the mean field approximation. Therefore, the value of $G(k,\omega)$ should only be important for ω close to ω_p. At the highest coupling strength of $\Gamma = 160$, the model of Tanaka and Ichimaru matches the MD data reasonably well for either a Gaussian or Lorentzian relaxation time. A reasonable estimate of the width of the plasmon peak is obtained, as noted previously [Ichimaru & Tanaka, 1986, Tanaka & Ichimaru, 1987].

At the intermediate k value ($ka = 3.09$, Figure 7.3), $G(k,\omega)$ shows rather more structure than at $ka = 1.02$, particularly at the largest coupling strengths of $\Gamma = 120$ and 160. At these coupling strengths, the sharp variation of both the real and imaginary parts of $G(k,\omega)$ around $\omega = \omega_p$ accounts for the high frequency peak in the DSF, discussed in Section 7.4. Again, for all Γ, the model of Hong and Kim departs from $G(k)$ and decays to its high frequency limit $G(k,\infty)$ much faster than the MD

[3] In [Ichimaru & Tanaka, 1986, Tanaka & Ichimaru, 1987], the Gaussian approximation is referred to as "scheme I", and the Lorentzian as "scheme II".

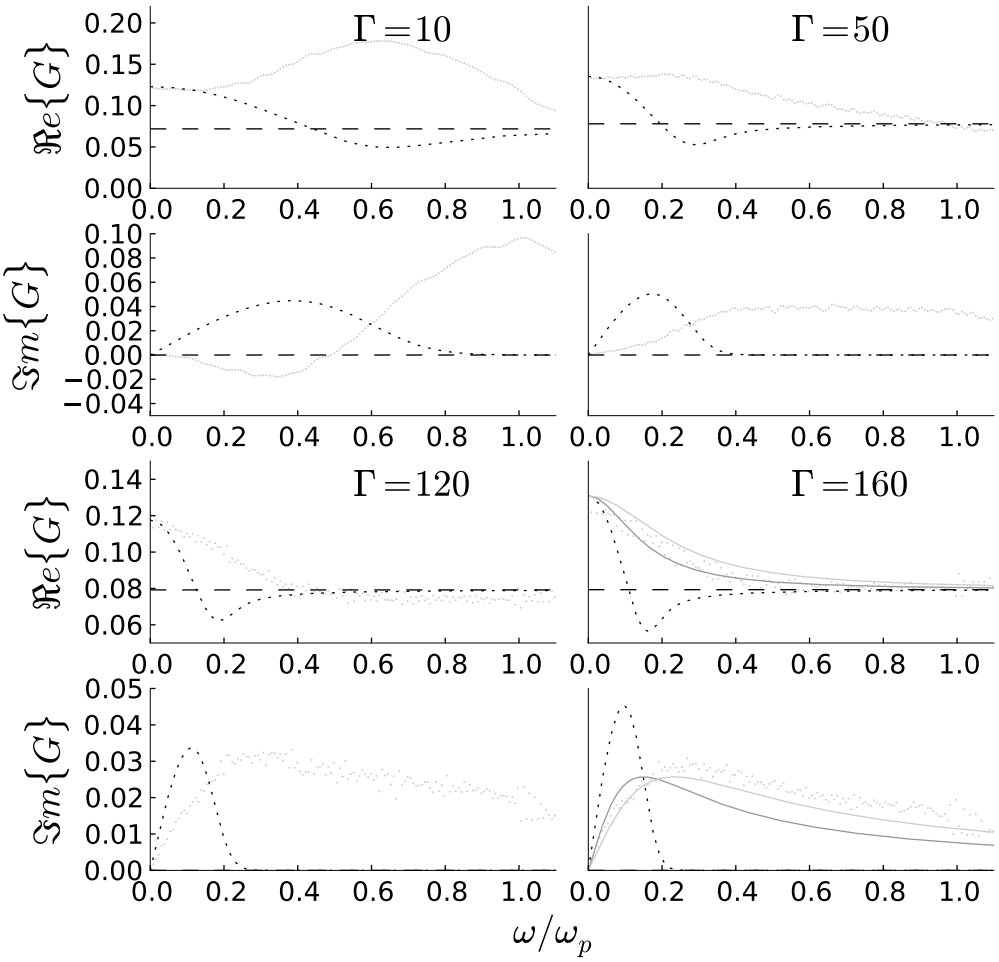

Figure 7.2: Real and imaginary parts of the LFC $G(k, \omega)$, as computed from MD, at $ka = 1.02$ (red dots). Also shown is the model of Hong and Kim, as given in Equation (7.8) (dotted line). For $\Gamma = 160$, the model of Tanaka and Ichimaru is shown for the relaxation time $\tau_M(k)$ in both the Gaussian approximation (light grey line) and the Lorentzian approximation (dark grey line). The dashed lines ($\Re e\{G\}$ only) show $G(k, \infty)$, as obtained from Equation (7.6), evaluated using the radial distribution function $g(r)$ from MD (see also Appendix G).

data does. Furthermore, at $\Gamma = 160$, the model of Tanaka and Ichimaru cannot capture the considerable structure in $G(k, \omega)$. At the large k value ($ka = 6.19$—Figure 7.4), again none of the models seem to give a good description of $G(k, \omega)$.

Finally, in order to illustrate the effects of the LFC on the DSF—which is usually the main quantity of interest—the models are compared to the DSF from MD (cf. Equation 7.3) for both the intermediate k value (Figure 7.5) and large k value (Figure 7.6). As shown in Figure 7.5, the discrepancies at the intermediate k value between the models and MD data that are evident in the LFC (Figure 7.3) are even more

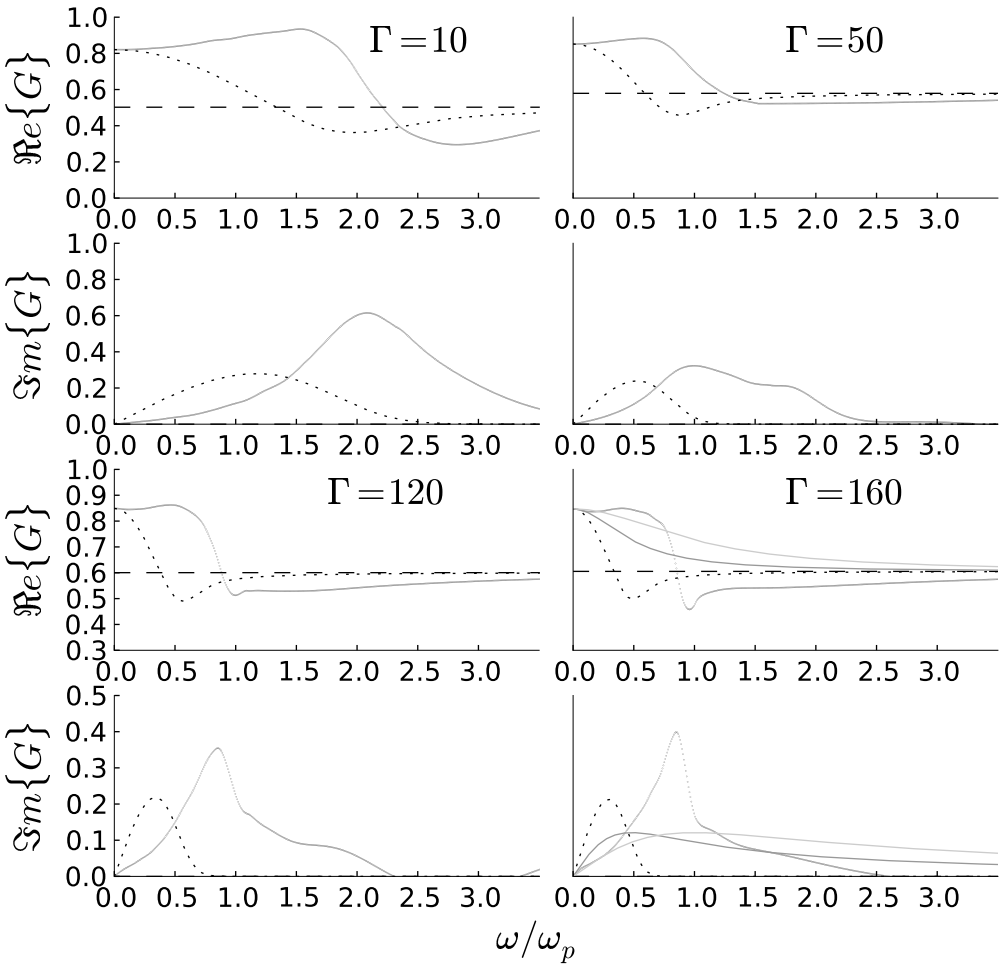

Figure 7.3: Same as Figure 7.2 but for $ka = 3.09$.

pronounced in the DSF. At the large k value, as shown in Figure 7.6, the model of Hong and Kim does give a reasonable qualitative description of the MD DSF, although the additional peak at $\omega \approx \omega_p$ for $\Gamma = 120$ and $\Gamma = 160$ suggests that the model overemphasizes collective effects in this regime.

7.8 Conclusion and future outlook

In this chapter, two approaches to describing the dynamics of the OCP were investigated: the memory function approach, which is a standard approach for normal liquids, and the dynamic local field correction (LFC) approach, which is more akin to plasma physics. The investigation was centered around the MD simulations for the intermediate scattering function, $F(k,t)$, of the OCP. The accuracy of the MD data allowed for computation of not only the DSF, but also the LFC, $G(k,\omega)$, which

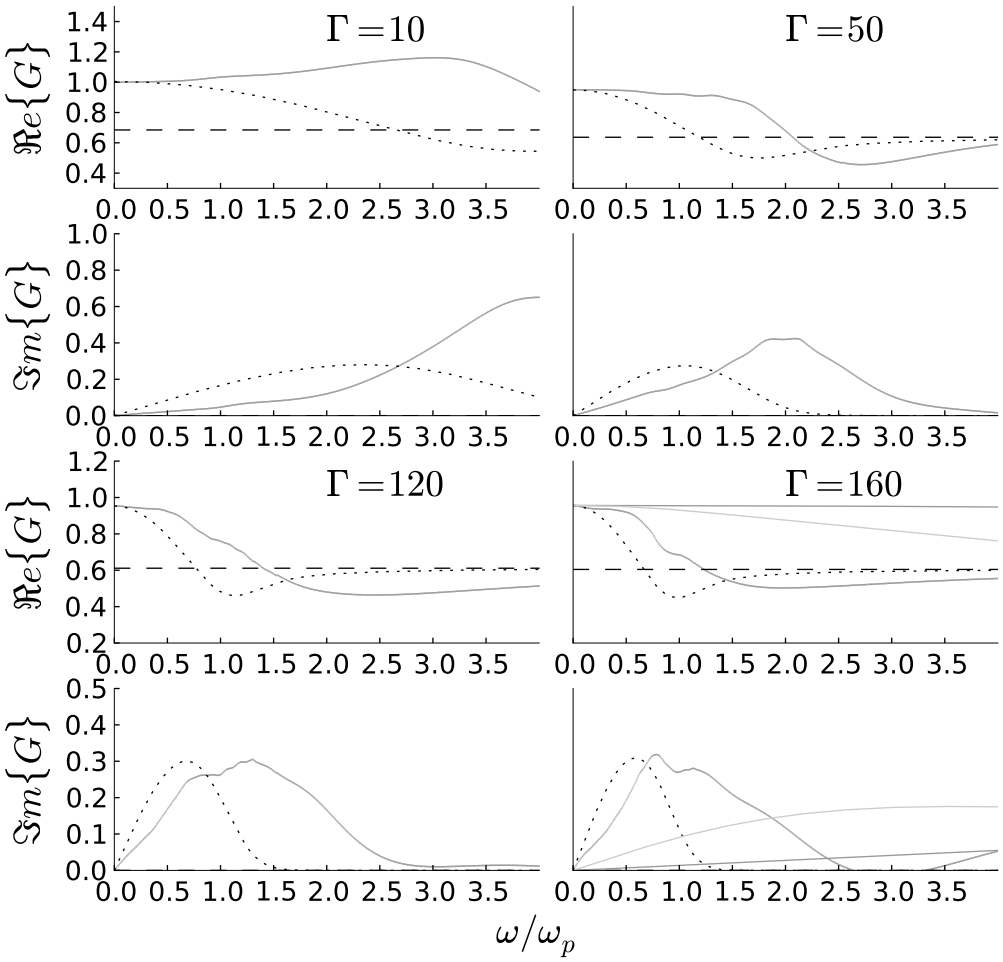

Figure 7.4: Same as Figure 7.2 but for $ka = 6.19$.

apparently has not been computed with MD prior to this investigation.

The conclusion of this chapter is that the memory function of the OCP is rather more simple to model than the LFC: while the memory function is very well reproduced by a Gaussian for all coupling strengths Γ and wave numbers k, the LFC has considerably more structure. Indeed, the more complex structure of the LFC is the reason why current models—those of Tanaka and Ichimaru [Ichimaru & Tanaka, 1986, Tanaka & Ichimaru, 1987] and Hong and Kim [Hong & Kim, 1991]—do not offer a good description for a wide range of conditions.

Future investigations of the LFC may be able to compute this tricky quantity with increased accuracy. This would allow the details of the LFC to be analysed quantitatively, which could elucidate hitherto unknown features OCP dynamics. In the meantime, it is hoped that the MD results presented in this chapter will find application among practitioners in the field of strongly coupled Coulomb systems.

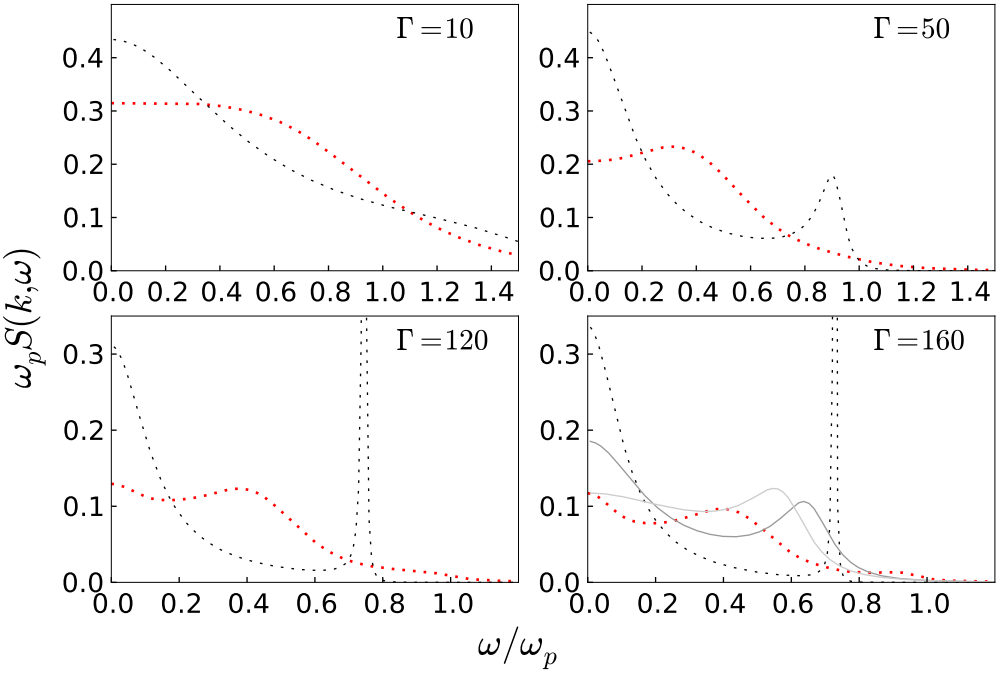

Figure 7.5: DSF from MD (red dots) compared with the models of Hong and Kim (dashed line), and Tanaka and Ichimaru with the relaxation time $\tau_M(k)$ in both the Gaussian approximation (light grey line) and the Lorentzian approximation (dark grey line) at $ka = 3.09$.

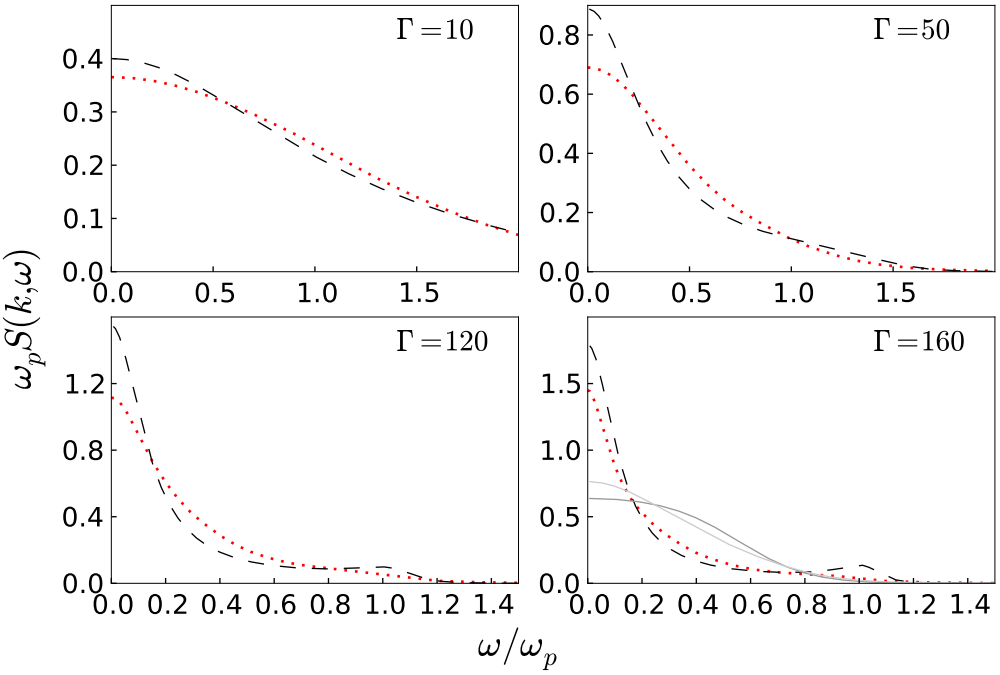

Figure 7.6: Same as Figure 7.5 but for $ka = 6.19$.

Chapter 8

Computing the shear viscosity of the YOCP

8.1 Motivation

The investigations presented in Chapters 4-7 have all in some way involved the thermodynamic and transport coefficients of the YOCP or OCP. These are thus clearly important quantities, and therefore the question of how exactly they can be determined is certainly of general interest.

The way in which the thermodynamic coefficients can be determined has already been outlined in Section 4.6 (see also Appendix D). Therefore, this chapter is devoted solely to transport coefficients. In particular, it is devoted to a discussion of how a particular transport coefficient—the shear viscosity η (henceforth also simply viscosity)—can be determined. The viscosity serves as a prototypical transport coefficient; the methods presented in this chapter have much in common with those for determining other transport coefficients, although of course the details differ.

This chapter is not an exhaustive description of the numerous methods by which the viscosity of the YOCP or OCP can be determined. Rather, two methods for determining the viscosity are presented: the "Green-Kubo method" and the "hydrodynamic method". Both are based on computing the equilibrium dynamics with MD simulations. Of the two methods, the Green-Kubo method has been widely used, for the YOCP, OCP and indeed many other systems (for the YOCP, see [Donkó *et al.*, 2010, Saigo & Hamaguchi, 2002, Salin & Caillol, 2003], for the OCP, [Bernu & Vieillefosse, 1978, Bernu *et al.*, 1977, Daligault, 2006], and for some examples of other systems, [Erpenbeck, 1988, Gonzalez & Abascal, 2010, Ryckaert *et al.*, 1989]), but the hydrodynamic method has been used relatively little (examples are [Balucani *et al.*,

2000, Palmer, 1994]), and apparently has never been used for either the YOCP or the OCP. The aim of this chapter—aside from giving an idea of how transport coefficients can be determined—is to investigate the feasibility of this alternative method in the YOCP case. To accomplish this, both methods are applied to the YOCP, and the results for the viscosity are compared. The results illustrate that the hydrodynamic method for computing the shear viscosity is indeed feasible and therefore complements the more widely used Green-Kubo method.

8.2 Summary of the investigation

For this investigation, the shear stress autocorrelation function, $H(t)$, and the transverse current correlation function, $C_t(k,t)$, defined in Sections 8.3 and 8.4, respectively, were computed with MD for the YOCP with $\kappa = 2$, for coupling parameters $\Gamma = 1$, 5, 10, 50, 120 and 175. This allowed the viscosity to be computed by both the "Green-Kubo method" (using the MD results for $H(t)$) and the "hydrodynamic method" (using the MD results for $C_t(k,t)$). Comparison of these results allowed the feasibility of the hydrodynamic method to be assessed.

8.3 Green-Kubo method

A standard way to compute the viscosity of a fluid is to use the following relation in which the viscosity η is expressed in terms of the time integral of the shear stress autocorrelation function $H(t)$ [Balucani & Zoppi, 2002]:

$$\eta = \int_0^\infty H(t)dt = \frac{1}{k_B T V} \int_0^\infty \langle \sigma^{zx}(0)\sigma^{zx}(t)\rangle dt \,. \tag{8.1}$$

In this Equation, V is the volume of the system (in an MD simulation, it is the volume of the simulation box), and the brackets $\langle \ldots \rangle$ denote the usual ensemble average. The shear stress autocorrelation function is given in terms of the zx component of the microscopic stress tensor,

$$\sigma^{zx}(t) = \sum_{i=1}^{N} \left[m v_{i,z} v_{i,x} - \frac{1}{2} \sum_{j=1 \neq i}^{N} (z_{ij} x_{ij}/r_{ij}) v'(r_{ij}) \right] . \tag{8.2}$$

Here m is the particle mass, $v_{i,z}$ is the z component of velocity of particle i at time t, $x_{ij} = |x_i - x_j|$, $z_{ij} = |z_i - z_j|$ and $v'(r_{ij})$ is the first derivative of the interaction potential with respect to r evaluated at $r_{ij} = |\boldsymbol{r}_i - \boldsymbol{r}_j|$. Equation (8.1) is a particular example of a so-called Green-Kubo relation, in which a transport coefficient of a

fluid is expressed in terms of the time integral of a time dependent correlation function (other similar expressions exist for the other transport coefficients, the thermal conductivity and bulk viscosity [Balucani & Zoppi, 2002]).

To implement this method with MD, σ^{zx} is first computed at each timestep using the positions and velocities of the particles. Replacing the ensemble average in Equation (8.1) by a time average in the normal way (see Section 3.11) then allows the shear stress autocorrelation function $H(t)$ to be computed. Finally, the time integral of $H(t)$ gives the viscosity η, as in Equation (8.1).

As mentioned previously, this method been used in other investigations to determine the viscosity of the YOCP [Saigo & Hamaguchi, 2002, Salin & Caillol, 2003]; the MD simulations used for the results presented in this chapter are for larger systems and longer times, and therefore the results are expected to be of higher accuracy.

Figure 8.1 shows a typical MD result for the reduced shear stress autocorrelation function, $\hat{H}(t) = H(t)/nma^2\omega_p^2$, along with its cumulative integral that allows the reduced shear viscosity, $\hat{\eta} = \eta/nma^2\omega_p$, to be computed. To compute $\hat{\eta}$, the upper limit of the integral in Equation (8.1) is replaced by some cutoff time t_{cutoff}—illustrated by the vertical line in Figure 8.1—which is less than the total simulation time of $819.1\omega_p^{-1}$. A cutoff time is necessary because of noise in the computed shear stress autocorrelation function, which grows as t increases due to the fact that the number of MD measurements decreases (as discussed previously in Section 3.11). The cutoff time was chosen differently for each value of Γ; while this arbitrary choice of t_{cutoff} is a somewhat undesirable necessity of the Green-Kubo method, it was found that the simulation was long enough that the final result for the viscosity is not particularly sensitive to the choice of t_{cutoff}, providing t_{cutoff} is selected to be close to the time at which the shear stress autocorrelation function from MD appears to decay to zero (see Figure 8.1, top panel) .

8.4 Hydrodynamic method

The hydrodynamic method for computing the shear viscosity, as it will be referred to here, is based on the transverse part of the linearised Naviér-Stokes equation. This can be written in terms of the wave number and time dependent transverse current (auto)correlation function, $C_t(k,t)$ [Boon & Yip, 1991]:

$$\frac{\partial}{\partial t}C_t(k,t) = -\frac{\eta}{nm}k^2 C_t(k,t)\,, \tag{8.3}$$

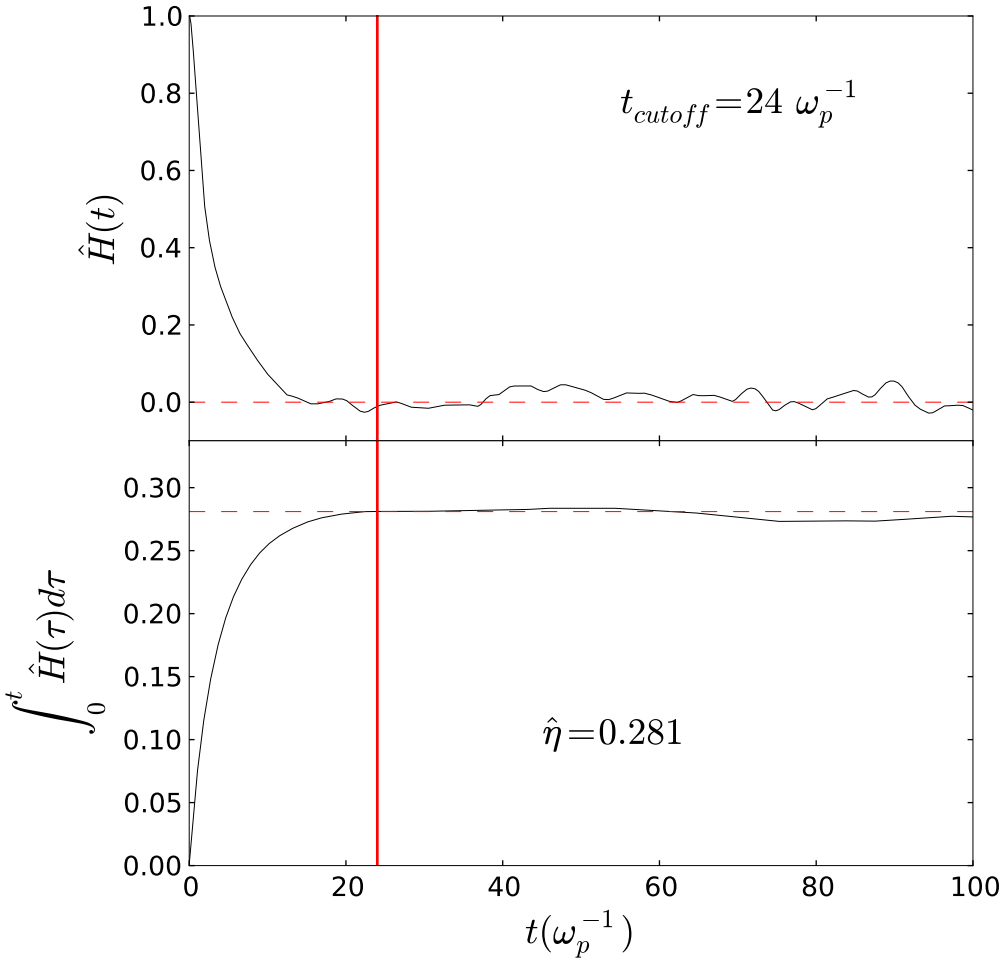

Figure 8.1: Illustration of the Green-Kubo method for determining the viscosity, for the particular conditions $\Gamma = 5$, $\kappa = 2$. The top panel illustrates the decay of the (reduced) shear stress autocorrelation function, showing the time after which it is effectively set to zero at $t = t_{cutoff}$ (vertical line) for the purpose of computing the (reduced) viscosity. The bottom panel illustrates the cumulative integral of the reduced shear stress autocorrelation function (i.e., the cumulative integral of the top panel). This gives a value for the reduced viscosity as indicated by the dashed horizontal line.

where the transverse current correlation function is defined as (see Section 2.2, Equation (8.4))

$$C_t(k,t) = \frac{1}{N}\left\langle \sum_{i=1}^{N}\sum_{j=1}^{N} v_{i,x}(t)v_{j,x}(0)\exp(ik(z_i(t)-z_j(0)))\right\rangle . \tag{8.4}$$

From Equation (8.3), one obtains an exponential decay for the transverse current correlation function:

$$\frac{C_t(k,t)}{C_t(k,0)} = \exp\left(-\frac{\eta}{nm}k^2 t\right) . \tag{8.5}$$

The hydrodynamic method consists of computing $C_t(k,t)$ with MD and then using Equation (8.5) to estimate the shear viscosity. To achieve this, as in the case of the Green-Kubo method, the statistical average in Equation (8.4) is, as usual, taken as a time average. Then, since the only unknown parameter in Equation (8.5) is the shear viscosity η, the MD result for $C_t(k,t)$ can be fitted to an exponential decay to yield the best estimate of the shear viscosity. As mentioned previously, although this method has been used in practical calculations for some time (e.g., [Balucani *et al.*, 2000, Palmer, 1994]), it does not appear to have been used to compute the viscosity of the YOCP. In fact, there *have* been recent MD calculations of $C_t(k,t)$ for the YOCP [Donkó *et al.*, 2010]; but in this previous work, no attempt was made to compute the viscosity by fitting to the hydrodynamic result, as is done here.

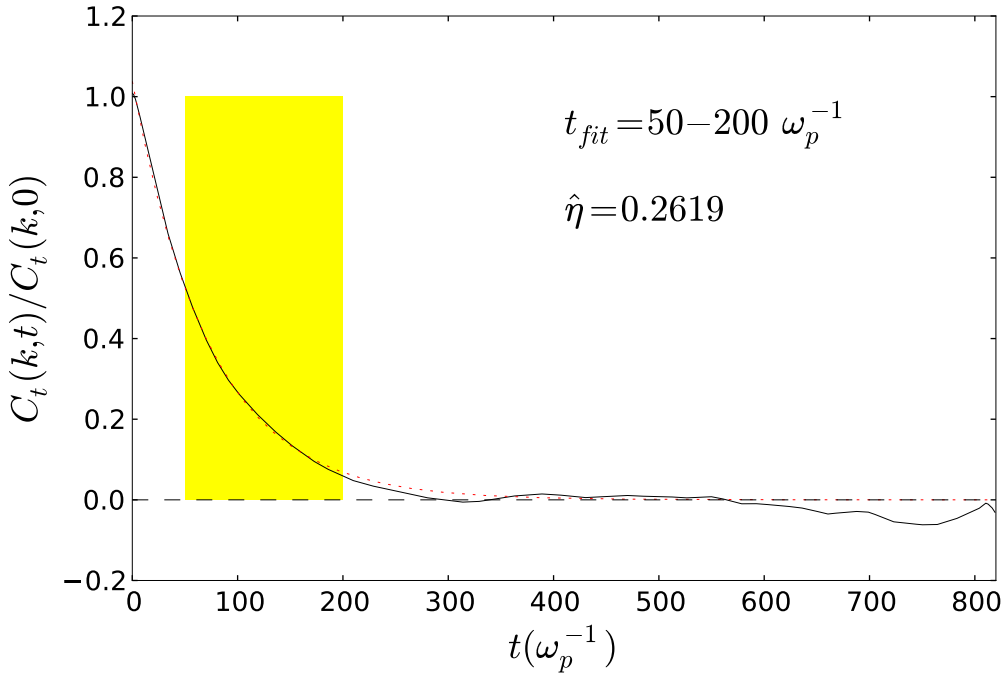

Figure 8.2: Normalised transverse current correlation function (solid line) for $\Gamma = 5$, $\kappa = 2$, $ka = 0.23$, and the exponential fit (dotted line). The region of MD data used for the fit is shaded.

Shown in Figure 8.2 is a typical MD result for the transverse current correlation function along with the exponential fit that allows the (reduced) shear viscosity to be estimated. As shown in Figure 8.2, the exponential fit is only applied to a particular

time interval (shaded), denoted by t_{fit}. The upper limit of this region, which was chosen to be $200\omega_p^{-1}$, is required because of the deteriorating quality of the MD data: as for all time dependent correlation functions, fewer averages contribute to the transverse current correlation function at long times, and therefore the MD data becomes more noisy. The reason that a lower limit on the time interval is required is instead a physical one. Specifically, the exponential decay of Equation (8.5) is only applicable when the hydrodynamic description on which it is based is applicable, i.e., at long time and length scales. Thus, only at sufficiently large t can $C_t(k,t)$ be expected to decay exponentially. Indeed, the short time behaviour of $C_t(k,t)$ as computed with MD can be seen to be Gaussian (as expected from a short time expansion of $C_t(k,t)$—see Section 2.5) rather than exponential. The chosen lower limit of $50\omega_p^{-1}$ ensures that this non-hydrodynamic behaviour of $C_t(k,t)$ at short times does not influence the fit for the shear viscosity.

As for long lengthscales, this means that the wave number k at which $C_t(k,t)$ is measured with MD must be small. Exactly how small was quantified by the investigation in Chapter 4; the hydrodynamic description of the YOCP is accurate for $k < k_{max}$, where $k_{max}\lambda_s \simeq 0.43$ (Equation (4.51)). For $\kappa = 2$, this gives $k_{max}a \simeq 0.86$. In the MD simulations, $C_t(k,t)$ was computed for $ka = 0.23$ (the minimum wave number accessible for the $N = 5000$ particle system). For this wave number, which is much smaller than k_{max}, the hydrodynamic description can be expected to be very accurate. This expectation is confirmed by the MD data: as shown in Figure 8.2, the exponential decay given by Equation (8.5) fits the MD data very well.

8.5 Comparison between methods

As shown in Figure 8.3, for $\kappa = 2$ both the "Green-Kubo method" and the "hydrodynamic method" give similar results for the shear viscosity of the YOCP. It is expected that this should be the case for all values of κ; further simulations could confirm this conclusion.

8.6 Conclusion and future outlook

In this short chapter, two methods for computing the viscosity of the YOCP using molecular dynamics (MD) simulations were investigated: the conventional Green-Kubo method, and the so-called "hydrodynamic method". The MD results demonstrated that the hydrodynamic method is feasible for the YOCP and therefore com-

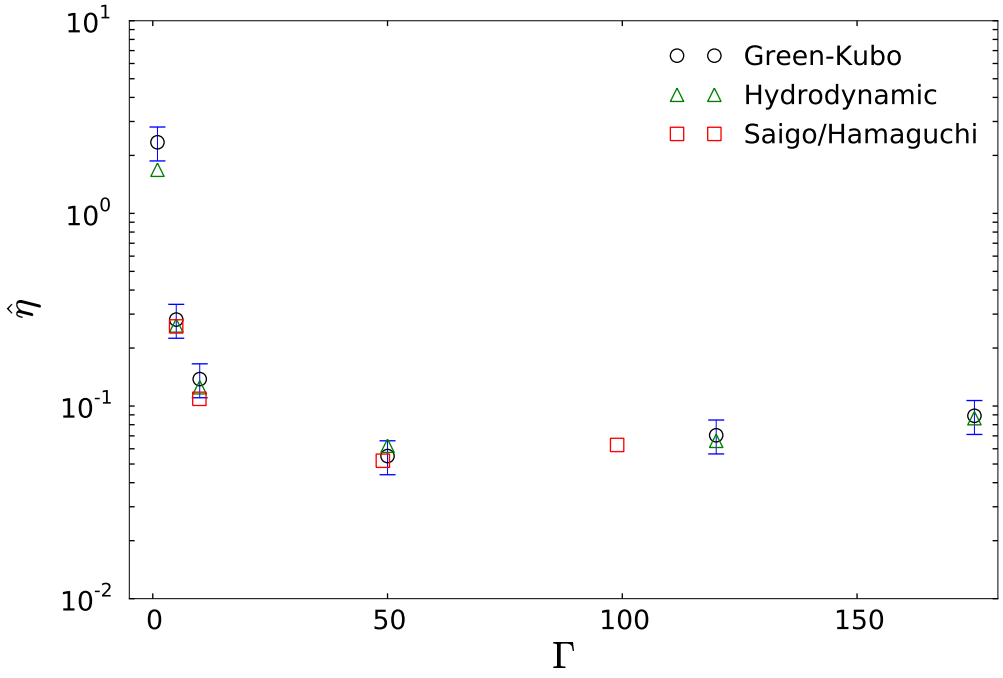

Figure 8.3: Comparison of viscosity for $\kappa = 2$ as computed by the Green-Kubo method (with 20% error bars) and the hydrodynamic method. Also shown is the good agreement obtained with the results of Saigo and Hamaguchi [Saigo & Hamaguchi, 2002].

plements the more widely used method based on the Green-Kubo relation. That is to say, this alternative method provides a way to validate the Green-Kubo result.

Future investigations might be able to use the type of analysis presented in this chapter to determine other transport coefficients of the YOCP, i.e., the bulk viscosity and thermal conductivity. This could offer a check of previous calculations of these important quantities.

Chapter 9

Summary

> "We ought then to regard the present state of the universe as the effect of its anterior state and as the cause of the one which is to follow. Given for one instant an intelligence which could comprehend all the forces by which nature is animated and the respective situation of the beings who compose it—an intelligence sufficiently vast to submit these data to analysis—it would embrace in the same formula the movements of the greatest bodies of the universe and those of the lightest atom; for it, nothing would be uncertain and the future, as the past, would be present to its eyes."
>
> —Pierre Simon Laplace, A Philosophical Essay on Probabilities [Laplace, 1902]

Computers allow the classical equations of motion—Newton's equations—to be solved to high precision, thus essentially fulfilling Laplace's vision of scientific determinism. However, the resulting data alone, although no doubt useful for some purposes, is essentially meaningless from the physicist's perspective without some kind of theoretical interpretation. Indeed, the physical understanding of any such 'raw' data—whether it originates from the 'real world' or from computer simulations—can only be evinced by its comparison to theoretical models. These models are required even when the 'exact' equations that are thought to govern the behaviour of the physical system under investigation are solvable (e.g., on a computer), since usually the system of interest is so overwhelmingly complicated that 'higher level' concepts are needed to discuss and understand the data. In no other area of physics is this more true than in the many-body physics of condensed matter systems; the underlying dynamics of a large number of interacting particles, whether governed by the Schrödinger equation of non-relativistic quantum mechanics, or given to sufficient

accuracy by the classical equations of motion, generate a rich variety of behaviours that can only be understood using higher level concepts than the particle trajectories themselves (or, in the quantum mechanical case, than the time evolution of the wavefunction). For example, the collective motion of molecules in a liquid—sound waves—effectively cease to exist if only the trajectories of the individual molecules are considered. Indeed, to stick with this particularly relevant example, the fact that a large body of theoretical and computational work on the physics of liquids has built up since the beginning of the 20th century [Balucani & Zoppi, 2002, Hansen & McDonald, 2006] is a testament to the fact that physicists seek far more than simply numerical data from an experiment or a computer simulation.

In this thesis, data for the equilibrium dynamics of non-ideal plasmas governed by the classical equations of motion was generated using the computer simulation method known as molecular dynamics (MD). Although generating the data accurately with MD was a major undertaking in itself (see Chapter 3), the real focus of the research was on understanding the data using theoretical models. Most of these were models for the dynamical structure (DSF), a quantity of special experimental and therefore theoretical significance in many-body physics in general. Data for the DSF of two different, but related, systems representing non-ideal plasmas—the Yukawa one-component plasma (YOCP) and the Coulomb one-component plasma (OCP)—was produced from the MD simulations. This MD data was examined in relation to theoretical models in Chapters 4-8.

Chapters 4 and 5 were investigations of the DSF of the YOCP. In Chapter 4, the emergence of macroscopic, that is, hydrodynamic, behaviour at long length scales was examined. This was done by comparing the DSF obtained from the MD simulations to the predictions of the hydrodynamic description, as given by the Naviér-Stokes equations. It was found that the hydrodynamic description of the YOCP is applicable for a surprisingly large range of length scales; the criterion for the maximum wave number at which the hydrodynamic description is applicable, k_{max}, determined from the MD data as $k_{max}\lambda_s \simeq 0.43$ (where λ_s is the screening length in the Yukawa interaction potential), gives a quantitative measure of this.

Chapter 5 built on this successful application of the hydrodynamic description of the YOCP. Models of *generalised* hydrodynamics, a well known formalism designed for extending the results of the conventional hydrodynamic description to larger wave numbers k (i.e., to shorter length scales) were investigated. One particular model—the Gaussian memory function model—was found to be an extremely good representation of the DSF of the YOCP for wave numbers beyond k_{max}. The model was found

to accurately reproduce the DSF obtained from MD simulations in terms of just three parameters and can therefore be viewed as an economical way of accurately condensing or representing such data.

Chapters 6 and 7 were investigations of the DSF of the other system studied, the OCP. In Chapter 6, the question of the very existence of a hydrodynamic description of the OCP—as posed by Baus and Hansen over thirty years ago [Baus & Hansen, 1980]—was examined. It was found that the 'collisionality' of the OCP does not overcome the mean field effects as the coupling parameter Γ is increased, in contrast to what was hypothesised by Baus and Hansen, and that therefore the conventional hydrodynamic description of the OCP is never applicable.

Chapter 7 was a comparison of two different approaches for describing the DSF of the OCP. The same generalised hydrodynamics approach that was applied successfully to the YOCP was contrasted with the dynamic local field correction (LFC) approach, which, rather than being based on extending the hydrodynamic description, is instead based on extending the mean field (Vlasov) picture of the OCP dynamics. It was found that the same Gaussian memory function model used for the YOCP (although with parameters that are qualitatively different in order to describe the plasmon peak in the OCP DSF) is also an excellent representation of the DSF of the OCP, as hinted at in the previous study of Hansen et al. [Hansen *et al.*, 1975]. In contrast, the MD data for the LFC was found to exhibit considerable structure, not described by any of the currently existing models. The conclusion of this chapter was therefore that the memory function of the OCP is rather more simple to model than the LFC: while the memory function is very well reproduced by a Gaussian, the LFC is considerably more complicated.

Finally, Chapter 8 was not directly concerned with the DSF of either the YOCP or OCP, but instead devoted the determination of transport coefficients. These are ubiquitous quantities in descriptions of the equilibrium dynamics of any system, and thus are relevant in some way to all of the preceding investigations in the thesis. Two ways in which a particular transport coefficient—the shear viscosity η—can be obtained from MD simulations were described and applied to the YOCP system. The aim of this investigation was to assess the utility of the so-called "hydrodynamic method" of computing the shear viscosity, and the conclusion was that this method is indeed viable and complements the more standard "Green-Kubo" method.

Taken as a whole, the research presented in Chapters 4-8 of this thesis represents a small contribution to the theoretical understanding of the YOCP and OCP systems. These systems are still actively studied, although it is perhaps fair to say that their

heyday was the era of Hansen and co-workers [Hansen, 1973, Hansen *et al.*, 1975, Vieillefosse & Hansen, 1975], which was later continued to some degree by Ichimaru and co-workers [Ichimaru, 1982]. Nevertheless, despite recent trends moving towards the study of more complicated, i.e., more 'realistic' systems, the OCP and YOCP will no doubt be studied for years to come. It is hoped that the work presented in this thesis can guide and inspire some of these future investigations. On a more mundane level, the MD data for the DSF of these systems that was produced for this thesis should certainly replace that of Hansen and co-workers, which—although a remarkable feat of computational physics at that time—is now more than thirty years old.

As well as contributing to the theoretical understanding of strongly coupled plasmas, the research presented in this thesis should find some application in the planning, understanding, and analysis of x-ray scattering experiments using high power lasers. This is particularly true for the studies of the YOCP, which is a system that can provide a reasonable representation of the ion dynamics in a strongly coupled plasma. As emphasised throughout the thesis, the fact that x-ray scattering experiments will soon by able to measure these ion dynamics was the primary motivation for these studies. Although more sophisticated modelling will no doubt be necessary to capture the details of the expected experimental scattering profile, the fairly comprehensive analysis of the DSF of the YOCP presented in this thesis is a useful first step. Indeed, the studies in Chapters 4, 5 and 8 should help to at least guide future experimental efforts; in fact, they are serving to assist to a limited degree with the planning of forthcoming experiments at high power laser facilities at the time of writing. The ultimate success of these experiments in the long term will be to achieve inertial confinement fusion.

Appendix A

Correlation functions in real and reciprocal space

In the case of two space dependent dynamical variables (which are real functions) A and B, the definition of a time dependent correlation function given in Equation (2.7) can be written in more explicit notation as

$$C_{AB}(\boldsymbol{r}', \boldsymbol{r}'', t) = \langle A(\boldsymbol{r}', t) B(\boldsymbol{r}'', 0) \rangle \,. \tag{A.1}$$

The corresponding correlation function for the Fourier components is

$$C_{AB}(\boldsymbol{k}, \boldsymbol{k}', t) = \langle A(\boldsymbol{k}, t) B^*(\boldsymbol{k}', 0) \rangle \,. \tag{A.2}$$

It should be noted that in both of these definitions, the translational invariance in time—or 'stationary property'—of C_{AB} has effectively been used (see Appendix B); this is the reason C_{AB} depends on t only, and not on two time variables t' and t''.

Similarly, translational invariance in space, which holds for homogeneous fluids, means that the time dependent correlation function in Equation (A.1) depends on the relative coordinates $\boldsymbol{r} = \boldsymbol{r}' - \boldsymbol{r}''$ only:

$$\begin{aligned} C_{AB}(\boldsymbol{r}', \boldsymbol{r}'', t) &= C_{AB}(\boldsymbol{r}' - \boldsymbol{r}'', t) \\ &= C_{AB}(\boldsymbol{r}, t) \,. \end{aligned} \tag{A.3}$$

In reciprocal space, translation invariance means that

$$\begin{aligned} C_{AB}(\boldsymbol{k}, \boldsymbol{k}', t) &= \langle A(\boldsymbol{k}, t) B^*(\boldsymbol{k}', 0) \rangle \delta_{\boldsymbol{k}\boldsymbol{k}'} \\ &= C_{AB}(\boldsymbol{k}, t) \,. \end{aligned} \tag{A.4}$$

Clearly, $C_{AB}(\boldsymbol{k}, t)$ is the spatial Fourier transform of $C_{AB}(\boldsymbol{r}, t)$:

$$C_{AB}(\boldsymbol{k}, t) = \int C_{AB}(\boldsymbol{r}, t) \exp(-i\boldsymbol{k} \cdot \boldsymbol{r}) d\boldsymbol{r} \,. \tag{A.5}$$

The above arguments can be applied to the particular case of density correlations, for which $A(\boldsymbol{r},t) = B(\boldsymbol{r},t) = N^{-1/2}\sum_{i=1}^{N}\delta(\boldsymbol{r}-\boldsymbol{r}_i(t))$. This then leads to the relation between the intermediate scattering function and the van Hove function given in Equation (2.17), which is

$$F(k,t) = \int G(r,t)\exp(-i\boldsymbol{k}\cdot\boldsymbol{r})d\boldsymbol{r}\,, \tag{A.6}$$

where the fact that for an isotropic system, the correlation functions in Equations (A.1) and (A.2) depend on $r = |\boldsymbol{r}|$ and $k = |\boldsymbol{k}|$ only has been used.

Appendix B

Useful properties of time dependent correlation functions

Some useful properties of time dependent correlation functions can be deduced most straighforwardly by writing the time evolution of a dynamical variable in terms of the Liouville operator[1]. The Liouville operator L is normally introduced by noting that in classical mechanics, the equation of motion for a dynamical variable $A(t)$ can be written as

$$\frac{dA(t)}{dt} = \{A(t), H\} \equiv iLA(t)\,, \tag{B.1}$$

where $\{\cdots,\cdots\}$ denotes the Poisson bracket and

$$L \equiv i\{H, \cdots\} \equiv i\sum_{i=1}^{N}\left[\frac{\partial H}{\partial \boldsymbol{r}_i}\cdot\frac{\partial}{\partial \boldsymbol{p}_i} - \frac{\partial H}{\partial \boldsymbol{p}_i}\cdot\frac{\partial}{\partial \boldsymbol{r}_i}\right]. \tag{B.2}$$

Equation (B.1) can be formally solved to give

$$A(t) = \exp(iLt)A(0)\,. \tag{B.3}$$

The definition of a time dependent correlation function given in Equation (2.7) can therefore be written as

$$C_{AB}(t) = \langle A(t)B^*(0)\rangle = \langle[\exp(iLt)A(0)]B^*(0)\rangle = \langle B^*(0)\exp(iLt)A(0)\rangle\,. \tag{B.4}$$

For the purposes of this appendix, the main advantage of writing time dependent correlation functions in terms of the operator L is this: it can be shown that, if the dynamical variables are thought of as vectors in an infinite dimensional vector space, and the classical statistical average is taken to represent the inner product on this

[1]This appendix is based on the discussion in Chapter 1 and Appendices A and B of the book by Balucani and Zoppi [Balucani & Zoppi, 2002].

space in the conventional mathematical sense, the Liouville operator L is Hermitian, that is $L^\dagger = L$ (see Appendix A of [Balucani & Zoppi, 2002] for a proof of this statement). This has the consequence that the operator $\exp(iLt)$ is unitary, that is, $[\exp(iLt)]^\dagger = \exp(-iLt)$. The unitarity property means that, from the definition of the Hermitian-conjugate, the following useful property of time dependent correlation functions can be demonstrated:

$$C_{AB}(t) = \langle B^*(0)\exp(iLt)A(0)\rangle = \langle A^*(0)[\exp(iLt)]^\dagger B(0)\rangle^* = C^*_{BA}(-t)\,. \tag{B.5}$$

This can be shown to be a special case of the stationarity property:

$$\langle B^*(0)A(t)\rangle = \langle B^*(\tau)A(t+\tau)\rangle\,, \tag{B.6}$$

which is proven as follows:

$$\begin{aligned}
\langle B^*(0)A(t)\rangle &= \langle B^*(0)\exp(iLt)A(0)\rangle \\
&= \langle A^*(0)[\exp(iLt)]^\dagger B(0)\rangle^* \\
&= \langle A^*(0)[\exp(-iL\tau)\exp(iL(t+\tau))]^\dagger B(0)\rangle^* \\
&= \langle A^*(0)\exp(-iL(t+\tau))\exp(iL\tau)B(0)\rangle^* \\
&= \langle A^*(0)\exp(-iL(t+\tau))B(\tau)\rangle^* \\
&= \langle B^*(\tau)[\exp(-iL(t+\tau))]^\dagger A(0)\rangle \\
&= \langle B^*(\tau)A(t+\tau)\rangle\,.
\end{aligned} \tag{B.7}$$

The stationarity property says that statistical averages are preserved under time translation. This property has effectively been used in the very definition of a time dependent correlation function given in Equation (2.7); the correlation between two dynamical variables at two unequal times only depends on the difference between the two times, and not on their absolute values.

Another useful general property of time correlation functions can be derived by considering what happens upon a sign change of all the momenta of the particles. Since the Hamiltonian only includes terms proportional to the squares of the momenta, it is unchanged, but it can be seen from Equation (B.2) that the Liouville operator L changes sign under this transformation. Thus, the transformation $\{\boldsymbol{r}^N, \boldsymbol{p}^N\} \to \{\boldsymbol{r}^N, -\boldsymbol{p}^N\}$ is effectively a time reversal of the propagator, which changes from $\exp(iLt)$ to $\exp(-iLt)$. Under such a time reversal, most dynamical variables $A(t)$ of interest are either invariant or change sign, that is,

$$\langle B^*(0)\exp(iLt)A(0)\rangle = \sigma_A\sigma_B\langle B^*(0)\exp(-iLt)A(0)\rangle\,, \tag{B.8}$$

where $\sigma_A, \sigma_B = \pm 1$ represent the signatures of $A(t)$ and $B(t)$ under time reversal. Equation (B.8) can be written as

$$C_{AB}(t) = \sigma_A \sigma_B C_{AB}(-t)\,. \tag{B.9}$$

In the case of time dependent *auto*correlation functions ($A(t) = B(t)$), which are the only time dependent correlation functions considered in this thesis (reflecting the fact that they are generally of special importance), this becomes

$$C_{AA}(t) = C_{AA}(-t)\,. \tag{B.10}$$

In other words, time dependent *auto*correlation functions—such as the intermediate scattering function $F(k,t)$—are always real and even in time.

Appendix C

Frequency moments

In the short time expansion of a time dependent autocorrelation function,

$$C_{AA}(t) = \sum_{n=0}^{\infty} (a_n/n!)t^n \,, \tag{C.1}$$

only the coefficients a_n with even n are non-zero (this is a consequence of the even nature of time dependent autocorrelation functions discussed in Appendix B). These coefficients are given by

$$a_n = \left(\frac{d^n C_{AA}(t)}{dt^n} \right)_{t=0} = (-i)^n \langle \omega^n \rangle \,, \tag{C.2}$$

where

$$\langle \omega^n \rangle = \int_{-\infty}^{\infty} \omega^n C_{AA}(\omega) d\omega \,. \tag{C.3}$$

The second equality in Equation (C.2) follows from the definition of the frequency spectrum of C_{AA}:

$$C_{AA}(t) = \int_{-\infty}^{\infty} C_{AA}(\omega) \exp(-i\omega t) d\omega \,. \tag{C.4}$$

The frequency moments are

$$\langle \omega^n \rangle = i^n \left(\frac{d^n C_{AA}(t)}{dt^n} \right)_{t=0} = i^n \left\langle B^*(0) \left(\frac{d^n A(t)}{dt^n} \right)_{t=0} \right\rangle \,. \tag{C.5}$$

A very useful identity for practical evaluation of the frequency moments can be obtained from the Hermitian nature of the Liouville operator L (see Appendix B):

$$\begin{aligned}\left\langle A^*(0)\left(\frac{d^nA(t)}{dt^n}\right)_{t=0}\right\rangle &= \left\langle A^*(0)iL\left(\frac{d^{n-1}A(t)}{dt^{n-1}}\right)_{t=0}\right\rangle \\ &= \left\langle\left(\frac{d^{n-1}A^*(t)}{dt^{n-1}}\right)_{t=0}(iL)^\dagger A(0)\right\rangle^* \\ &= -\left\langle\left(\frac{d^{n-1}A^*(t)}{dt^{n-1}}\right)_{t=0}\left(\frac{dA(t)}{dt}\right)_{t=0}\right\rangle^* \\ &= -\left\langle\left(\frac{dA^*(t)}{dt}\right)_{t=0}\left(\frac{d^{n-1}A(t)}{dt^{n-1}}\right)_{t=0}\right\rangle .\end{aligned}$$

This identity can be iterated, leading to the following expressions for the second and fourth frequency moments:

$$\langle\omega^2\rangle = -\langle A^*(0)\ddot{A}(0)\rangle = \langle\dot{A}^*(0)\dot{A}(0)\rangle \tag{C.6}$$

$$\langle\omega^4\rangle = \langle A^*(0)\dddot{A}(0)\rangle = \langle\ddot{A}^*(0)\ddot{A}(0)\rangle\,, \tag{C.7}$$

where the dots denote differentiation with respect to time. In the remainder of this appendix, Equations (C.6) and (C.7) are used to calculate the second and fourth frequency moments, $\langle\omega^2\rangle$ and $\langle\omega^4\rangle$, of the dynamical structure factor $S(k,\omega)$ of the YOCP and OCP. It is shown that these are given by Equations (2.45) and (2.46) respectively.

To compute $\langle\omega^2\rangle$, Equation (C.6) is used with

$$A(t) = \frac{1}{\sqrt{N}}n(\boldsymbol{k},t)\,, \tag{C.8}$$

where

$$n(\boldsymbol{k},t) = \sum_{i=1}^{N}\exp(-i\boldsymbol{k}\cdot\boldsymbol{r}_i(t))\,, \tag{C.9}$$

which gives

$$\dot{A}(0) = -\frac{i}{\sqrt{N}}\sum_{i=1}^{N}\boldsymbol{k}\cdot\boldsymbol{v}_i\exp(-i\boldsymbol{k}\cdot\boldsymbol{r}_i)\,, \tag{C.10}$$

$$\dot{A}^*(0) = \frac{i}{\sqrt{N}}\sum_{i=1}^{N}\boldsymbol{k}\cdot\boldsymbol{v}_i\exp(i\boldsymbol{k}\cdot\boldsymbol{r}_i)\,, \tag{C.11}$$

$$\tag{C.12}$$

where $\boldsymbol{v}_i(t) = \dot{\boldsymbol{r}}_i(t)$ and the notation is such that $\boldsymbol{r}_i \equiv \boldsymbol{r}_i(0)$. Substituting these expressions into Equation (C.6) gives

$$\langle \omega^2 \rangle = \frac{1}{N} \left\langle \sum_{i=1}^{N} \sum_{j=1}^{N} (\boldsymbol{k} \cdot \boldsymbol{v}_i)(\boldsymbol{k} \cdot \boldsymbol{v}_j) \exp(-i\boldsymbol{k} \cdot (\boldsymbol{r}_i - \boldsymbol{r}_j)) \right\rangle , \tag{C.13}$$

$$= \frac{1}{N} \frac{1}{Z} \int \sum_{i=1}^{N} \sum_{j=1}^{N} (\boldsymbol{k} \cdot \boldsymbol{v}_i)(\boldsymbol{k} \cdot \boldsymbol{v}_j) \exp(-i\boldsymbol{k} \cdot (\boldsymbol{r}_i - \boldsymbol{r}_j)) \exp(-\beta H) d\boldsymbol{r}^N d\boldsymbol{p}^N , \tag{C.14}$$

where Equation (2.8) for the ensemble average $\langle \cdots \rangle$ has been used. Because the potential in the Hamiltonian H is pairwise additive, integration over the position coordinates for all terms in the double summation other than those for which $i = j$ gives zero. Equation (C.14) thus reduces to

$$\langle \omega^2 \rangle = \left(\frac{\beta}{2\pi m} \right)^{3N/2} \int (\boldsymbol{k} \cdot \boldsymbol{v}_1)^2 \exp\left(-\frac{\beta}{2m} \sum_{i=1}^{N} p_i^2 \right) d\boldsymbol{p}^N , \tag{C.15}$$

where the factor in front of the integral comes from the $1/Z$ term in Equation (C.14). The integral can be performed in a Cartesian co-ordinate system chosen such that the z axis of the co-ordinate system is parallel to the wave-vector $\boldsymbol{k}$; this gives

$$\langle \omega^2 \rangle = \left(\frac{\beta}{2\pi m} \right)^{N/2} \frac{k^2}{m^2} \int p_{1,z}^2 \exp\left(-\frac{\beta}{2m} \sum_{i=1}^{N} p_{i,z}^2 \right) dp_{1,z} dp_{2,z} \cdots dp_{N,z} , \tag{C.16}$$

$$= \left(\frac{\beta}{2\pi m} \right)^{1/2} \frac{k^2}{m^2} \int p_{1,z}^2 \exp\left(-\frac{\beta}{2m} p_{1,z}^2 \right) dp_{1,z} , \tag{C.17}$$

$$= \frac{2k^2}{\sqrt{\pi}\beta m} \int_{-\infty}^{\infty} x^2 \exp(-x^2) dx \tag{C.18}$$

where $p_{i,z}$ denotes the z component of momentum of particle i, and in the last line the substitution $x = \sqrt{\frac{\beta}{2m}} p_{1,z}$ has been made. Performing the integration in Equation C.18 gives $\sqrt{\pi}/2$, and therefore

$$\langle \omega^2 \rangle = \frac{k^2}{m\beta} , \tag{C.19}$$

which is the expression for the second frequency moment given in Equation (2.45).

Computation of $\langle \omega^4 \rangle$ is slightly more tricky; this derivation is based on Chapter 1 of [Balucani & Zoppi, 2002], which should be consulted for the missing details. From

Equations (C.8) and (C.9),

$$\ddot{A}(0) = \frac{1}{\sqrt{N}} \sum_{i=1}^{N} [-i\boldsymbol{k} \cdot \dot{\boldsymbol{v}}_i - (\boldsymbol{k} \cdot \boldsymbol{v}_i)^2] \exp(-i\boldsymbol{k} \cdot \boldsymbol{r}_i) \,, \tag{C.20}$$

$$\ddot{A}^*(0) = \frac{1}{\sqrt{N}} \sum_{i=1}^{N} [i\boldsymbol{k} \cdot \dot{\boldsymbol{v}}_i - (\boldsymbol{k} \cdot \boldsymbol{v}_i)^2] \exp(i\boldsymbol{k} \cdot \boldsymbol{r}_i) \,. \tag{C.21}$$

Substituting these expressions into Equation (C.7) gives

$$\begin{aligned} \langle \omega^4 \rangle = \frac{1}{N} \Big\langle \sum_{i=1}^{N} \sum_{j=1}^{N} \{ &(\boldsymbol{k} \cdot \boldsymbol{v}_i)^2 (\boldsymbol{k} \cdot \boldsymbol{v}_j)^2 + i[(\boldsymbol{k} \cdot \dot{\boldsymbol{v}}_i)(\boldsymbol{k} \cdot \boldsymbol{v}_j)^2 - (\boldsymbol{k} \cdot \boldsymbol{v}_i)^2 (\boldsymbol{k} \cdot \dot{\boldsymbol{v}}_j)] \\ &+ (\boldsymbol{k} \cdot \dot{\boldsymbol{v}}_i)(\boldsymbol{k} \cdot \dot{\boldsymbol{v}}_j) \} \exp(-i\boldsymbol{k} \cdot (\boldsymbol{r}_i - \boldsymbol{r}_j)) \Big\rangle \,. \end{aligned} \tag{C.22}$$

Evaluating the right hand side of this equation involves considering terms for which $i = j$, as well as cross terms for which $i \neq j$ (unlike in the $\langle \omega^2 \rangle$ case, for which these cross terms give zero). As shown in Section 1.4 of [Balucani & Zoppi, 2002], the $i = j$ terms give[1]

$$\langle \omega^4 \rangle|_{i=j} = \frac{k^2}{m\beta} \left[\frac{3k^2}{m\beta} + \Omega_E^2 \right] \,, \tag{C.23}$$

where

$$\Omega_E^2 = (n/3m) \int \nabla^2 v(r) g(r) d\boldsymbol{r} \,, \tag{C.24}$$

is known as the *Einstein frequency*. Clearly—unlike in the $\langle \omega^2 \rangle$ case—the fourth moment is dependent on the particle interactions (through both the interaction potential $v(r)$ and the radial distribution function $g(r)$ that appear in Equation (C.24)). This is to be expected, since, according to the classical equations of motion, the terms in Equation (C.22) proportional to the derivative of the particle velocities are related to the force, which in term is related to the particle interactions. The remaining contribution to $\langle \omega^4 \rangle$ from the cross terms for which $i \neq j$ (see Section 1.6 of [Balucani & Zoppi, 2002]) is

$$\langle \omega^4 \rangle|_{i \neq j} = -\frac{k^2}{m\beta} \Omega_k^2 \,, \tag{C.25}$$

where

$$\Omega_k^2 = \frac{4\pi n}{3m} \int_0^\infty r^2 \{ v''(r)[j_0(kr) - 2j_2(kr)] + (2/r) v'(r)[j_0(kr) + j_2(kr)] \} g(r) \,. \tag{C.26}$$

Here $j_0(x) = \sin x/x$ and $j_2(x) = (3/x^2)[(\sin x/x) - \cos x] - \sin x/x$ are the spherical Bessel functions of order 0 and 2 respectively. The complete expression for the fourth

[1] This is the 'self' part of fourth moment—see also Footnote 4 in Section 2.4.

moment obtained by adding the $i = j$ and $i \neq j$ contributions is therefore

$$\langle \omega^4 \rangle = \frac{k^2}{m\beta} \left[\frac{3k^2}{m\beta} + \Omega_0^2 - \Omega_k^2 \right] , \tag{C.27}$$

which is valid for any interaction potential $v(r)$. By specifying $v(r)$ to be either the Yukawa interaction potential,

$$v(r) = \frac{(Ze)^2 \exp(-r/\lambda_s)}{4\pi\epsilon_0 r} , \tag{C.28}$$

or the Coulomb interaction potential,

$$v(r) = \frac{(Ze)^2}{4\pi\epsilon_0 r} , \tag{C.29}$$

it can be put into the rather simpler form valid for either the YOCP or OCP systems, as given previously in Equations (2.46)-(2.49). To do this, the Einstein frequency is written in reduced units as

$$\frac{\Omega_E^2}{\omega_p^2} = \frac{1}{\omega_p^2}(4\pi n/3m) \int_0^\infty \frac{1}{r^2} \frac{\partial}{\partial r} \left(r^2 \frac{\partial}{\partial r} \right) v(r) g(r) dr , \tag{C.30}$$

where the Laplacian in spherical coordinates has been written explicitly. For the YOCP, this gives

$$\frac{\Omega_E^2}{\omega_p^2} = \frac{\kappa^2}{3} \int_0^\infty \bar{r} \exp(-\kappa\bar{r}) g(\bar{r}) d\bar{r} . \tag{C.31}$$

For the OCP, the Einstein frequency is given by

$$\frac{\Omega_E^2}{\omega_p^2} = \frac{1}{3} . \tag{C.32}$$

Finally, after some algebraic manipulations, Ω_k^2 can be given in reduced units as

$$\begin{aligned} \frac{\Omega_k^2}{\omega_p^2} = q^2 \int_0^\infty \frac{1}{\bar{r}} g(\bar{r}) \exp(-y) \Bigg[2 \left(\frac{y^2}{3} + y + 1 \right) \times \\ \left(\frac{\sin x}{x} + \frac{3\cos x}{x^2} - \frac{3\sin x}{x^3} \right) + \frac{y^2 \sin x}{3x} \Bigg] d\bar{r} \qquad \text{(C.33)} \\ \equiv q^2 M(x, y) , \qquad \text{(C.34)} \end{aligned}$$

where $q = ka$ is the reduced wave number, $x = q\bar{r}$, and $y = \kappa\bar{r}$. In reduced units, the complete expression for the fourth moment is therefore

$$\frac{\langle \omega^4 \rangle}{\omega_p^4} = \frac{1}{3\Gamma} \left[\frac{q^4}{\Gamma} + q^2 \frac{\Omega_E^2}{\omega_p^2} - q^2 M(q\bar{r}, \kappa\bar{r}) \right] , \tag{C.35}$$

as given previously in Equation (2.46). One further simplification can be made to this formula in the OCP case. Since $y = 0$ for the OCP, the function $M(x, y)$ reduces to

$$M(x, 0) = 2q^2 \int_0^\infty \frac{1}{\bar{r}} g(\bar{r}) \left(\frac{\sin x}{x} + \frac{3\cos x}{x^2} - \frac{3\sin x}{x^3} \right) d\bar{r} \,. \tag{C.36}$$

The fourth moment in the OCP case is therefore often written in the form (e.g., [Hansen *et al.*, 1975])

$$\frac{\langle \omega^4 \rangle}{\omega_p^4} = \frac{1}{3\Gamma} \left[\frac{q^4}{\Gamma} + q^2 - 2q^2 I(q) \right] , \tag{C.37}$$

where

$$I(q) = \int_0^\infty \frac{1}{\bar{r}} [g(\bar{r}) - 1] \left(\frac{\sin q}{q} + \frac{3\cos q}{q^2} - \frac{3\sin q}{q^3} \right) d\bar{r} \,. \tag{C.38}$$

The replacement of $g(\bar{r})$ by $g(\bar{r})-1$ going between Equation (C.36) and (C.38) requires adding the term

$$-2q^2 \int_0^\infty \frac{1}{\bar{r}} \left(\frac{\sin q}{q} + \frac{3\cos q}{q^2} - \frac{3\sin q}{q^3} \right) d\bar{r} \,. \tag{C.39}$$

This term can be shown to be equal to $(2/3)q^2$, and is taken into account in the middle term of Equation (C.37) (which includes this $(2/3)q^2$ as well as the $(1/3)q^2$ from the $q^2\Omega_E^2/\omega_p^2$ term in Equation (C.35)).

Appendix D

Expressions for the thermodynamic coefficients

The first step in deriving expressions for the thermodynamic coefficients of the YOCP and OCP is to split the internal energy of the system, U, into ideal and excess parts:

$$\begin{aligned} U &= U_0 + U_{ex} \\ &= U_0 + Nk_BTu(\Gamma, \kappa)\,, \end{aligned} \tag{D.1}$$

where the ideal part $U_0 = \frac{3}{2}Nk_BT$ is simply the internal energy of the ideal gas. Equation (D.1) has been written in terms of the *reduced excess internal energy* $u(\Gamma, \kappa)$; in doing this, the fact that for the YOCP and OCP the reduced excess internal energy depends only on the dimensionless parameters Γ and κ has been used. Another relation that proves useful in deriving expressions for the thermodynamic coefficients is the relation between U and the pressure P [Baus & Hansen, 1980]:

$$\frac{P}{P^0} = 1 + \frac{1}{2}\frac{U - U^0}{U^0} = 1 + \frac{1}{3}\frac{\beta(U - U^0)}{N}\,, \tag{D.2}$$

where $P^0 = nk_BT$ is the ideal gas pressure. In this appendix, expressions for the heat capacity at constant volume,

$$C_V = \left(\frac{\partial U}{\partial T}\right)_V\,, \tag{D.3}$$

the isothermal compressibility,

$$\chi_T = -\frac{1}{V}\left(\frac{\partial V}{\partial P}\right)_T\,, \tag{D.4}$$

and the heat capacity at constant pressure,

$$C_V = \left(\frac{\partial U}{\partial T}\right)_P\,, \tag{D.5}$$

are derived in terms of $u(\Gamma, \kappa)$.

From Equation (D.1), the heat capacity at constant volume is

$$\begin{aligned}\frac{C_V}{Nk_b} &= \frac{3}{2} + \left(\frac{\partial}{\partial T}[Tu(\Gamma,\kappa)]\right)_V \\ &= \frac{3}{2} + u(\Gamma,\kappa) + T\left(\frac{\partial}{\partial T}u(\Gamma,\kappa)\right)_V \end{aligned} \tag{D.6}$$

To compute the partial derivative, it should be noted that κ is simply a number that governs the decay of the interaction potential in the YOCP; it does not depend on temperature (or volume, or any other parameters of the system)[1]. The partial derivative with respect to temperature can therefore be converted into a partial derivative with respect to the remaining parameter, Γ, using the chain rule of calculus:

$$\begin{aligned}\frac{\partial}{\partial T} &= \frac{\partial \Gamma}{\partial T}\frac{\partial}{\partial \Gamma} \\ &= -\frac{\Gamma}{T}\frac{\partial}{\partial \Gamma}\,. \end{aligned} \tag{D.7}$$

This gives

$$\frac{C_V}{Nk_b} = \frac{3}{2} + u(\Gamma,\kappa) - \Gamma\frac{\partial}{\partial \Gamma}u(\Gamma,\kappa)\,, \tag{D.8}$$

which can be written more compactly as

$$\frac{C_V}{Nk_B} - \frac{3}{2} = -\Gamma^2\frac{\partial}{\partial \Gamma}\left[\frac{u(\Gamma,\kappa)}{\Gamma}\right]\,. \tag{D.9}$$

To derive an expression for the isothermal compressibility, χ_T, the pressure P is first written in terms of $u(\Gamma, \kappa)$. From Equations (D.1) and (D.2),

$$P = P_0\left[1 + \frac{1}{3}u(\Gamma,\kappa)\right] = \frac{Nk_BT}{V}\left[1 + \frac{1}{3}u(\Gamma,\kappa)\right]\,. \tag{D.10}$$

The inverse of the isothermal compressibility is therefore

$$\begin{aligned}\chi_T^{-1} &= -V\left(\frac{\partial P}{\partial V}\right)_T \\ &= -V\left[\frac{\partial}{\partial V}\left(\frac{Nk_BT}{V}\right) + \frac{1}{3}u(\Gamma,\kappa)\frac{\partial}{\partial V}\left(\frac{Nk_BT}{V}\right) + \frac{1}{3}\frac{Nk_BT}{V}\frac{\partial}{\partial V}u(\Gamma,\kappa)\right]\,. \end{aligned} \tag{D.11}$$

[1]Of course, if attempting to map a real physical plasma to the YOCP system, the chosen value of λ_s, and hence κ, will often require knowledge of the thermodynamic state of the plasma (e.g., λ_{TF} or λ_D—see Section 1.5); but from the standpoint of the YOCP system, κ is simply a constant numerical value.

Again, using the chain rule:

$$\begin{aligned}\frac{\partial}{\partial V} &= \frac{\partial \Gamma}{\partial V}\frac{\partial}{\partial \Gamma} \\ &= -\frac{1}{3}\frac{\Gamma}{V}\frac{\partial}{\partial \Gamma}\,,\end{aligned} \tag{D.12}$$

which gives

$$\chi_T^{-1} = \frac{Nk_BT}{V} + \frac{1}{3}\frac{Nk_BT}{V}u(\Gamma,\kappa) + \frac{1}{9}\frac{Nk_BT}{V}\Gamma\frac{\partial u(\Gamma,\kappa)}{\partial \Gamma}\,, \tag{D.13}$$

so that, finally,

$$\frac{\chi_T^0}{\chi_T} = 1 + \frac{1}{3}u(\Gamma,\kappa) + \frac{1}{9}\Gamma\frac{\partial u(\Gamma,\kappa)}{\partial \Gamma}\,. \tag{D.14}$$

To derive an expression for the remaining thermodynamic coefficient, the heat capacity at constant pressure, C_P, the following well known thermodynamic relation is needed [Gaskell, 2008]:

$$\frac{C_P - C_V}{Nk_B} = \alpha^2T^2\left[\frac{\chi_T}{\chi_T^0}\right]^{-1}\,, \tag{D.15}$$

where

$$\alpha = \frac{1}{V}\left(\frac{\partial V}{\partial T}\right)_T \tag{D.16}$$

is the coefficient of thermal expansion. The coefficient of thermal expansion can be written as:

$$\alpha = \frac{V}{T}\left(\frac{\partial P}{\partial U}\right)_T\frac{C_V}{Nk_B}\left[\frac{\chi_T}{\chi_T^0}\right] \tag{D.17}$$

To see this, the right hand side of Equation (D.17) can be written out in full:

$$\alpha = \left(\frac{\partial P}{\partial U}\right)_T\left(\frac{\partial U}{\partial T}\right)_V \times -\frac{1}{V}\left(\frac{\partial V}{\partial P}\right)_T\,, \tag{D.18}$$

or, using Equation (D.16),

$$\left(\frac{\partial V}{\partial T}\right)_P = -\left(\frac{\partial P}{\partial U}\right)_T\left(\frac{\partial U}{\partial T}\right)_V\left(\frac{\partial V}{\partial P}\right)_T\,, \tag{D.19}$$

where the relation $\chi_T^0 = 1/nk_BT$ has been used. By writing $\left(\frac{\partial U}{\partial T}\right)_V = \left(\frac{\partial U}{\partial P}\right)_T\left(\frac{\partial P}{\partial T}\right)_V$, this becomes

$$\left(\frac{\partial V}{\partial T}\right)_P = -\left(\frac{\partial P}{\partial U}\right)_T\left(\frac{\partial U}{\partial P}\right)_T\left(\frac{\partial P}{\partial T}\right)_V\left(\frac{\partial V}{\partial P}\right)_T\,, \tag{D.20}$$

or

$$\left(\frac{\partial P}{\partial T}\right)_V\left(\frac{\partial V}{\partial P}\right)_T\left(\frac{\partial T}{\partial V}\right)_P = -1\,. \tag{D.21}$$

The identity in Equation (D.21) is known as the "Euler triple product rule" (see, e.g. [Callen, 1985] for a derivation). Substituting Equation (D.17) for α into Equation (D.15) gives

$$\frac{C_P}{Nk_B} = \frac{C_V}{Nk_B} + \left[\left(\frac{\partial P}{\partial U}\right)_T\right]^2 \left(\frac{C_V}{Nk_B}\right)^2 \frac{\chi_T}{\chi_T^0}\,. \tag{D.22}$$

For an ideal gas ($P = P_0$), Equation (D.22) clearly gives the expected result ($C_P = C_V + Nk_B$). In the case of the YOCP and the OCP, using Equation (D.2),

$$\frac{C_P}{Nk_B} = \frac{C_V}{Nk_B} + \frac{1}{9}\left(\frac{C_V}{Nk_B}\right)^2 \frac{\chi_T}{\chi_T^0}\,. \tag{D.23}$$

This equation completes the task of specifying the thermodynamic coefficients in terms of $u(\Gamma, \kappa)$: Equations (D.9), (D.14) and (D.23) are the required expressions for C_V, χ_T and C_P. To evaluate these expressions, a formula for $u(\Gamma, \kappa)$ is needed. As mentioned in Section 4.6, $u(\Gamma, \kappa)$ has been estimated numerically to reasonably high accuracy, and for a large number of (Γ,κ) values by Hamaguchi, Farouki and Dubin [Hamaguchi *et al.*, 1996], and by Caillol and Gilles [Caillol & Gilles, 2000b]. For the comparison in Table 4.2, the expression given by Hamaguchi, Farouki and Dubin has been used. This is [Hamaguchi *et al.*, 1996]

$$u(\Gamma, \kappa) = a(\kappa)\Gamma + b(\kappa)\Gamma^s + c(\kappa) + d(\kappa)\Gamma^{-s}\,, \tag{D.24}$$

where, for $\kappa \leq 1$,

$$a(\kappa) = E_{bcc} + \delta a(\kappa)\,, \tag{D.25}$$

with

$$E_{bcc}(\kappa) = -0.895929 - 0.103731\kappa^2 + 0.003084\kappa^4 - 0.000131\kappa^6\,, \tag{D.26}$$

$$\delta a(\kappa) = -0.003366 + 0.000660\kappa^2 - 0.000089\kappa^4\,, \tag{D.27}$$

$$\delta b(\kappa) = 0.565004 - 0.026134\kappa^2 - 0.002689\kappa^4\,, \tag{D.28}$$

$$\delta c(\kappa) = -0.206893 - 0.086384\kappa^2 + 0.018278\kappa^4\,, \tag{D.29}$$

$$\delta d(\kappa) = -0.031402 + 0.042429\kappa^2 - 0.008037\kappa^4\,. \tag{D.30}$$

For selected larger values of κ (i.e., $\kappa > 1$), $a(\kappa)$, $b(\kappa)$, $c(\kappa)$ and $d(\kappa)$ are given in Table VIII of [Hamaguchi *et al.*, 1997]. The numbers for $\kappa = 2$ are used in this thesis; these are

$$a(2.0) = -1.270571\,, \tag{D.31}$$

$$b(2.0) = 0.442193\,, \tag{D.32}$$

$$c(2.0) = -0.382900\,, \tag{D.33}$$

$$d(2.0) = 0.100506\,. \tag{D.34}$$

Appendix E

Alternative form of the hydrodynamic DSF

In this appendix, Equation (5.1) for the hydrodynamic DSF is derived. This endeavour starts from the hydrodynamic form of the intermediate scattering function [Balucani & Zoppi, 2002, Boon & Yip, 1991],

$$F^H(k,t) = S(k)\left[\frac{\gamma-1}{\gamma}\exp(-D_T k^2|t|) + \frac{1}{\gamma}\exp(-\sigma k^2|t|)\{\cos c_s kt + [\sigma + (\gamma-1)D_T]\frac{k}{c_s}\sin c_s kt\}\right]. \quad \text{(E.1)}$$

According to the relation between the DSF and the Laplace transform of $F(k,t)$, (Equation (4.19)),

$$S(k,\omega) = \frac{1}{\pi}\Re e[F(k, z=\omega)], \quad \text{(E.2)}$$

the hydrodynamic DSF obtained from Equation (E.1) is

$$\frac{S^H(k,\omega)}{S(k)/2\pi} = \frac{\gamma-1}{\gamma}\frac{2D_T k^2}{\omega^2 + (D_T k^2)^2} + \frac{1}{\gamma}\left[\frac{\sigma k^2}{(\omega + c_s k)^2 + (\sigma k^2)^2} + \frac{\sigma k^2}{(\omega - c_s k)^2 + (\sigma k^2)^2}\right] + \frac{1}{\gamma}[\sigma + (\gamma-1)D_T]\frac{k}{c_s}\left[\frac{\omega + c_s k}{(\omega + c_s k)^2 + (\sigma k^2)^2} - \frac{\omega - c_s k}{(\omega - c_s k)^2 + (\sigma k^2)^2}\right]. \quad \text{(E.3)}$$

In the derivation of the hydrodynamic DSF in Section 4.4, the third term in the above equation, and hence the term proportional to $\sin c_s kt$ in $F^H(k,t)$, was effectively ignored (cf. Equation (4.43)). As discussed by Boon and Yip [Boon & Yip, 1991], this third term is in most cases negligible, contributing only a small 'wing' to each of the Brillouin peaks.

If the ratio of specific heats γ is taken to be equal to unity, the hydrodynamic intermediate scattering function in Equation (E.1) reduces to

$$F^H(k,t) = S(k)\exp(-(\eta_l/2)k^2|t|)[\cos\tilde{c}_s kt + \frac{\eta_l k}{2\tilde{c}_s}\sin\tilde{c}_s kt]\,, \tag{E.4}$$

where $\tilde{c}_s$ is the isothermal sound speed, and the fact that for $\gamma = 1$ the sound attenuation coefficient σ reduces to $\eta_l/2$, where $\eta_l = (\frac{4}{3}\eta + \zeta)/mn$ is the kinematic viscosity (cf. Equation (4.40)), has been used. The Laplace transform of this equation (using the usual convention given in Equation (4.20)) is

$$\begin{aligned} F^H(k,z) &= S(k)\left[\frac{-z^2 - iz\eta_l k^2 + (\eta_l k^2/2)^2 + (\tilde{c}_s k)^2}{-iz + \eta_l k^2}\right]^{-1} \\ &= S(k)\left[-iz + \frac{(\tilde{c}_s k)^2}{-iz + \eta_l k^2}\right]^{-1}\,, \end{aligned} \tag{E.5}$$

where the term of order k^4 has been neglected in going from the first to the second line. By using Equation (E.2), the hydrodynamic DSF is then found to be

$$\frac{S^H(k,\omega)}{S(k)} = \frac{1}{\pi}\frac{(\tilde{c}_s k)^2 k^2 \eta_l}{[\omega^2 - (\tilde{c}_s k)^2]^2 + [\omega k^2 \eta_l]^2}\,, \tag{E.6}$$

as given in Equation (5.1).

Appendix F

MD results for the DSF of the OCP and the YOCP

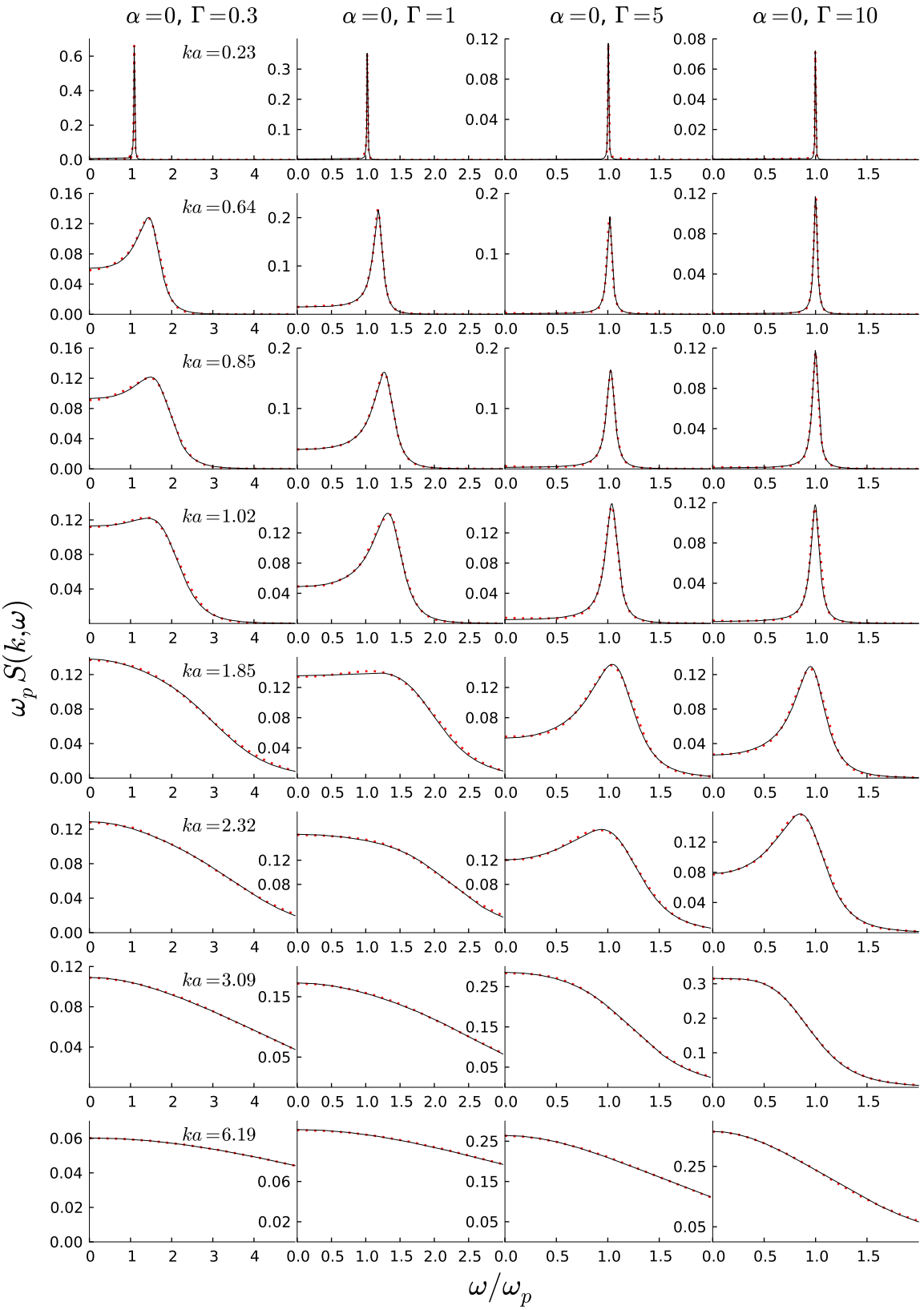

Figure F.1: MD results for the DSF of the OCP for $\Gamma = 0.3, 1, 5$ and 10 (dots), and the memory function fits (solid lines)

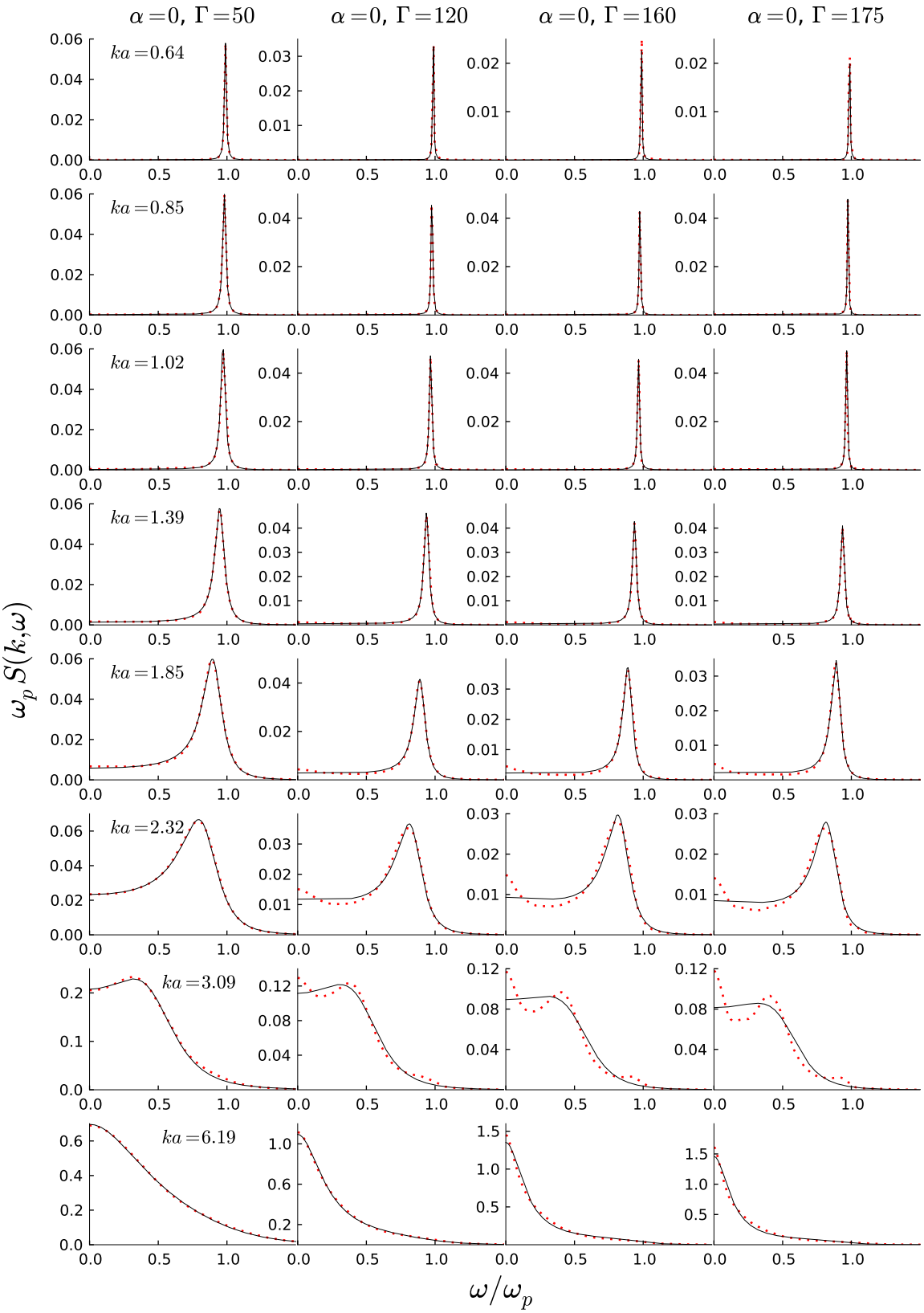

Figure F.2: Same as Figure F.1 but for $\Gamma = 10, 50, 120$ and175.

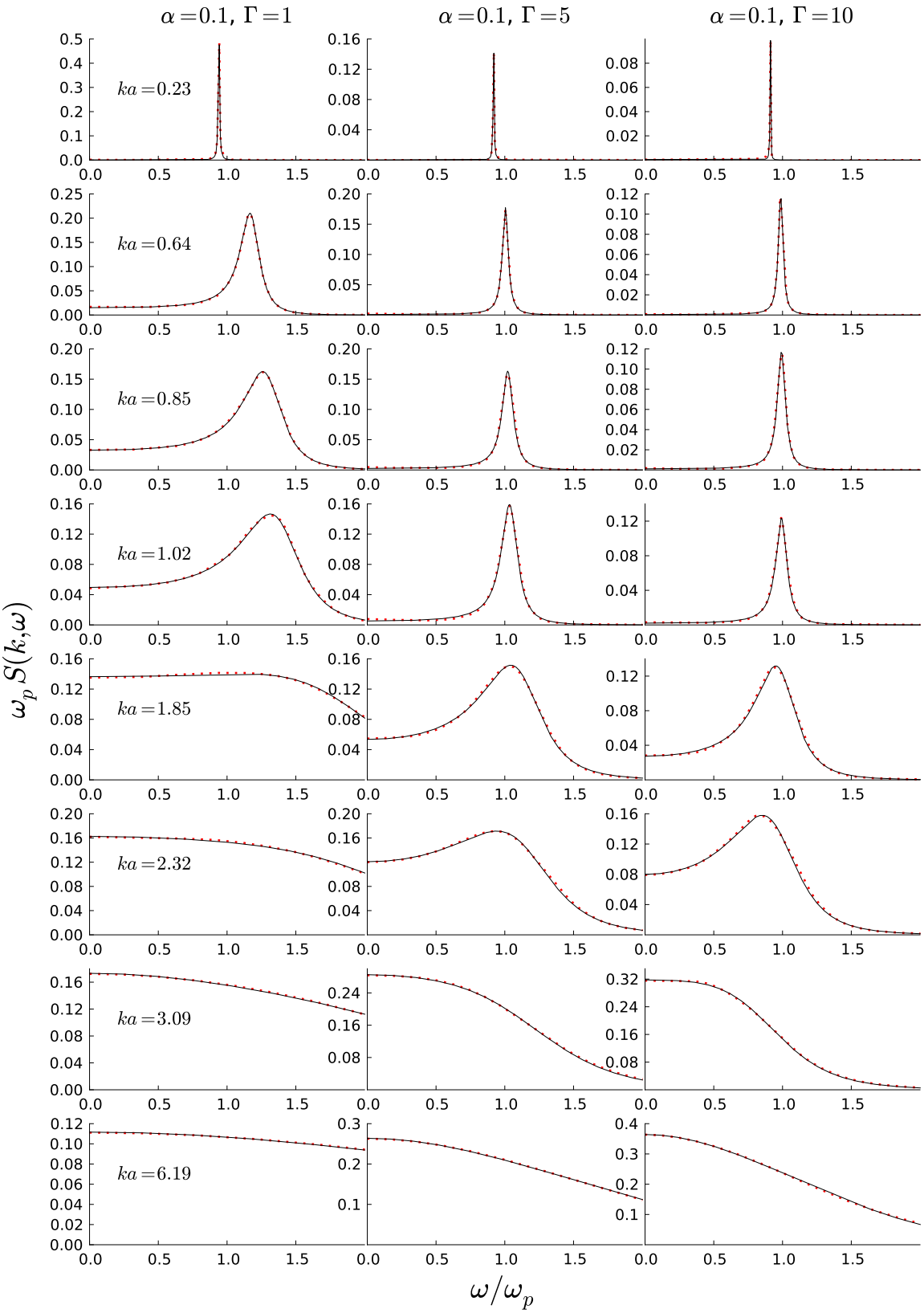

Figure F.3: MD results for the DSF of the YOCP at $\kappa = 0.1$ and $\Gamma = 1, 5$ and 10 (dots), and the memory function fits (solid lines).

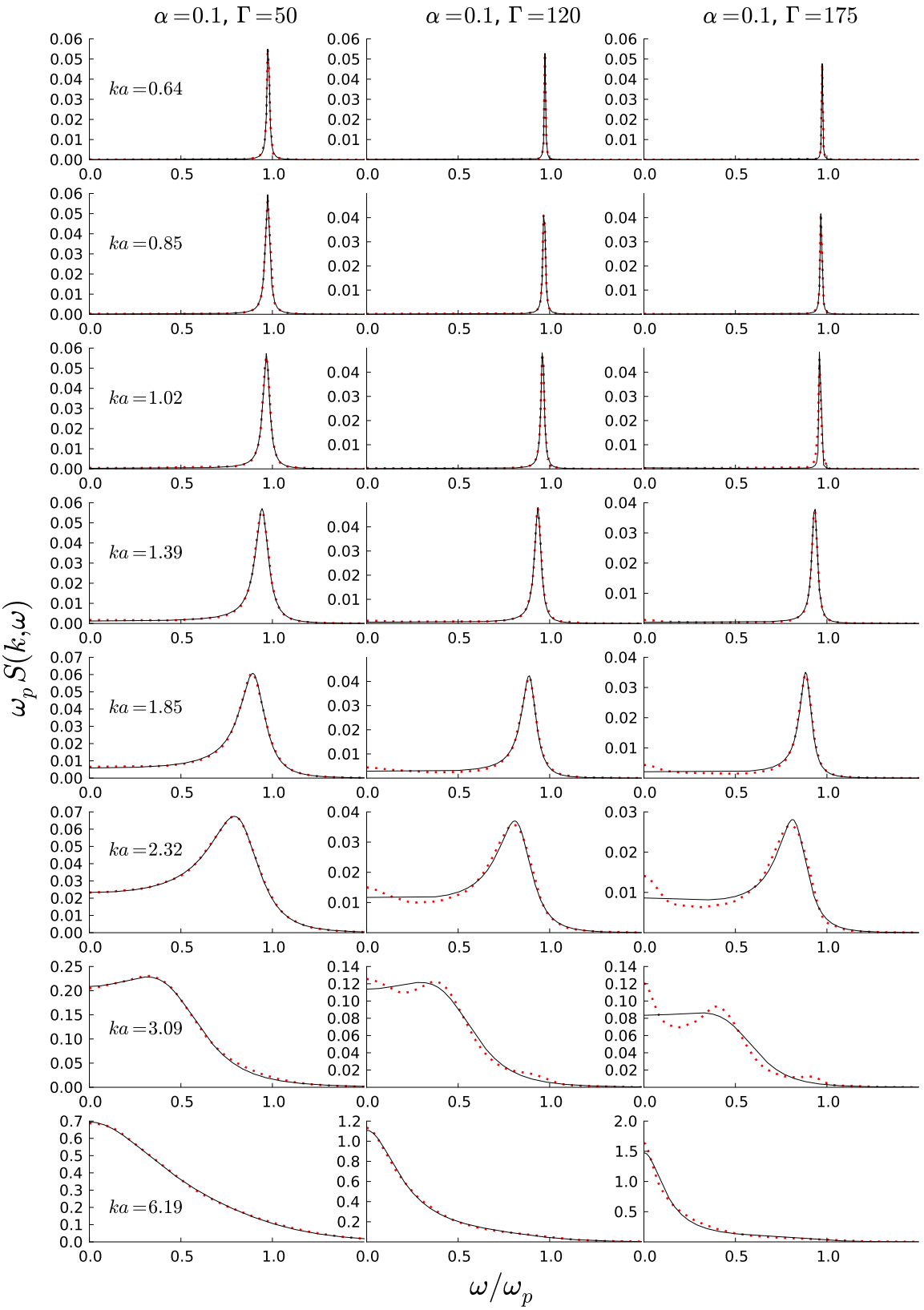

Figure F.4: Same as Figure F.3 but for $\Gamma = 50, 120$ and 175.

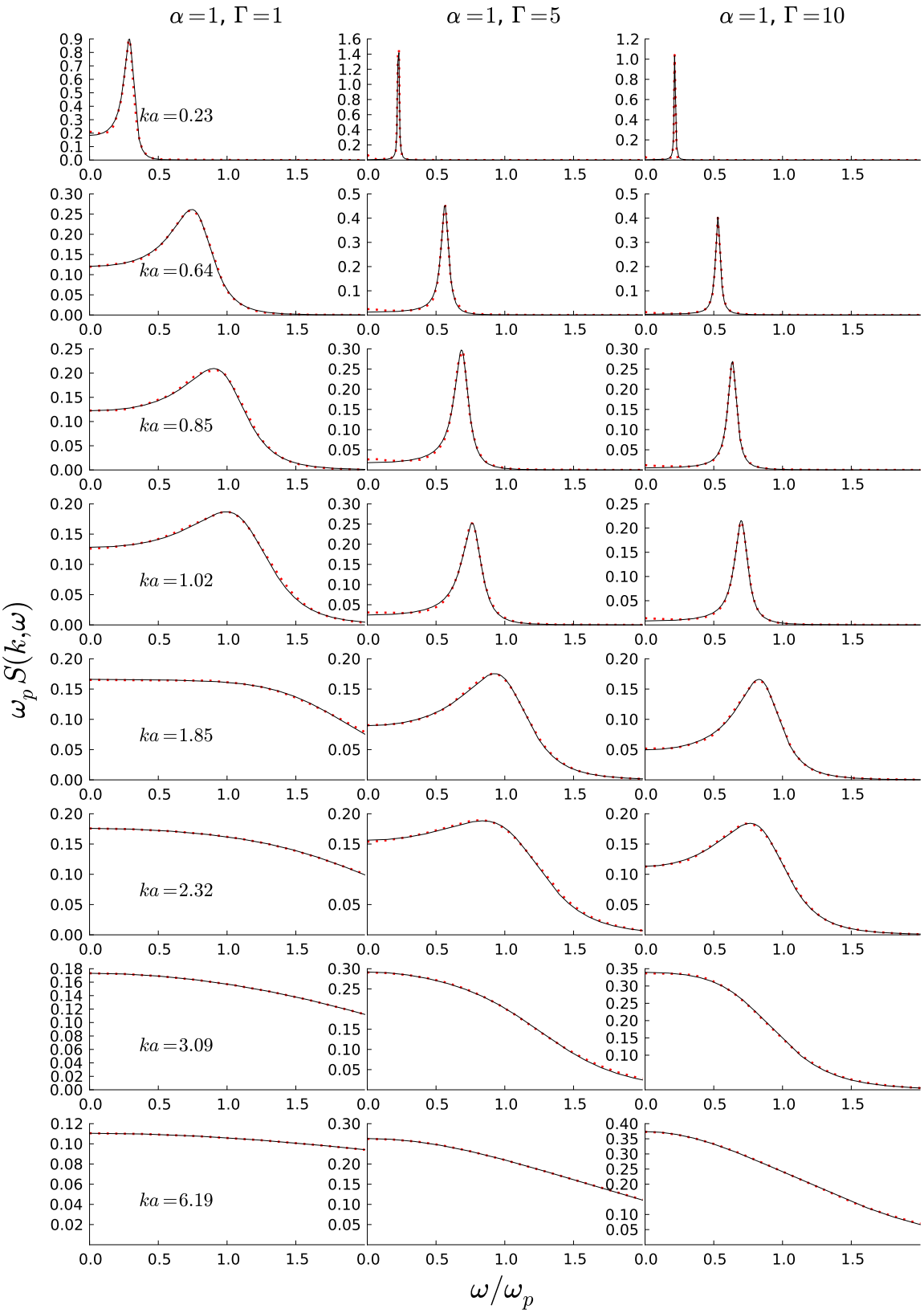

Figure F.5: MD results for the DSF of the YOCP at $\kappa = 1$ and $\Gamma = 1, 5$ and 10 (dots), and the memory function fits (solid lines).

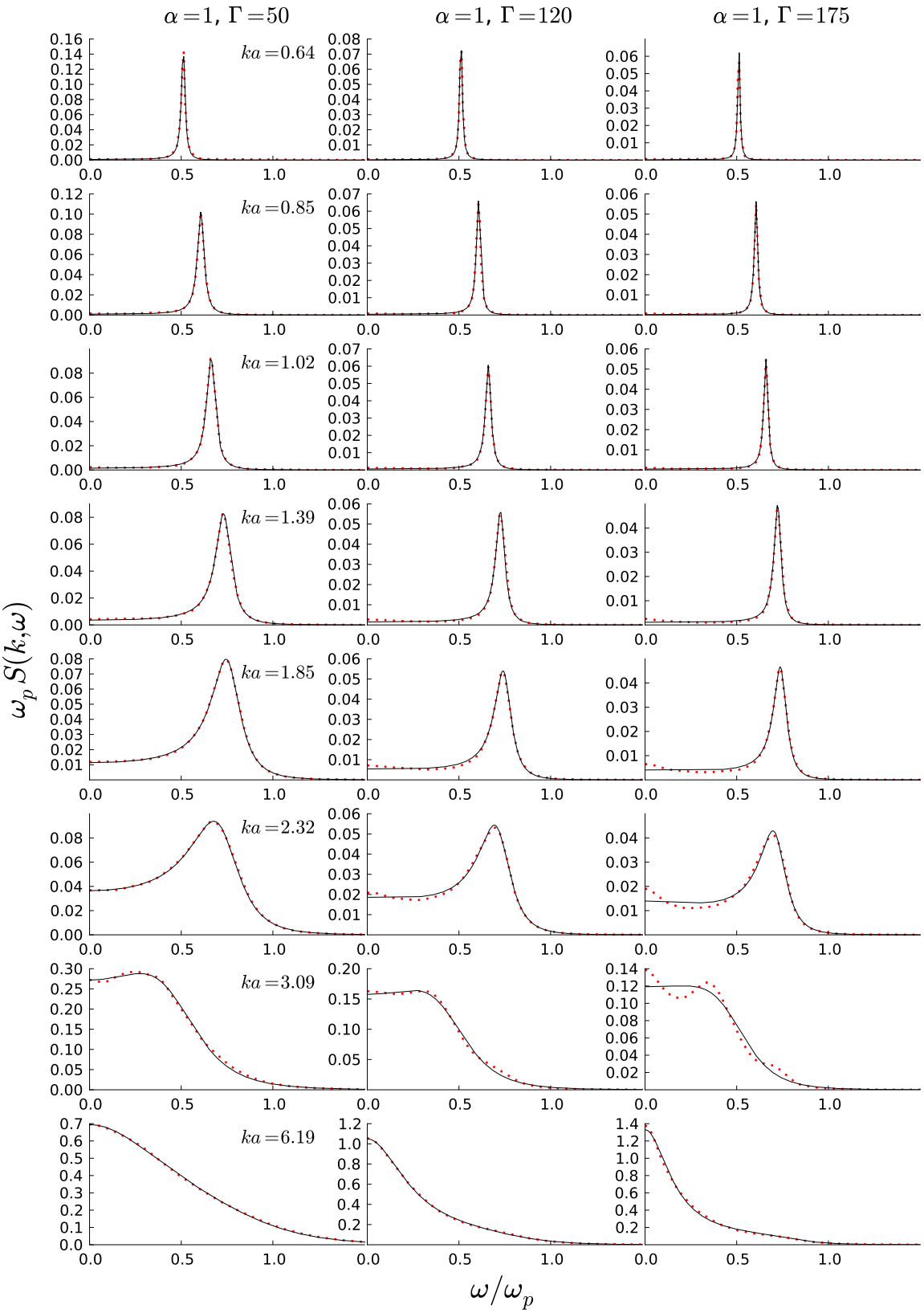

Figure F.6: Same as Figure F.5 but for $\Gamma = 50, 120$ and 175.

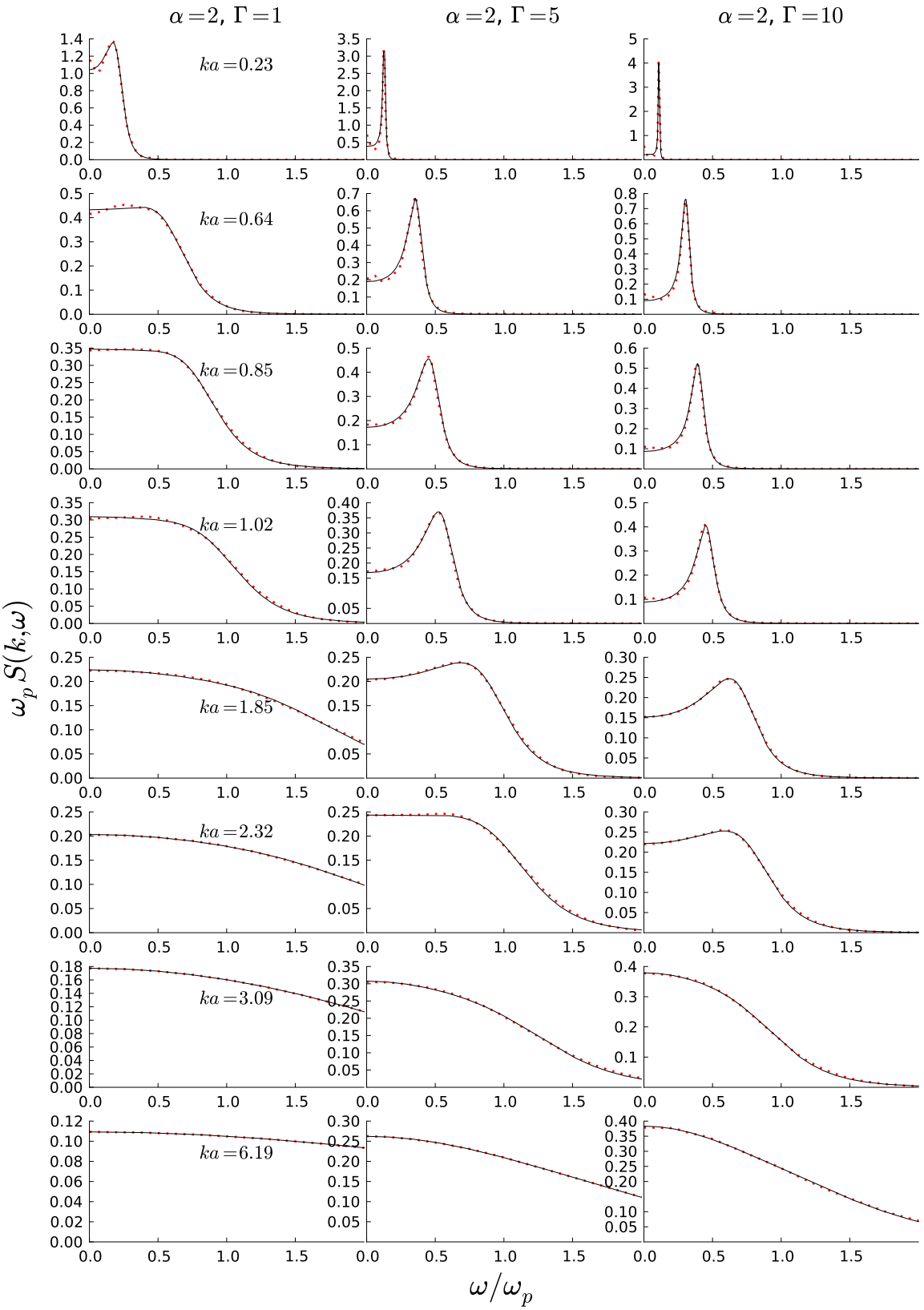

Figure F.7: MD results for the DSF of the YOCP at $\kappa = 2$ and $\Gamma = 1, 5$ and 10 (dots), and the memory function fits (solid lines).

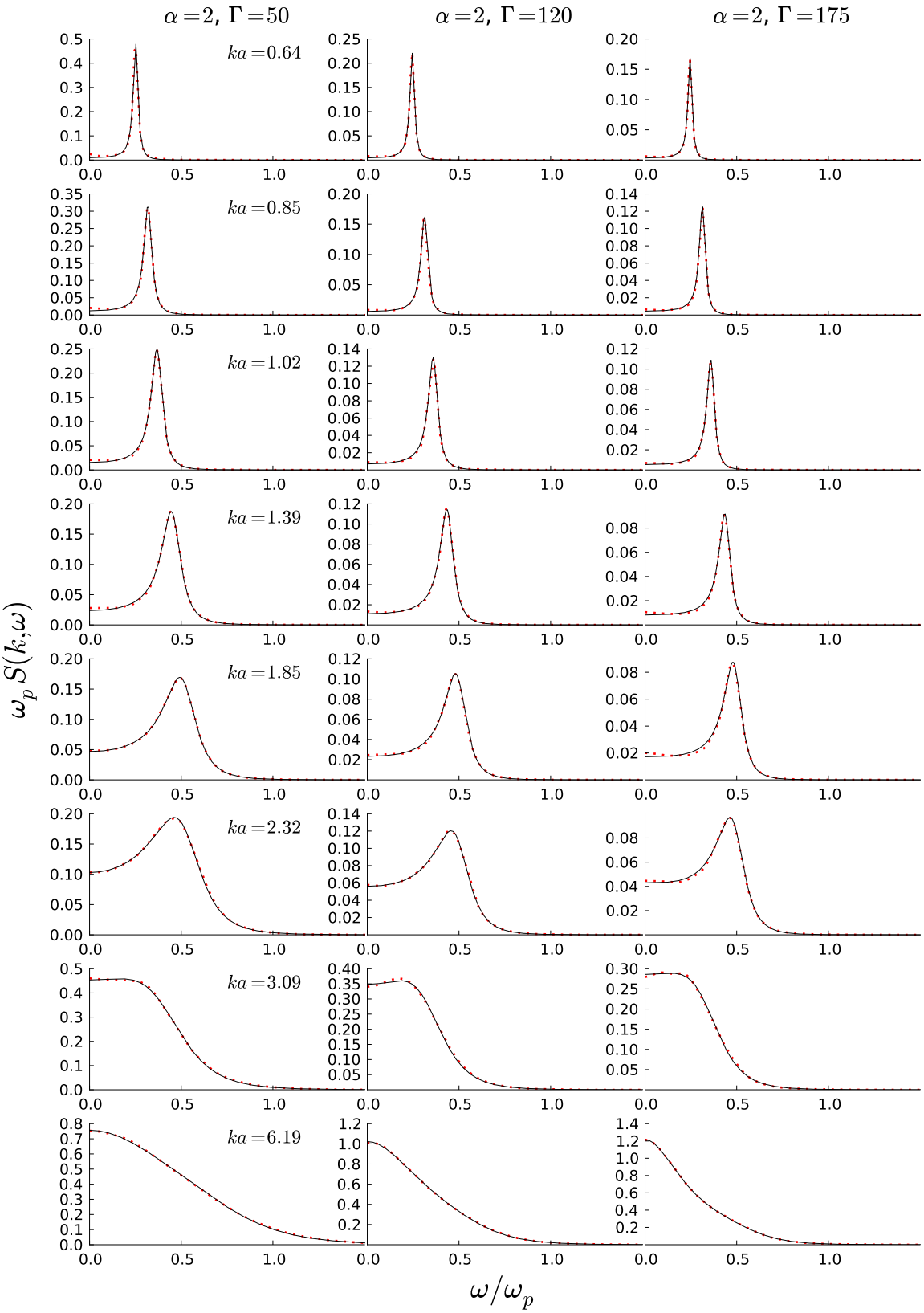

Figure F.8: Same as Figure F.7 but for $\Gamma = 50, 120$ and 175.

Appendix G

Properties of the LFC

In this appendix, the expressions given in Equations (7.5) and (7.6) for the static LFC, $G(k) \equiv G(k,0)$, and the high frequency limit of the LFC, $G(k,\omega \to \infty)$, are derived.

The first step in deriving the static LFC, $G(k) \equiv G(k,0)$, is to rearrange the definition of the LFC in terms of the response function (Equation (7.2)),

$$\chi(k,\omega) = \frac{\chi^0(k,\omega)}{1 - v(k)[1 - G(k,\omega)]\chi^0(k,\omega)}\,, \tag{G.1}$$

as

$$G(k,\omega) = 1 + \left(\frac{1}{\chi(k,\omega)} - \frac{1}{\chi^0(k,\omega)}\right)\frac{1}{v(k)}\,. \tag{G.2}$$

To determine $G(k,0)$, expressions for $\chi(k,0)$ and $\chi^0(k,0)$ are needed. These can be obtained from the Kramers-Kronig relation[1] for the response function [Ichimaru, 2004], which is

$$\chi(k,z) = \frac{1}{\pi}\int_{-\infty}^{\infty} \frac{\chi^{''}(k,\omega)}{\omega - z} d\omega\,, \tag{G.3}$$

where $\chi^{''}(k,\omega) \equiv \Im m\{\chi(k,\omega)\}$ is the imaginary part of the response function. Using this relation,

$$\chi(k,0) = \frac{1}{\pi}\int_{-\infty}^{\infty} \frac{\chi^{''}(k,\omega)}{\omega} d\omega\,, \tag{G.4}$$

$$= -\frac{n}{k_B T}\int_{-\infty}^{\infty} S(k,\omega) d\omega\,, \tag{G.5}$$

$$= -\frac{n}{k_B T} S(k)\,, \tag{G.6}$$

[1]The Kramers-Kronig relation is a mathematical consequence of the fact that the density response function is analytic in the upper half plane; such relations are ubiquitous in physics (see, e.g., [Arfken & Weber, 2005] for further details).

where the fluctuation dissipation theorem (Equation (7.3)),

$$S(k,\omega) = -\frac{k_B T}{\pi n \omega}\,\chi''(k,\omega)\,, \tag{G.7}$$

has been used to express the imaginary part of the response function in terms of the DSF. Substituting Equation (G.6) into Equation (G.2), and using the fact that $S^0(k) = 1$ then gives

$$G(k) = 1 + \left[1 - \frac{1}{S(k)}\right]\frac{n}{k_B T}\frac{1}{v(k)}\,, \tag{G.8}$$

which is Equation (7.5).

Deriving the expression for the high frequency limit of the LFC, $G(k,\omega\to\infty)$, as given in Equation (7.6), requires slightly more work. The first step is to consider a high frequency expansion of Equation (G.1). As $\omega\to\infty$, the second term on the denominator of this equation (the symbol Δ is used in place of $v(k)[1-G(k,\omega)]$ for conciseness),

$$\Delta\chi^0(k,\omega) \equiv v(k)[1-G(k,\omega)]\chi^0(k,\omega)\,, \tag{G.9}$$

tends to zero. The high frequency expansion of Equation (G.1) can be written as

$$\chi(k,\omega\to\infty) = \chi^0(k,\omega\to\infty)[1+\Delta\chi^0(k,\omega\to\infty)+\Delta^2[\chi^0(k,\omega\to\infty)]^2+\cdots \tag{G.10}$$

To continue, the high frequency limit of the ideal gas response function is needed. The ideal gas response function, defined in Equation (7.4), is

$$\chi^0(k,\omega) = -\frac{n}{k_B T}\left(1 - 2\sqrt{\frac{m}{2k_B T}}\frac{\omega}{k}D\left(\sqrt{\frac{m}{2k_B T}}\frac{\omega}{k}\right) + i\sqrt{\frac{\pi m}{2k_B T}}\exp(-\frac{m\omega^2}{2k_B T k^2}\right)\,. \tag{G.11}$$

Now, as $x\to\infty$ [Ichimaru, 2004],

$$D(x) \to \frac{1}{2x} + \frac{1}{4x^3} + \cdots\,, \tag{G.12}$$

and so

$$\chi^0(k,\omega\to\infty) = \frac{nk^2}{m}\frac{1}{\omega^2} + \frac{3k_B T n k^4}{m^2}\frac{1}{\omega^4}\,, \tag{G.13}$$

$$= \frac{\alpha}{\omega^2} + \frac{\beta}{\omega^4}\,, \tag{G.14}$$

where

$$\alpha = \frac{nk^2}{m}\,, \tag{G.15}$$

$$\beta = \frac{3k_B T n k^4}{m^2}\,. \tag{G.16}$$

Substituting Equation (G.14) for the high frequency expansion of the ideal gas response function into Equation (G.10) gives

$$\chi(k,\omega\to\infty) = \left(\frac{\alpha}{\omega^2}+\frac{\beta}{\omega^4}\right)\left[1+\Delta\left(\frac{\alpha}{\omega^2}+\frac{\beta}{\omega^4}\right)+\cdots\right], \tag{G.17}$$

$$\approx \frac{\alpha}{\omega^2}+[\beta+\Delta\alpha^2]\frac{1}{\omega^4}, \tag{G.18}$$

where in the second line terms that are higher order than $O\left(\frac{1}{\omega^4}\right)$ have been ignored. Reinstating the symbols α, β and Δ in Equation (G.18) gives

$$\chi(k,\omega\to\infty) = \frac{nk^2}{m}\frac{1}{\omega^2}+\left[\frac{3k_BTnk^4}{m^2}+\frac{n^2k^4}{m^2}v(k)(1-G(k,\omega\to\infty))\right]\frac{1}{\omega^4}. \tag{G.19}$$

The desired expression for high frequency limit of $G(k,\omega)$ is obtained by comparing the above equation to an alternative high frequency expansion of the response function. This alternative expansion comes from the Kramers-Kronig relation for the response function given in Equation (G.3), which can be written as

$$\chi(k,z) = -\frac{1}{\pi}\frac{1}{z}\int_{-\infty}^{\infty}\frac{\chi^{''}(k,\omega)}{1-\omega/z}d\omega. \tag{G.20}$$

As $z\to\infty$,

$$\chi(k,z\to\infty) = -\frac{1}{\pi}\frac{1}{z}\int_{-\infty}^{\infty}\chi^{''}(k,\omega)\left[1+\frac{\omega}{z}+\left(\frac{\omega}{z}\right)^2+\left(\frac{\omega}{z}\right)^3+\cdots\right]d\omega, \tag{G.21}$$

$$= -\frac{1}{\pi}\sum_{p=1}^{\infty}\frac{1}{z^p}\int_{-\infty}^{\infty}\omega^p\frac{\chi^{''}(k,\omega)}{\omega}d\omega. \tag{G.22}$$

Next, the fluctuation dissipation theorem of Equation (G.7) is used to write Equation (G.22) in terms of the frequency moments of the DSF as

$$\chi(k,z\to\infty) = \frac{n}{k_BT}\sum_{p=1}^{\infty}\frac{1}{z^{2p}}\int_{-\infty}^{\infty}\omega^{2p}S(k,\omega)d\omega, \tag{G.23}$$

$$= \frac{n}{k_BT}\sum_{p=1}^{\infty}\frac{1}{z^{2p}}\langle\omega^{2p}\rangle, \tag{G.24}$$

where the fact that the odd frequency moments vanish since $S(k,\omega)$ is even in ω (which is a simple consequence of the even nature of the intermediate scattering function $F(k,t)$, shown in Appendix B) has been used. Equating the terms proportional to $1/\omega^2$ and $1/\omega^4$ in the two high frequency expansions of the response function given in Equations (G.19) and (G.24) then gives

$$\langle\omega^2\rangle = \frac{k_BT}{m}k^2, \tag{G.25}$$

which is simply the relation for the second frequency moment given in Equation (2.44) (an alternative and more direct derivation of this result is given in Appendix C), and

$$\langle \omega^4 \rangle = \frac{3(k_B T)^2}{m^2} k^4 + \frac{n k_B T k^4}{m^2} v(k)(1 - G(k, \omega \to \infty)) \,, \tag{G.26}$$

which can be written in reduced units (where $q = ka$) as

$$\frac{\langle \omega^4 \rangle}{\omega_p^4} = \frac{1}{3\Gamma} \left[\frac{q^4}{\Gamma} + q^2 - q^2 G(q, \omega \to \infty) \right] . \tag{G.27}$$

As shown in Appendix C, the fourth moment of the DSF of the OCP can be also written as

$$\frac{\langle \omega^4 \rangle}{\omega_p^4} = \frac{1}{3\Gamma} \left[\frac{q^4}{\Gamma} + q^2 - 2q^2 I(q) \right] \tag{G.28}$$

Finally then, comparing Equations (G.27) and (G.28) gives the high frequency limit of the LFC,

$$G(q, \omega \to \infty) = 2I(q) \,, \tag{G.29}$$

which is Equation (7.6).

Appendix H

Other MD results

In this appendix, MD results for the so called 'negative dispersion' of the OCP plasmon mode and for the self diffusion coefficient of both the YOCP and OCP are presented. The purpose of presenting these additional results here is that they could prove useful to others in future investigations of the YOCP and OCP systems.

'Negative dispersion' of the OCP plasmon refers to $d\omega(k)/dk < 0$, where $\omega(k)$ is the position of the plasmon peak in the DSF (this is the sharp peak seen at small wave numbers in Figures F.1 and F.2). The study of when exactly (specifically, at what value of Γ) the onset of negative dispersion occurs at long wavelengths [Mithen *et al.*, 2012c] was prompted by a relatively contemporary interest in this feature of OCP dynamics [Arkhipov *et al.*, 2010].

The position of the plasmon peak obtained from MD simulations was fitted to the polynomial

$$\omega(k)/\omega_p = 1 + \frac{b}{2!}(ka)^2 + \frac{c}{4!}(ka)^4 + \frac{d}{6!}(ka)^6\,, \tag{H.1}$$

for $\Gamma = 8, 9, 9.5$ and 10. The quality of this fit is indicated in Figure H.1, and the values obtained for the fitting parameters b, c and d are tabulated in Table H.1. From the b coefficient, it can be deduced that negative dispersion at long wavelengths sets in between $\Gamma = 9.5$ and $\Gamma = 10$. The position of the plasmon peak for several Γ values in the range $1 - 120$ is shown in Figure H.2 in order to illustrate the extent of its variation in the fluid regime. For further discussion of these results, the reader is referred to [Mithen *et al.*, 2012c].

The self diffusion coefficient, D, is a quantity of interest in fluids in general [Hansen & McDonald, 2006]; it has been investigated relatively recently for the OCP system [Daligault, 2006]. A standard way to compute the self diffusion coefficient is using

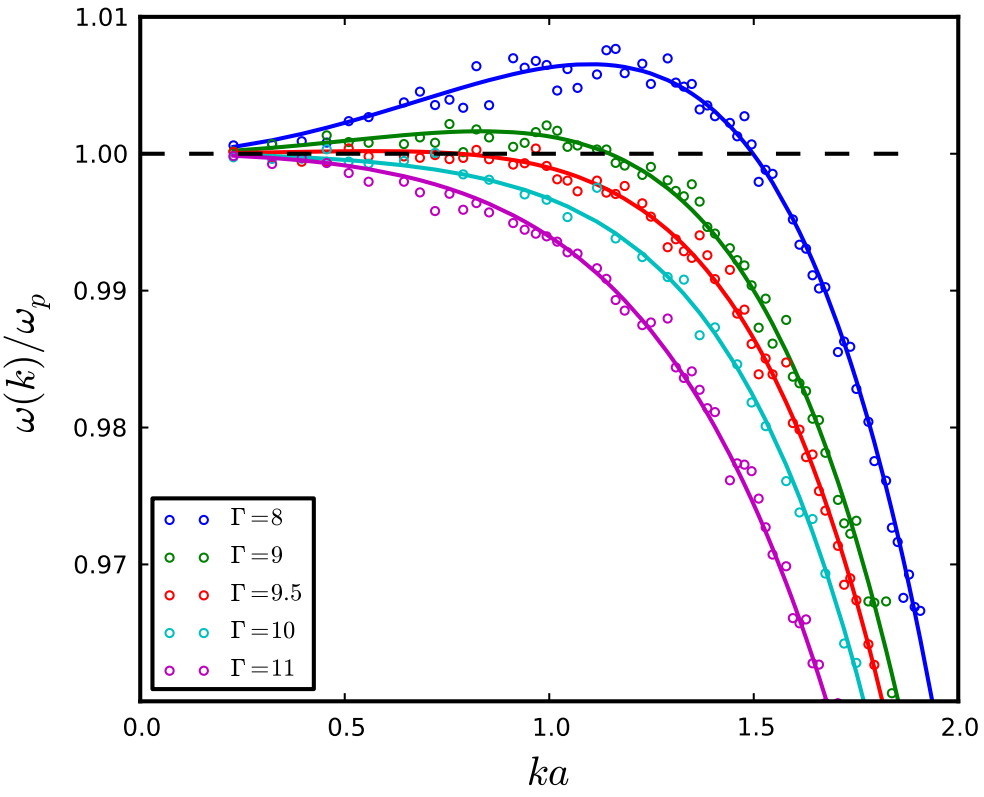

Figure H.1: Position of plasmon peak as obtained from MD simulations (open circles) along with the least squares fits to the functional form in Equation H.1 with the parameters shown in Table H.1 (solid lines).

	$\Gamma = 8$	$\Gamma = 9$	$\Gamma = 9.5$	$\Gamma = 10$	$\Gamma = 11$
b	0.01948	0.00887	0.00221	-0.00304	-0.00523
c	-0.06467	-0.06113	-0.03124	-0.02160	-0.07313
d	-0.52751	-0.44733	-0.59515	-0.61923	-0.27276

Table H.1: Parameters obtained from the fit given in Equation (H.1).

the Green-Kubo relation

$$D = \int_0^\infty Z(t)dt\,, \tag{H.2}$$

where $Z(t)$ is the velocity autocorrelation function (VACF), defined in Section 2.2 (Equation (2.22)). The VACF of the OCP and YOCP was computed with MD for a number of (Γ,κ) values. The results obtained for the reduced self diffusion coefficient, $\hat{D} = D/a^2\omega_p$ (where a is the average inter-particle distance and ω_p is the plasma frequency), are given in Table H.2.

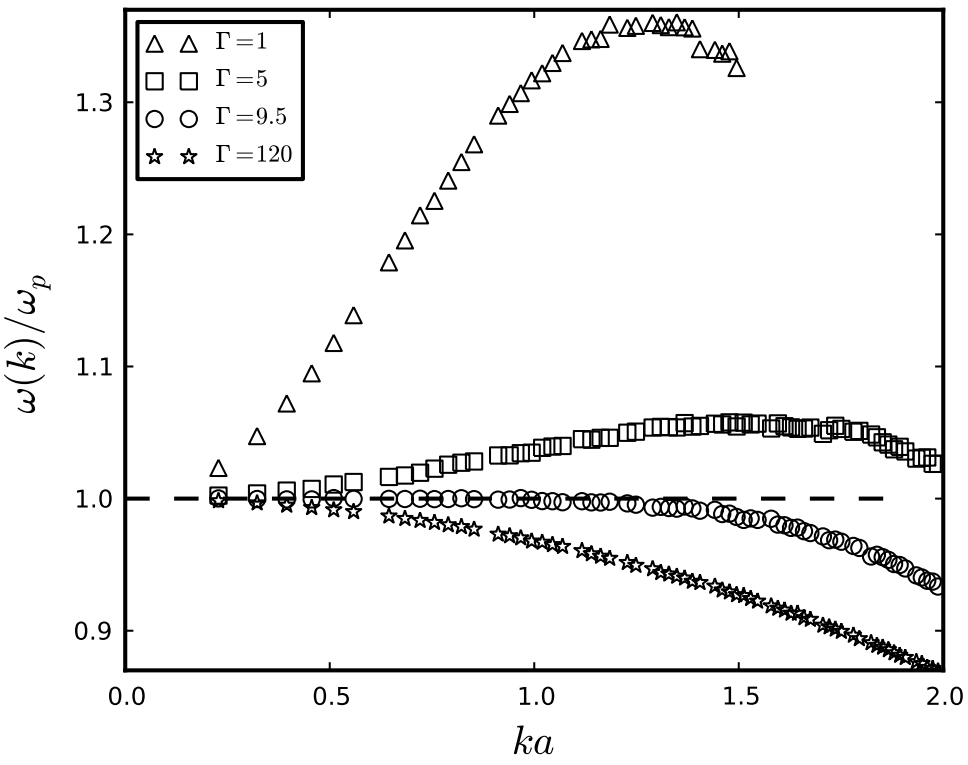

Figure H.2: Position of plasmon peak for a range of Γ values, as obtained from MD simulations.

OCP ($\kappa = 0$)	
Γ	$\hat{D}$
1	2.03
5	0.266
10	0.130
50	0.0208
120	0.00497
160	0.00268
175	0.00221

$\kappa = 0.1$	
Γ	$\hat{D}$
1	2.02
5	0.267
10	0.132
50	0.0209
120	0.00500
175	0.00213

$\kappa = 1$	
Γ	$\hat{D}$
1	2.61
5	0.307
10	0.149
50	0.0257
120	0.0139
175	0.00806

$\kappa = 2$	
Γ	$\hat{D}$
1	4.09
5	0.449
10	0.204
50	0.0399
120	0.0139
175	0.00806

Table H.2: Reduced self diffusion coefficient $\hat{D} = D/a^2\omega_p$ as computed from MD using the Green-Kubo relation in Equation (H.2).

Appendix I

List of Publications

- J. P. Mithen, J. Daligault and G. Gregori, Comparative merits of the memory function and dynamic local field correction of the classical one-component plasma, Phys. Rev. E *85*, 056407 (2012).
- J. P. Mithen, J. Daligault and G. Gregori, Onset of negative dispersion in the one-component plasma, AIP Conf. Proc. *1421*, 5861 (2012).
- J. P. Mithen, J. Daligault and G. Gregori, Molecular Dynamics Simulations for the Shear Viscosity of the One-Component Plasma, Contrib. Plasma Phys. *52*, 5861 (2012).
- J. P. Mithen, J. Daligault, B. J. B. Crowley and G. Gregori, Density fluctuations in the Yukawa one-component plasma: An accurate model for the dynamical structure factor, Phys. Rev. E *84*, 046401 (2011).
- J. P. Mithen, J. Daligault and G. Gregori, Extent of validity of the hydrodynamic description of ions in dense plasmas, Phys. Rev. E *83*, 015401 (2011).
- R. Schmidt, B. J. B. Crowley, J. Mithen, and G. Gregori, Quantum hydrodynamics of strongly coupled electron fluids, Phys. Rev. E *85*, 046408 (2012).
- G. Gregori, A. Ravasio, C. D. Murphy, K. Schaar, A. Baird, A. R. Bell, A. Benuzzi-Mounaix, R. Bingham, C. Constantin, R. P. Drake, M. Edwards, E. T. Everson, C. D. Gregory, Y. Kuramitsu, W. Lau, J. Mithen, C. Niemann, H.-S. Park, B. A. Remington, B. Reville, A. P. L. Robinson, D. D. Ryutov, Y. Sakawa, S. Yang, N. C. Woolsey, M. Koenig and F. Miniati, Generation of scaled protogalactic seed magnetic fields in laser-produced shock waves, Nature *481*, 480 (2012).

- P. Koester, N. Booth, C. A. Cecchetti, Hui Chen, R. G. Evans, G. Gregori, L. Labate, T. Levato, Bin Li, M. Makita, J. Mithen, C. Murphy, M. Notley, R. Pattathil, D. Riley, N. Woolsey and L. A. Gizzi, High resolution X-ray spectroscopy in fast electron transport studies, Proc. of SPIE *8080*, 80802E (2011).

- A. Pelka, G. Gregori, D. O. Gericke, J. Vorberger, S. H. Glenzer, M. M. Gnther, K. Harres, R. Heathcote, A. L. Kritcher, N. L. Kugland, B. Li, M. Makita, J. Mithen, D. Neely, C. Niemann, A. Otten, D. Riley, G. Schaumann, M. Schollmeier, An. Tauschwitz, and M. Roth, Ultrafast Melting of Carbon Induced by Intense Proton Beams, Phys. Rev. Lett. *105*, 265701 (2010).

- S. Toleikis, T. Bornath, T. Döppner, S. Düsterer, R. R. Fäustlin, E. Förster, C. Fortmann, S. H. Glenzer, S. Göde, G. Gregori, R. Irsig, T. Laarmann, H. J. Lee, B. Li, K.-H. Meiwes-Broer, J. Mithen, B. Nagler, A. Przystawik, P. Radcliffe, H. Redlin, R. Redmer, H. Reinholz, G. Röpke, F. Tavella, R. Thiele, J. Tiggesbäumker, I. Uschmann, S. M. Vinko, T. Whitcher, U. Zastrau, B. Ziaja and T. Tschentscher, Probing near-solid density plasmas using soft x-ray scattering, J. Phys. B *43*, 194017 (2010).

- Hui Chen, S. C. Wilks, D. D. Meyerhofer, J. Bonlie, C. D. Chen, S. N. Chen, C. Courtois, L. Elberson, G. Gregori, W. Kruer, O. Landoas, J. Mithen, J. Myatt, C. D. Murphy, P. Nilson, D. Price, M. Schneider, R. Shepherd, C. Stoeckl, M. Tabak, R. Tommasini, and P. Beiersdorfer, Relativistic Quasimonoenergetic Positron Jets from Intense Laser-Solid Interactions, Phys. Rev. Lett. *105*, 015003 (2010).

- S. M. Vinko, U. Zastrau, S. Mazevet, J. Andreasson, S. Bajt, T. Burian, J. Chalupsky, H. N. Chapman, J. Cihelka, D. Doria, T. Döppner, S. Düsterer, T. Dzelzainis, R. R. Fäustlin, C. Fortmann, E. Frster, E. Galtier, S. H. Glenzer, S. Göde, G. Gregori, J. Hajdu, V. Hajkova, P. A. Heimann, R. Irsig, L. Juha, M. Jurek, J. Krzywinski, T. Laarmann, H. J. Lee, R. W. Lee, B. Li, K.-H. Meiwes-Broer, J. P. Mithen, B. Nagler, A. J. Nelson, A. Przystawik, R. Redmer, D. Riley, F. Rosmej, R. Sobierajski, F. Tavella, R. Thiele, J. Tiggesbäumker, S. Toleikis, T. Tschentscher, L. Vysin, T. J. Whitcher, S. White, and J. S. Wark, Electronic Structure of an XUV Photogenerated Solid-Density Aluminum Plasma, Phys. Rev. Lett. *104*, 225001 (2010).

- R. R. Fäustlin, Th. Bornath, T. Döppner, S. Düsterer, E. Förster, C. Fortmann, S. H. Glenzer, S. Göde, G. Gregori, R. Irsig, T. Laarmann, H. J. Lee, B. Li, K.-H. Meiwes-Broer, J. Mithen, B. Nagler, A. Przystawik, H. Redlin, R. Redmer, H. Reinholz, G. Röpke, F. Tavella, R. Thiele, J. Tiggesbumker, S. Toleikis, I. Uschmann, S. M. Vinko, T. Whitcher, U. Zastrau, B. Ziaja, and Th. Tschentscher, Observation of Ultrafast Nonequilibrium Collective Dynamics in Warm Dense Hydrogen, Phys. Rev. Lett. *104*, 125002 (2010).

- S. Toleikis, R. R. Fäustlin, L. Cao, T. Döppner, S. Düsterer, E. Förster, C. Fortmann, S. H. Glenzer, S. Göde, G. Gregori, R. Irsig, T. Laarmann, H. J. Lee, B. Li, J. Mithen, K.-H. Meiwes-Broer, A. Przystawik, P. Radcliffe, R. Redmer, F. Tavella, R. Thiele, J. Tiggesbäumker, N. X. Truong, I. Uschmann, U. Zastrau, Th. Tschentscher, Soft X-ray scattering using FEL radiation for probing near-solid density plasmas at few electron volt temperatures, High Energy Density Phys. *6*, 15 (2009).

- M. Roth, I. Alber, V. Bagnoud, C. R. D. Brown, R. Clarke, H. Daido, J. Fernandez, K. Flippo, S. Gaillard, C. Gauthier, M. Geissel, S. Glenzer, G. Gregori, M. Günther, K. Harres, R. Heathcote, A. Kritcher, N. Kugland, S. LePape, B. Li, M. Makita, J. Mithen, C. Niemann, F. Nürnberg, D. Offermann, A. Otten, A. Pelka, D. Riley, G. Schaumann, M. Schollmeier, J. Schütrumpf, M. Tampo, A. Tauschwitz, and An. Tauschwitz, Proton acceleration experiments and warm dense matter research using high power lasers, Plasma Phys. Control. Fusion *51*, 124039 (2009).

- R. R. Fäustlin, S. Toleikis, Th. Bornath, T. Döppner, S. Düsterer, E. Förster, C. Fortmann, S. H. Glenzer, S. Göde, G. Gregori, R. Irsig, T. Laarmann, H. J. Lee, B. Li, K.-H. Meiwes-Broer, J. Mithen, A. Przystawik, H. Redlin, R. Redmer, H. Reinholz, G. Röpke, F. Tavella, R. Thiele, J. Tiggesbaäumker, I. Uschmann, U. Zastrau, and Th. Tschentscher, Soft X-Ray Thomson Scattering in Warm Dense Hydrogen at FLASH, Proc. of SPIE *7451*, 74510D (2009).

Bibliography

Ailawadi, N.K., Rahman, A. & Zwanzig, R. (1971). Generalized hydrodynamics and analysis of current correlation functions. *Phys. Rev. A*, **4**, 1616–1625.

Allen, M.P. & Tildesley, D.J. (1988). *Computer Simulation of Liquids*. OUP, New York.

Arfken, G.B. & Weber, H.J. (2005). *Mathematical Methods For Physicists International Student Edition (sixth edition)*. Academic Press, London.

Arkhipov, Y.V., Askaruly, A., Ballester, D., Davletov, A.E., Tkachenko, I.M. & Zwicknagel, G. (2010). Dynamic properties of one-component strongly coupled plasmas: The sum-rule approach. *Phys. Rev. E*, **81**, 026402.

Balescu, R. (1975). *Equilibrium and Nonequilibrium Statistical Mechanics*. Wiley, London.

Balescu, R. (1997). *Statistical Dynamics: Matter out of Equilibrium*. Imperial College Press, London.

Balucani, U. & Zoppi, M. (2002). *Dynamics of the Liquid State*. OUP, Oxford.

Balucani, U., Brodholt, J.P., Jedlovszky, P. & Vallauri, R. (2000). Viscosity of liquid water from computer simulations with a polarizable potential model. *Phys. Rev. E*, **62**, 2971–2973.

Baus, M. & Hansen, J.P. (1980). Statistical mechanics of simple coulomb systems. *Phys. Rep.*, **59**, 1–94.

Bernu, B. & Vieillefosse, P. (1978). Transport coefficients of the classical one-component plasma. *Phys. Rev. A*, **18**, 2345–2355.

Bernu, B., Vieillefosse, P. & Hansen, J. (1977). Transport coefficients of the classical one-component plasma. *Physics Letters A*, **63**, 301–303.

Boon, J. & Yip, S. (1991). *Molecular Hydrodynamics*. Dover, New York.

Bouras, I., Molnár, E., Niemi, H., Xu, Z., El, A., Fochler, O., Greiner, C. & Rischke, D.H. (2009). Relativistic shock waves in viscous gluon matter. *Phys. Rev. Lett.*, **103**, 032301.

Brush, S.G., Sahlin, H.L. & Teller, E. (1966). Monte carlo study of a one-component plasma .i. *J. Chem. Phys.*, **45**, 2102–2118.

Caillol, J. & Gilles, D. (2000a). Numerical simulations of screened coulomb systems. a comparison between hyperspherical and periodic boundary conditions. *Journal of Statistical Physics*, **100**, 905–932.

Caillol, J.M. & Gilles, D. (2000b). Monte carlo simulations of the yukawa one-component plasma. *Journal of Statistical Physics*, **100**, 933–947.

Callen, H.B. (1985). *Thermodynamics and an Introduction to Thermostatistics (second edition)*. Wiley, New York.

Carraresi, L., Celli, M. & Barocchi, F. (1993). The rayleigh-brillouin light scattering spectrum of dense argon gas between 70 and 260 mpa at t = 298 k: the sound velocity and the specific heats ratio . *Physics and Chemistry of Liquids*, **25**, 91–100.

Chen, F.F. (2006). *Introduction to Plasma Physics and Controlled Fusion: Vol. 1 (second edition)*. Springer, New York.

Chihara, J. (1987). Difference in x-ray scattering between metallic and non-metallic liquids due to conduction electrons. *Journal of Physics F: Metal Physics*, **17**, 295.

Chihara, J. (2000). Interaction of photons with plasmas and liquid metals - photoabsorption and scattering. *Journal of Physics: Condensed Matter*, **12**, 231.

D. H. Froula, N.C.L., S. H. Glenzer & Sheffield, J. (2010). *Plasma Scattering of Electromagnetic Radiation*. Academic Press, London.

Daligault, J. (2006). Liquid-state properties of a one-component plasma. *Phys. Rev. Lett.*, **96**, 065003.

Davidson, R.C., Arnett, D., Dahlburg, J. & Dimotakis, P. (2003). *Frontiers in high energy density physics: the X-games of contemporary science*. The National Academies Press, Washington, D.C.

de Schepper, I.M., Cohen, E.G.D., Bruin, C., van Rijs, J.C., Montfrooij, W. & de Graaf, L.A. (1988). Hydrodynamic time correlation functions for a lennard-jones fluid. *Phys. Rev. A*, **38**, 271–287.

Debye, P. & Hückel, E. (1923). Zur theorie der elektrolyte. i. gefrierpunktserniedrigung und verwandte erscheinungen [the theory of electrolytes. i. lowering of freezing point and related phenomena]. *Phys. Z.*, **24**, 185–206.

Deserno, M. & Holm, C. (1998). How to mesh up ewald sums. i. a theoretical and numerical comparison of various particle mesh routines. *The Journal of Chemical Physics*, **109**, 7678–7693.

Dewitt, H. & Slattery, W. (1999). Screening enhancement of thermonuclear reactions in high density stars. *Contributions to Plasma Physics*, **39**, 97–100.

Dimonte, G. & Daligault, J. (2008). Molecular-dynamics simulations of electron-ion temperature relaxation in a classical coulomb plasma. *Phys. Rev. Lett.*, **101**, 135001.

Donkó, Z. (2009). Molecular dynamics simulations of strongly coupled plasmas. *Journal of Physics A: Mathematical and Theoretical*, **42**, 214029.

Donkó, Z. & Hartmann, P. (2004). Thermal conductivity of strongly coupled yukawa liquids. *Phys. Rev. E*, **69**, 016405.

Donkó, Z. & Nyíri, B. (2000). Molecular dynamics calculation of the thermal conductivity and shear viscosity of the classical one-component plasma. *Physics of Plasmas*, **7**, 45–50.

Donkó, Z., Kalman, G.J. & Golden, K.I. (2002). Caging of particles in one-component plasmas. *Phys. Rev. Lett.*, **88**, 225001.

Donkó, Z., Kalman, G.J. & Hartmann, P. (2008). Dynamical correlations and collective excitations of yukawa liquids. *J. Phys.: Condens. Matter*, **20**, 413101.

Donkó, Z., Goree, J. & Hartmann, P. (2010). Viscoelastic response of yukawa liquids. *Phys. Rev. E*, **81**, 056404.

Dubin, D.H.E. (1990). First-order anharmonic correction to the free energy of a coulomb crystal in periodic boundary conditions. *Phys. Rev. A*, **42**, 4972–4982.

Erpenbeck, J.J. (1988). Shear viscosity of the lennard-jones fluid near the triple point: Green-kubo results. *Phys. Rev. A*, **38**, 6255–6266.

Evans, D.E. & Katzenstein, J. (1969). Laser light scattering in laboratory plasmas. *Reports on Progress in Physics*, **32**, 207.

Ewald, P.P. (1921). Die berechnung optischer und elektrostatischer gitterpotentiale. *Annalen der Physik*, **369**, 253–287.

Fäustlin, R.R., Bornath, T., Döppner, T., Düsterer, S., Förster, E., Fortmann, C., Glenzer, S.H., Göde, S., Gregori, G., Irsig, R., Laarmann, T., Lee, H.J., Li, B., Meiwes-Broer, K.H., Mithen, J., Nagler, B., Przystawik, A., Redlin, H., Redmer, R., Reinholz, H., Röpke, G., Tavella, F., Thiele, R., Tiggesbäumker, J., Toleikis, S., Uschmann, I., Vinko, S.M., Whitcher, T., Zastrau, U., Ziaja, B. & Tschentscher, T. (2010). Observation of ultrafast nonequilibrium collective dynamics in warm dense hydrogen. *Phys. Rev. Lett.*, **104**, 125002.

Ferziger, J.H. & Kaper, H.G. (1972). *Mathematical Theory of Transport Processes in Gases*. Elsevier, USA.

Fortmann, C., Bornath, T., Redmer, R., Reinholz, H., Röpke, G., Schwarz, V. & Thiele, R. (2009). X-ray thomson scattering cross-section in strongly correlated plasmas. *Laser and Particle Beams*, **27**, 311–319.

Frenkel, D. & Smit, B. (2001). *Understanding Molecular Simulation (second edition)*. Academic Press, London.

García Saiz, E., Gregori, G., Khattak, F.Y., Kohanoff, J., Sahoo, S., Shabbir Naz, G., Bandyopadhyay, S., Notley, M., Weber, R.L. & Riley, D. (2008). Evidence of short-range screening in shock-compressed aluminum plasma. *Phys. Rev. Lett.*, **101**, 075003.

Gaskell, D.R. (2008). *Introduction to the thermodynamics of materials (fifth edition)*. Taylor & Francis, London.

Gedalin, M. (1996). Covariant relativistic hydrodynamics of multispecies plasma and generalized ohm's law. *Phys. Rev. Lett.*, **76**, 3340–3343.

Glenzer, S.H. & Redmer, R. (2009). X-ray thomson scattering in high energy density plasmas. *Rev. Mod. Phys.*, **81**, 1625–1663.

Glenzer, S.H., Landen, O.L., Neumayer, P., Lee, R.W., Widmann, K., Pollaine, S.W., Wallace, R.J., Gregori, G., Höll, A., Bornath, T., Thiele, R., Schwarz, V., Kraeft, W.D. & Redmer, R. (2007). Observations of plasmons in warm dense matter. *Phys. Rev. Lett.*, **98**, 065002.

Gonzalez, M.A. & Abascal, J.L.F. (2010). The shear viscosity of rigid water models. *The Journal of Chemical Physics*, **132**, 096101.

Gregori, G. & Gericke, D.O. (2009). Low frequency structural dynamics of warm dense matter. *Physics of Plasmas*, **16**, 056306.

Gregori, G., Kortshagen, U., Heberlein, J. & Pfender, E. (2002). Analysis of thomson scattered light from an arc plasma jet. *Phys. Rev. E*, **65**, 046411.

Gregori, G., Glenzer, S.H. & Landen, O.L. (2003a). Strong coupling corrections in the analysis of x-ray thomson scattering measurements. *Journal of Physics A: Mathematical and General*, **36**, 5971.

Gregori, G., Glenzer, S.H., Rozmus, W., Lee, R.W. & Landen, O.L. (2003b). Theoretical model of x-ray scattering as a dense matter probe. *Phys. Rev. E*, **67**, 026412.

Gregori, G., Glenzer, S.H., Rogers, F.J., Pollaine, S.M., Landen, O.L., Blancard, C., Faussurier, G., Renaudin, P., Kuhlbrodt, S. & Redmer, R. (2004). Electronic structure measurements of dense plasmas. *Physics of Plasmas*, **11**, 2754–2762.

Gregori, G., Ravasio, A., Hll, A., Glenzer, S. & Rose, S. (2007). Derivation of the static structure factor in strongly coupled non-equilibrium plasmas for x-ray scattering studies. *High Energy Density Physics*, **3**, 99 – 108.

Greytak, T.J. & Benedek, G.B. (1966). Spectrum of light scattered from thermal fluctuations in gases. *Phys. Rev. Lett.*, **17**, 179–182.

Hamaguchi, S., Farouki, R.T. & Dubin, D.H.E. (1996). Phase diagram of yukawa systems near the one-component-plasma limit revisited. *The Journal of Chemical Physics*, **105**, 7641–7647.

Hamaguchi, S., Farouki, R.T. & Dubin, D.H.E. (1997). Triple point of yukawa systems. *Phys. Rev. E*, **56**, 4671–4682.

Hansen, J.P. (1973). Statistical mechanics of dense ionized matter. i. equilibrium properties of the classical one-component plasma. *Phys. Rev. A*, **8**, 3096–3109.

Hansen, J.P. & McDonald, I.R. (2006). *Theory of Simple Liquids (third edition)*. Academic Press, London.

Hansen, J.P., McDonald, I.R. & Pollock, E.L. (1975). Statistical mechanics of dense ionized matter. iii. dynamical properties of the classical one-component plasma. *Phys. Rev. A*, **11**, 1025–1039.

Hartmann, P., Donkó, Z., Tierney, K.P., Lee, C.J. & Kalman, G.J. (2009). Higher harmonic generation in strongly coupled plasmas. *Journal of Physics A: Mathematical and Theoretical*, **42**, 214040.

Hockney, R. & Eastwood, J. (1981). *Computer Simulations Using Particles*. McGraw-Hill, New York.

Hong, J. & Kim, C. (1991). Dynamic structure of strongly coupled one-component plasmas. *Phys. Rev. A*, **43**, 1965–1971.

Ichimaru, S. (1982). Strongly coupled plasmas: high-density classical plasmas and degenerate electron liquids. *Rev. Mod. Phys.*, **54**, 1017–1059.

Ichimaru, S. (2004). *Statistical Plasma Physics: v. 1: Basic Principles*. Westview Press, London.

Ichimaru, S. & Tanaka, S. (1986). Generalized viscoelastic theory of the glass transition for strongly coupled, classical, one-component plasmas. *Phys. Rev. Lett.*, **56**, 2815–2818.

Ichimaru, S., Iyetomi, H. & Tanaka, S. (1987). Statistical physics of dense plasmas: Thermodynamics, transport coefficients and dynamic correlations. *Physics Reports*, **149**, 91 – 205.

Johnson, D.W. (1975). A fourier series method for numerical kramers-kronig analysis. *Journal of Physics A: Mathematical and General*, **8**, 490.

Krall, N.A. & Trivelpiece, A.W. (1973). *Principles of Plasma Physics*. McGraw-Hill, New York.

Kremp, D., Schlanges, M. & Kraeft, W.D. (2005). *Quantum statistics of Nonideal Plasmas*. Springer-Verlag, Berlin.

Kugler, A.A. (1975). Theory of the local field correction in an electron gas. *Journal of Statistical Physics*, **12**, 35–87.

Landau, L.D. & Lifshitz, E.M. (1987). *Fluid Mechanics (second edition)*. Butterworth-Heinemann, Oxford.

Laplace, P.S. (1902). *"A Philosophical Essay on Probabilities", translated into English from the original French 6th ed. by Truscott, F.W. and Emory,F.L.*. Wiley, New York.

Levesque, D., Verlet, L. & Kürkijarvi, J. (1973). Computer "experiments" on classical fluids. iv. transport properties and time-correlation functions of the lennard-jones liquid near its triple point. *Phys. Rev. A*, **7**, 1690–1700.

Lindl, J.D., Amendt, P., Berger, R.L., Glendinning, S.G., Glenzer, S.H., Haan, S.W., Kauffman, R.L., Landen, O.L. & Suter, L.J. (2004). The physics basis for ignition using indirect-drive targets on the national ignition facility. *Physics of Plasmas*, **11**, 339–491.

Mansour, M.M., Garcia, A.L., Lie, G.C. & Clementi, E. (1987). Fluctuating hydrodynamics in a dilute gas. *Phys. Rev. Lett.*, **58**, 874–877.

March, N.H. (2005). *Liquid Metals: Concept and Theory*. Cambridge University Press, New York.

March, N.H. & Tosi, M.P. (1991). *Atomic Dynamics in Liquids*. Dover, New York.

McCracken, B. & Stott, P. (2005). *Fusion: the Energy of the Universe*. Elsevier, London.

Mijakovi, M., Kei, B., Zorani, L., Sokoli, F., Asenbaum, A., Pruner, C., Wilhelm, E. & Perera, A. (2011). Ethanol-water mixtures: ultrasonics, brillouin scattering and molecular dynamics. *Journal of Molecular Liquids*, **164**, 66 – 73.

Mithen, J.P., Daligault, J., Crowley, B.J.B. & Gregori, G. (2011a). Density fluctuations in the yukawa one-component plasma: An accurate model for the dynamical structure factor. *Phys. Rev. E*, **84**, 046401.

Mithen, J.P., Daligault, J. & Gregori, G. (2011b). Extent of validity of the hydrodynamic description of ions in dense plasmas. *Phys. Rev. E*, **83**, 015401.

Mithen, J.P., Daligault, J. & Gregori, G. (2012a). Comparative merits of the memory function and dynamic local-field correction of the classical one-component plasma. *Phys. Rev. E*, **85**, 056407.

Mithen, J.P., Daligault, J. & Gregori, G. (2012b). Molecular dynamics simulations for the shear viscosity of the one-component plasma. *Contrib. Plasma Phys.*, **52**, 58–61.

Mithen, J.P., Daligault, J. & Gregori, G. (2012c). Onset of negative dispersion in the one-component plasma. *AIP Conference Proceedings*, **1421**, 68–72.

Mon, K.K., Gann, R. & Stroud, D. (1981). Thermodynamics of liquid metals: The hard-sphere versus one-compoent-plasma reference systems. *Phys. Rev. A*, **24**, 2145–2150.

Mori, H. (1965). Transport, collective motion, and brownian motion. *Progress of Theoretical Physics*, **33**, 423–455.

Mountain, R.D. (1966). Spectral distribution of scattered light in a simple fluid. *Rev. Mod. Phys.*, **38**, 205–214.

Murillo, M.S. (2010). X-ray thomson scattering in warm dense matter at low frequencies. *Phys. Rev. E*, **81**, 036403.

Palmer, B.J. (1994). Transverse-current autocorrelation-function calculations of the shear viscosity for molecular liquids. *Phys. Rev. E*, **49**, 359–366.

Pelka, A., Gregori, G., Gericke, D.O., Vorberger, J., Glenzer, S.H., Günther, M.M., Harres, K., Heathcote, R., Kritcher, A.L., Kugland, N.L., Li, B., Makita, M., Mithen, J., Neely, D., Niemann, C., Otten, A., Riley, D., Schaumann, G., Schollmeier, M., Tauschwitz, A. & Roth, M. (2010). Ultrafast melting of carbon induced by intense proton beams. *Phys. Rev. Lett.*, **105**, 265701.

Poll, P.D., Ashcroft, N.W. & DeWitt, H.E. (1988). One-component plasma bridge function. *Phys. Rev. A*, **37**, 1672–1678.

Press, W.H., Teukolsky, S.A., Vetterling, W.T. & Flannery, B.P. (1992). *Numerical Recipes in C, 2nd ed.*. Cambridge, New York.

Redmer, R. & Röpke, G. (2010). Progress in the theory of dense strongly coupled plasmas. *Contributions to Plasma Physics*, **50**, 970–985.

Remington, B.A., Drake, R.P. & Ryutov, D.D. (2006). Experimental astrophysics with high power lasers and z pinches. *Rev. Mod. Phys.*, **78**, 755–807.

Rhodes, R. (2005). *Dark Sun*. Simon & Schuster, New York.

Ross, J.S., Glenzer, S.H., Palastro, J.P., Pollock, B.B., Price, D., Divol, L., Tynan, G.R. & Froula, D.H. (2010). Observation of relativistic effects in collective thomson scattering. *Phys. Rev. Lett.*, **104**, 105001.

Ross, M., DeWitt, H.E. & Hubbard, W.B. (1981). Monte carlo and perturbation-theory calculations for liquid metals. *Phys. Rev. A*, **24**, 1016–1020.

Rostoker, N. & Rosenbluth, M.N. (1960). Test Particles in a Completely Ionized Plasma. *Physics of Fluids*, **3**, 1–14.

Ryckaert, J.P., Bellemans, A., Ciccotti, G. & Paolini, G.V. (1989). Evaluation of transport coefficients of simple fluids by molecular dynamics: Comparison of green-kubo and nonequilibrium approaches for shear viscosity. *Phys. Rev. A*, **39**, 259–267.

Saigo, T. & Hamaguchi, S. (2002). Shear viscosity of strongly coupled yukawa systems. *Physics of Plasmas*, **9**, 1210–1216.

Salin, G. & Caillol, J.M. (2003). Equilibrium molecular dynamics simulations of the transport coefficients of the yukawa one component plasma. *Physics of Plasmas*, **10**, 1220–1230.

Scopigno, T., Balucani, U., Ruocco, G. & Sette, F. (2002). Inelastic x-ray scattering study of the collective dynamics in liquid sodium. *Phys. Rev. E*, **65**, 031205.

Tanaka, S. & Ichimaru, S. (1987). Dynamic theory of correlations in strongly coupled, classical one-component plasmas: Glass transition in the generalized viscoelastic formalism. *Phys. Rev. A*, **35**, 4743–4754.

Velarde, G. & Carpintero-Santamaría, N. (2007). *Inertial Confinement Nuclear Fusion: A Historical Approach by Its Pioneers*. Foxwell & Davies, London.

Verlet, L. (1967). Computer "experiments" on classical fluids. i. thermodynamical properties of lennard-jones molecules. *Phys. Rev.*, **159**, 98–103.

Vieillefosse, P. & Hansen, J.P. (1975). Statistical mechanics of dense ionized matter. v. hydrodynamic limit and transport coefficients of the classical one-component plasma. *Phys. Rev. A*, **12**, 1106–1116.

Vinko, S.M., Ciricosta, O., Cho, B.I., Engelhorn, K., Chung, H.K., Brown, C.R.D., Burian, T., Chalupsky, J., Falcone, R.W., Graves, C., Hajkova, V., Higginbotham, A., Juha, L., Krzywinski, J., Lee, H.J., Messerschmidt, M., Murphy, C.D., Ping, Y., Scherz, A., Schlotter, W., Toleikis, S., Turner, J.J., Vysin, L., Wang, T., Wu, B., Zastrau, U., Zhu, D., Lee, R.W., Heimann, P.A., Nagler, B. & Wark, J.S. (2012). Creation and diagnosis of a solid-density plasma with an x-ray free-electron laser. *Nat. Phys.*, **0**, 1–5.

Yokoyama, I. & Naito, S. (1989). Entropies and specific heats of liquid transition metals: one-component plasma model. *Physica B: Condensed Matter*, **154**, 309–312.

Zwanzig, R. (1961). *Boulder Lectures in Theoretical Physics, volume 3, p. 106*. Wiley-Interscience, New York.